Handbook on Secondary Particle Production and Transport by High-Energy Heavy Ions

(with CD-Rom)

Takashi Nakamura
Lawrence Heilbronn

Handbook on Secondary Particle Production and Transport by High-Energy Heavy Ions

(with CD-Rom)

Handbook on Secondary Particle Production and Transport by High-Energy Heavy Ions

(with CD-Rom)

Takashi Nakamura
Tohoku University, Japan

Lawrence Heilbronn
Lawrence Berkeley National Laboratory, USA

World Scientific

NEW JERSEY • LONDON • SINGAPORE • BEIJING • SHANGHAI • HONG KONG • TAIPEI • CHENNAI

Published by

World Scientific Publishing Co. Pte. Ltd.

5 Toh Tuck Link, Singapore 596224

USA office: 27 Warren Street, Suite 401-402, Hackensack, NJ 07601

UK office: 57 Shelton Street, Covent Garden, London WC2H 9HE

British Library Cataloguing-in-Publication Data
A catalogue record for this book is available from the British Library.

HANDBOOK ON SECONDARY PARTICLE PRODUCTION AND TRANSPORT BY HIGH-ENERGY HEAVY IONS

Copyright © 2006 by World Scientific Publishing Co. Pte. Ltd.

All rights reserved. This book, or parts thereof, may not be reproduced in any form or by any means, electronic or mechanical, including photocopying, recording or any information storage and retrieval system now known or to be invented, without written permission from the Publisher.

For photocopying of material in this volume, please pay a copying fee through the Copyright Clearance Center, Inc., 222 Rosewood Drive, Danvers, MA 01923, USA. In this case permission to photocopy is not required from the publisher.

ISBN 981-256-558-2

Namangan davlat universiteti
inv. № 25051
Axborot-resurs markazi

Printed in Singapore by Mainland Press

Preface

The high-energy heavy-ion accelerator facilitates the progress of accelerator science and research, such as the discovery of new super-heavy nuclei and unstable nuclei, and the clinical studies and treatment of cancer. The high-energy heavy-ion constituents of cosmic radiation are also considered in space exploration. Heavy ion accelerator facilities are now operating or planned for construction around the world, and radioactive beam facilities using the spallation products from intense heavy ion beams are also under construction for these various purposes. In these high-energy heavy-particle facilities many secondary particles are created from nucleus-nucleus interactions, and these particles, especially neutrons, can produce radioactivities induced in accelerator and structural materials, air, water, and soil, and can penetrate through the facility building into the surrounding environment. It is therefore quite necessary to evaluate the emission of secondary particles, especially neutrons and the creation of the residual nuclei in various materials, in order to estimate the source terms of accelerator shielding design, and also to calculate the dose delivered in the human body during therapeutic irradiation.

When one of the authors, Takashi Nakamura, had performed the shielding design of the HIMAC facility (Heavy Ion Medical Accelerator in Chiba) at the National Institute of Radiological Sciences (NIRS), Japan more than 15 years ago, there existed no available experimental data on neutron production from heavy ions and no available computer codes for the heavy-ion transport calculation at all. The HIMAC accelerator is being operated for heavy-ion therapy mainly using C ion

beam and has been opened for scientific research studies since 1994. A Japanese group (Tohoku University, High Energy Accelerator Research Organization (KEK), Institute of Physical and Chemical Research (RIKEN), National Institute of Radiological Sciences (NIRS), headed by Takashi Nakamura) has done a series of systematic experiments on secondary particle production and transport by heavy ions over the past ten years since 1994. In 2000, an American group (Lawrence Berkeley National Laboratory (LBNL), Michigan State University, and Colorado University) coordinated by Lawrence H. Heilbronn, joined the HIMAC experiments.

In this handbook, we have compiled the experimental results on DDX (double differential neutron production cross section data), TTY (thick target neutron production yield data), heavy-ion produced neutron transport data, and spallation products production cross-section data taken at HIMAC. In addition to the HIMAC results, we have included some experimental results taken at other heavy ion accelerators with energies near or above 100 MeV/nucleon. Also, we have included the calculation models and codes for heavy ion reaction and transport. The numerical data recorded in the CD Rom is attached in the handbook. We do hope that this handbook will be useful for various applications.

We, the authors, very gratefully acknowledge the following persons for providing us the numerical data together with the tables and graphs in their experimental and computational work:

For DDX (double differential neutron production cross section data), Mr. Hisaki Sato, Tohoku University (Present address: Toshiba Co. Ltd.) and Dr. Yoshiyuki Iwata (NIRS). For TTY (thick target neutron production yield data), Dr. Tadahiro Kurosawa, Tohoku University (Present address: Advanced Industrial Science and Technology). For neutron transport data, Dr. Michiya Sasaki, Tohoku University (Present address: Central Research Institute of Electric Power Industries), Dr. Tomoya Nunomiya, Tohoku University (Present address: Fuji Electric Systems Co. Ltd.) and Dr. Reginald Ronnigen (Michigan State University). For spallation products production cross section data, Dr. Hiroshi Yashima, Tohoku University (Present address: Research Reactor Institute, Kyoto University) and Dr. Yuri Titarenko (Institute for Theoretical and Experimental Physics, Russia). For moving source

model, Dr. Takashi Kato, Tohoku University (Present address: Nikken Sekkei Co. Ltd.). For giving many references and supporting comments with the PHITS code, Dr. Hiroshi Iwase, Tohoku University (Present address: GSI (Gesellschaft fuer Schwerionenforschung), Germany).

Takashi Nakamura, Prof. Emeritus,
Tohoku University, Cyclotron and Radioisotope Center

Lawrence H. Heilbronn, Ph. D.
Lawrence Berkeley Laboratory, University of California

The Authors

Dr. Takashi Nakamura was born in Nara, Japan, in 1939. In 1962, he graduated from Kyoto University, School of Nuclear Engineering. In 1964, he received his master's degree from the Graduate School of Engineering at Kyoto University, and later that year became a research associate in the faculty of the School of Engineering at Kyoto University. In May of 1970, he received his Ph.D from the Graduate School of Engineering at Kyoto University. From April 1973 to March 1974, he was a guest researcher at the Atomic Energy Research Institute of Sweden. In 1975, he became an associate professor at the Institute for Nuclear Study, University of Tokyo. In 1986, he accepted the position of professor at the Cyclotron and Radioisotope Center at Tohoku University, and in 1999 he became a professor in the Graduate School of Engineering, Tohoku University. During his time at Tohoku University, he was also a guest professor at the Institute of Space and Astronautical Science (1987 – 1990), and was a guest professor at the National Institute of Radiological Sciences. Since 2003, he has been Professor Emeritus at Tohoku University and a Visiting Professor at the Cyclotron and Radioisotope Center at Tohoku University. During his professional career, he has received numerous awards, including the Ichimura Award (Innovative technological invention) in 1986, the Best Paper Award of the Atomic Energy Society of Japan (1995), the Distinguished Service Award for Nuclear Safety by the Minister of the Science and Technology

Agency of Japan (2000), and the American Health Physics Society William C. Morgan Lecturer Award (presented at the annual meeting in Cleveland, OH, USA, in 2001). From March 2001 to March 2003 he was the president of the Japan Health Physics Society. He is currently the President of the Asia Oceania Radiation Protection Association and the Deputy President of the Radiation Council of Japan.

Dr. Lawrence Heilbronn was born in Saginaw, Michigan, USA in 1956. He received his Ph.D. in experimental nuclear physics from Michigan State University in 1991. Prior to that, he received a M.S. from the University of Illinois in 1984 and a B.A. from the University of Montana in 1982. He is currently a staff scientist in the Life Sciences division at Lawrence Berkeley National Laboratory, where he has been working since 1991. He has received two Outstanding Performance Awards from the director of LBNL for work on the dosimetry of radiobiological experiments conducted at high-energy heavy-ion facilities. In 2000, he met Dr. Nakamura and joined his collaboration in measuring secondary neutron yields and cross sections at HIMAC. That association and research has led to the writing of this handbook.

Contents

Chapter 1

Introduction

High-energy heavy-ion accelerators facilitate the progress of accelerator science and research. Research topics, such as the discovery of new super-heavy and unstable nuclei, a new composition and damage research for material science, observation of the beam-plasma interaction and development of the inertial confinement fusion, clinical studies and treatments of the cancer therapy and radiotherapy surgeries, and the quest for the origin of the elements and the universe have benefited from the use of heavy-ion accelerators. Many heavy-ion accelerator facilities are now operating or are planned for construction in the world, and radioactive beam facilities using the spallation products from intense heavy ion beams are also under construction for various purposes. In these high-energy heavy-particle facilities, many secondary particles are created from nucleus-nucleus interactions, and these particles, especially neutrons, can produce radioactivities induced in accelerator and structural materials, air, water, and soil, and can penetrate through the facility building into the surrounding environment. It is therefore quite necessary to evaluate the emission of the secondary particles and the creation of the residual nuclei in various materials.

The high-energy heavy-ion constituents of cosmic radiation must also be considered in determining the risk to astronauts from radiation exposure in long-term missions, such as the extended stays on the International Space Station project (ISS) and prolonged missions to the moon and Mars. The interactions and transport phenomena of heavy ions in a medium including the human body must be well understood to estimate the dose absorbed by the patients during cancer treatment, to

estimate the exposure of astronauts and scientists in space and to design the shielding of accelerator facilities.

1.1 Radiation in Space Environment

The ionizing radiation environment in space is very complex, consisting of a low-level background of galactic cosmic radiation (GCR), transient solar particle events (SPE), and, while in the Earth orbit, the trapped electron and proton radiation belts. Figures 1.1 and 1.2 show the elemental composition and the differential energy spectra of galactic cosmic radiation on the international space station (ISS) orbit calculated [1.1] by the GCR code CREME [1.2], respectively. The GCR energy range extends up to several hundred GeV and distributions have a peak at energies of several hundred MeV to 1 GeV. About 98% of the GCR consists of protons and heavy ions, and 2% consists of electrons. The former component contains 87 % protons, 12 % He, and 1 % heavy ions. The energy spectrum, flux, and composition of SPE changes by an orders of magnitude during solar flares, with energies from several MeV to several tens of GeV, as shown in Fig. 1.3. SPE contains about 80 - 90 % protons, 10 - 20 % He and about 1 % heavy ions.

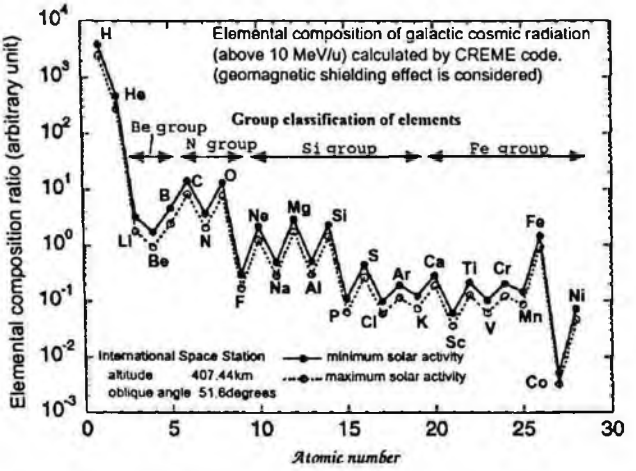

Figure 1.1: Elemental composition of galactic cosmic radiation on ISS orbits (courtesy of Ref. 1.1).

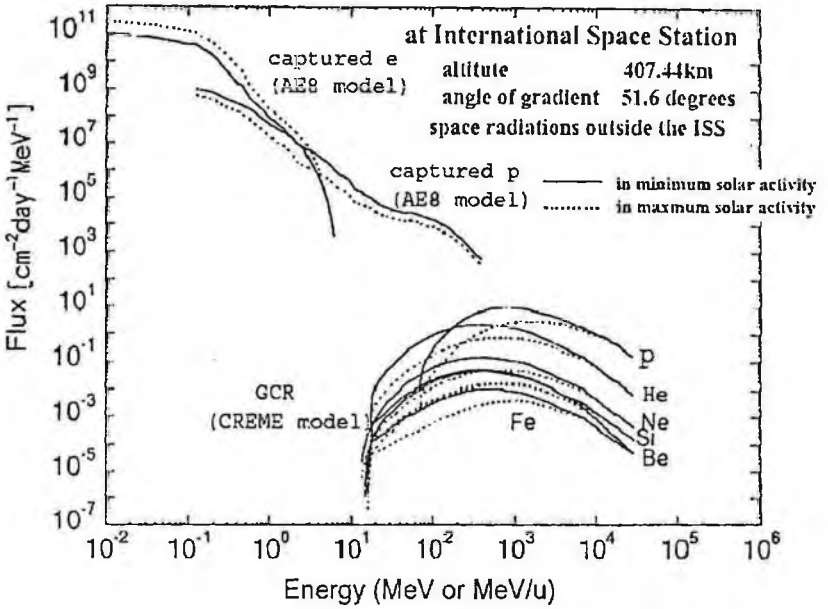

Figure 1.2: SPE and GCR energy spectra in the ISS orbit [1.1] calculated by the CREME code (courtesy of Ref. 1.2).

When these radiations traverse the shielding material of a space vehicle, they interact with the constituent elements through specific atomic and nuclear processes, including breaking up of ions into smaller fragments and producing secondary radiation that can penetrate more deeply into or through the material. The composition and intensity of these transmitted radiations (secondaries and fragments) depend on the elemental constituents of the specific materials. The radiation-induced injury in biological tissue depends on the composition and intensity of the transmitted particles. An extremely important secondary particle component in this respect is the neutron, which has no charge and its flux can not be reduced in atomic interactions thus being extremely damaging to biological tissue. Current theoretical models have shown the secondary neutrons to be a major contributor to exposures within possible lunar habitats and on the Martian surface, and recent studies have shown that neutrons could comprise 30 to 60 percent of the dose

equivalent on the ISS (International Space Station). A recent review of the neutron flux in the Earth's atmosphere has raised serious questions about the adequacy of our understanding of the production and propagation of neutrons by GCR in atmospheric components. Any advances in the specification of shielding for habitats on the moon or Mars require measurements of the transmitted neutron component within lunar and Martian shielding materials and improvements in databases and computational procedures.

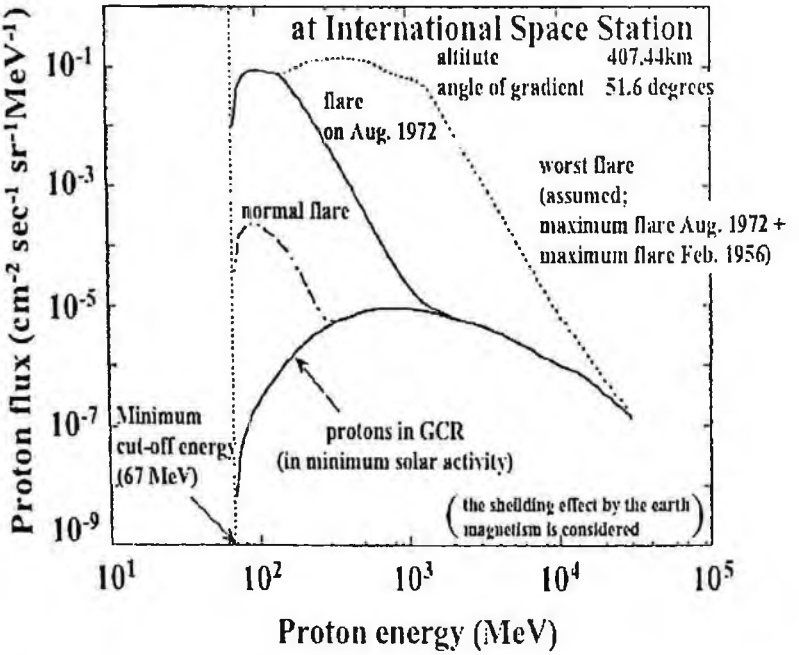

Figure 1.3: SPE and GCR proton energy spectra in the ISS orbit [1.1] calculated by the CREME code (courtesy of Ref. 1.2).

1.2 Heavy-Ion Accelerators for Medical Applications

It is important to use a type of radiation, which is well suited to medical treatment, especially in cancer therapy. The curative effect can be compared using the relative biological effectiveness (RBE) and the

oxygen enhancement ratio (OER). Fast neutrons and heavy ions exhibit three times the RBE and half times the OER of gamma rays and electrons, which are conventionally used in cancer therapy, as shown in Fig. 1.4.

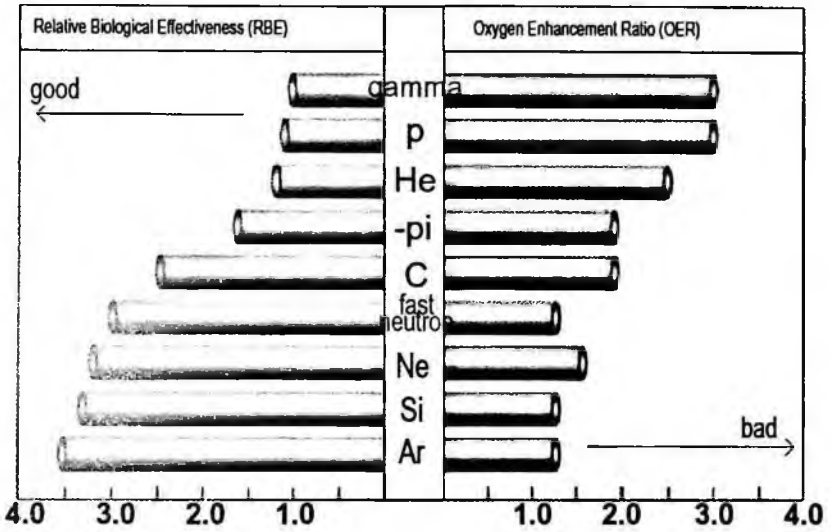

Figure 1.4: Relative biological effectiveness RBE and oxygen enhancement ratio OER of various radiations from gamma ray to Ar particle (courtesy of Ref. 1.3).

It is also important to avoid exposing normal tissue to the radiation. For this purpose, a good evaluation of the profile of the depth-dose distribution in the human body is required. Figure 1.5 shows the dose distributions in the human body of various radiations. Gamma rays and neutrons give the largest fraction of dose in the vicinity of the surface of the body (on the skin). They attenuate with depth, but reach deeply inside the body, where the normal tissue is located. It is possible to give a higher dose to a tumor in a deep position of the body by using the cross-firing method, however this method needs much time and complex processes for clinical treatment planning. Compared to gamma rays and neutrons, protons and heavy ions give a high dose locally just before stopping, as shown in Fig. 1.5. By using this strong localization of the

depth-dose distribution, the tumor area can be locally irradiated while keeping the normal tissue under a low dose field.

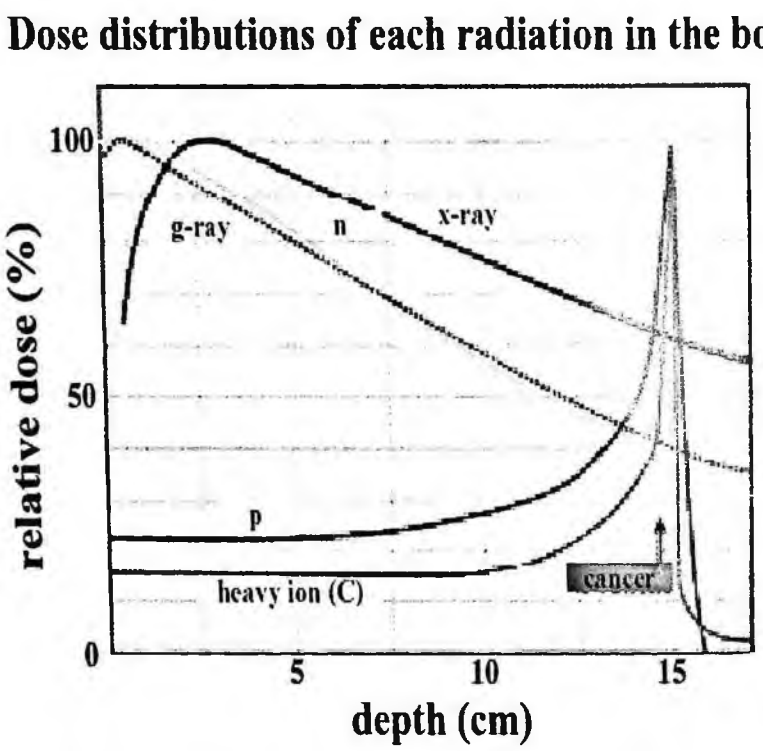

Figure 1.5: Dose distributions in the human body of various radiations (courtesy of Ref. 1.3).

From 1977 to 1992, 223 patients were treated with charged particles at the Lawrence Berkeley Laboratory (LBL), USA, for treatment of skull tumors, with good success. The Harvard Cyclotron Laboratory (HCL), in association with Massachusetts General Hospital (MGH), USA, has been treating patients with proton beam continuously since 1961. In 1985 a consortium of physicians, physicists and engineers formed an international working group, the Proton Therapy Cooperative Group (PTCOG), to further advance the study of clinical proton beam therapy. In 1990, Loma Linda University Medical Center (LLUMC), USA

became the first proton beam treatment center dedicated to clinical cancer treatments.

Heavy-ion therapy began at the Bevalac, Lawrence Berkeley Laboratory (LBL), in 1975, first using a Ne ion. That therapy program continued until the Bevalac was decommissioned in 1992. Since 1994 the HIMAC (Heavy Ion Medical Accelerator in Chiba) at the National Institute of Radiological Sciences (NIRS), Japan, has being operated for heavy-ion therapy, mainly using C beams. More recently, heavy-ion therapy started running at SIS (SchwerIonen Synchrotron) at GSI (Gesellschaft fuer Schwerionenforschung), Germany, using C ions from 1998, and at the Hyogo Ion Beam Medical Center, Japan using C ions from 2002. In addition there are many other facilities in the world, which employ proton and heavy-ion therapies.

The data on secondary particles ejected from the target and the spallation products in the target bombarding by the heavy ion beam are quite important to estimate the source terms of the accelerator shielding design and also to calculate the dose delivered in the human body during the therapeutic irradiation.

1.3 Radioisotope (RI) Beam Factory in Large-Scale Heavy-Ion Accelerators

In recent years the advent of radioisotope (RI) beams has opened up a number of new fascinating scientific fields. The RIKEN (Institute of Physical and Chemical Research) Accelerator Research Facility (RARF), Japan has undertaken construction of the RI beam factory (RIBF) as a next generation facility that is capable of providing the world's most intense RI beams over the whole range of atomic masses. The other RI beam facilities worldwide are:

ATLAS: Exotic Beam Facility at ANL, U.S.A

ISOLDE: Isotope Separation On Line Facility For Production of Radioactive Ion Beam at CERN

GANIL: Grand Accelerator D'Ions Lourdes, France

International Accelerator Facility at GSI, Germany

HRIBF: Holifield Radioactive Ion Beam Facility at ORNL, U.S.A.

ISAC: Isotope Separator and Accelerator at TRIUMF, Canada

E-Arena: Exotic Beam Facility at KEK, Japan.

These accelerators can accelerate very intense high-energy heavy-ion beams in order to produce sufficient yields of radioisotope beams through projectile and target fragmentation. Because of the high intensities used at these accelerators, it is very important in the design phase of the facility to evaluate the potential for radiation damage to the local materials (accelerator and structural materials, air, water, and soil), as well as evaluate the potential radiation exposures to humans (radiation workers and nearby inhabitants) in and around the facility. The high-energy heavy ion potentially creates a large amount of secondary fragments and residual nuclei when interacting with other nuclei. In the case of secondary particles, heavy ions are stopped readily in materials; however, they produce secondary particles through subsequent nuclear reactions before stopping. Secondary neutrons and gamma rays of no charge, especially neutrons, strongly penetrate the shielding and must be carefully considered in the design.

1.4 Purpose of This Handbook

When one of the authors, Nakamura, did the shielding design of the HIMAC heavy-ion medical accelerator facility more than 15 years before, there existed no available experimental data on neutron production from heavy ions and no available computer codes for the heavy-ion transport calculation at all. Therefore, we had to use the neutron production from He ions as a source term in the shielding design [1.4], which was calculated by the HERMES code [1.5]. Later, we

confirmed that the calculated results gave a large overestimation to the only existing experimental result by Cecil *et al.* [1.6] at the time.

Now, the HIMAC accelerator has been operating continuously for almost ten years, and our group has done systematic experiments to measure neutron TTY (Thick Target Yield) using the HIMAC heavy-ion beams. The measured results were actually used for the shielding design of the RIKEN RIBF. In addition, various other experiments have been done on secondary particle production and transport by heavy-ions for the past ten years at HIMAC. In this handbook, we compiled these experimental results along with some experimental results taken using other heavy-ion accelerators. In this handbook, we also included the calculation models and codes for heavy ion reaction and transport. The numerical data recorded in the CD Rom is attached in the handbook. We do hope that this handbook will be useful for various applications.

Chapter 2

Secondary Neutron Yields from Thick Targets

2.1 Overview of Measured Systems

The utility of measuring secondary neutron yields in thick-target, heavy-ion reactions lies in the relatively wide range of interactions that are possible in the target (at least compared with thin-target, cross-section measurements). This is especially true for targets that are thick enough to stop the primary beam. There, interactions with the primary beam occur over all energies up to the incident beam energy. In addition, secondary beam fragments can also interact in the target, producing neutrons, and secondary neutrons interact as they are transported through the target. The physical layout of these experiments is relatively simple. As such, these data provide a stringent test of the physics input to heavy-ion transport model calculations while keeping uncertainties due to modeling complex geometries to a minimum.

Table 2.1 contains a list of the secondary neutron thick-target data sets presented here. Unless otherwise noted, all targets are thick enough to stop the primary beam. The first column contains the beam ion species and beam energy in MeV/nucleon. The second column lists the targets used with each beam, with the thickness of the target noted in parentheses in units of cm. The third column lists the spectra that were measured. TTY indicates that double-differential thick target yields were measured, n/dΩ indicates that angular distributions were measured, and "total" indicates that total neutron yields were extracted. The total yields were usually limited to the angular range used in the measurements, so in most cases the total yields were not strictly "total" in the sense that they

cover the distribution over all 4π steradians. The fourth column indicates the laboratory angles where spectra were measured. The fifth column lists the minimum neutron energy that was measured at each angle indicated in the fourth column. In some cases the minimum neutron energy measured at a particular energy varied from target to target, so the reader is cautioned to refer to the data tables to obtain the minimum measured energy for each system and angle. The last column indicates the accelerator facility where the measurements took place. HIMAC is the Heavy Ion Medical Applications Center at the National Institute of Radiological Sciences in Chiba, Japan. NSCL is the National Superconducting Cyclotron Laboratory at Michigan State University in East Lansing, Michigan, USA. SREL is the now defunct Space Radiation Effects Laboratory that was located in Newport News, Virginia, USA. Bevalac is the now defunct high-energy, heavy-ion accelerator that was at Lawrence Berkeley National Laboratory in Berkeley, CA, USA.

Table 2.1: General information in regards to the heavy-ion, thick-target neutron yield experiments described here. The beam ion and energy, target material and thickness, type of measured spectra, laboratory angle, minimum measured neutron energy, and accelerator facility are shown.

Beam ion and energy (MeV/nucleon)	Targets (cm)	Measured spectra	θ (deg)	Emin (MeV)	Facility
He (100)	C (5.0) Al (4.0) Cu (1.5) Pb (1.5)	TTY n/dΩ total	0, 7.5, 15, 30, 60, 90	5.5, 5, 4, 3.5, 3.5, 3	HIMAC
He (155)	Al (8.26)	TTY n/dΩ total	10, 30, 45, 60, 90, 125, 160	10, 3, 3, 7, 4, 3, 3	NSCL
He (160)	Pb (3.937)	TTY Total	0, 45, 90, 120, 150	10, 3, 13, 13, 13	SREL
He (177.5)	C (14.73) H_2O (22.86) Steel (4.445) Pb (3.937)	TTY Total	0, 6, 15, 30, 45, 60, 90, 120, 135, 150	3, 10, 11, 11, 3, 10, 3, 13, 3, 13	SREL

Table 2.1 (continued)

Beam ion and energy (MeV/nucleon)	Targets (cm)	Measured spectra	θ (deg)	Emin (MeV)	Facility
He (180)	C (16.0) Al (12.0) Cu (4.5) Pb (5.0)	TTY n/dΩ total	0, 7.5, 15, 30, 60, 90	17, 11, 5.5, 6.5, 3.5, 3.5	HIMAC
C (100)	C (2.0) Al (1.0) Cu (0.5) Pb (0.5)	TTY n/dΩ total	0, 7.5, 15, 30, 60, 90	4, 4, 3.5, 3.5, 3, 3	HIMAC
C (155)	Al (8.26)	TTY n/dΩ total	10, 30, 45, 60, 90, 125, 160	10, 3, 3, 7, 4, 3, 3	NSCL
C (180)	C (6.0) Al (4.0) Cu (1.5) Pb (1.5)	TTY n/dΩ total	0, 7.5, 15, 30, 60, 90	5.5, 5.5, 3.5, 2.5, 3, 2.5	HIMAC
C (400)	C (20.0) Al (15.0) Cu (5.0) Pb (5.0)	TTY n/dΩ total	0, 7.5, 15, 30, 60, 90	8.5, 5, 3.5, 3, 3, 3	HIMAC
Ne (100)	C (1.0) Al (1.0) Cu (0.5) Pb (0.5)	TTY n/dΩ total	0, 7.5, 15, 30, 60, 90	6, 6, 5, 5.5, 5.5, 5	HIMAC
Ne (180)	C (4.0) Al (3.0) Cu (1.0) Pb (1.0)	TTY n/dΩ total	0, 7.5, 15, 30, 60, 90	9,6, 3.5, 3.5, 3, 3	HIMAC
Ne (400)	C (11.0) Al (9.0) Cu (3.0) Pb (3.0)	TTY n/dΩ total	0, 7.5, 15, 30, 60, 90	6, 5.5, 4, 3, 3, 3	HIMAC
Si (800)	C (23.0) Cu (6.5)	TTY n/dΩ total	0, 7.5, 15, 30, 60, 90	11, 8, 8, 4, 3.5, 3.5	HIMAC
Ar (400)	C (7.0) Al (5.5) Cu (2.0) Pb (2.0)	TTY n/dΩ total	0, 7.5, 15, 30, 60, 90	10, 7, 3.5, 3.5, 3, 3	HIMAC

Table 2.1 (continued)

Beam ion and energy (MeV/nucleon)	Targets (cm)	Measured spectra	θ (deg)	Emin (MeV)	Facility
Fe (400)	C (6.0) Al (4.0) Cu (1.5) Pb (1.5)	TTY n/dΩ total	0, 7.5, 15, 30, 60, 90	12, 11, 7, 4, 3, 3	HIMAC
Nb (272)	Nb (1.0) Al (1.27)	TTY n/dΩ n/dE total	3, 6, 9, 12, 16, 20, 24, 28, 32, 36, 40, 48, 56, 64, 72, 80	20 20 (all angles	Bevalac Bevalac
Nb (435)	Nb (0.51)	TTY n/dΩ n/dE total	3, 6, 9, 12, 16, 20, 24, 28, 32, 36, 40, 48, 56, 64, 72, 80	20 (all angles	Bevalac
Xe (400)	C (3.0) Al (2.0) Cu (1.0) Pb (1.0)	TTY n/dΩ total	0, 7.5, 15, 30, 60, 90	10, 6, 5, 3.5, 3.5, 3.5	HIMAC

2.2 Experimental Details

All of the experiments described here used the time-of-flight method to measure neutron energies. Table 2.1 shows the accelerator facilities that were used in the experiments. Details about the particular experiments at each facility are described below.

2.2.1 HIMAC experiments

Beams extracted from the synchrotron had a pulse width between 0.5 sec and 1 sec. One beam pulse was delivered every 3.3 seconds, and each pulse had a micro time-structure of 5MHz. Beam intensities were maintained at $1x10^5$-$1x10^6$ particles per pulse. Beam-spot sizes on the target were, in general, ~1.5cm in diameter. The beam height was 1.25m above the concrete floor of the experimental area.

Figure 2.1 shows a schematic diagram of the experimental setup. A thin NE102A plastic scintillator (30mm diameter by 0.5 mm thick) was placed just behind the exit window (made of 0.1mm thick Al) of the

beam line as a beam-pickup scintillator. The output pulses of this scintillator were used as start signals for the TOF measurement and were also used to count the absolute number of projectiles incident to the target. To avoid the counting loss due to voltage sag in the photomultiplier that is induced by high beam current, the voltages of the last three dynodes were externally supplied by a constant voltage power supply. The targets were set on the beam line 10-cm downstream from the beam pickup scintillator. NE213 liquid scintillators (12.7cm diameter by 12.7cm thick) were used for the neutron detector (E counter). In addition to the three detectors shown in Fig. 2.1, three other detectors were placed at 7.5° (5 m flight path), 30° (3 m flight path), and 60° (2 m flight path).

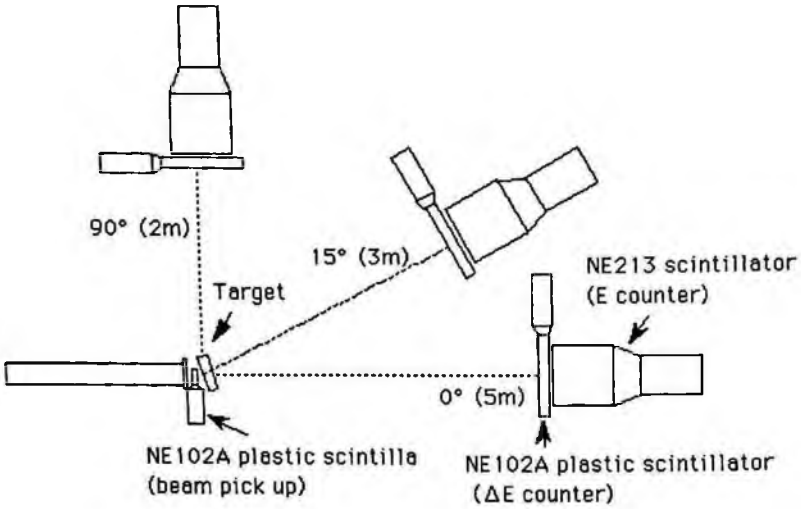

Figure 2.1: Schematic diagram of the general setup in the HIMAC experiments. The detectors at 0°, 15°, and 90° are shown, along with their respective flight paths (not to scale). The target was rotated 45° relative to the beam axis for measurements with the 90° detector (courtesy of Ref. 2.6).

The targets were 10-cm by 10-cm square, with their lengths indicated in Table 2.2. The face of the target was placed perpendicular to the

direction of the beam, except in the case of the measurements conducted at 30°, 60°, and 90°, where the target was rotated 45° relative to the beam. NE102A plastic scintillators (15x15 cm square by 0.5cm thick) were placed directly in front of the E counter as the ΔE counter to discriminate charged particles from neutrons and photons. To minimize neutron scattering, no local shielding was used near the detector. By interposing a Fe shadow bar (15x15cm square by 60cm thick) between the target and detector, the background neutron components from room scattering were measured.

Table 2.2: Thicknesses of the targets (in cm) used in the HIMAC thick-target yield experiments.

Beam	Target Thickness (cm)
100 MeV/nucleon He	C (5.0), Al (4.0), Cu (1.5), Pb (1.5)
100 MeV/nucleon C	C (2.0), Al (2.0), Cu (0.5), Pb (0.5)
100 MeV/nucleon Ne	C (1.0), Al (1.0), Cu (0.5), Pb (0.5)
180 MeV/nucleon He	C (16.0), Al (12.0), Cu (4.5), Pb (5.0)
180 MeV/nucleon C	C (6.0), Al (4.0), Cu (1.5), Pb (1.5)
180 MeV/nucleon Ne	C (4.0), Al (3.0), Cu (1.0), Pb (1.0)
400 MeV/nucleon C	C (20.0), Al (15.0), Cu (5.0), Pb (5.0)
400 MeV/nucleon Ne	C (11.0), Al (8.0), Cu (3.0), Pb (3.0)
400 MeV/nucleon Ar	C (7.0), Al (5.5), Cu (2.0), Pb (2.0)
400 MeV/nucleon Fe	C (4.0), Al (3.0), Cu (1.5), Pb (1.5)
400 MeV/nucleon Xe	C (3.0), Al (2.0), Cu (1.0), Pb (1.0)
800 MeV/nucleon Si	C (23.0), Cu (6.5)

Relative to the thickness of the E counters, the ΔE counters are extremely thin, and as such, have an extremely low probability of detecting a neutron or gamma ray that passes through it. Any event detected in the E counter that also scintillated in the ΔE counter was assumed to be a charged particle. In this way, neutron and gamma-ray events were separated from charged particle events. After applying the charged/uncharged particle discrimination, neutron and gamma-ray events were separated from each other by using two-dimensional total-slow pulse height graphical plots. In these plots, two distinct bands of events are evident, one for neutron events and the other for gamma-ray events. The two bands show a clear separation from each other down to

the lowest energy thresholds used in the data analysis. After obtaining the neutron TOF spectra, they are converted to energy spectra, using relativistic kinematics. The number of events at each neutron energy is corrected for the energy-dependent neutron detection efficiency. The experimentally determined detection efficiency for the scintillators used in the HIMAC experiments has been published by Nakao *et al.* [2.1], [2.2], but there are no data for neutrons of energy higher than 206 MeV. As such, the neutron detection efficiencies were calculated with the Monte Carlo code by Cecil *et al.*[2.3] over all energies. The time dispersion $\Delta\tau$ is taken as the FWHM of the prompt γ-ray peak observed in each neutron TOF spectrum. In general, the observed widths of the prompt peaks in the time spectra were on the order of 0.9 ns. The energy resolution for the highest energy neutrons at 15° and 30° (approximately 2000 MeV) is about 20%. At 60° and 90°, the energy resolution for the highest measured neutron energies (approximately 600 MeV) is about 40%. At each angle, as neutron energy decreases, the percent resolution also decreases. For all the spectra reported here, the widths of the energy bins are equal to or greater than the corresponding energy resolutions.

Additional experimental details may be found in Refs. [2.4], [2.5], [2.6], and [2.7].

2.2.2 NSCL experiments

Beams of fully-stripped 155 MeV/nucleon ^{4}He and ^{12}C were delivered by the K500 cyclotron at Michigan State University's National Superconducting Cyclotron Laboratory (NSCL). The period of the beam was 41.6 ns, and beam bursts were typically 1- to 3-ns wide. Beam spot size on the target was approximately 0.5 cm in diameter. The target for both beams was a 13.34-cm-long, 1.78-cm-diameter cylinder of Al with a 5.08-cm-long, 1.59-cm-diameter bore cut into the entrance of the target. The axis of the beam coincided with the cylindrical axis of the target.

The target was suspended inside a 91.44-cm diameter steel scattering chamber with a 3.2-mm-thick wall. Typical pressure inside the beam line and scattering chamber was 10^{-6} Torr. The aluminum target was held on a target ladder that could be moved in and out of the beam. For

normalization purposes, the number of beam particles incident on the target was calculated from the total amount of charge collected in the Al target, as read by a current integrator (the target was electrically isolated from the target ladder). The target ladder position was monitored remotely using a camera set up directly outside a see-through port located at –135 degrees on the scattering chamber. The target ladder also held a scintillating phosphor that was periodically moved into the beam to check on beam positioning.

Neutron detectors were placed outside the scattering chamber. The neutron detectors consisted of liquid scintillator held inside a cylindrical cell made of either glass or aluminum. The liquid scintillator was either BC-501 or NE-213, both of which have pulse-shape discrimination properties that allow for the separation of neutron events and gamma-ray events in the detectors. The detector cells were typically 12.7 cm in diameter and either 5.08- or 7.62-cm long.

Figure 2.2 shows a schematic view of the experimental setup. Arrays of seven detectors were placed at 10°, 30°, 45°, and 60° (beam left). An array of three detectors was placed at 90 degrees (beam left). Single detectors were placed at 125° and 160° (beam left), and at –30°, -45°, and –60° (beam right). The detectors at 10°, 30°, 45° (beam left) were placed approximately 405 cm from the target position. The detectors at 60° (beam left) were about 354 cm from the target, the detectors at 90° were about 242 cm from the target, and the detectors at 30°, 45°, and 60° (beam right) were about 204 cm from the target. The single detectors at 125° and 160° were 233 cm and 203 cm, respectively, from the target. Solid plastic "veto" scintillators, 6.35-mm thick and 12.7-cm in diameter, were placed between the target and the neutron detectors to detect charged particles with enough energy to make it into the neutron detectors. Background neutrons were measured by placing brass or steel "shadow bar" cylinders in the direct line between the target and neutron detectors. The shadow bars stopped all neutrons coming directly from the target, thus allowing only room-scattered, background neutrons to register in the detectors. Additional experimental details such as exact flight-path lengths and shadow bars lengths, may be found in Ref. [2.8].

Namangan davlat universiteti
inv. № 25051

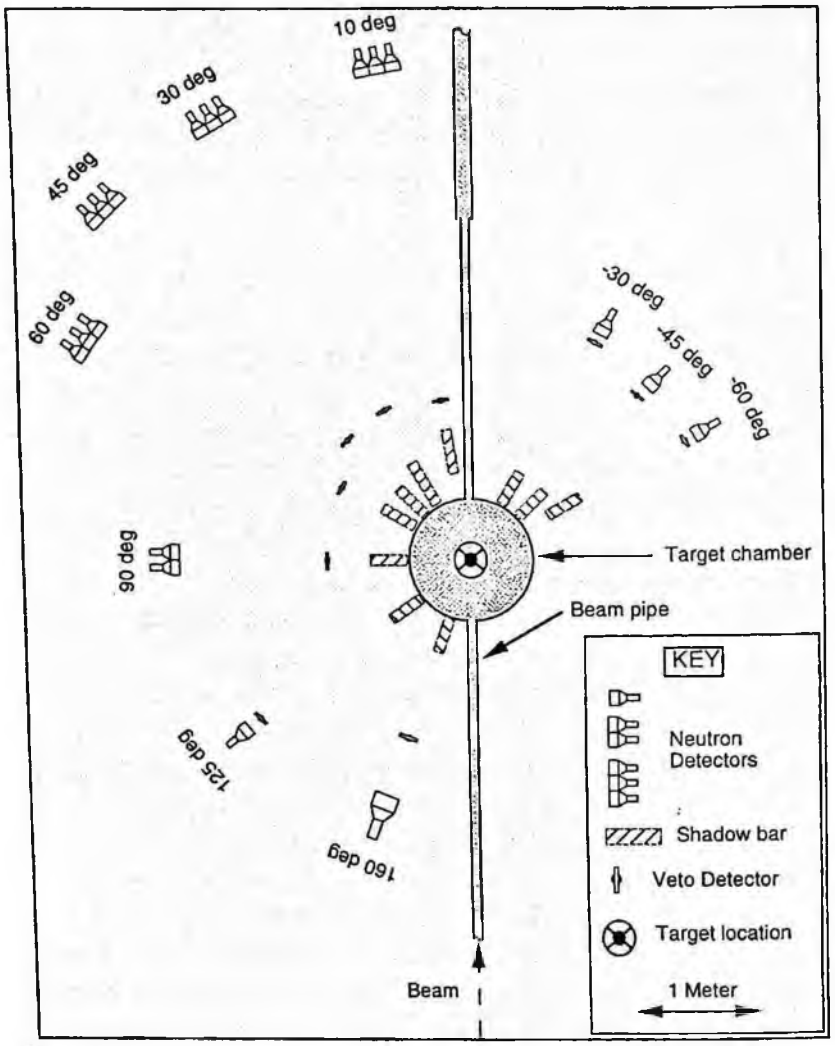

Figure 2.2: Overhead schematic view of the experimental setup used for the NSCL experiments (courtesy of Ref. 2.9).

The data were recorded on an event-by-event basis, with electronic logic and computer acquisition triggered by any event in a neutron detector that was above the detector's constant fraction discriminator's (CFD's) threshold. Typical CFD thresholds were set to one to three

times the ^{60}Co Compton edge. The following information was recorded for each valid event:

(1) - Identification number of the neutron detector in which the event took place
(2) - Total charge collected in the anode pulse from the neutron detector
(3) - Charge collected in the tail of the anode pulse from the neutron detector
(4) - Relative time between the event in the neutron detector and a radio-frequency signal from the cyclotron
(5) - Flag indicating whether or not the companion veto detector also registered an event
(6) - Total charge collected in the anode signal from the veto detector

Items 2 and 3 were used to discriminate events initiated by gamma rays from hadron events in the neutron detectors, using the methodology described in Ref. 11. Items 5 and 6 were used to discriminate events initiated by charged particles from neutron events in the neutron detectors. In addition to the items listed above, information regarding live time, prescale factors, total charge collected in the target, and total number of events in each detector was recorded from each run.

2.2.3 Bevalac experiments

Niobium beams with energies of 272 and 435 MeV/nucleon were accelerated at Lawrence Berkeley Laboratory's Bevalac facility. The beams were delivered in 1-s-long spills every 6 s, with approximately $3x10^5$ particles per spill on target. Two beam-defining scintillators were placed upstream from the target for the purpose of identifying beam particles focused on the target with a minimum divergence. A valid beam particle was defined by the coincidence between the two scintillators.

Figure 2.3 shows the general experimental layout used for the Bevalac experiments. A total of 16 neutron detectors were placed at 3°, 6°, 9°, 12°, 16°, 20°, 24°, 28°, 32°, 36°, 40°, 48°, 56°, 64°, 72°, and 80° in

the laboratory. All neutron detectors were 10.16-cm-thick by 101.6-cm-high rectangular slabs of NE102. The widths of the neutron detector (as seen from the perspective of the target location) varied from 2.5 cm at the most forward angles to 50.8 cm at the back-most angles. Directly in front of each neutron detector was a 6.4 mm thick NE102 scintillator with a height and width slightly larger than the accompanying neutron detector. This scintillator was used to reject any charged particles from the target that were incident on the neutron detector. A 1-cm-thick Nb target was used for the 435 MeV/nucleon run, and a 0.51-cm-thick Nb target and a 1.27-cm-thick Al target were used for the 272 MeV/nucleon runs. The targets were housed in a scattering chamber that had a thin Mylar window positioned between the target and neutron detectors. The centers of the targets and neutron detectors were approximately 3 m above the floor of the experimental hall. Table 2.3 indicates the flight paths to each detector.

Table 2.3: Widths and flight paths (in cm) for the neutron detectors used in the Bevalac experiments. Flight paths indicate the distance from the target to the front face of the detector.

Laboratory angle (deg)	Width (cm)	Flight Path (cm)
3	2.5	840
6	2.5	840
9	12.7	840
12	12.7	840
16	25.4	840
20	25.4	840
24	25.4	840
28	25.4	840
32	25.4	840
36	25.4	840
40	50.8	840
48	50.8	800
56	50.8	750
64	50.8	700
72	50.8	620
80	50.8	600

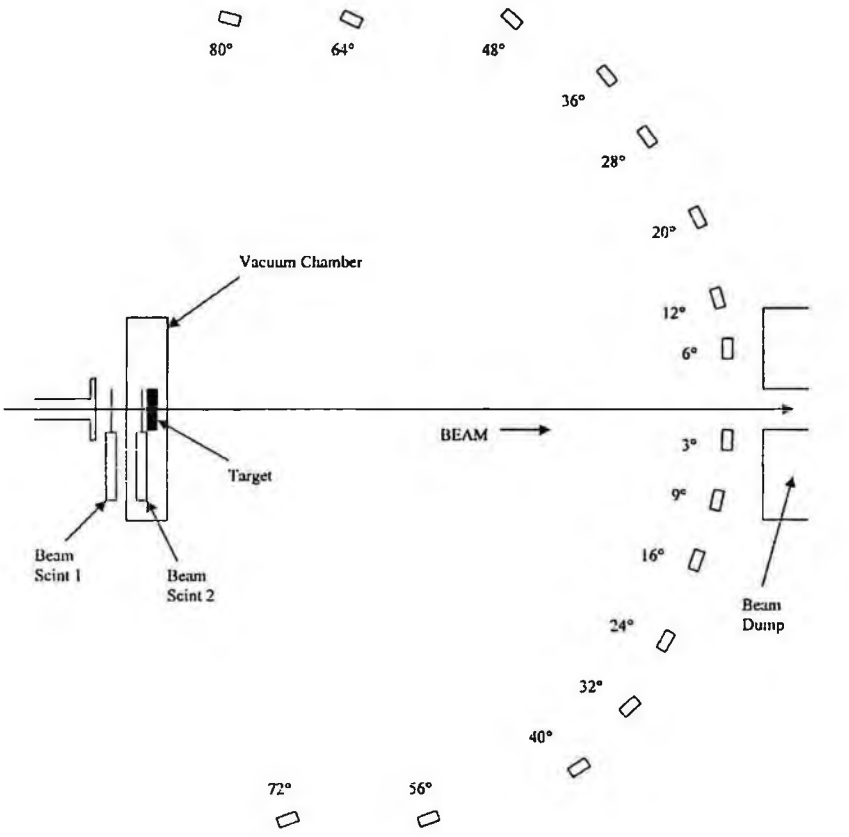

Figure 2.3: Schematic representation of the Bevalac experimental setup.

Background neutrons were not measured. The contribution to the spectra from background (room-scattered) neutrons was estimated for each detector using regions in the measured TDC spectra that were outside the kinematical boundaries for neutrons coming directly from the target. Neutron energy thresholds were set fairly high (about 20 MeV) in the off-line analysis to reduce the contribution from background neutrons. The loss of neutron flux from scattering in materials between the target and neutron detector was also estimated. For neutrons above

100 MeV, the loss of flux was estimated to be less than 5 %. For the lowest measured neutron energies, about 20 MeV, the loss of flux was the greatest and was estimated to be 15%. The reported neutron yields were corrected for the estimated background contributions and loss of flux. Neutron energies were determined by measuring the time of flight between a signal from the beam particle telescope and a mean-timed signal from the neutron detector. In this process, the detection efficiency of the neutron detector was also calculated using the code of Cecil *et al.*[2.3]. The timing resolution of the 435 MeV/nucleon run was measured by the width [full width at half maximum (FWHM)] of the prompt gamma-ray peak. It varied from 0.8 to 1.4 ns depending on the detector used. The timing resolution increased for the 272 MeV/nucleon runs to values between 1.4 and 1.7 ns. The raw TDC data for each detector and each run were rebinned such that the minimum bin width was at least the size of the appropriate timing resolution. Energy spectra were then produced from the rebinned TDC spectra.

Additional experimental details may be found in [2.9].

2.2.4 SREL experiments

The systems studied at the Space Radiation Effects Laboratory were 710 MeV ^{4}He (177.5 MeV/nucleon) stopping in carbon, water, steel and lead targets, and 640 MeV ^{4}He (160 MeV/nucleon) stopping in a lead target. The target thicknesses are listed in Table 2.1. The carbon and steel targets were rotated 23.5° relative to the beam axis. The lead target was rotated 22.5° relative to the beam axis. The water target was contained in a 22.9-cm long by 15.2-cm diameter aluminum cylinder. The cylinder's wall thickness was 1.4 mm. At the beam entrance to the cylinder was a 0.05-mm thick aluminum wall, and at the other end of the cylinder was a 3.2-mm thick window. The water target was not rotated relative to the beam axis.

The number of beam particles incident upon the target was counted using a coincidence between two 0.79-cm thick NE-102 scintillators. That coincidence was also used as part of the timing circuit in the time-of-flight measurement. Typical beam intensities were 5×10^4 particles per

second. The beam spot size was approximately 2-cm high by 3-cm wide. Data taking runs were between 1 and 4 hours.

Six cylindrical NE-102 neutron detectors were deployed in two different arrangements to yield measurements at 0°, 6°, 15°, 30°, 45°, 60°, 90°, 120°, and 150°. The two different configurations are shown schematically in Figures 2.4 and 2.5. The "forward" configuration (Fig. 2.4) had detectors placed between 0 and 45 degrees. The detector at -45° (beam left) was 20.3-cm thick by 23.9-cm diameter placed 5 meters from the target. The detectors at -15° and -30° were 21.6-cm thick by 12.7-cm diameter, and were also placed 5 meters from the target. The detector placed at 0° was 10.2-cm thick by 12.7-cm diameter, with a flight path of 4.9 meters from the target. The 6° detector was placed 6° above the beam axis in the forward direction. It was 10.2-cm thick by 12.7-cm diameter, and was placed 4.9 meters from the target. A 5.1-cm diameter by 5.1-cm thick NE-213 counter was placed at +45° (beam right), 1 meter from the target.

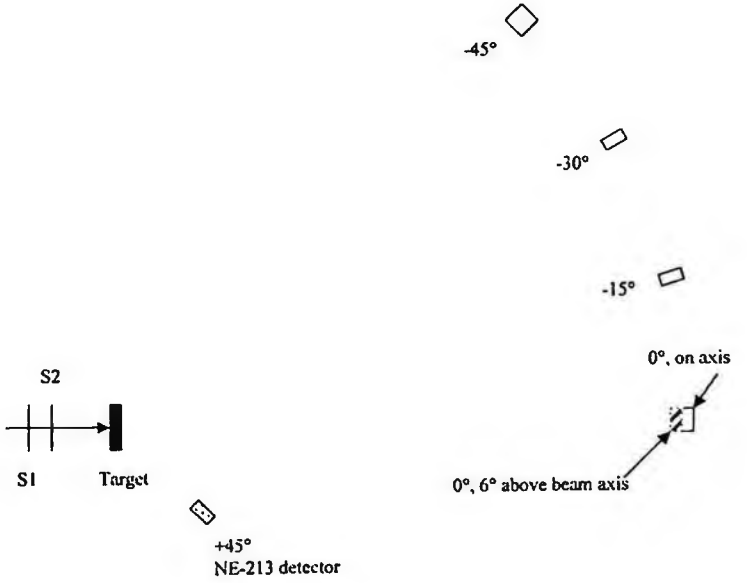

Figure 2.4: The "forward" detector configuration used in the SREL experiments. S1 and S2 are the two beam-telescope scintillators.

The "backward" configuration (Fig. 2.5) had detectors placed between 60° and 150°. NE-102 counters were placed at -60° (10.2-cm thick by 12.7-cm diameter, 3-meter flight path), -90° (21.6-cm thick by 12.7-cm diameter, 3-meter flight path), +120° (21.6-cm thick by 12.7-cm diameter, 2-meter flight path), and +150° (20.3-cm thick by 23.9-cm diameter, 2-meter flight path). In this configuration, the 5.1-cm diameter by 5.1-cm thick NE-213 counter was placed 1 meter from the target at 0°, -90°, and +135°. In both configurations, the NE-213 counter was used to measure the low-energy component of the neutron spectra.

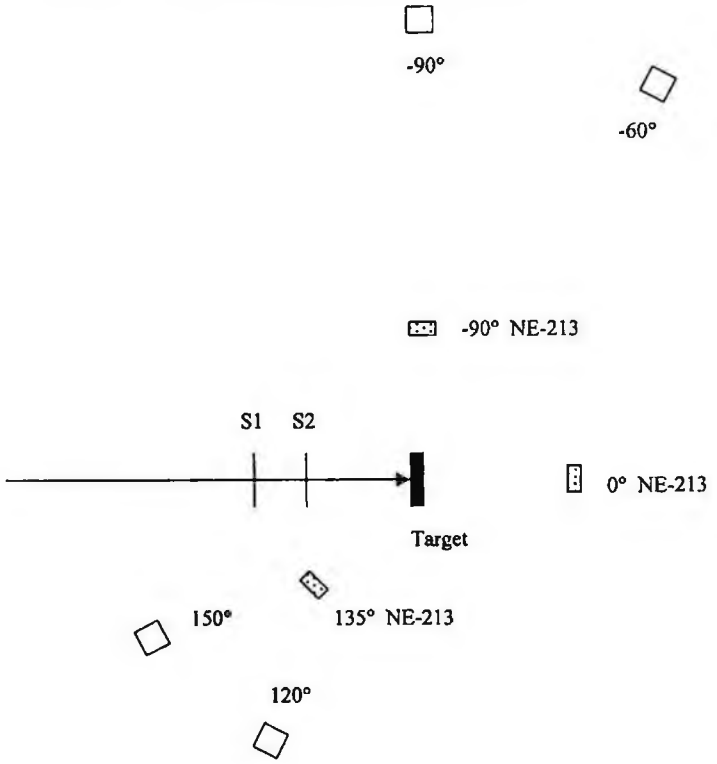

Figure 2.5: The "backward" detector configuration used in the SREL experiments.

Background events were not measured. Instead, the background was estimated by noting the number of counts in the region of the TOF

spectrum below the discrimination threshold and in the region on the fast side of the prompt gamma-ray peak. The authors assumed the background was flat from the slow side of the TOF spectrum to a point at 1.2 times the flight time of the high-energy peak observed in the spectrum, and then extrapolated linearly to the background level on the fast side of the spectrum. The authors estimate that a 25% uncertainty in background determination lead to an uncertainty in the extracted yields of no more than 7%.

Corrections to the data were made for detection efficiency using the Kent State neutron detection-efficiency code developed by Cecil, *et al.* [2.3]. Background subtraction was made using the method described above. The authors estimate that less than 1% of the neutron yield came from interactions of the beam with non-target materials such as exit windows and the water-target entrance window. Corrections were made for data acquisition system live time and for beam pile up.

Data was recorded on an event-by-event basis. All corrections mentioned above were applied in the offline analysis. Additional experimental details may be found in [2.10].

2.3 Results

2.3.1 Double-differential spectra

The double-differential thick-target yields (TTY) from the HIMAC series of experiments are shown in Figures 2.6 through 2.29. The statistical and systematic (normalization) uncertainties are not shown in order to provide an uncluttered display of the data. The principle investigators of the HIMAC experiments reported statistical uncertainties of 2 to 5% for the low-to-mid energy ranges (5 to 400 MeV), with uncertainties increasing to about 30% for the highest energies. The uncertainty in the number of beam particles incident upon the targets was estimated to be less than 3%. The uncertainty in solid angle acceptance due to detector size was determined to be less than 10%, and the uncertainty in the correction for detector efficiency was estimated to be about 10%. The

total systematic (normalization) uncertainty due to the factors described above is no more than 15%.

In general, the spectra in the forward direction have a broad peak at the high-energy end. The peak energy usually occurs at about 60 to 70% of the beam energy per nucleon. As the target mass becomes lighter and the projectile mass increases, the high-energy peak becomes more prominent. For example, the dependence on target mass can be clearly seen comparing the 400 MeV/nucleon C + C system with the 400 MeV/nucleon C + Pb system (Figs. 2.18 and 2.19). Comparing the 400 MeV/nucleon C + Pb and Xe + Pb systems (Figs. 2.19 and 2.27) shows a good example of the dependence on projectile mass. Most of the neutrons in this high-energy, forward region come from the breakup of the projectile and direct knock-on processes. Neutrons with up to 2.5 times the incoming beam energy per nucleon can be produced by these processes.

At energies below 20 MeV, the spectra are dominated by the breakup of the target. Because the target remnant is moving slowly in the lab frame, that source of neutrons is essentially isotropic. As such, target-like neutrons can be seen at all angles. As target mass increases, the relative contribution to the overall spectra from target breakup increases. This feature can be seen by comparing 400 MeV/nucleon C + C and C + Pb spectra (Figs. 2.18 and 2.19) at low energies.

At intermediate energies and intermediate angles, the spectra are dominated by the decay of the overlap region, where a sizeable number of projectile nucleons and target nucleons mix and can undergo several nucleon-nucleon collisions. As the impact parameter of the projectile-target interaction decreases, the likelihood of a surviving projectile source and target source also decreases, and the contribution of the overlap region becomes the dominant source. Because interactions in a thick-target experiment occur over all projectile energies up to the incident beam energy, one cannot definitively say that an intermediate-energy neutron at forward angles came from a projectile source or an overlap source, however.

Double-differential spectra from the Bevalac series of experiments can be seen in Figures 2.29 through 2.31. Figures 2.32 through 2.34 show the spectra from the SREL experiments, and the NSCL

experiments are displayed in Figs. 2.35 through 2.36. Statistical uncertainties are displayed. The same general features seen in the HIMAC double-differential spectra are observed in these systems. As the angle increases, the contribution from the projectile-like source decreases. Because the thresholds are higher in these spectra than the HIMAC spectra, there is less information regarding the contribution from the breakup of the target.

2.3.2 Angular distributions

Angular distributions from all systems are shown in Figs. 2.37-2.43 and 2.45-2.47. The HIMAC spectra (Figs. 2.37-2.41) were generated by integrating above 5 MeV. The threshold for the Bevalac spectra is 20 MeV, and 10 MeV for the SREL and NSCL spectra. The spectra from the 400 MeV/nucleon systems (Figs. 2.39-2.40) illustrate some of the points made above in the discussion of the double-differential spectra; namely, the contribution from projectile fragmentation is more pronounced for lighter-mass targets (as seen at forward angles), and the contribution from target-like sources increases as target mass increases (as seen at backward angles). In general, as the beam energy increases and beam mass increases, the angular spectra become more forward-focussed.

The lines shown in selected angular distributions show fits using the following equation:

$$Y = a_1 \exp(-a_2\theta) + a_3 \exp(-a_4\theta), \tag{2.1}$$

where Y is the yield (# per steradian per ion), θ is the angle (in degrees) and a_1, a_2, a_3, and a_4 are fit parameters. The two exponents represent the contributions to the spectra from the projectile-like source and the decay of the overlap region. Because target-like neutrons only go up to about 20 MeV, and because the angular spectra are generated by integrating over all energies, the contribution from target-like neutrons is dominated by the contributions from the other sources (especially for

spectra with relatively high neutron energy threshold). Table 2.4 shows the fit parameters to all the angular distributions using Eqn. 2.1. The units of a_1 and a_3 are number per steradian per ion, and the units of a_2 and a_4 are 1/deg.

Table 2.4: Fit parameters used in Eqn. 2.1 for the angular distributions in the indicated systems.

System	a_1 (#/(sr·ion))	a_2 (1/deg)	a_3 (#/(sr·ion))	a_4 (1/deg)
100 AMeV He + C	0.43	0.067	0.023	0.018
100 AMeV He + Al	0.40	0.076	0.051	0.023
100 AMeV He + Cu	0.31	0.059	0.013	0.000
100 AMeV He + Pb	0.21	0.052	0.022	0.026
100 AMeV C + C	0.73	0.097	0.108	0.035
100 AMeV C + Al	0.52	0.083	0.053	0.024
100 AMeV C + Cu	0.43	0.082	0.064	0.023
100 AMeV C + Pb	0.29	0.075	0.073	0.018
100 AMeV Ne + C	0.64	0.080	0.023	0.018
100 AMeV Ne + Al	0.46	0.069	0.013	0.010
100 AMeV Ne + Cu	0.32	0.062	0.018	0.009
100 AMeV Ne + Pb	0.26	0.051	0.013	0.000
155 AMeV He + Al	0.43	0.066	0.060	0.021
155 AMeV C + Al	0.20	0.074	0.050	0.0232
160 AMeV He + Pb	0.31	0.051	0.0093	0.000
177.5 AmeV He + C	0.96	0.064	0.043	0.015
177.5 AmeV He + water	0.77	0.064	0.063	0.021
177.5 AmeV He + steel	0.56	0.062	0.065	0.0145
177.5 AmeV He + Pb	0.49	0.051	0.022	0.0041
180 AMeV He + C	1.23	0.12	0.50	0.033
180 AMeV He + Al	1.03	0.095	0.30	0.025
180 AMeV He + Cu	0.63	0.090	0.33	0.027
180 AMeV He + Pb	0.49	0.060	0.18	0.014
180 AMeV C + C	2.32	0.235	1.09	0.041
180 AMeV C + Al	1.69	0.244	0.91	0.039
180 AMeV C + Cu	1.55	0.108	0.29	0.024
180 AMeV C + Pb	1.03	0.100	0.27	0.017
180 AMeV Ne + C	2.76	0.153	0.68	0.040
180 AMeV Ne + Al	2.18	0.142	0.43	0.033
180 AMeV Ne + Cu	1.33	0.173	0.56	0.037
180 AMeV Ne + Pb	0.99	0.134	0.35	0.021
272 AMeV Nb + Al	37	0.29	2.44	0.059

Table 2.4 (continued)

System	a_1 (#/(sr·ion))	a_2 (1/deg)	a_3 (#/(sr·ion))	a_4 (1/deg)
272 AMeV Nb + Nb	24	0.29	1.79	0.052
400 AMeV C + C	18.6	0.20	2.84	0.038
400 AMeV C + Al	12.1	0.18	1.88	0.032
400 AMeV C + Cu	9.0	0.16	1.33	0.028
400 AMeV C + Pb	6.1	0.13	1.05	0.018
400 AMeV Ne + C	41.5	0.33	3.03	0.039
400 AMeV Ne + Al	7.2	0.28	1.43	0.028
400 AMeV Ne + Cu	15.8	0.24	1.97	0.028
400 AMeV Ne + Pb	4.30	0.22	1.32	0.022
400 AMeV Ar + C	66.0	0.15	12.0	0.051
400 AMeV Ar + Al	44.0	0.15	10.0	0.048
400 AMeV Ar + Cu	29.0	0.15	8.9	0.046
400 AMeV Ar + Pb	18.0	0.15	6.8	0.037
400 AMeV Fe + C	69.0	0.20	5.5	0.047
400 AMeV Fe + Al	46.0	0.19	4.9	0.045
400 AMeV Fe + Cu	28.0	0.18	4.0	0.037
400 AMeV Fe + Pb	18.0	0.18	3.2	0.029
400 AMeV Xe + C	330.0	0.18	10.0	0.050
400 AMeV Xe + Al	130.0	0.20	10.0	0.050
400 AMeV Xe + Cu	100.0	0.22	7.8	0.045
400 AMeV Xe + Pb	68.0	0.23	6.0	0.033
435 AMeV Nb + Nb	90	0.41	5.4	0.052
800 AMeV Si + C	150.0	0.16	53.0	0.052
800 AMeV Si + Cu	80.0	0.15	26.0	0.040

The forward-focussed neutrons are represented by the first exponential term in Eqn. 2.1. In general, the value of a_1 increases with the product of the neutron number of the projectile and the range of each target, and decreases with the square of the mass number of the target. The value of a_2 remains about the same for each projectile and decreases with increasing target mass. The decay of the overlap region is represented by the second exponential term in Eqn. 2.1. The value of a_3 increases with projectile energy per nucleon and decreases, in general, as the target mass increases. The value of a_4 increases with the total kinetic energy of the projectile.

Comparing systems with the same projectile and target mass, it is found that the point where there are equal contributions from the projectile source and the overlap source shows a dependence on the momentum of the projectile. For the 272 MeV/nucleon Nb + Nb system, the point of equal contributions is at 12°, whereas for the 435 MeV/nucleon Nb + Nb system the point of equal contributions is at 9°. There is, roughly, a 25% change in beam momentum going from 272 to 435 MeV/nucleon, and the point of equal contribution also shifts by about 25% going from the lower energy to the higher energy.

2.3.3 Total yields

Table 2.5 shows the total yields from each system, along with the neutron energy threshold and angular range used to determine those yields. Plots of total yields above 5 MeV (Fig. 2.49) and above 10 MeV (Fig. 2.50) are shown for selected systems.

Table 2.5: Total yields (number per ion) for the indicated systems. The neutron energy threshold and angular range used to determine the yields are indicated in the second and third columns, respectively.

System	Threshold	Angular range	Yield (#/ion)
100 AMeV He + C	5 MeV	0° - 90°	0.26
100 AMeV He + Al	5 MeV	0° - 90°	0.26
100 AMeV He + Cu	5 MeV	0° - 90°	0.28
100 AMeV He + Pb	5 MeV	0° - 90°	0.30
100 AMeV C + C	5 MeV	0° - 90°	0.31
100 AMeV C + Al	5 MeV	0° - 90°	0.27
100 AMeV C + Cu	5 MeV	0° - 90°	0.28
100 AMeV C + Pb	5 MeV	0° - 90°	0.31
100 AMeV Ne + C	5 MeV	0° - 90°	0.28
100 AMeV Ne + Al	5 MeV	0° - 90°	0.26
100 AMeV Ne + Cu	5 MeV	0° - 90°	0.25
100 AMeV Ne + Pb	5 MeV	0° - 90°	0.30
155 AMeV He + Al	10 MeV	0° - 180°	0.348 ± 0.013
155 AMeV C + Al	10 MeV	0° - 180°	0.179 ± 0.005
160 AMeV He + Pb	10 MeV	0° - 180°	0.39
177.5 AmeV He + C	10 MeV	0° - 180°	0.58
177.5 AmeV He + water	10 MeV	0° - 180°	0.52
177.5 AmeV He + steel	10 MeV	0° - 180°	0.51

Table 2.5 (continued)

System	Threshold	Angular range	Yield (#/ion)
177.5 AmeV He + Pb	10 MeV	0° - 180°	0.51
180 AMeV He + C	5 MeV	0° - 90°	0.90
180 AMeV He + Al	5 MeV	0° - 90°	0.84
180 AMeV He + Cu	5 MeV	0° - 90°	0.76
180 AMeV He + Pb	5 MeV	0° - 90°	0.90
180 AMeV C + C	5 MeV	0° - 90°	1.27
180 AMeV C + Al	5 MeV	0° - 90°	1.11
180 AMeV C + Cu	5 MeV	0° - 90°	0.91
180 AMeV C + Pb	5 MeV	0° - 90°	1.07
180 AMeV Ne + C	5 MeV	0° - 90°	0.99
180 AMeV Ne + Al	5 MeV	0° - 90°	0.85
180 AMeV Ne + Cu	5 MeV	0° - 90°	0.76
180 AMeV Ne + Pb	5 MeV	0° - 90°	0.96
272 AMeV Nb + Al	20 MeV	0° - 90°	2.1 ± 0.3
272 AMeV Nb + Nb	20 MeV	0° - 90°	1.7 ± 0.2
400 AMeV C + C	5 MeV	0° - 90°	4.3
400 AMeV C + Al	5 MeV	0° - 90°	3.7
400 AMeV C + Cu	5 MeV	0° - 90°	3.3
400 AMeV C + Pb	5 MeV	0° - 90°	3.8
400 AMeV Ne + C	5 MeV	0° - 90°	4.5
400 AMeV Ne + Al	5 MeV	0° - 90°	2.6
400 AMeV Ne + Cu	5 MeV	0° - 90°	4.2
400 AMeV Ne + Pb	5 MeV	0° - 90°	3.2
400 AMeV Ar + C	5 MeV	0° - 90°	14.2
400 AMeV Ar + Al	5 MeV	0° - 90°	11.4
400 AMeV Ar + Cu	5 MeV	0° - 90°	10.3
400 AMeV Ar + Pb	5 MeV	0° - 90°	10.2
400 AMeV Fe + C	5 MeV	0° - 90°	7.8
400 AMeV Fe + Al	5 MeV	0° - 90°	6.7
400 AMeV Fe + Cu	5 MeV	0° - 90°	6.2
400 AMeV Fe + Pb	5 MeV	0° - 90°	6.3
400 AMeV Xe + C	5 MeV	0° - 90°	27.0
400 AMeV Xe + Al	5 MeV	0° - 90°	15.2
400 AMeV Xe + Cu	5 MeV	0° - 90°	12.8
400 AMeV Xe + Pb	5 MeV	0° - 90°	11.2
435 AMeV Nb + Nb	20 MeV	0° - 90°	4.5 ± 0.5
800 AMeV Si + C	5 MeV	0° - 90°	51.6
800 AMeV Si + Cu	5 MeV	0° - 90°	37.0

Results from the SREL experiments indicate that the total neutron yields above 10 MeV for the 177.5 MeV/nucleon systems are, to first order, independent of target mass. Furthermore, Cecil *et al.* [2.10] determined the total yields as a function of neutron energy threshold, and found the following relationship:

$$Y(T_n) = 2.35T_n^{-0.65}, \tag{2.2}$$

where T_n is the neutron energy threshold.

Comparing the total yields from the two 272 MeV/nucleon Nb systems, Heilbronn *et al.* [2.8] reported that the ratio of the neutron multiplicities followed a relationship first developed by Madey *et al.* [2.11] for neutron cross section measurements, namely;

$$M(Nb/Al, T > T_0) = \frac{\sigma_{Al}}{\sigma_{Nb}}\left[\frac{A_{Nb}^{1/3} + A_{Nb}^{1/3}}{A_{Al}^{1/3} + A_{Nb}^{1/3}}\right]^{\alpha(T_0)}. \tag{2.3}$$

$M(Nb/Al,T>T_0)$ is the ratio of the average Nb + Nb neutron multiplicity to the average Nb + Al neutron multiplicity above a neutron-energy threshold T_0, A_{Nb} and A_{Al} are the mass numbers of Nb and Al, σ_{Nb} and σ_{Al} are the total reaction cross sections for Nb + Nb and Nb + Al, respectively, and $\alpha_0(T_0)$ is the sole parameter that comes from a fitting in Ref. [2.11]. For a threshold of 20 MeV, $\alpha_0(T_0=20)$ is 4.57.

Kurosawa *et al.* [2.7] found that the HIMAC results verified the result found in Ref. [2.10] that the total yield shows very little dependence on target mass. Clearly, there is a dependence on projectile mass, and they found that the total yields above 5 MeV integrated between 0° and 90° could be estimated with the following formula:

$$Y = \frac{1.5\times10^{-6}}{N_T^{1/3}} E_P^2\left(A_P^{1/3} + A_T^{1/3}\right)^2 N_P \frac{A_P}{Z_P^2}, \tag{2.4}$$

where N_T and N_P are the neutron numbers of the target and projectile, A_T and A_P are the mass numbers of the target and projectile, Z_P is the atomic number of the projectile, and E_P is the incident energy per nucleon.

2.4 Double-Differential Thick-Target Yields from the HIMAC Experiments (Plots)

Figures 2.6 through 2.28 show the double-differential thick-target yields from all the systems measured by Kurosawa, et al. at the HIMAC facility at NIRS, Chiba, Japan. The angles are indicated by the symbols in the legend, and the spectra are in units of the number of neutrons per MeV per steradian per incoming beam ion.

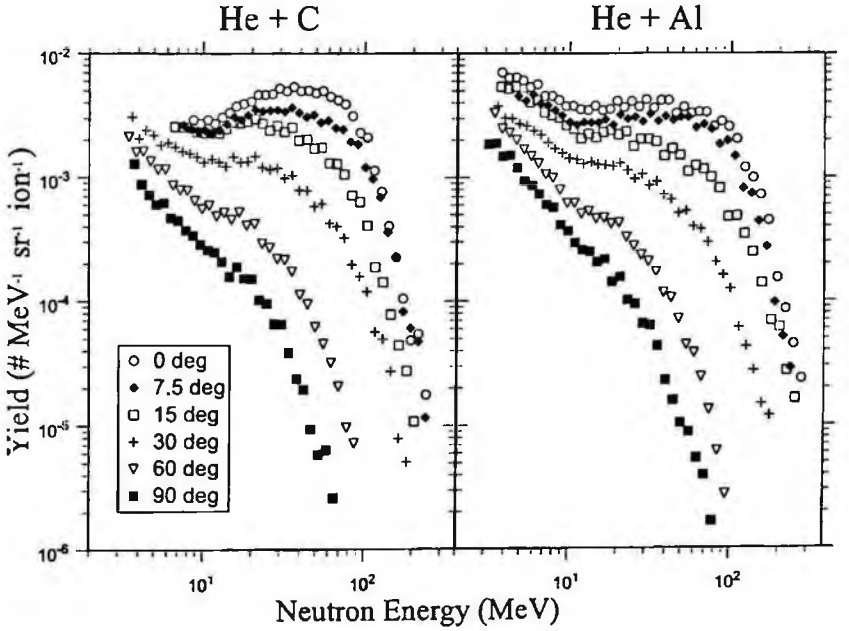

Figure 2.6: Double differential thick-target yields from 100 MeV/nucleon He stopping in carbon (left plot) and aluminum (right plot).

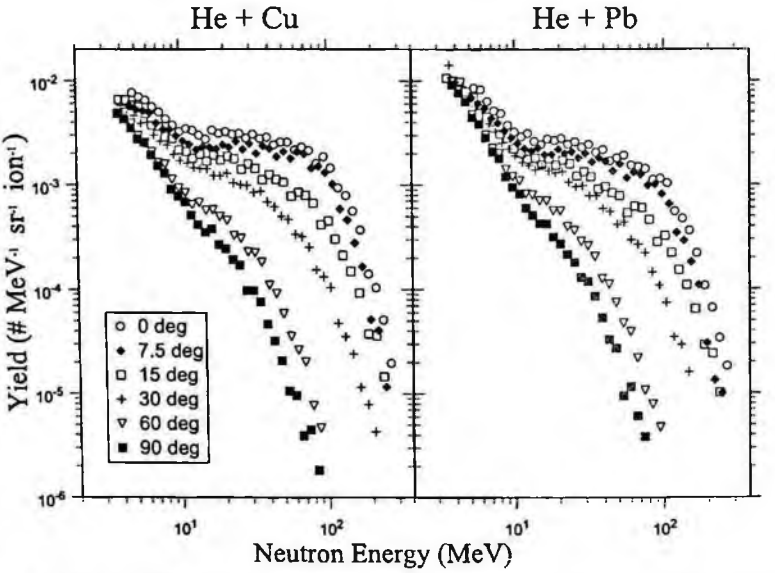

Figure 2.7: Double differential thick-target yields from 100 MeV/nucleon He stopping in copper (left plot) and lead (right plot).

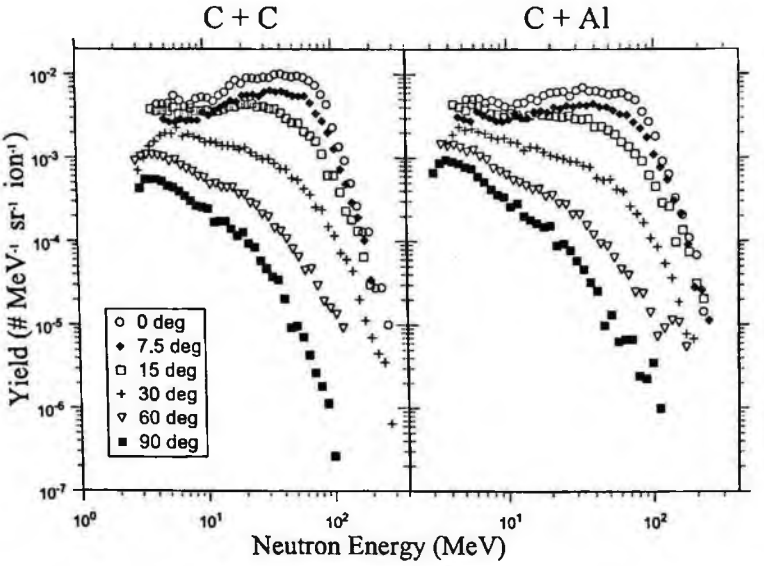

Figure 2.8: Double differential thick-target yields from 100 MeV/nucleon C stopping in carbon (left plot) and aluminum (right plot).

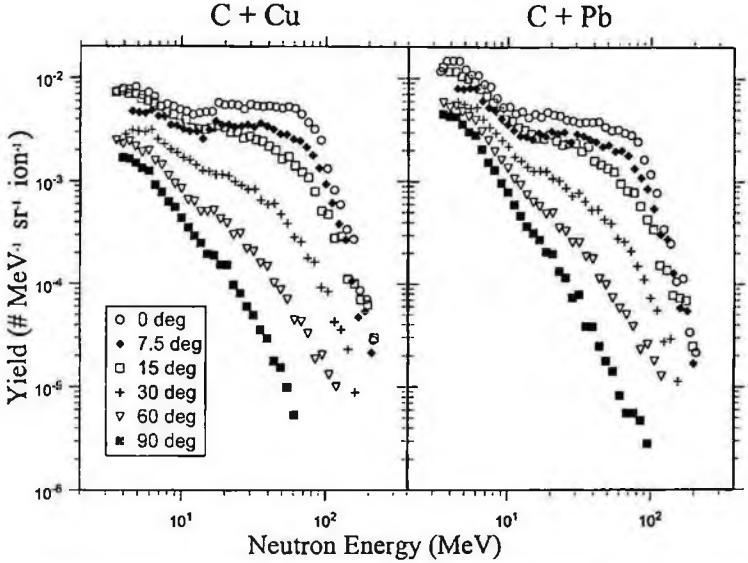

Figure 2.9: Double differential thick-target yields from 100 MeV/nucleon C stopping in copper (left plot) and lead (right plot).

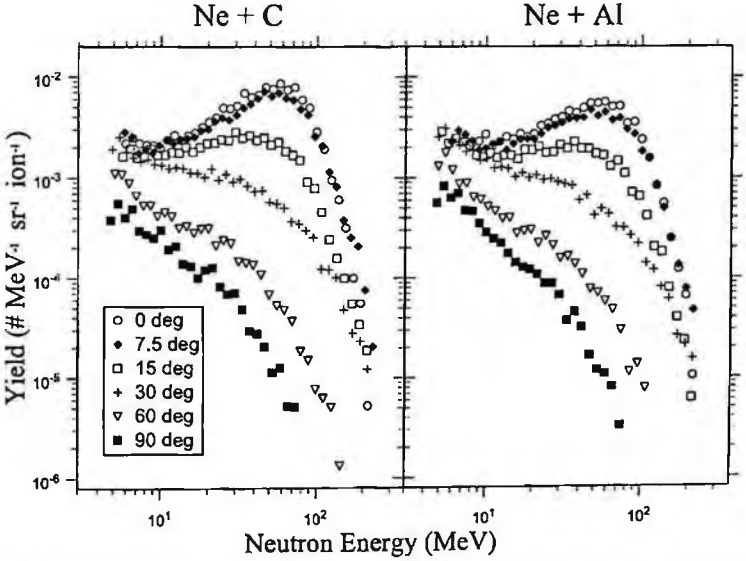

Figure 2.10: Double differential thick-target yields from 100 MeV/nucleon Ne stopping in carbon (left plot) and aluminum (right plot).

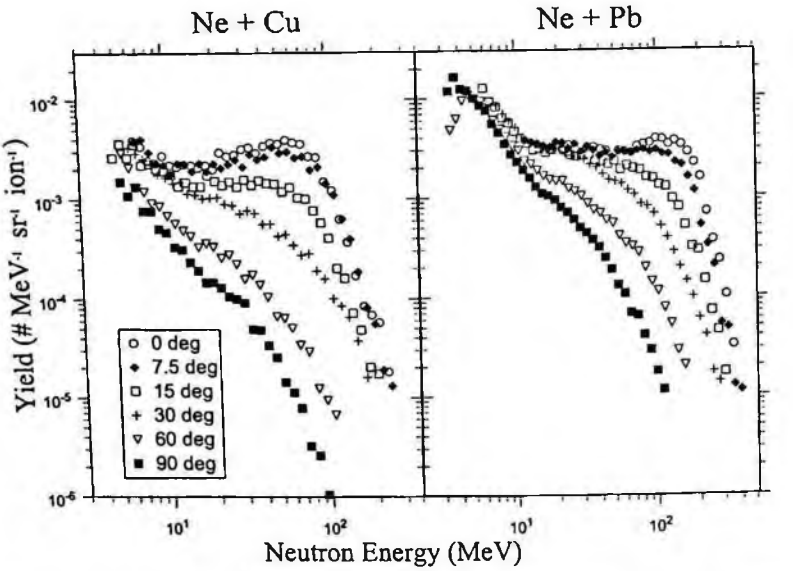

Figure 2.11: Double differential thick-target yields from 100 MeV/nucleon Ne stopping in copper (left plot) and lead (right plot).

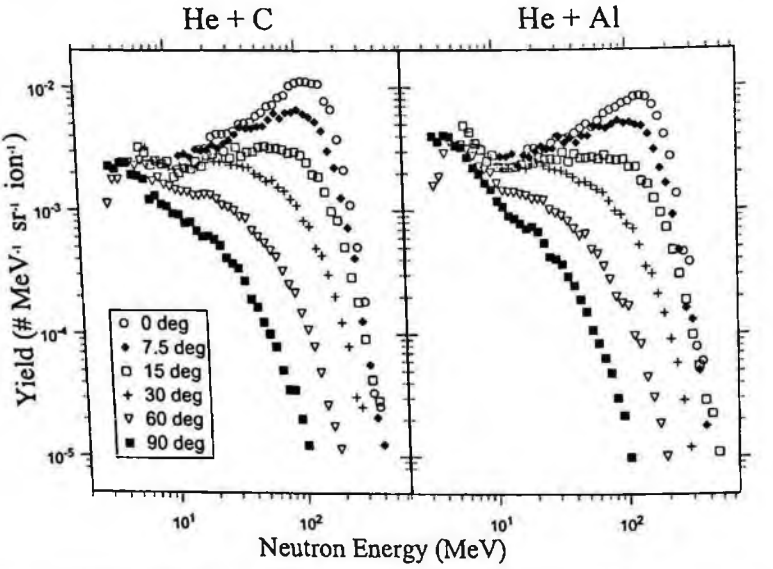

Figure 2.12: Double differential thick-target yields from 180 MeV/nucleon He stopping in carbon (left plot) and aluminum (right plot).

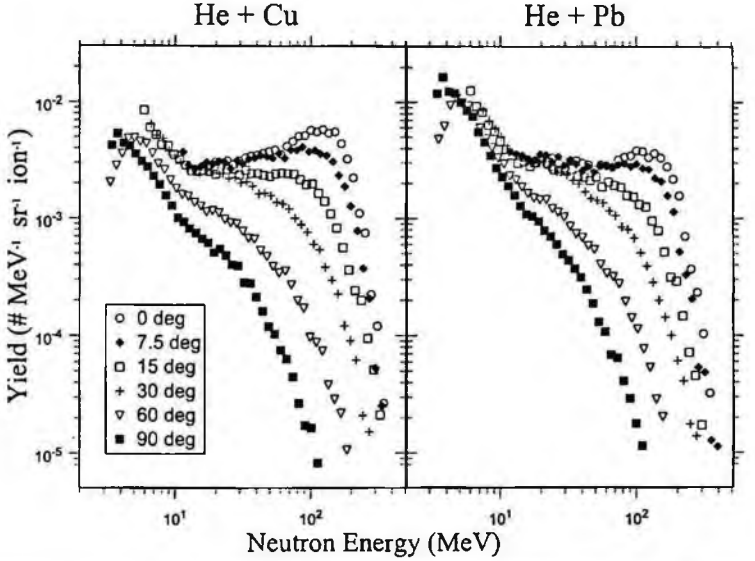

Figure 2.13: Double differential thick-target yields from 180 MeV/nucleon He stopping in copper (left plot) and lead (right plot).

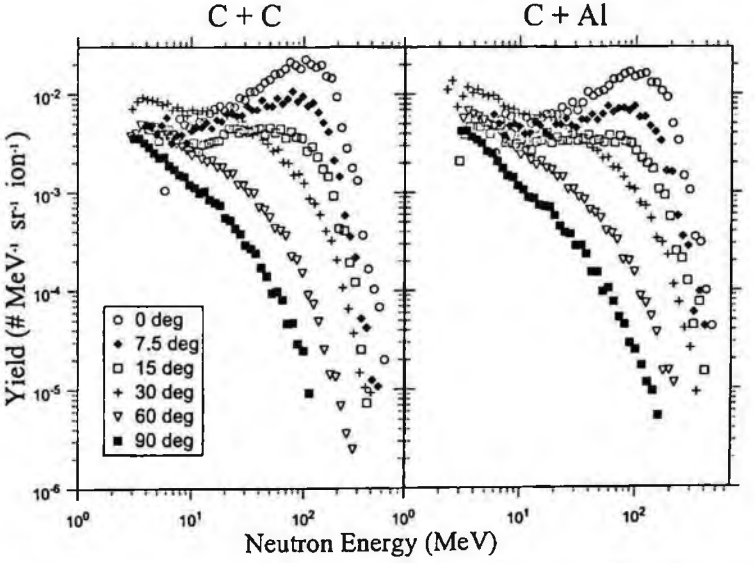

Figure 2.14: Double differential thick-target yields from 180 MeV/nucleon C stopping in carbon (left plot) and aluminum (right plot).

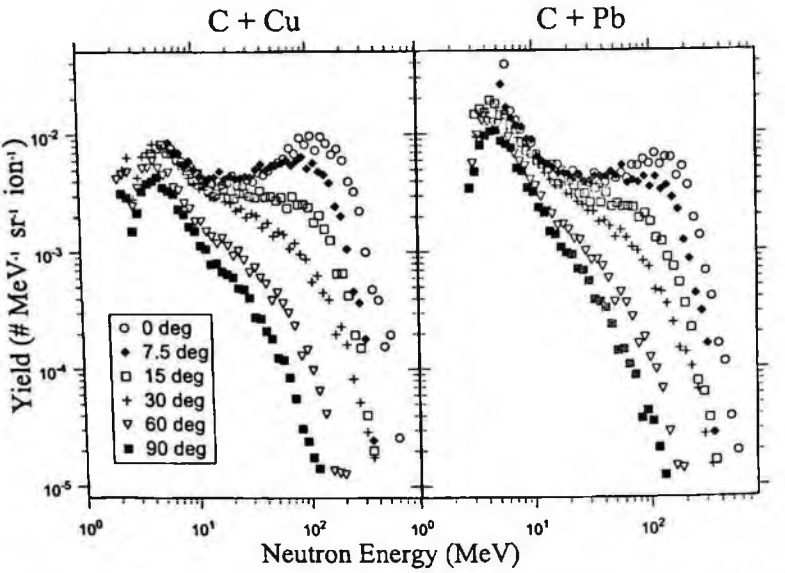

Figure 2.15: Double differential thick-target yields from 180 MeV/nucleon C stopping in copper (left plot) and lead (right plot).

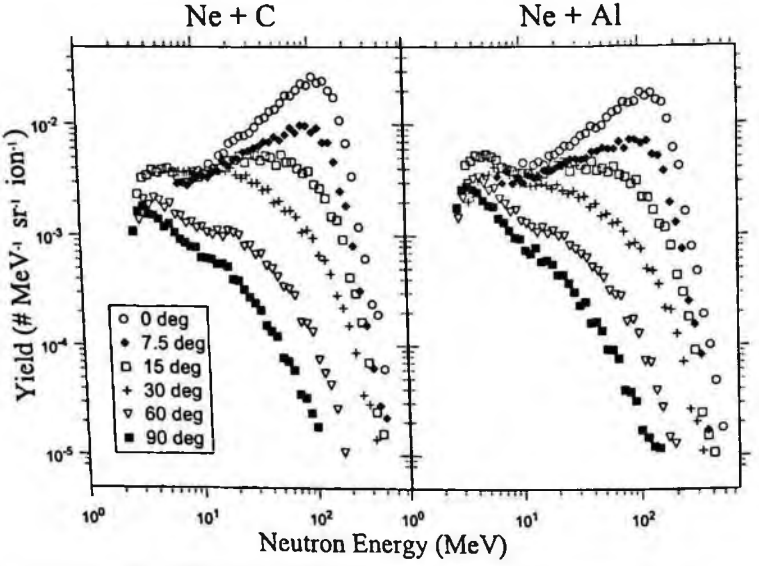

Figure 2.16: Double differential thick-target yields from 180 MeV/nucleon Ne stopping in carbon (left plot) and aluminum (right plot).

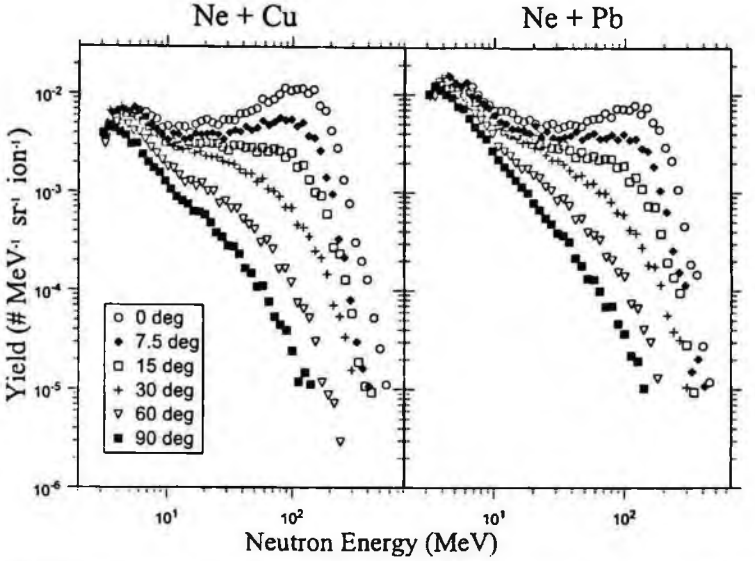

Figure 2.17: Double differential thick-target yields from 180 MeV/nucleon Ne stopping in copper (left plot) and lead (right plot).

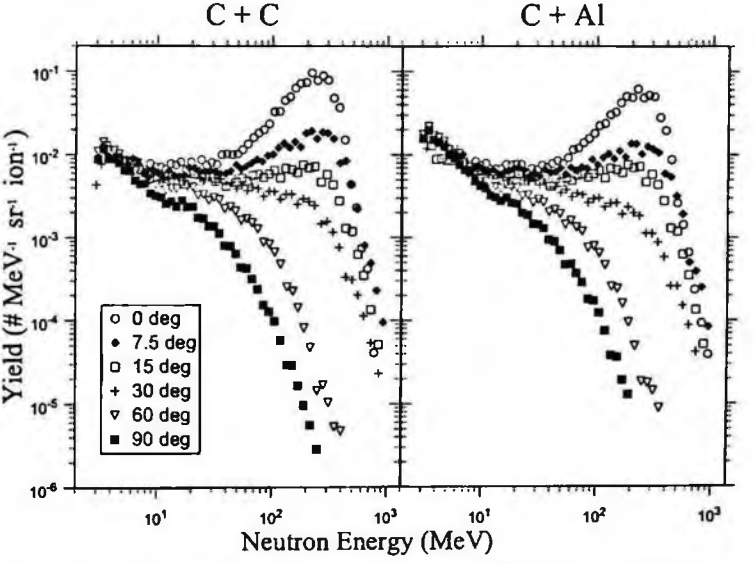

Figure 2.18: Double differential thick-target yields from 400 MeV/nucleon C stopping in carbon (left plot) and aluminum (right plot).

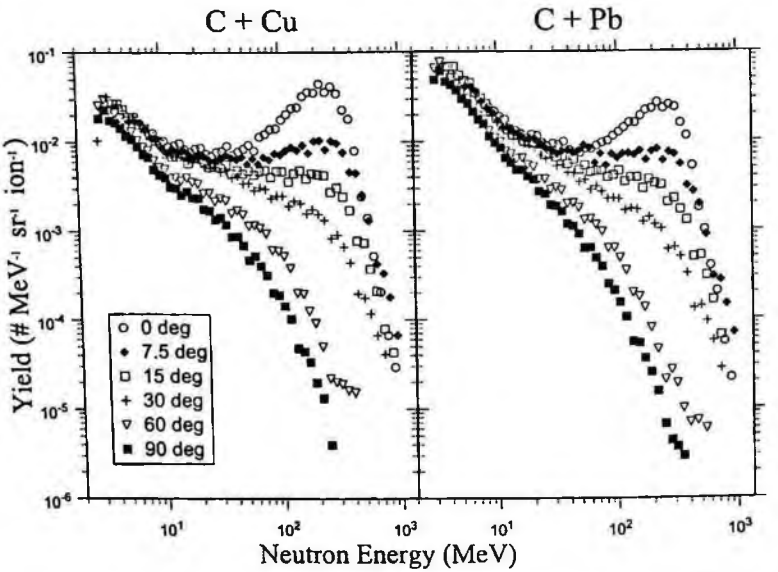

Figure 2.19: Double differential thick-target yields from 400 MeV/nucleon C stopping in copper (left plot) and lead (right plot).

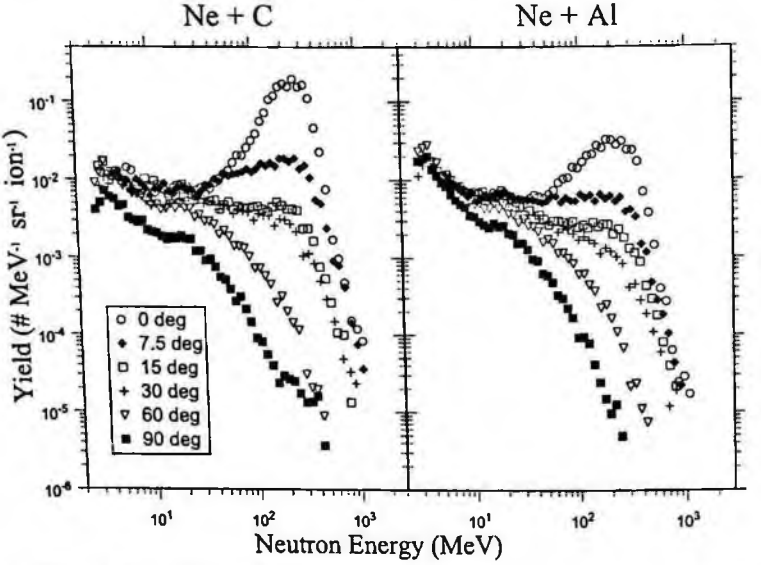

Figure 2.20: Double differential thick-target yields from 400 MeV/nucleon Ne stopping in carbon (left plot) and aluminum (right plot).

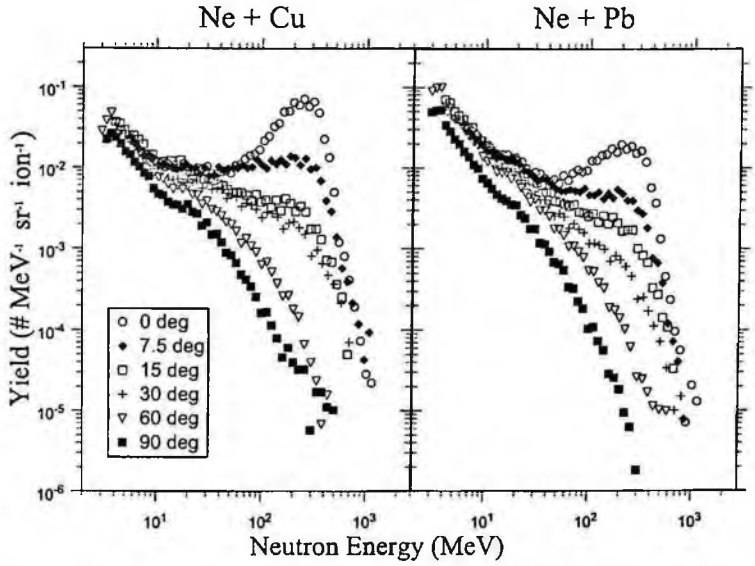

Figure 2.21: Double differential thick-target yields from 400 MeV/nucleon Ne stopping in copper (left plot) and lead (right plot).

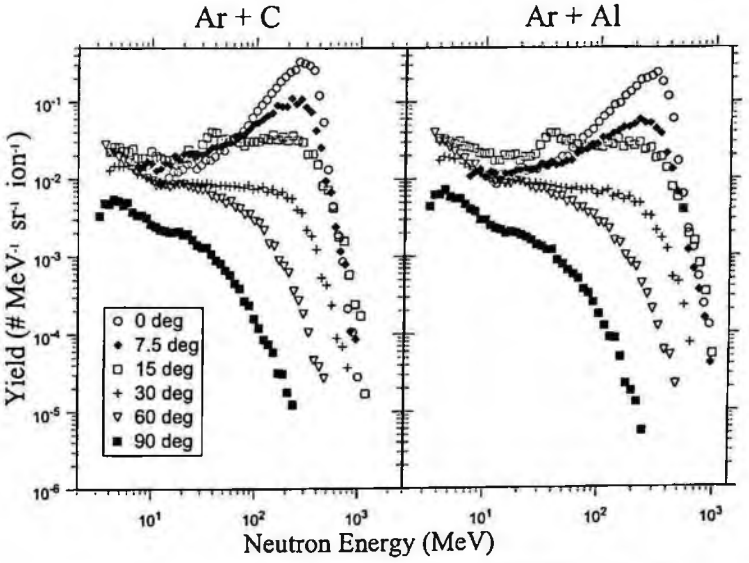

Figure 2.22: Double differential thick-target yields from 400 MeV/nucleon Ar stopping in carbon (left plot) and aluminum (right plot).

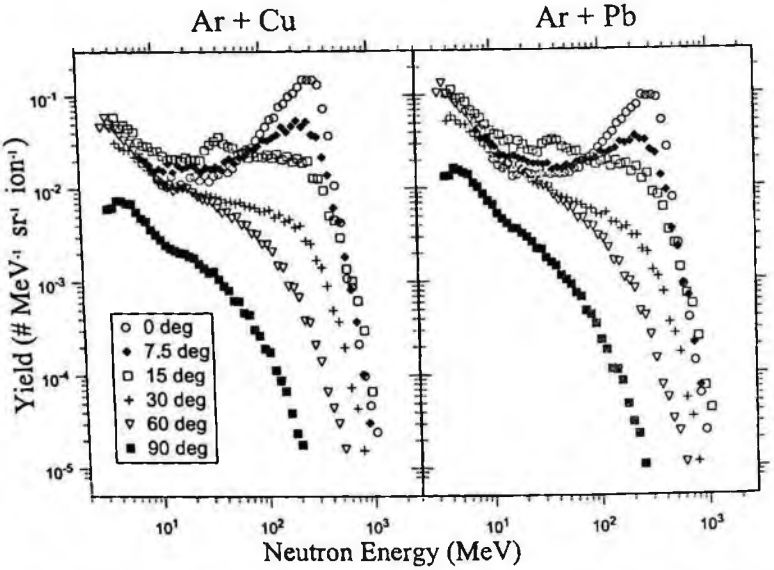

Figure 2.23: Double differential thick-target yields from 400 MeV/nucleon Ar stopping in copper (left plot) and lead (right plot).

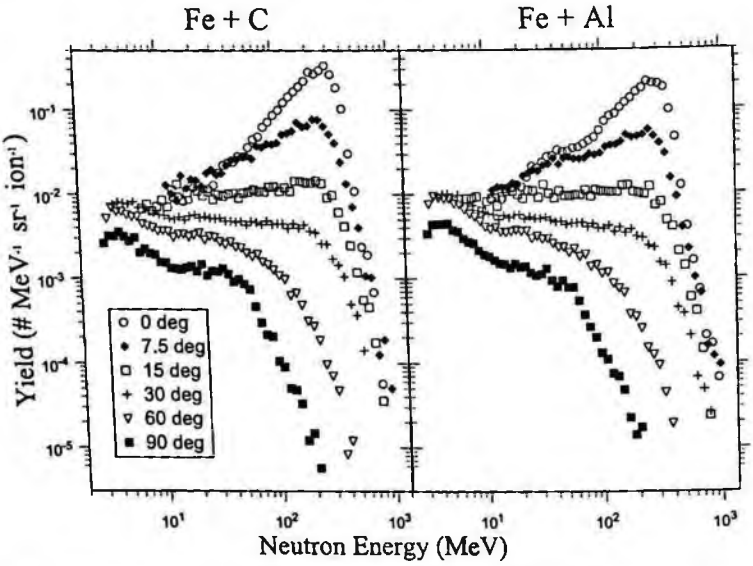

Figure 2.24: Double differential thick-target yields from 400 MeV/nucleon Fe stopping in carbon (left plot) and aluminum (right plot).

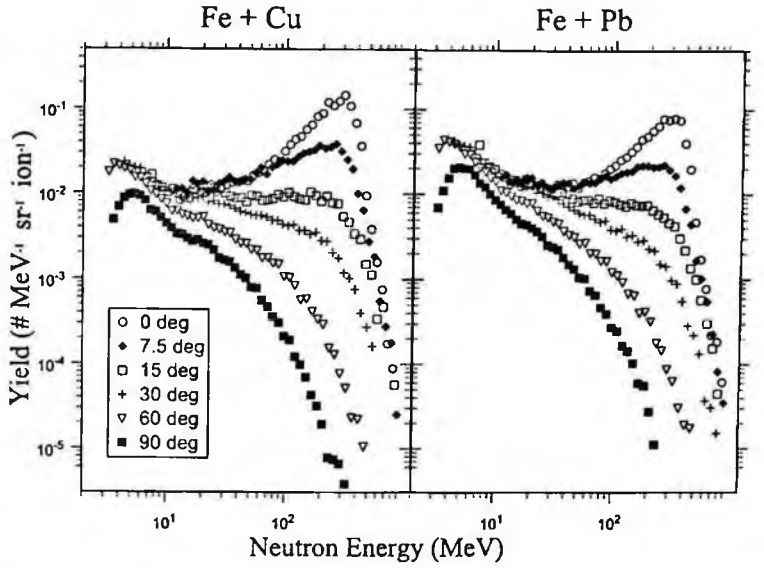

Figure 2.25: Double differential thick-target yields from 400 MeV/nucleon Fe stopping in copper (left plot) and lead (right plot).

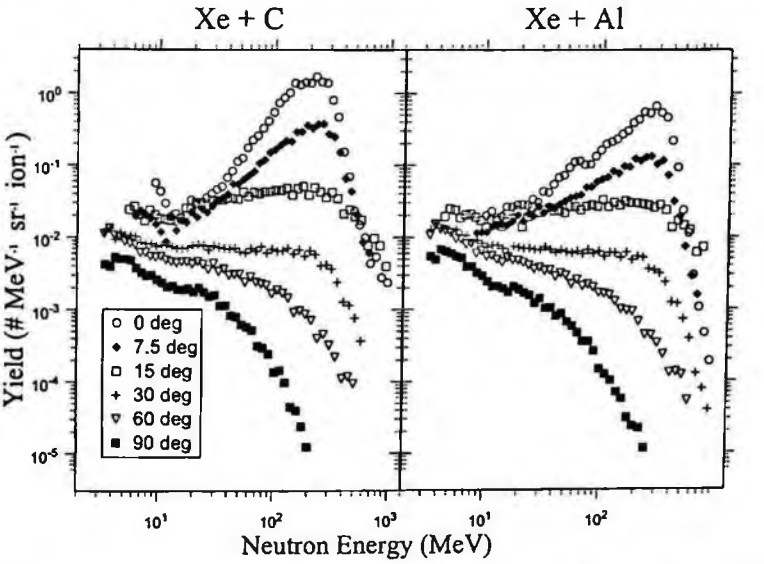

Figure 2.26: Double differential thick-target yields from 400 MeV/nucleon Xe stopping in carbon (left plot) and aluminum (right plot).

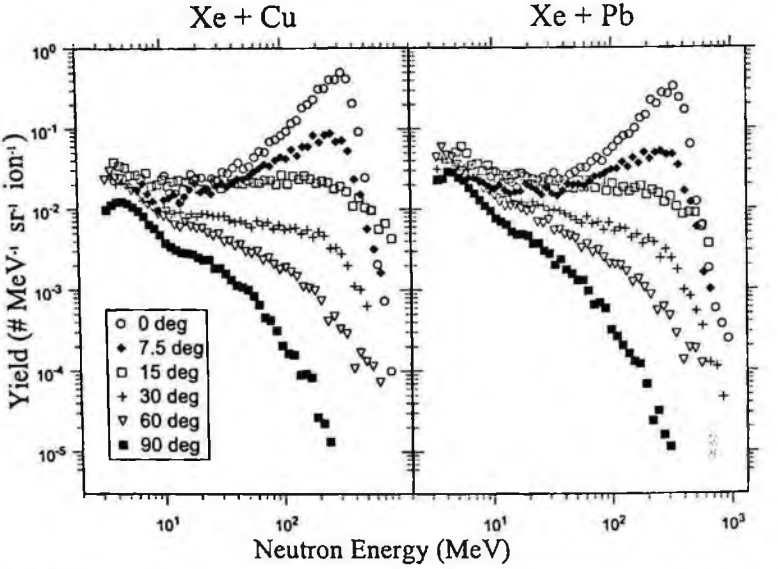

Figure 2.27: Double differential thick-target yields from 400 MeV/nucleon Xe stopping in copper (left plot) and lead (right plot).

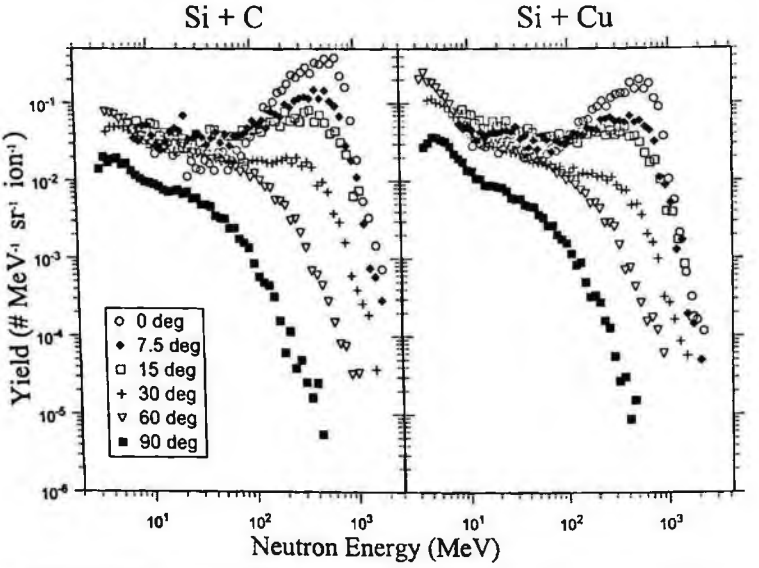

Figure 2.28: Double differential thick-target yields from 800 MeV/nucleon Si stopping in carbon (left plot) and copper (right plot).

2.5 Double-Differential Thick-Target Yields from the Bevalac Experiments

Figures 2.29 through 2.31 show the double-differential thick-target yields from the systems measured by Heilbronn, et al. at the Bevalac facility at Lawrence Berkeley National Laboratory. Angles are indicated by the symbols in the legend in each plot. The spectra are in units of the number of neutrons per MeV per steradian per incoming beam ion.

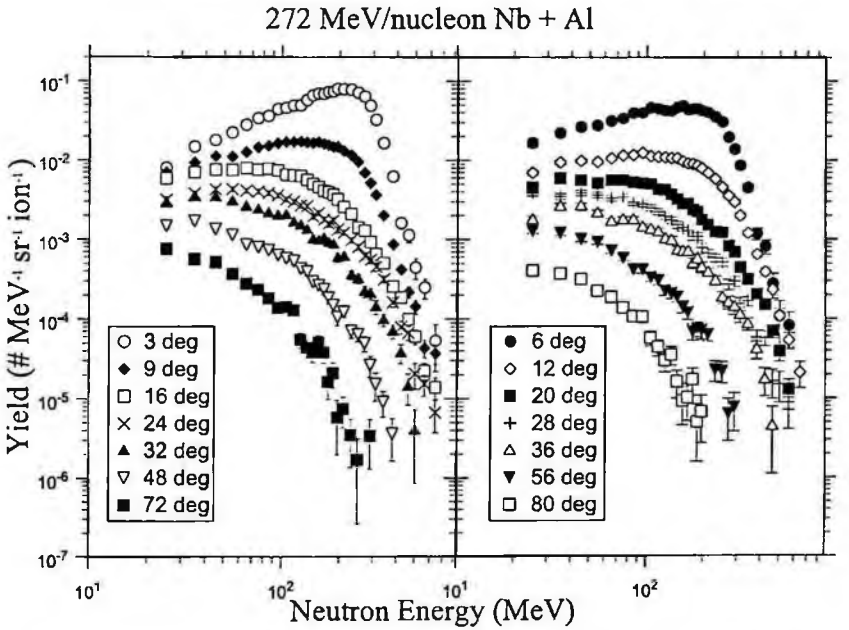

Figure 2.29: Double differential thick-target yields from 272 MeV/nucleon Nb stopping in an aluminum target.

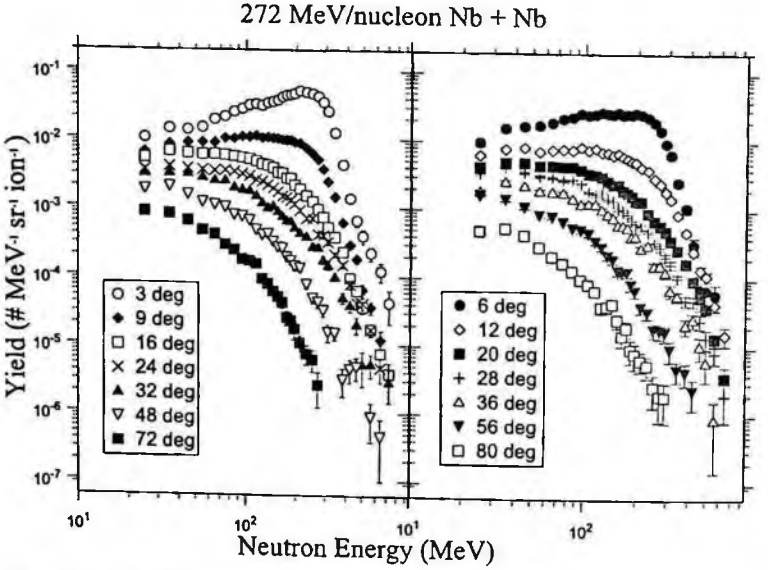

Figure 2.30: Double differential thick-target yields from 272 MeV/nucleon Nb stopping in a niobium target.

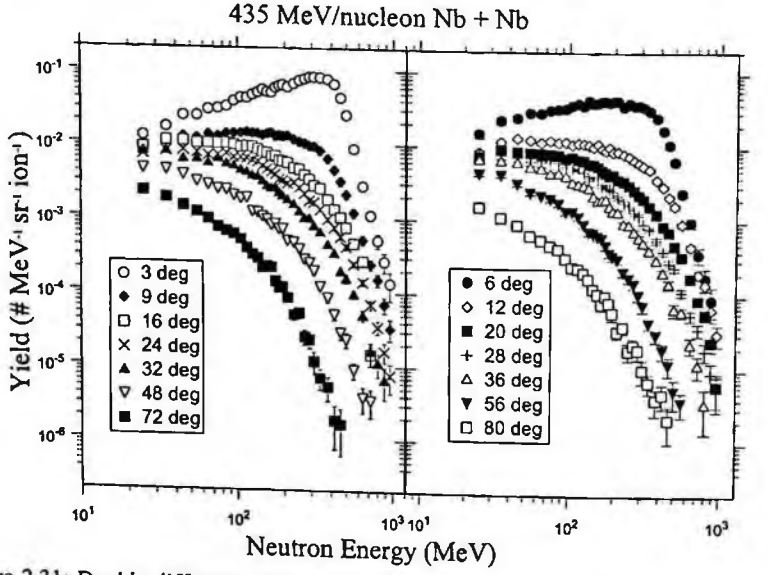

Figure 2.31: Double differential thick-target yields from 435 MeV/nucleon Nb stopping in a niobium target.

2.6 Double-Differential Thick-Target Yields from the SREL Experiments

Figures 2.32 through 2.34 show the double-differential thick-target yields from 177.5 MeV/nucleon He stopping in carbon, water, steel and lead targets, and 160 MeV/nucleon He stopping in lead. The angles are indicated by the symbols shown in the legends in each plot. The spectra are in units of the number of neutrons per MeV per steradian per incoming beam ion.

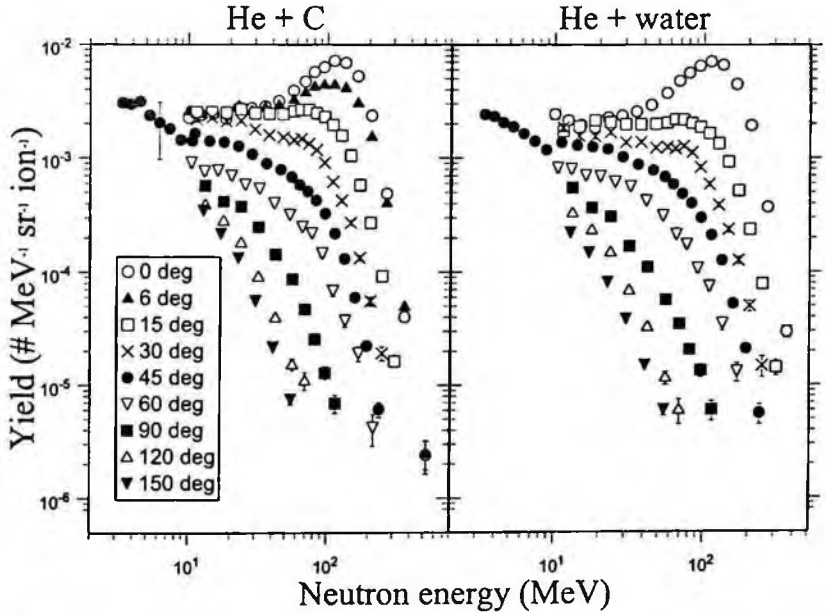

Figure 2.32: Double differential thick-target yields from 177.5 MeV/nucleon He stopping in carbon (left plot) and water (right plot).

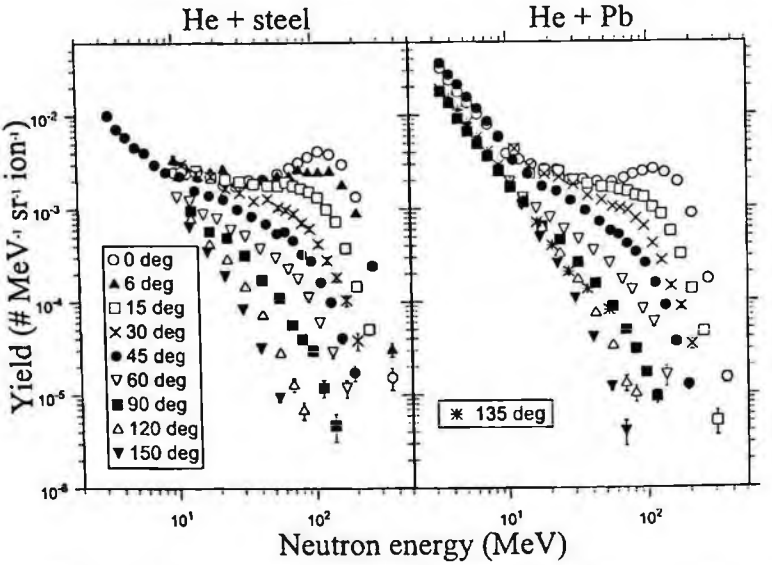

Figure 2.33: Double differential thick-target yields from 177.5 MeV/nucleon He stopping in steel (left plot) and lead (right plot).

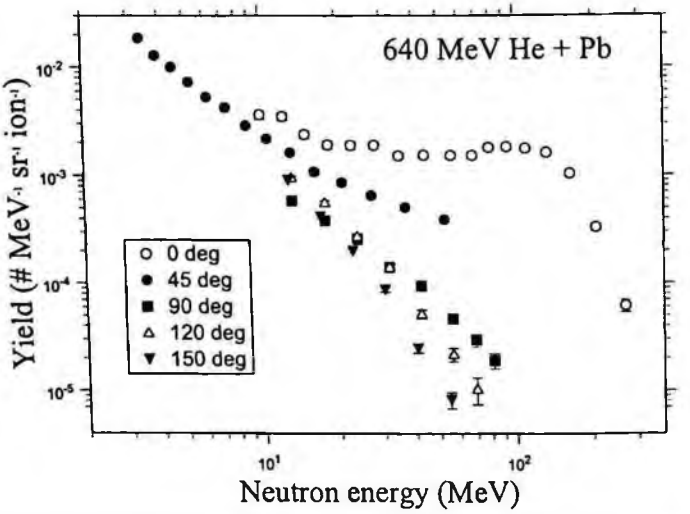

Figure 2.34: Double differential thick-target yields from 160 MeV/nucleon He stopping in a lead target.

2.7 Double-Differential Thick-Target Yields from the NSCL Experiments

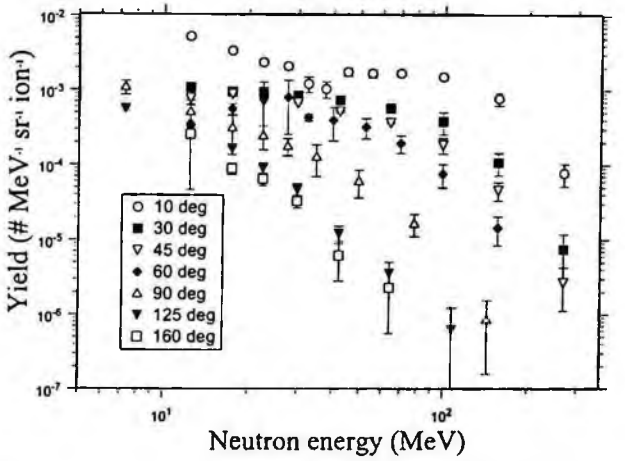

Figure 2.35: Double differential thick-target yields from 155 MeV/nucleon He stopping in aluminum.

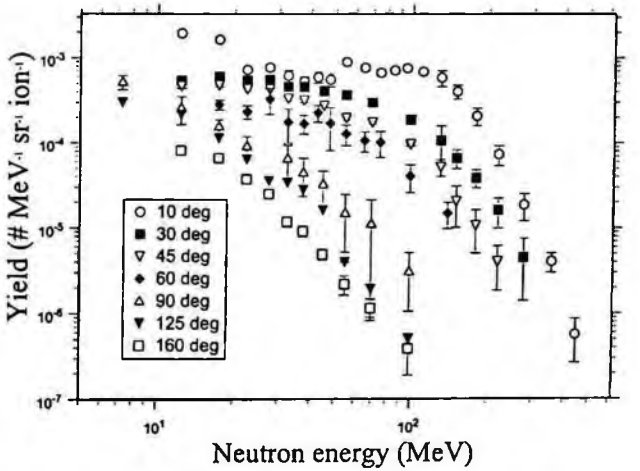

Figure 2.36: Double differential thick-target yields from 155 MeV/nucleon C stopping in aluminum.

2.8 Angular Distributions of Thick-Target Neutron Yields above 5 MeV from the HIMAC Experiments

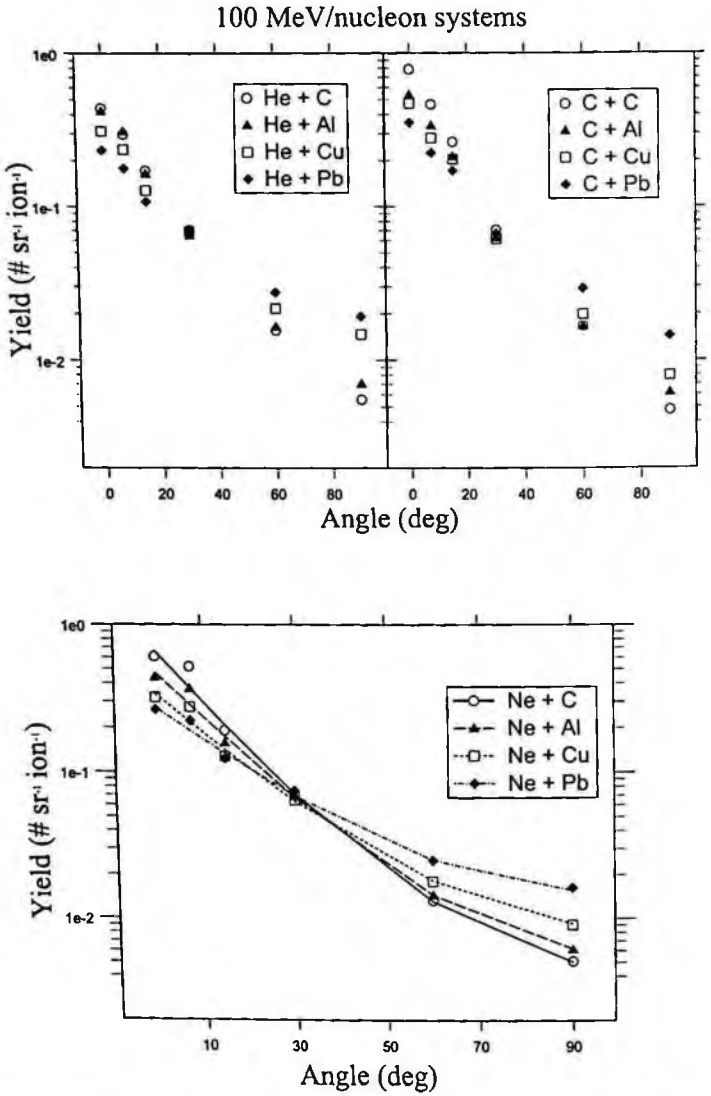

Figure 2.37: Angular distributions from 100 MeV/nucleon He (upper left), C (upper right) and Ne (lower plot) systems. The lines in the lower plot come from a fit explained in the text.

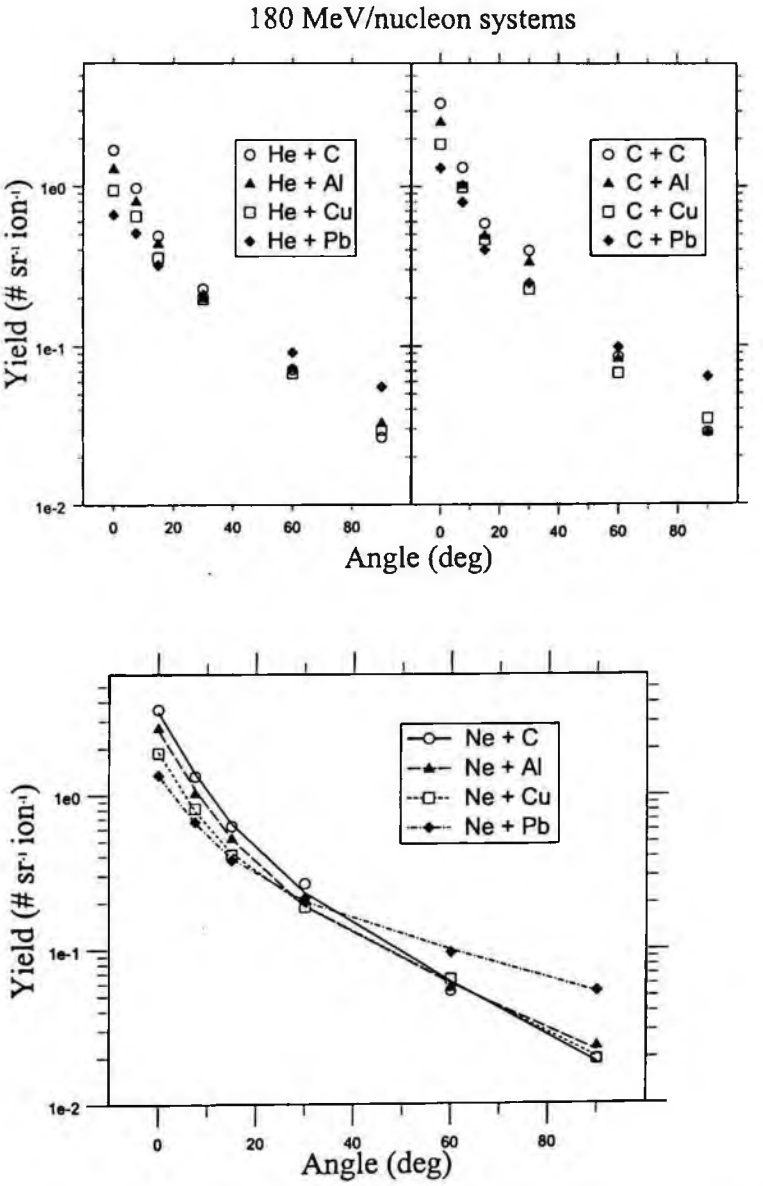

Figure 2.38: Angular distributions from 180 MeV/nucleon He (upper left), C (upper right) and Ne (lower plot) systems. The lines in the lower plot come from a fit explained in the text.

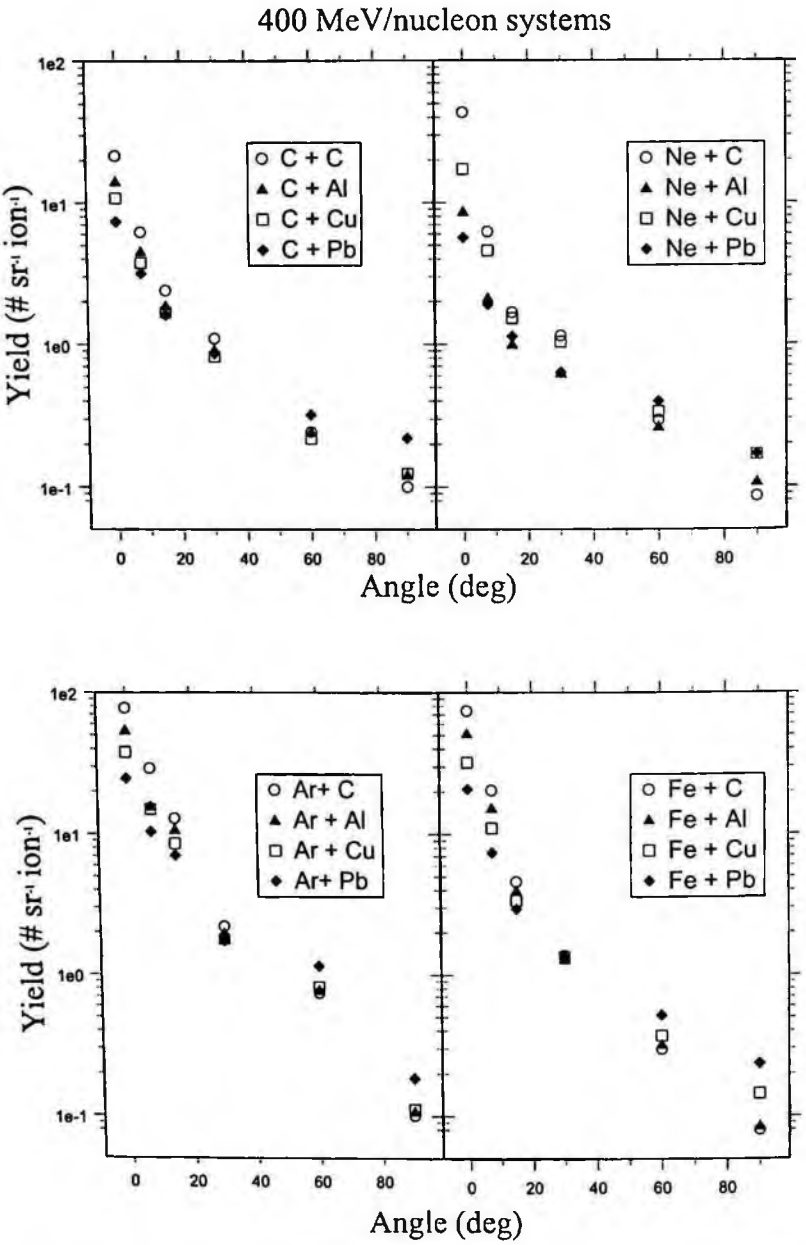

Figure 2.39: Angular distributions from 400 MeV/nucleon C (upper left), Ne (upper right), Ar (lower left) and Fe (lower right) systems.

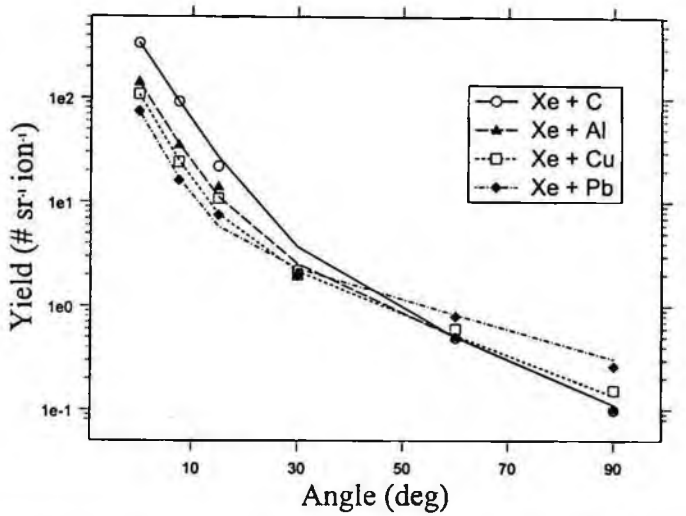

Figure 2.40: Angular distributions from the 400 MeV/nucleon Xe systems. The lines come from a fit explained in the text.

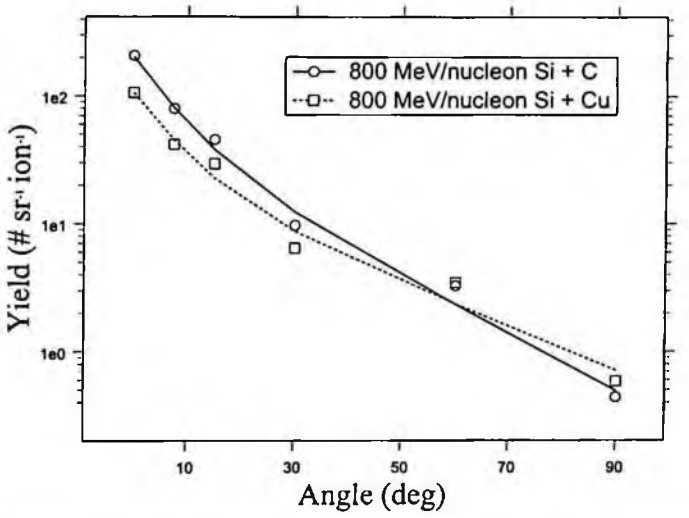

Figure 2.41: Angular distributions from the 800 MeV/nucleon Si systems. The lines come from a fit explained in the text.

2.9 Angular and Energy Distributions of Thick-Target Neutron Yields above 20 MeV from the Bevalac Experiments

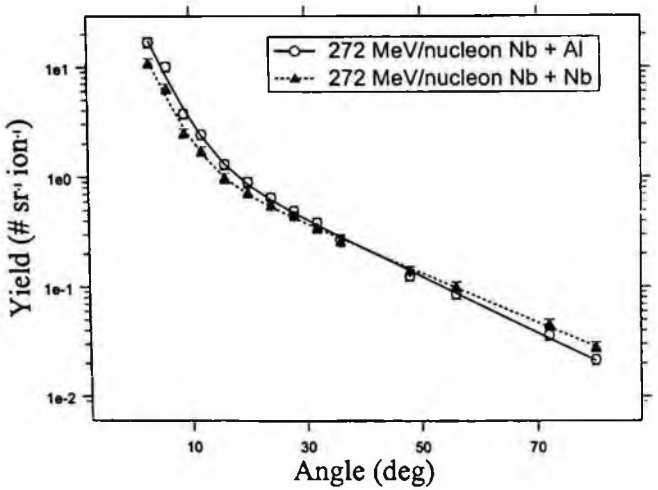

Figure 2.42: Angular distributions from the 272 MeV/nucleon Nb systems. The lines come from a fit explained in the text.

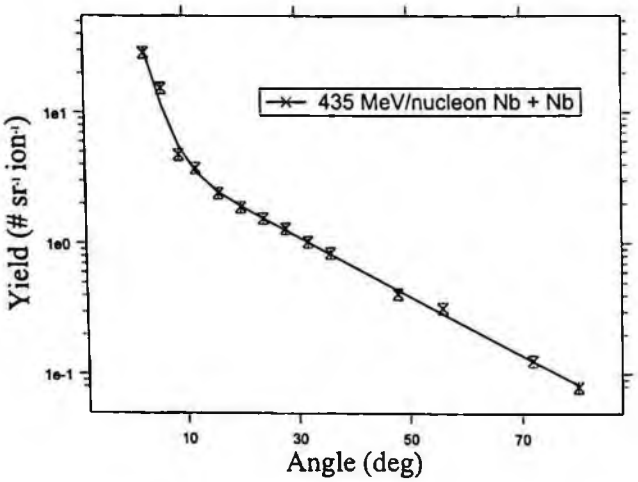

Figure 2.43: Angular distributions from the 435 MeV/nucleon Nb systems. The line comes from a fit explained in the text.

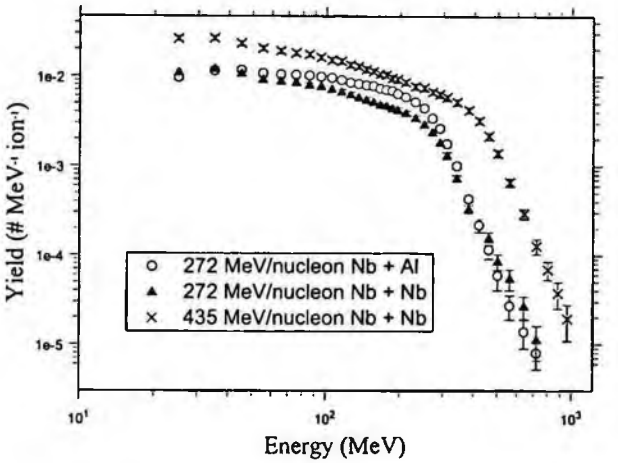

Figure 2.44: Energy distributions from all three Nb systems.

2.10 Angular Distributions of Thick-Target Neutron Yields above 10 MeV from the SREL Experiments

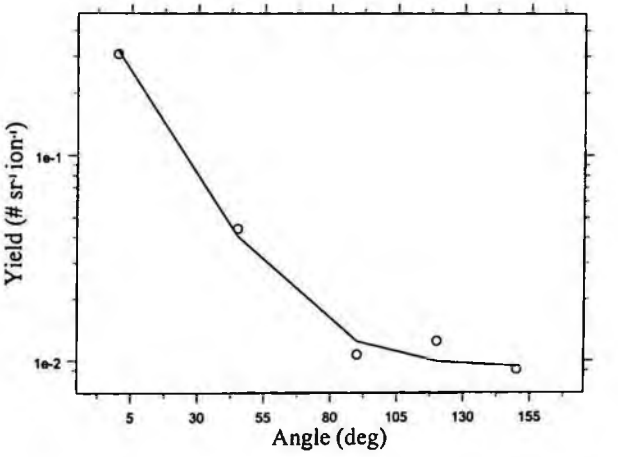

Figure 2.45: Angular distribution from 160 MeV/nucleon He + Pb. The line comes from a fit explained in the text.

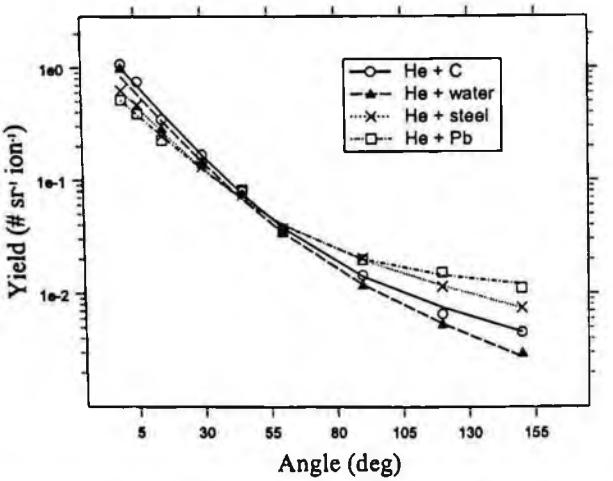

Figure 2.46: Angular distributions from the 177.5 MeV/nucleon He systems. The lines come from a fit explained in the text.

2.11 Angular and Energy Distributions of Thick-Target Neutron Yields above 10 MeV from the NSCL Experiments

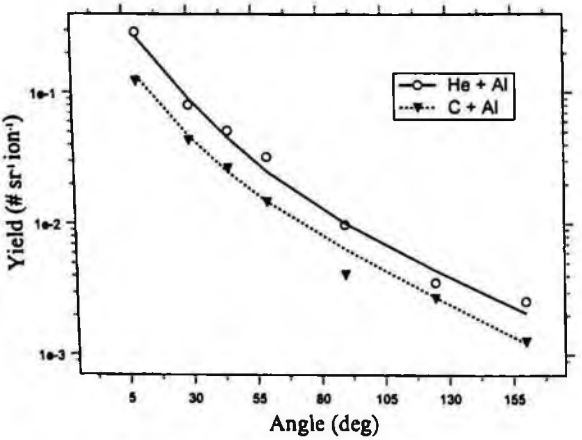

Figure 2.47: Angular distributions from 155 MeV/nucleon He + Al and C + Al. The lines come from a fit explained in the text.

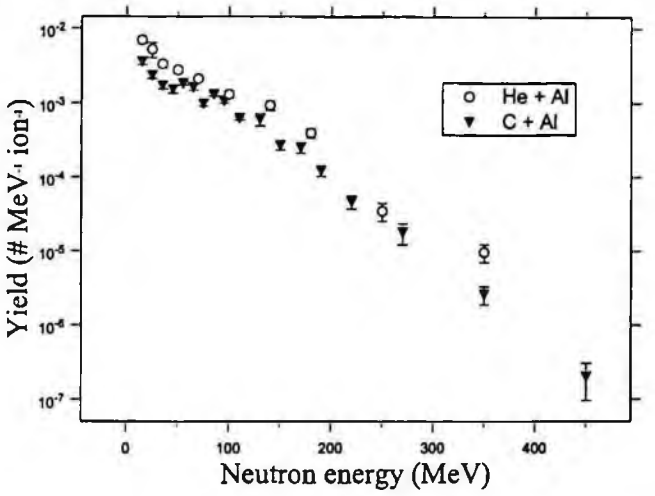

Figure 2.48: Energy distributions for 155 MeV/nucleon He and C stopping in Al.

2.12 Total Yields for Systems with Al, C, Cu or Pb Targets

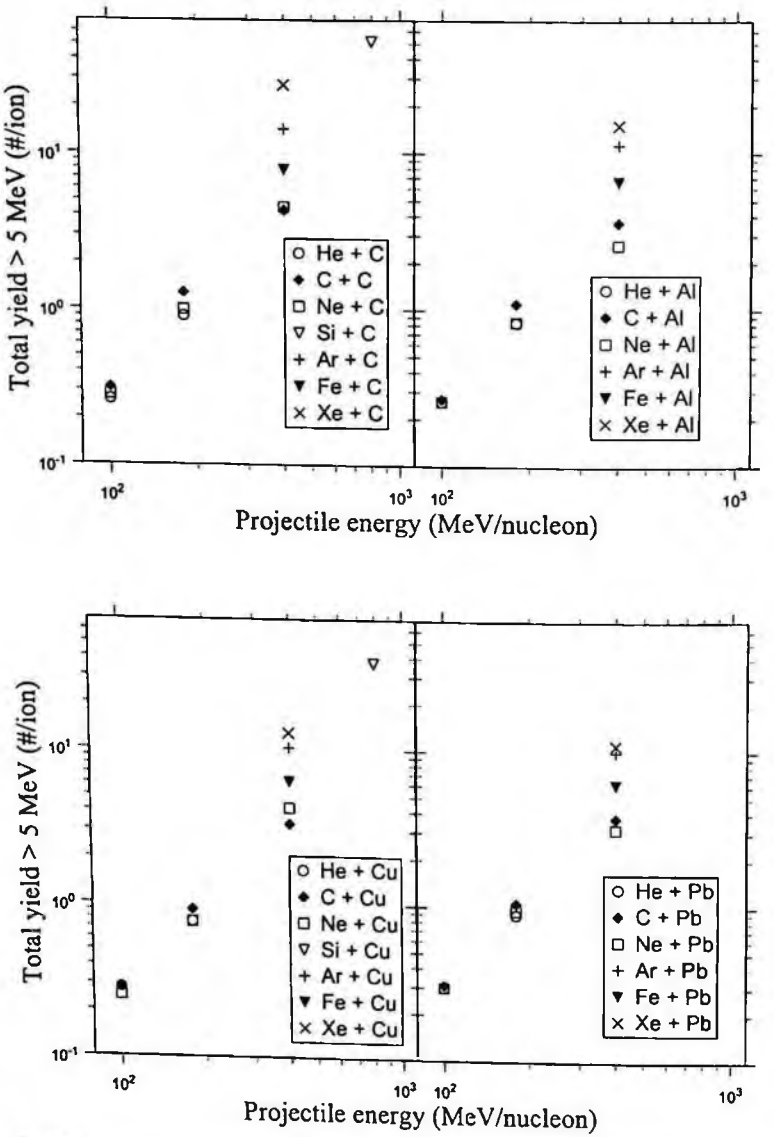

Figure 2.49: Total yields above 5 MeV for C targets (upper left), Al targets (upper right), Cu targets (lower left) and Pb targets (lower right).

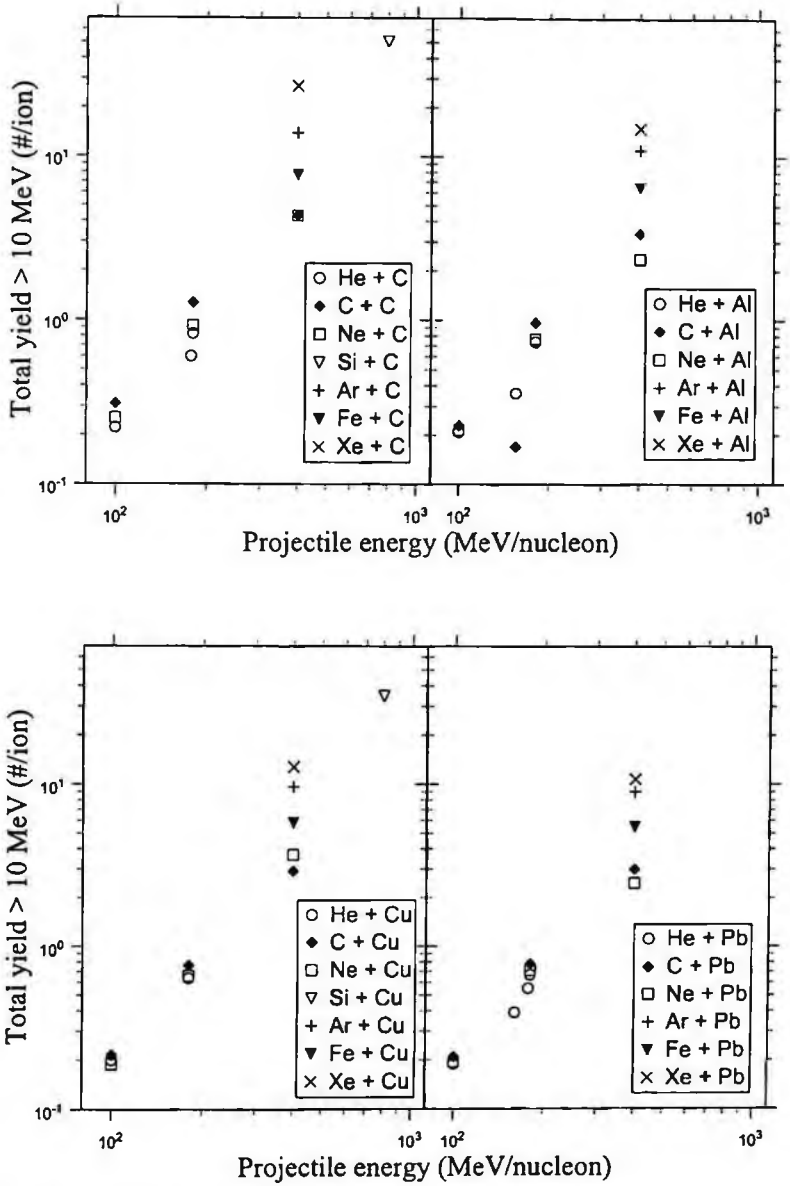

Figure 2.50: Total yields above 10 MeV for C targets (upper left), Al targets (upper right), Cu targets (lower left) and Pb targets (lower right).

Chapter 3

Secondary Neutron Production Cross Sections

3.1 Overview of Measured Systems

The production of secondary neutrons from heavy-ion interactions is an important consideration in many basic and applied fields. The dose received in normal, healthy tissue from neutrons produced by heavy-ion radiotherapy beams must be accounted for in order to limit any side effects from the treatment. In both deep space and low-earth orbital missions, secondary neutrons can be a significant component of the overall dose received by personnel working in those environments. At accelerator facilities, heavy-ion beams are utilized for basic science, including the production of radioactive isotopes using beams of high intensity. There, secondary neutrons are the primary concern for shielding design and for lifetime of various components that make up the accelerator facility.

To determine what effects secondary neutrons have in the scenarios described above, researchers rely on state-of-the-art models, both analytical and Monte-Carlo, to predict the magnitude and characteristics of the secondary neutron field. The accuracy of the models' predictions ultimately relies on their ability to correctly model the relevant production cross sections. To that end, an experimental data base of neutron production cross sections is needed over a wide range of ion species and energies, and target mass. The data sets presented here are for high-energy (E/A greater than about 100 MeV/nucleon) heavy-ions ($Z \geq 2$) interacting in targets ranging from lithium to lead. It is not an

exhaustive list of secondary neutron cross sections; the data sets selected here generally have a wide range in angle and energy and target mass.

Table 3.1 contains a list of the secondary neutron cross sections presented here. The first column contains the beam ion species and beam energy in MeV/nucleon. The second column lists the targets used with each. The third column lists the spectra that were measured. DDX indicates that double-differential cross sections were measured, n/dΩ indicates that angular distributions were reported, and "total" indicates that total neutron yields were extracted from the data. The total cross sections were usually limited to the angular range used in the measurements, so in most cases the total yields were not strictly "total" in the sense that they cover the distribution over all 4π steradians. The fourth column indicates the laboratory angles where spectra were measured. The fifth column lists the minimum neutron energy that was measured at each angle indicated in the fourth column. In some cases the minimum neutron energy measured at a particular energy varied from target to target, so the reader is cautioned to refer to the data tables to obtain the minimum measured energy for each system and angle. The sixth column indicates the facility where the measurements took place. RIKEN is the Institute of Physical and Chemical Research in Japan, and HIMAC is the Heavy Ion Medical Accelerator in Chiba, Japan. SB3 and PH2 refer to two different beam lines at HIMAC. Additional experimental details are described in the section below.

Table 3.1: General information in regards to the heavy-ion, thin-target neutron cross-section experiments described here. The beam ion and energy, target material and thickness, type of measured spectra, laboratory angle, and minimum measured neutron energy.

Beam ion and energy (MeV/nucleon)	Targets	Measured spectra	θ (deg)	Emin (MeV)	Facility
He (135)	C, Al, Cu, Pb	ddx, n/dΩ total	0, 15, 30, 50, 80, 110	10 (all angles)	RIKEN
He (230)	Al, Cu	ddx, n/dΩ total	5, 10, 20, 30, 40, 60, 80	5.5, 5, 4, 3.5, 3.5, 3	HIMAC (PH2)
C (135)	C, Al, Cu, Pb	ddx, n/dΩ total	0, 15, 30, 50, 80, 110	10 (all angles)	RIKEN

Table 3.1 (continued)

Beam ion and energy (MeV/nucleon)	Targets	Measured spectra	θ (deg)	Emin (MeV)	Facility
C (290)	C, Cu, Pb, marsbar	ddx, n/dΩ total	5, 10, 20, 30, 40, 60, 80	10, 3, 3, 7, 4, 3, 3	HIMAC (SB3)
C (400)	Li, C, CH_2, Al, Cu, Pb	ddx, n/dΩ total	5, 10, 20, 30, 40, 60, 80	8.5, 5, 3.5, 3, 3, 3	HIMAC (PH2 and SB3)
N (400)	C, Cu	ddx, n/dΩ total	5, 10, 20, 30, 40, 60, 80	6, 6, 5, 5.5, 5.5, 5	HIMAC (PH2)
Ne (135)	C, Al, Cu, Pb	ddx, n/dΩ total	0, 15, 30, 50, 80, 110	10 (all angles)	RIKEN
Ne (337)	C, Al, Cu, U	ddx total	30, 45, 60, 90	12 (all angles)	LBL Bevalac
Ne (400)	C, Cu, Pb, ISS wall	ddx, n/dΩ total	5, 10, 20, 30, 40, 60, 80	9,6, 3.5, 3.5, 3, 3	HIMAC (SB3)
Ne (600)	Li, C, CH_2, Al, Cu, Pb, marsbar	ddx, n/dΩ total	5, 10, 20, 30, 40, 60, 80	6, 5.5, 4, 3, 3 3	HIMAC (PH2 and SB3)
Ar (95)	C, Al, Cu, Pb	ddx, n/dΩ total	0, 30, 50, 80, 110	10 (all angles)	RIKEN
Ar (400)	C, Cu, Pb	ddx, n/dΩ total	5, 10, 20, 30, 40, 60, 80	10, 7, 3.5, 3.5, 3, 3	HIMAC (PH2 and SB3)
Ar (560)	C, Cu, Pb, marsbar	ddx, n/dΩ total	5, 10, 20, 30, 40, 60, 80	10, 7, 3.5, 3.5, 3, 3	HIMAC (PH2)
Fe (500)	Li, CH_2, Al	ddx, n/dΩ total	5, 10, 20, 30, 40, 60, 80	12, 11, 7, 4, 3, 3	HIMAC (PH2)
Kr (400)	Li, C, CH_2, Al, Cu, Pb	ddx, n/dΩ total	5, 10, 20, 30, 40, 60, 80	20 (all angles)	HIMAC (PH2)
Xe (400)	C, CH_2, Al, Cu, Pb	ddx, n/dΩ total	5, 10, 20, 30, 40, 60, 80	10, 6, 5, 3.5, 3.5, 3.5	HIMAC (PH2 and SB3)

3.2 Experimental Details

All of the experiments described here used the time-of-flight method to measure neutron energies. Details about the particular experiments at each facility are described below.

3.2.1 HIMAC experiments

Beams extracted from the synchrotron had a pulse width between 0.5 sec and 1 sec. One beam pulse was delivered every 3.3 seconds. A thin NE102A plastic scintillator was placed just downstream from the exit window (made of 0.1-mm thick Al) of the beam line as a beam-pickup scintillator. The thickness of that scintillator varied between 0.1 and 0.5 mm, depending on the beam ion species and energy. The output pulses of this scintillator were used as start signals for the TOF measurement and were also used to count the absolute number of projectiles incident to the target. To avoid the counting loss due to voltage sag in the photomultiplier that is induced by high beam current, the voltages of the last three dynodes were externally supplied by a constant voltage power supply. Beam intensities were maintained between $1x10^4$-$1x10^5$ particles per pulse. The targets were set on the beam line 10 cm (SB3 beam line) or 19.5 cm (PH2 beam line) downstream from the beam pickup scintillator. Beam-spot sizes on the target were, in general, ~1.5 cm in diameter. The beam height was 1.25m above the concrete floor of the experimental area for both beam lines.

For the experiments conducted on the SB3 beam line, the beam then traveled approximately 20 meters after passing through the target, and the stopped in a beam dump located in a second room, downstream from the primary experimental hall. Figure 3.1 shows a schematic diagram of the experimental setup on the SB3 beam line. A set of quadrupole magnets, located about 7 meters downstream from the target, was used to focus the beam into the beam dump. For the experiments conducted on the PH2 beam line, the beam traveled 7 meters into a well-shielded beam dump. Figure 3.2 shows a photograph of the general layout used on the PH2 beam course. Figure 3.3 shows a view of the beam dump used on the PH2 beam course. The beam dump was much close to the neutron detectors on the PH2 beam course. Background rates were generally higher at the forward detector positions (5-20 degrees) for the runs on this beam line than they were on the SB3 beam line. Comparison of spectra from identical systems taken on both beam lines showed no difference (within uncertainties) after background subtraction.

NE213 liquid scintillators (12.7-cm diameter by 12.7-cm thick) were used for the neutron detectors. Table 3.2 gives the flight paths and angle (in the lab) used for each neutron detector. The same flight paths and angles were used on both beam lines. The same configuration was used for all the systems studied, except the 600 MeV/nucleon Ne + Al, CH_2, Li and marsbar targets, and the 400 MeV/nucleon Xe + Li, CH_2, and Al targets. For those experiments, detectors N1 (5°), N2 (10°), N3 (20°), N5 (40°), and N7 (80°) were used.

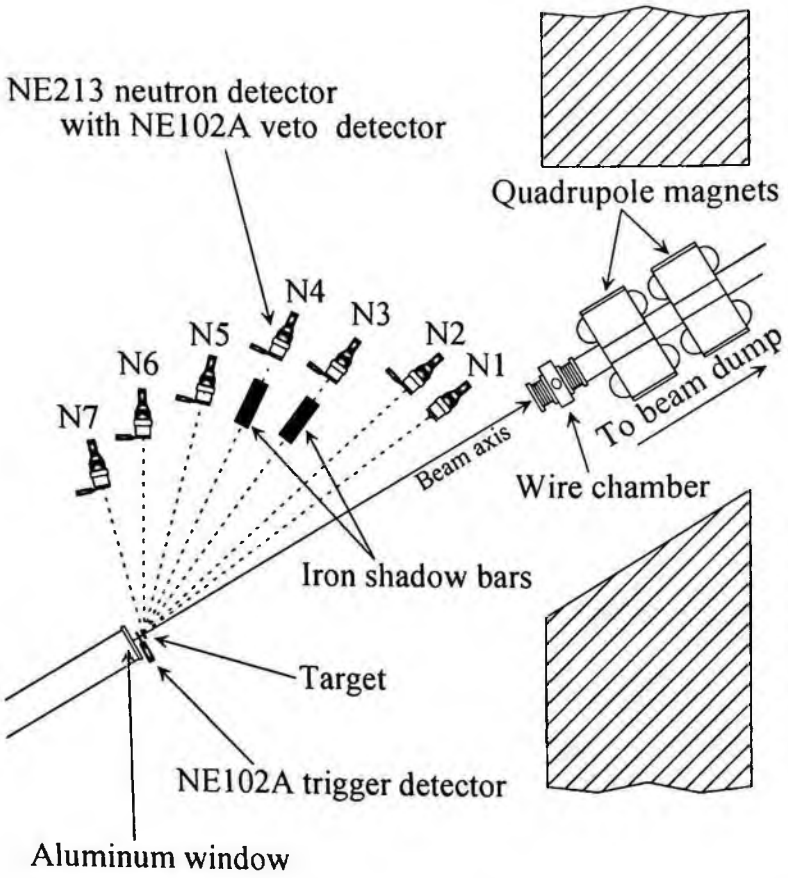

Figure 3.1: Schematic diagram of the experimental setup on the HIMAC SB3 beam line (courtesy of Ref. 3.1).

Figure 3.2: General layout of the experimental setup on the SB2 beam line. The yellow tube is a He-filled tube that was used to reduce the background created by beam interactions in air. The picture was taken from the top of the beam dump.

Table 3.2: Neutron detector information for the experiments conducted at HIMAC. The uncertainty in the solid angle is reported as a percentage.

Detector	Flight Path Length (cm)	Lab angle (deg)	Solid angle (msr)
N1	506	5	0.494 ± 5.0%
N2	506	10	0.494 ± 5.0%
N3	456	20	0.608 ± 5.6%
N4	456	30	0.608 ± 5.6%
N5	406	40	0.767 ± 6.2%
N6	356	60	0.998 ± 7.1%
N7	306	80	1.35 ± 8.3%

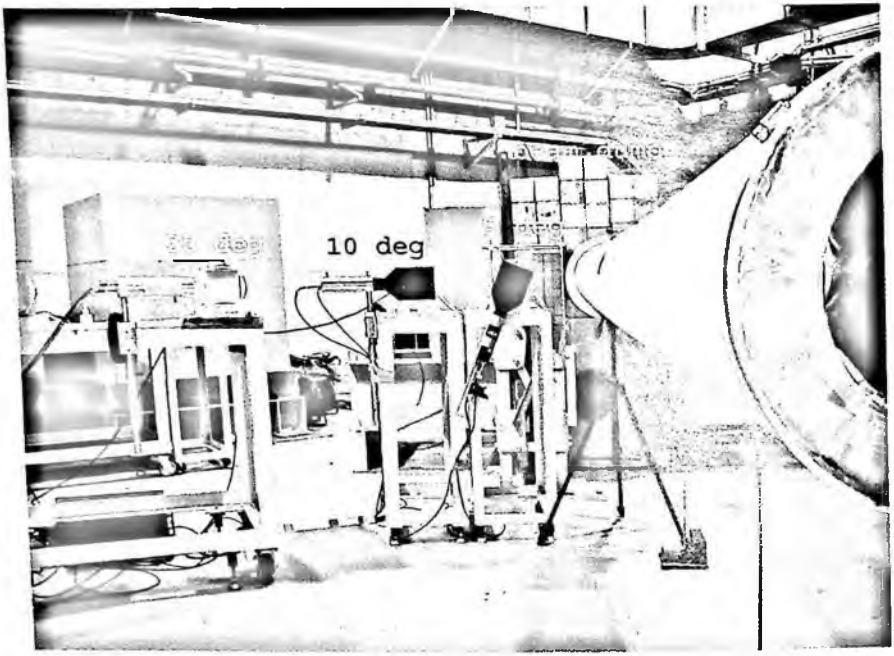

Figure 3.3: A view looking downstream on the PH2 beam course showing the beam dump directly behind the He-filled tube.

Table 3.3 gives the target thickness (in g/cm^2) for each system studied. In general, targets were chosen such that the energy loss through the target was on the order of 5 to 10 percent of the incident energy. The target called "marsbar" is a 5.0-g/cm^2 thick (2.5-cm thick), 10-cm by 10-cm composite brick made up of 85% (by weight) simulated Martian regolith and 15% polyethylene. It is regarded as a reasonable approximation of what may be used for habitat construction on the surface of Mars: bricks composed of Martian soil, using a polymer binder produced by mixing components of Mars' CO_2 atmosphere and water. Table 3.4 shows a breakdown of the elemental composition of Martian soil. Factoring in the percentages (by weight) of polyethylene and regolith in the marsbar target, there are a total of 4.20×10^{22} atoms per gram of target. The marsbar is thick enough to produce an appreciable energy loss as the beam traverses through the target. The C beam has an incident energy of 290 MeV/nucleon, and an exit energy of 240

MeV/nucleon (median energy of 265 MeV/nucleon). The Ne beam has an incident energy of 600 MeV/nucleon and an exit energy of 540 MeV/nucleon (median energy of 570 MeV/nucleon). Based on other measurements [3.1] it is believed that the cross sections will not vary much over the range of beam energies through the target.

Table 3.3: Target species and thickness (g/cm^2) used with the indicated beams for the experiments at HIMAC

Beam (energy) (MeV/nucleon)	Target	Thickness (g/cm^2)
He (230)	Al	5.40
	Cu	5.38
C (290)	C	1.80
	Cu	4.47
	Pb	2.27
	Marsbar	5.0 (see text)
C (400)	C	9.00
	Cu	13.4
	Pb	9.08
N (400)	C	1.78
	Cu	2.69
Ne (400)	C	1.80
	Cu	4.47
	Pb	2.27
	ISS wall	2.97 (See text)
Ne (600)	Li	2.974
	C	3.60
	CH_2	2.40
	Al	3.98
	Cu	4.47
	Pb	4.54
	Marsbar	5.0 (see text)
Ar (400)	C	0.72
	Cu	1.34
	Pb	1.70
Ar (560)	C	1.08
	Cu	1.79
	Pb	2.27
	Marsbar	5.0 (see text)
Fe (500)	Li	0.903
	CH_2	0.957
	Al	1.285

Table 3.3 (continued)

Beam (energy) (MeV/nucleon)	Target	Thickness (g/cm^2)
Kr (400)	Li	0.47
	C	0.55
	CH_2	0.46
	Al	0.54
	Cu	0.90
	Pb	1.02
Xe (400)	Li	0.48
	C	0.27
	CH_2	0.20 (PH2)
	CH_2	0.30 (SB3)
	Al	0.26
	Cu	0.45
	Pb	0.57

Table 3.4: Martian regolith composition

Element	Atomic density (atoms/g)
O	1.67×10^{22}
Mg	1.62×10^{21}
Si	5.83×10^{21}
Ca	7.81×10^{20}

The target called "ISS wall" is a section of the wall used in some parts of the International Space Station. It is regarded as an example of typical material for the design of transit vehicles and orbital vehicles used in space exploration. The ISS wall is comprised of 1.89 g/cm^2 of aluminum, 0.218 g/cm^2 of Nomex® honeycomb wall, 0.08 g/cm^2 of Nomex® cloth, 0.06 g/cm^2 Durette® batting, and 0.72 g/cm^2 silicon rubber. The 1.89 g/cm^2 aluminum is a combination of two pieces: an outer "bumper" hull, and an inner pressure wall. Like the marsbar target, the ISS wall target was 10-cm wide and 10-cm high. The 400 MeV/nucleon Ne beam incident upon the ISS wall has an exit energy of 360 MeV/nucleon (median energy of 380 MeV/nucleon).

NE102A plastic scintillators (15x15 cm square by 0.5 cm thick) were placed directly in front of the E counter as the ΔE counter to discriminate charged particles from neutrons and photons. Relative to the thickness of

the neutron detectors, the ΔE counters are extremely thin, and as such, have an extremely low probability of detecting a neutron or gamma ray that passes through it. Any event detected in the E counter that also scintillated in the ΔE counter was assumed to be a charged particle. In this way, neutron and gamma-ray events were separated from charged particle events.

After applying the charged/uncharged particle discrimination, neutron and gamma-ray events were separated from each other by using two-dimensional total-slow pulse height graphical plots. In these plots, two distinct bands of events are evident, one for neutron events and the other for gamma-ray events. The two bands show a clear separation from each other down to the lowest energy thresholds used in the data analysis.

An iron shadow bar (15x15 cm square by 60 cm thick) was placed periodically between the target and detector, with approximately 15 cm between the upstream face of the neutron detector and the downstream edge of the shadow bar. Data taken with the shadow bars in position give a measure of the background neutron components from room scattering. In general, about ¼ to 1/3 of the total beam time at each angle was spent measuring the background contribution.

After obtaining the neutron TOF spectra, they are converted to energy spectra, using relativistic kinematics. The number of events at each neutron energy is corrected for the energy-dependent neutron detection efficiency. The experimentally determined detection efficiency for the scintillators used in the HIMAC experiments has been published by Nakao *et al.*, but there are no data for neutrons of energy higher than 206 MeV [3.2], [3.3]. As such, the neutron detection efficiencies were calculated with the Monte Carlo code by Cecil *et al.*[3.4] over all energies. The overall time resolution $\Delta\tau$ is taken as the FWHM of the prompt γ-ray peak observed in each neutron TOF spectrum. In general, and the observed widths of the prompt peaks in the time spectra were on the order of 0.9 to 1.2 ns.

Data was acquired on an event-by-event basis. Acquisition live times varied between 60% and 90%. The trigger for a valid event was a coincidence between a signal in the trigger detector and a signal in one (or more) of the neutron detectors. For each event, the following

information was recorded: (1) the magnitude of the signal from the trigger detector, as measured by a charge-integrating analog-to-digital converter (QDC); the magnitudes of the (2) total and (3) slow components of the pulse from the neutron detector's photomultiplier tubes, as measured by a QDC; (4) the time difference between the signal from the trigger detector and the trigger-event coincidence gate, as measured with a time-to-digital converter (TDC); and (5) the "self" time difference between the signal from neutron detector and the trigger-event gate signal.

Additional experimental details may be found in Refs. [3.1] and [3.5]

3.2.2 RIKEN experiments

Beams of 135 MeV/nucleon He, C, and Ne, and 95 MeV/nucleon Ar were transported through the beam swinger system at RIKEN into a scattering chamber that held the target. A diagram of the experimental setup may be seen in Figure 3.4. A single NE-213 neutron detector (same dimensions as the detectors used for the HIMAC experiments) was placed 847 cm from the target position. After passing through the target, beam particles were bent by a dipole magnet towards a beam dump. Neutrons moving in the forward direction from the target position continued 7 m through a beam pipe, and exited through a 3-cm thick acrylic vacuum window, into air.

Before entering the neutron detector, the neutrons passed through a 120-cm thick, 22 x 22 cm-square iron collimator. Concrete blocks, 240-cm thick, surrounded the collimator in order to shield the detector from background neutron that came from the beam dump. A 0.5-cm thick NE-102A plastic scintillator was placed directly in front of the neutron detector in order to detect any charged particles that were incident upon the neutron detector. The number of beam particles incident upon the target were counted with a Faraday cup coupled to the beam dump.

The RF from the cyclotron was used as the stop signal in the time-of-flight measurement (start was a signal from the neutron detector). The beam swinger allowed measurements of neutron spectra at 0, 15, 30, 50, 80 and 110 degrees relative to the beam direction into the target. Measurement of background spectra through the use of shadow bars was

not possible. Background rates were estimated to be low due to the extensive shielding around the collimator and beam dump. Blank target runs were taken, and background rates could be estimated from those measurements, as well. The targets used were C (0.216 g/cm^2), Al (0.162 g/cm^2), Cu (0.268 g/cm^2), and Pb (0.340 g/cm^2).

Data was acquired on an event-by-event basis. Charged particles were eliminated by using ΔE-E plots made from the NE-102A (ΔE) and NE-213 (E) data. Gamma-ray events were eliminated using the pulse-shape discrimination properties of NE-213 liquid scintillator.

Additional experimental details may be found in Ref. [3.6].

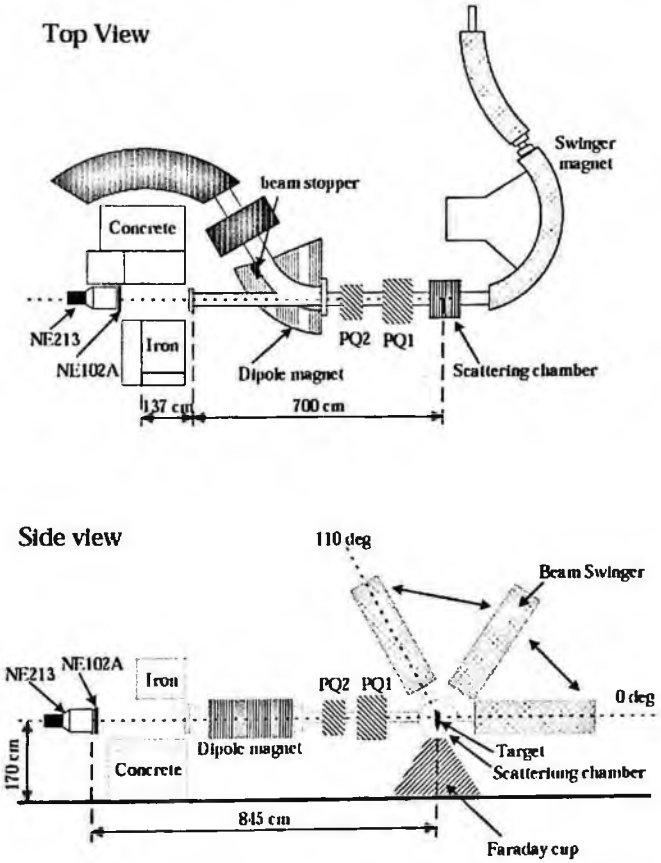

Figure 3.4: The experimental setup used in the RIKEN experiments (courtesy Ref. 3.6).

3.2.3 Bevalac experiments

The Ne beam at extraction had an energy of 407 MeV/nucleon, and had an energy of 369 MeV/nucleon when incident upon the target. Beam spot size was 4 cm (vertical) by 5 cm (horizontal). The carbon, aluminum, copper and depleted uranium targets had areal densities of 3.06 ± 0.04 g/cm^2, 3.38 ± 0.04 g/cm^2, 3.81 ± 0.04 g/cm^2, and 5.60 ± 0.06 g/cm^2, respectively, which in turn led to about a 20% energy loss in the target. Beam energy at the center of the target was approximately 337 MeV/nucleon, and results are reported at that energy. Each target was 10 cm square. A two-element scintillator telescope placed upstream from the target was used as a beam monitor and to provide a start signal in the time-of-flight measurement. The first element ("S1", 20 cm square, 0.63-cm thick) was placed 10 m upstream from the target, and the second element ("S2", 7.5-cm square, 0.8-mm thick) was placed directly upstream from the target. Both the targets and S2 were rotated 45° relative to the beam. Approximately 20% of the beam counts in S1 were not detected in coincidence in S2.

Neutron energies were determined using the time-of-flight method. Start signals were provided by the beam telescope, stop signals provided by a mean-timed signal from one of the four neutron detectors. The plastic NE-102 neutron detectors were place at 30° (5.05-m flight path), 45° (5.60-m flight path), 60° (6.04-m flight path) and 90° (4.17-m flight path). Each neutron detector was 1.02-m long by 10.2-cm thick. The detectors at 30° and 45° were 12.7-cm high, and the others were 25.4-cm high. A phototube was placed at each end of the neutron detector, and the signals from each pair were mean timed. A 0.63-cm thick NE-102 scintillator was placed in front of each neutron detector to detect charged particles. Background spectra were measured using shadow shields. Event rates were checked at each angle with and without a shadow shield at a nearby detector to verify that neutron scattering from the shields did not contaminate neighboring detectors. Runs with and without shadow shields were normalized to each other using the number of incident beam particles for each run and correcting for the live time in each run.

Additional details may be found in Refs. [3.7] and [3.8].

3.3 Results

3.3.1 Analysis of HIMAC experiments

Neutron energy spectra were generated from the raw time-of-flight data. Overall energy resolution was estimated by:

$$\frac{\Delta E_n}{E_n} = \frac{E_n + M_n}{E_n} \frac{\beta^2}{1-\beta^2} \sqrt{\left(\frac{\Delta L}{L}\right)^2 + \left(\frac{\Delta t}{t}\right)^2}, \tag{3.1}$$

where Δt refers to the overall timing resolution, t refers to the time of flight, L refers to the flight path, E_n and β refer to the usual kinematical quantities, M_n is the neutron rest mass (in MeV/c^2), and ΔL refers to the thickness of the neutron detector (12.7 cm). Table 3.5 shows the energy resolutions as a function of detector number (numbers referenced in experimental details section) and neutron energy. Energy resolution improves as the neutron energy decreases, so the values listed in Table 3.5 show the upper bounds of neutron energy resolution. The double-differential spectra were binned in energy such that the minimum bin width was equal to or greater than the corresponding energy resolution (in MeV) for the mean value of the energy in that bin.

Table 3.5: Energy resolution for the given neutron detectors and neutron energies.

Neutron detector	% resolution ($\Delta E/E$) for $E_n = 200$ MeV	% resolution ($\Delta E/E$) for $E_n = 400$ MeV	% resolution ($\Delta E/E$) for $E_n = 600$ MeV
N1 (5°)	7.75	10.7	13.8
N2 (10°)	7.75	10.7	13.8
N3 (20°)	8.60	11.8	14.4
N4 (30°)	8.60	11.8	14.4
N5 (40°)	9.66	13.3	17.3
N6 (60°)	11.0	15.2	19.7
N7 (80°)	12.8	17.7	22.9

Cross sections were normalized to the number of incoming beam particles. The number of incident beam particles was counted using the trigger detector. Events in which the trigger detector fired more than once during the trigger-detector/neutron-detector coincidence were excluded from the analysis, and the number of beam particles in those events were excluded from the normalization.

In order to express the cross sections in units of barns, the data were also normalized to the number of scattering sites per unit area. For elemental targets, the calculation of the number of scattering sites is straightforward. For composite targets, each atomic constituent of the material was considered a scattering site. Thus, for the marsbar target, a normalization factor of 0.2102 scattering sites per barn was calculated using the information from Table 3.4, along with the reported ratio of polyethylene-to-marsbar in the target. For the ISS wall target, a normalization factor of 0.0632 scattering sites per barn was calculated using information from the manufacturer. If one wishes to express the cross sections in units of number of neutrons per incoming ion per g/cm^2 of target, then: (1) for the marsbar target, multiply cross sections expressed in barns by 0.042 (=0.2102 ÷ 5.0 g/cm^2), and (2) for the ISS wall target, multiply cross sections expressed in barns by 0.0213 (=0.0632 ÷ 2.97 g/cm^2).

Table 3.6: Systematic uncertainties from the HIMAC experiments. The uncertainty described as "blank target yield" refers to neutrons produced by materials close to the target, and applies to the SB3 beam line experiments, only.

Source of systematic uncertainty	Estimated % uncertainty on normalization
Detection efficiency	≈ 10 %
Angular acceptance	≤ 10 %
Threshold determination	≤ 5 %
Target depth	≤ 5%
Attenuation	2 % to 50 % (a)
Blank target	3 % to 30 % (b)

(a) Neutron flux attenuation depends on neutron energy and angle detected. The worst case is for low-energy neutrons at 80°. For most energies and angles, the attenuation is about 10%.

(b) The contribution from "blank target" neutrons is worse at forward angles.

Unless otherwise noted, the uncertainties shown in the figures are statistical, only. The systematic uncertainties were estimated from the following factors: (1) uncertainty in target depth, (2) uncertainty in QDC calibration (affects threshold determination in efficiency calculation), (3) uncertainty in detection efficiency, (4) attenuation of neutrons through the target and other intervening materials, (5) production of neutrons from materials close to the target (SB3 measurements only; PH2 beam line measurements included blank target runs), and (6) angular acceptance of each neutron detector (see Table 3.2). Table 3.6 lists the estimated values for each source of systematic error.

3.3.2 Analysis of RIKEN experiments

Neutron energies were calculated from the time-of-flight measurements. The energy resolution was calculated in the same manner as for the HIMAC experiments, using Eqn 3.1. The overall time resolution, as determined by the FWHM of the prompt gamma-ray peak, was about 1.1 ns. The corresponding energy resolution for a 100 MeV neutron was about 3%.

The statistical uncertainties varied from 2 to 5 percent for low to medium energy neutrons (10 to 100 MeV), and around 30% for the highest energies. Background measurements were not made directly; instead, a measurement with target and another one without target were compared, and background was estimated from that. The background component was found to be less than 10%. The systematic uncertainty in the number of incident beam particles was estimated to be less than 5%. The uncertainty in the angular acceptance was less than 2%. The uncertainty in the efficiency calculation was estimated to be about 16%. The overall normalization uncertainty, then, was within 17%.

3.3.3 Analysis of Bevalac experiments

The timing resolution of the neutron detectors, as determined by measuring the FWHM of the prompt gamma-ray peaks, varied between 400 and 600 ps. Energy resolution was determined using the same method outlined in Eqn. 3.1. The factors contributing to the overall

normalization (systematic) uncertainty include the number of incident ions (1%), solid angle (1%), flight path (2%), neutron detection efficiency (5%-10%), target thickness (3%), attenuation through the target (2%), and attenuation through the air (2%).

3.3.4 Double-differential spectra

Figures 3.5 through 3.61 show the double-differential neutron production cross sections for the indicated systems. At forward angles (0° for the RIKEN experiments, 5° for the HIMAC experiments), there is a prominent peak centered near the beam energy per nucleon. As the angle increases, the prominence of the peak decreases to a point at about 20° where the peak is insignificant. The high-energy neutrons in the region of this forward peak come mainly from the breakup of the projectile, along with direct knock-out neutrons from the target. Neutrons are detected at energies 2 to 3 times the beam energy per nucleon, which is a phenomenon attributable to the collective Fermi motion inside the nucleus adding a momentum kick during the collision. At energies below 10 – 20 MeV, the spectra are dominated at all angles by the decay of the target remnant. The exponential behavior of the cross section with energy in this region suggests the target remnant decays by an equilibrium process. At intermediate energies (above 10 to 20 MeV, below the beam energy per nucleon), there is a component that becomes less pronounced as the angle increases. This component is dominated by the pre-equilibrium decay of the overlap region between the projectile and the target.

3.3.5 Angular distributions

Figures 3.62 through 3.65 show the angular distributions from the 95 MeV/nucleon Ar systems and the 135 MeV/ nucleon He, C, and Ne systems. The distributions were generated by integrating the spectra over neutron energies above 20 MeV. Each plot shows the angular distribution for the indicated target (C, Al, Cu, and Pb). The lines drawn on the plots are a guide to the eye. As the projectile mass increases, the angular distribution is more forward peaked (compare Figs. 3.63 and

3.65). At larger angles ($\geq 30°$), the slope of the angular distribution appears to be the same, independent of projectile mass.

The angular distributions from selected HIMAC measured systems are shown in Figures 3.66 through 3.70. At forward angles, the yield decreases rapidly with increasing angle. There, the yield is primarily due to direct knock-out processes and the breakup of the projectile. At large angles, the yields also decrease with increasing angle, although not as rapidly as they do at forward angles. Here, the yields come predominantly from the pre-equilibrium decay of the overlap region. In general, as the target mass decreases, the distribution becomes more forward focussed. This may be due to the decrease in the number of target-like neutrons that contribute to the bulk of the yield at large angles. As the mass of the projectile increases (at the same energy per nucleon), the yield becomes more forward-focussed due to the increase in the number of projectile-like neutrons (compare Figs. 3.68 and 3.69).

The lines shown in selected angular distributions show fits using the following equation:

$$Y = a_1 \exp(-a_2\theta) + a_3 \exp(-a_4\theta), \tag{3.2}$$

where Y is the angular cross section (mb per steradian per ion), θ is the angle (in degrees) and a_1, a_2, a_3, and a_4 are fit parameters. The two exponents represent the contributions to the spectra from the projectile-like source and the decay of the overlap region. Because target-like neutrons only go up to about 20 MeV, and because the angular spectra are generated by integrating over all energies, the contribution from target-like neutrons is dominated by the contributions from the other sources (especially for spectra with relatively high neutron energy threshold). Table 3.7 shows the fit parameters to all the angular distributions using Eqn. 3.2. The units of a_1 and a_3 are mb per steradian per ion, and the units of a_2 and a_4 are 1/deg.

Table 3.7: Fit parameters used in Eqn. 3.2 for the angular distributions in the indicated systems.

System	a_1 (mb/sr)	a_2 (1/deg)	a_3 (mb/sr)	a_4 (1/deg)
95 AMeV Ar + C	10600	0.155	1340	0.048
95 AMeV Ar + Al	15300	0.137	2440	0.043
95 AMeV Ar + Cu	22700	0.118	4030	0.038
95 AMeV Ar + Pb	47200	0.109	8780	0.032
135 AMeV He + C	279	0.078	45.6	0.024
135 AMeV He + Al	508	0.079	120	0.023
135 AMeV He + Cu	786	0.058	146	0.016
135 AMeV He + Pb	1690	0.106	863	0.021
135 AMeV C + C	705	0.168	405	0.043
135 AMeV C + Al	1230	0.146	681	0.034
135 AMeV C + Cu	1830	0.163	1430	0.035
135 AMeV C + Pb	5870	0.173	3000	0.029
135 AMeV Ne + C	1880	0.122	360	0.034
135 AMeV Ne + Al	3070	0.106	677	0.030
135 AMeV Ne + Cu	3810	0.115	1920	0.033
135 AMeV Ne + Pb	5840	0.131	4860	0.029
230 AMeV He + Al	1353	0.101	590	0.032
230 AMeV He + Cu	4080	0.161	1390	0.030
290 AMeV C + C	18039	0.235	2413	0.050
290 AMeV C + Cu	38684	0.196	4509	0.035
290 AMeV C + Pb	134440	0.159	8904	0.023
290 AMeV C + marsbar	31670	0.246	2100	0.030
400 AMeV C + C	128450	0.845	1757	0.042
400 AMeV C + Cu	126190	0.681	4848	0.032
400 AMeV C + Pb	23245	0.214	8872	0.021
400 AMeV N + C	550280	0.959	3494	0.049
400 AMeV N + Cu	43471	0.387	8413	0.037
400 AMeV Ne + C	45049	0.282	6491	0.051
400 AMeV Ne+ Cu	55585	0.204	14808	0.037
400 AMeV Ne + Pb	154810	0.133	27650	0.026
400 AMeV Ne + ISS wall	34500	0.123	2440	0.012
400 AMeV Ar + C	505200	0.339	14564	0.054
400 AMeV Ar + Cu	804260	0.287	36486	0.042
400 AMeV Ar + Pb	1177800	0.245	69452	0.033
400 AMeV Kr + Li	4081500	0.686	20111	0.061
400 AMeV Kr + C	3847400	0.658	25107	0.057
400 AMeV Kr + CH_2	6652800	0.658	29627	0.057
400 AMeV Kr + Al	4159500	0.621	52463	0.057

Table 3.7 (continued)

System	a_1 (mb/sr)	a_2 (1/deg)	a_3 (mb/sr)	a_4 (1/deg)
400 AMeV Kr + Cu	10210000	0.779	78904	0.050
400 AMeV Kr + Pb	1999400000	1.676	130080	0.038
400 AMeV Xe + Li	4321800	0.595	37394	0.074
400 AMeV Xe + C	3624200	0.550	45944	0.069
400 AMeV Xe + CH_2	7159700	0.578	42890	0.060
400 AMeV Xe + Al	2776200	0.467	52493	0.053
400 AMeV Xe + Cu	3452900	0.467	87947	0.049
400 AMeV Xe + Pb	7102700	0.571	157570	0.037
560 AMeV Ar + C	200730	0.235	11256	0.053
560 AMeV Ar + Cu	375890	0.232	62558	0.047
560 AMeV Ar + Pb	583590	0.177	62026	0.030
600 AMeV Ne + Li	130.0	0.20	10.0	0.050
600 AMeV Ne + C	103330	0.404	4104	0.044
600 AMeV Ne + CH_2	69.0	0.20	5.5	0.047
600 AMeV Ne + Al	7.2	0.28	1.43	0.028
600 AMeV Ne + marsbar	127000	0.33	10300	0.048
600 AMeV Ne + Cu	55585	0.205	14808	0.037
600 AMeV Ne + Pb	154810	0.133	4104	0.027

The forward-focussed neutrons are represented by the first exponential term in Eqn. 3.2. In general, the value of a_1 increases with the product of the neutron number of the projectile and the range of each target, and decreases with the square of the mass number of the target. The value of a_2 remains about the same for each projectile and decreases with increasing target mass. The decay of the overlap region is represented by the second exponential term in Eqn. 3.2. The value of a_3 increases with projectile energy per nucleon and decreases, in general, as the target mass increases. The value of a_4 increases with the total kinetic energy of the projectile.

3.3.6 Total yields

Table 3.8 lists the total cross sections (in barns) for the indicated systems, neutron energy threshold, and angular ranges. The total cross sections were obtained by numerically integrating the experimental angular distributions. In some cases the lower and upper limit in polar

angle was the range in detection angle. In other cases the lower and upper limits were modest extensions in polar angle over the detection range (for example, some of the HIMAC data has been integrated over 0° to 90°, even though the detectors ranged in angle between 5° and 80°).

Table 3.8: The total cross sections (in barns) for the indicated systems. The threshold indicates the lower limit in neutron energy, and the angular range indicates the range in polar angle used in the numerical integration.

System	Threshold	Angular range	σ (b)
95 AMeV Ar + C	20 MeV	0° - 110°	14.2
95 AMeV Ar + Al	20 MeV	0° - 110°	22.7
95 AMeV Ar + Cu	20 MeV	0° - 110°	35.9
95 AMeV Ar + Pb	20 MeV	0° - 110°	77.2
135 AMeV He + C	20 MeV	0° - 110°	0.61
135 AMeV He + Al	20 MeV	0° - 110°	1.3
135 AMeV He + Cu	20 MeV	0° - 110°	2.6
135 AMeV He + Pb	20 MeV	0° - 110°	6.3
135 AMeV C + C	20 MeV	0° - 110°	1.8
135 AMeV C + Al	20 MeV	0° - 110°	4.0
135 AMeV C + Cu	20 MeV	0° - 110°	7.1
135 AMeV C + Pb	20 MeV	0° - 110°	17.3
135 AMeV Ne + C	20 MeV	0° - 110°	3.1
135 AMeV Ne + Al	20 MeV	0° - 110°	6.2
135 AMeV Ne + Cu	20 MeV	0° - 110°	11.5
135 AMeV Ne + Pb	20 MeV	0° - 110°	26.7
290 AMeV C + C	10 MeV	5° - 80°	1.86
290 AMeV C + Cu	10 MeV	5° - 80°	6.08
290 AMeV C + Pb	10 MeV	5° - 80°	22.1
290 AMeV C + Marsbar	3 MeV	0° - 90°	4.0
337 AMeV Ne + C	25 MeV	30° - 90°	1.03
337 AMeV Ne + Al	25 MeV	30° - 90°	1.80
337 AMeV Ne + Cu	25 MeV	30° - 90°	4.59
337 AMeV Ne + Pb	25 MeV	30° - 90°	17.10
400 AMeV C + C	10 MeV	5° - 80°	1.43
400 AMeV C + Cu	10 MeV	5° - 80°	6.08
400 AMeV C + Pb	10 MeV	5° - 80°	17.0
400 AMeV Ne + C	10 MeV	5° - 80°	4.37
400 AMeV Ne + Cu	10 MeV	5° - 80°	15.8
400 AMeV Ne + Pb	10 MeV	5° - 80°	52.8
400 AMeV Ne + ISS wall	3 MeV	0° - 90°	12.5
600 AMeV Ne + C	10 MeV	5° - 80°	3.74

Table 3.8 (continued)

System	Threshold	Angular range	σ (b)
600 AMeV Ne + Cu	10 MeV	5° - 80°	18.7
600 AMeV Ne + Pb	10 MeV	5° - 80°	57.2
600 AMeV Ne + Marsbar	3 MeV	0° - 90°	10.4
400 AMeV Ar + C	10 MeV	5° - 80°	10.7
400 AMeV Ar + Cu	10 MeV	5° - 80°	37.0
400 AMeV Ar + Pb	10 MeV	5° - 80°	96.9
560 AMeV Ar + C	10 MeV	5° - 80°	9.6
560 AMeV Ar + Cu	10 MeV	5° - 80°	49.0
560 AMeV Ar + Pb	10 MeV	5° - 80°	102

The total cross sections as a function of target mass number from the RIKEN experiments are shown in Fig. 3.71. Analysis of the RIKEN data by Sato *et al.* revealed that the total cross sections above 20 MeV (integrated from 0° to 90°) could be parameterized with the following:

$$\sigma = 1.38 \times A_t^{1/2} \times N_p \left(A_p^{1/3} + A_t^{1/3} - b_0 \right)^2, \tag{3.3}$$

where σ is the total cross section in mb, A_t and A_p are the mass numbers of the target and projectile, N_p is the neutron number of the projectile, and b_0 is given by:

$$b_0 = 1.581 - 0.876\left(A_p^{-1/3} + A_t^{-1/3} \right). \tag{3.4}$$

Figure 3.72 shows the total cross sections as a function of target mass number from selected systems measured at HIMAC. Qualitatively, the total cross sections in Fig. 3.72 show the same behavior as a function of target-mass number as do the cross sections in Fig. 3.71. The dependence of the total cross section on the beam energy is shown in Figs. 3.73 through 3.75. Figure 3.73 shows the total cross sections as a function of target mass number for C beams ranging from 135 to 400 MeV/nucleon, Fig. 3.74 shows the total cross sections as a function of target mass number for Ne beams ranging from 135 to 600 MeV/nucleon, and Fig. 3.75 shows the total cross sections as a function

of target mass number for Ar beams ranging from 95 to 560 MeV/nucleon. As a reminder, the 95- and 135-MeV/nucleon systems were integrated over neutron energies above 20 MeV, and the other systems were integrated over neutron energies above 10 MeV. Most of the data suggests there is little variation in the total cross section as a function of beam energies ranging from 100 to 600 MeV/nucleon.

3.4 Double Differential Neutron Production Cross Sections from HIMAC Experiments

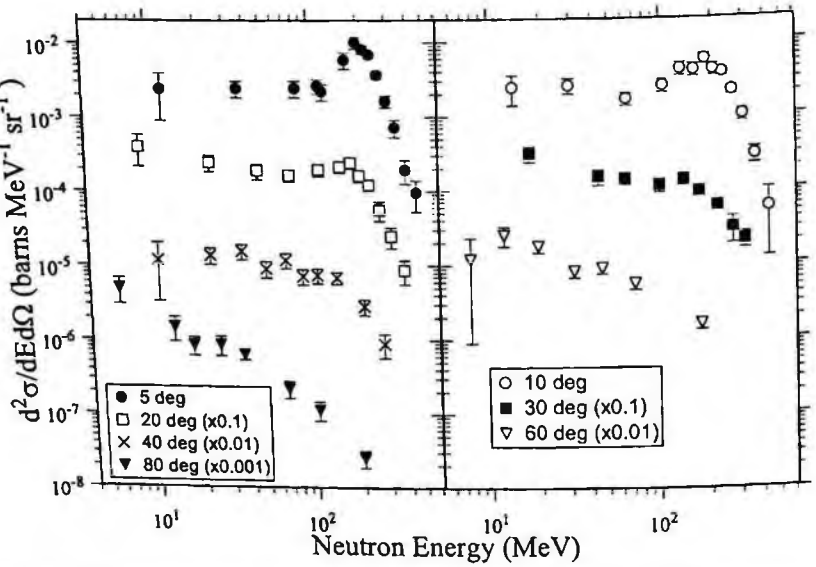

Figure 3.5: Double differential neutron production cross sections from 230 MeV/nucleon He + Al (data not published).

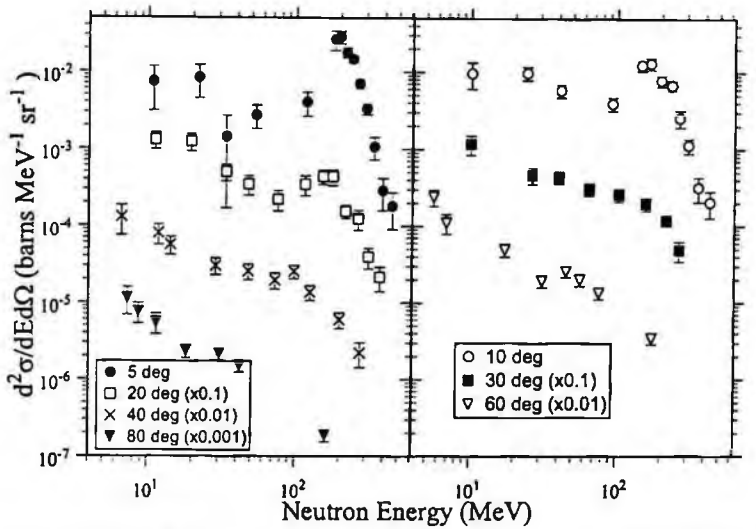

Figure 3.6: Double differential neutron production cross sections from 230 MeV/nucleon He + Cu (data not published).

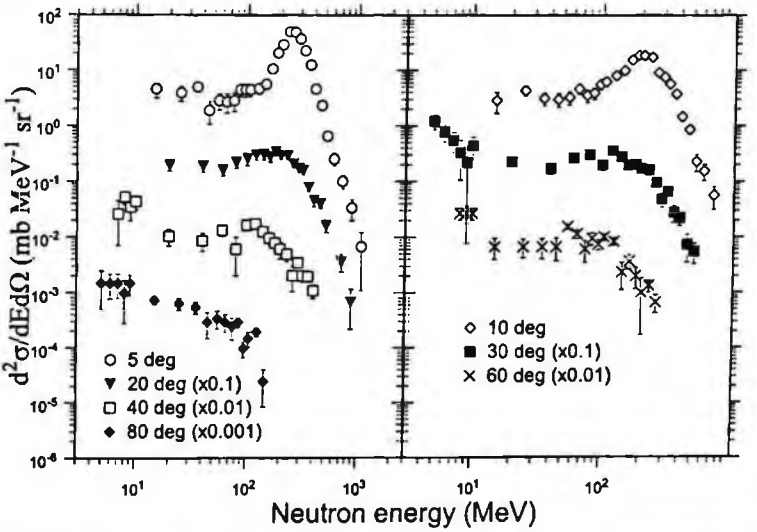

Figure 3.7: Double differential neutron production cross sections from 290 MeV/nucleon C + C.

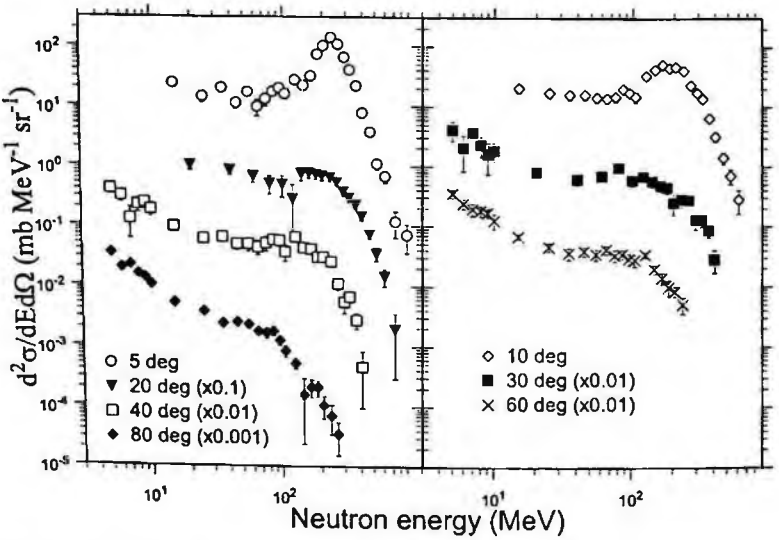

Figure 3.8: Double differential neutron production cross sections from 290 MeV/nucleon C + Cu.

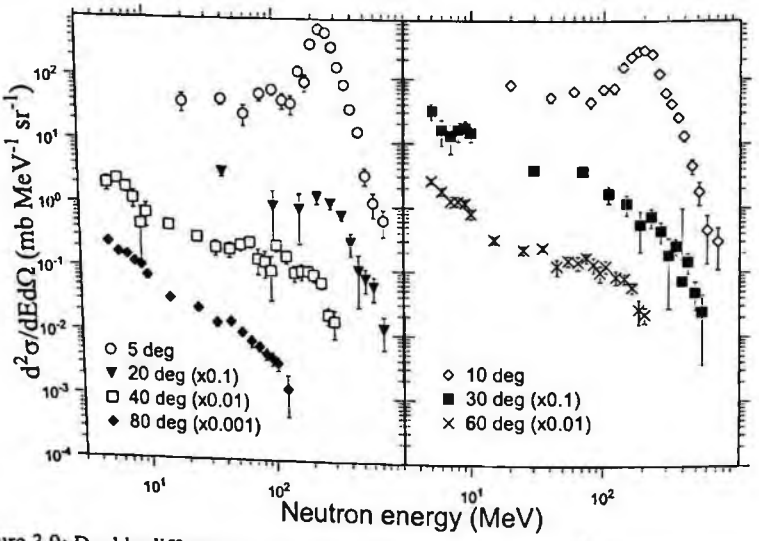

Figure 3.9: Double differential neutron production cross sections from 290 MeV/nucleon C + Pb.

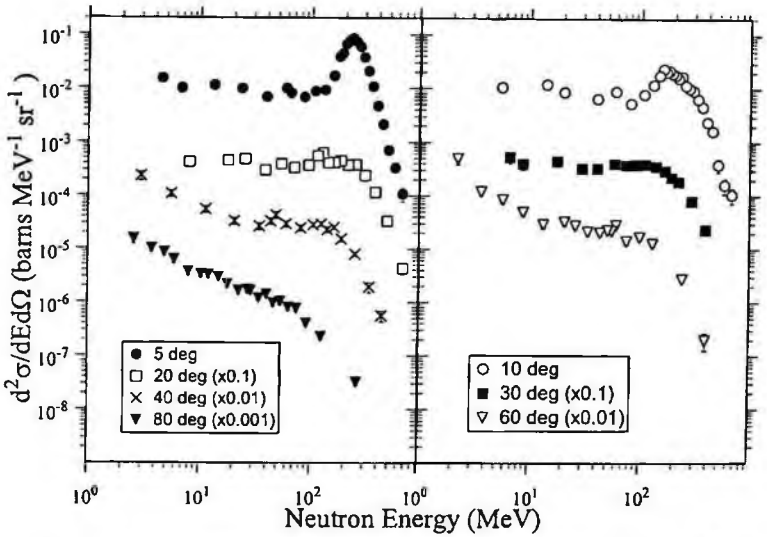

Figure 3.10: Double differential neutron production cross sections from 290 MeV/nucleon C + Martian regolith (data not published).

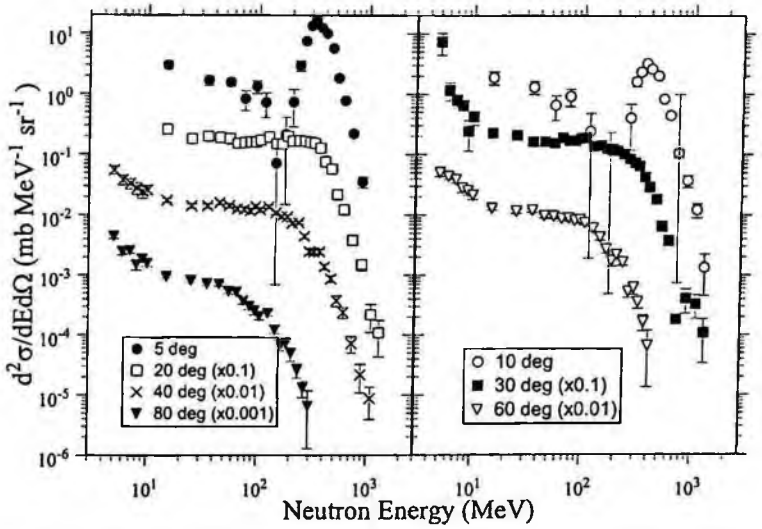

Figure 3.11: Double differential neutron production cross sections from 400 MeV/nucleon C + C.

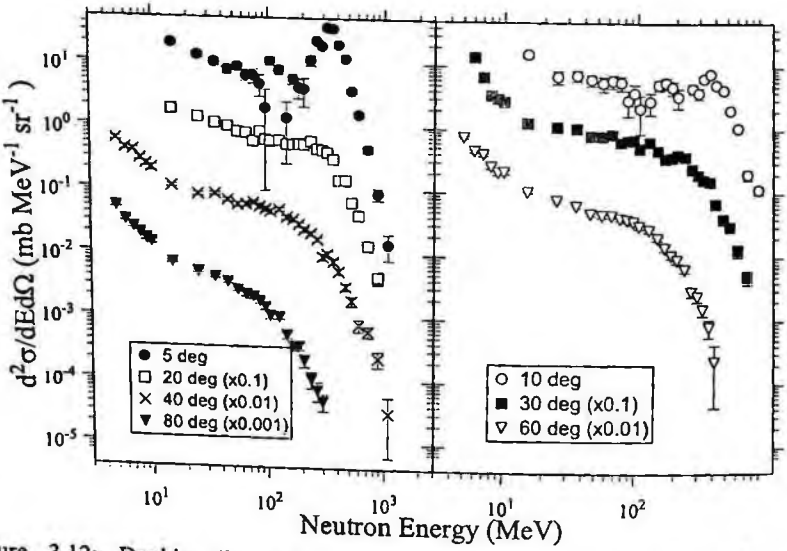

Figure 3.12: Double differential neutron production cross sections from 400 MeV/nucleon C + Cu.

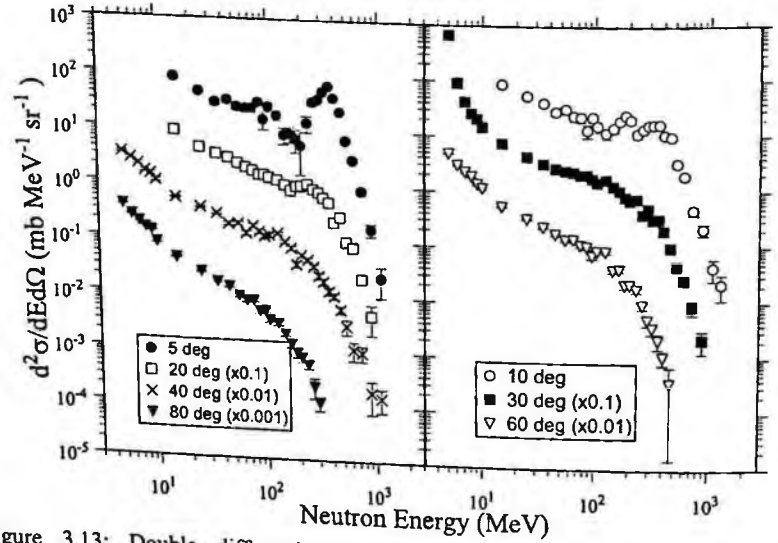

Figure 3.13: Double differential neutron production cross sections from 400 MeV/nucleon C + Pb.

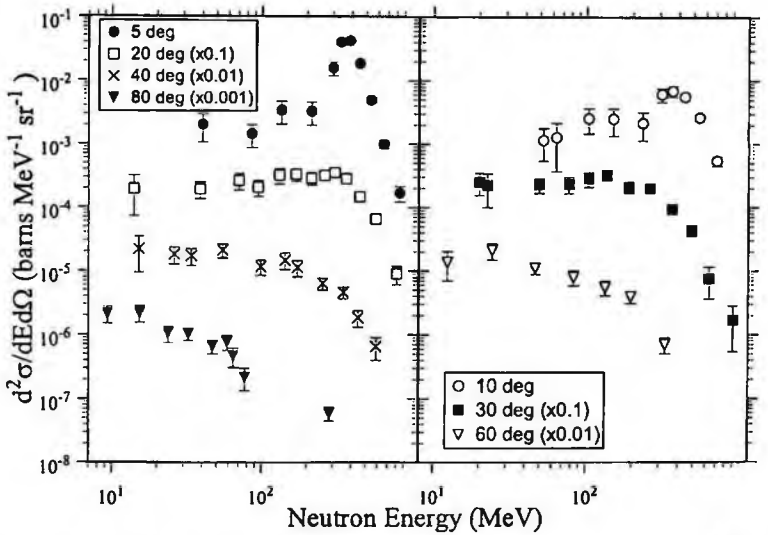

Figure 3.14: Double differential neutron production cross sections from 400 MeV/nucleon N + C (data not published).

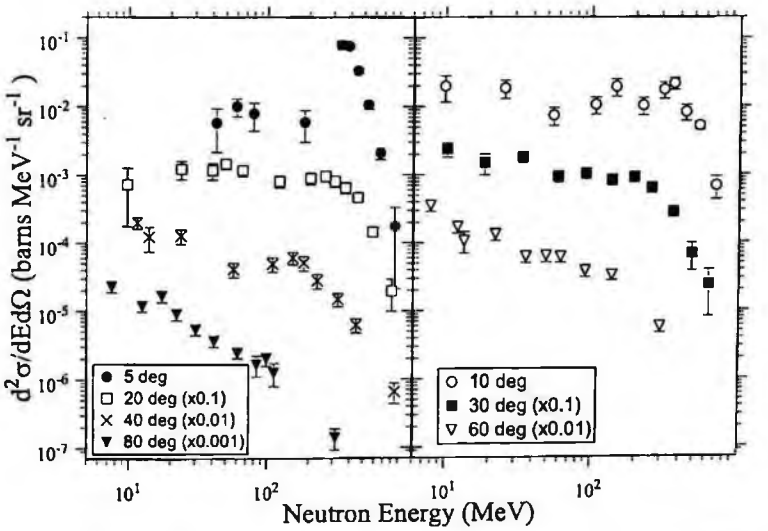

Figure 3.15: Double differential neutron production cross sections from 400 MeV/nucleon N + Cu (data not published).

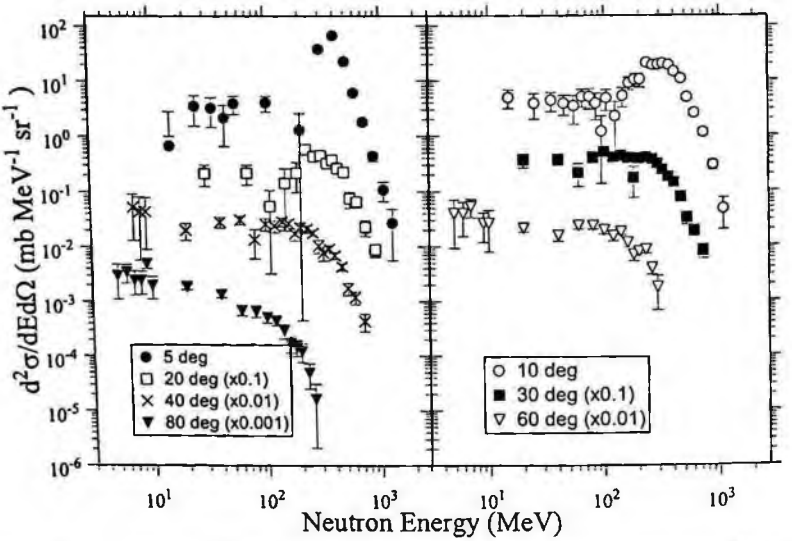

Figure 3.16: Double differential neutron production cross sections from 400 MeV/nucleon Ne + C.

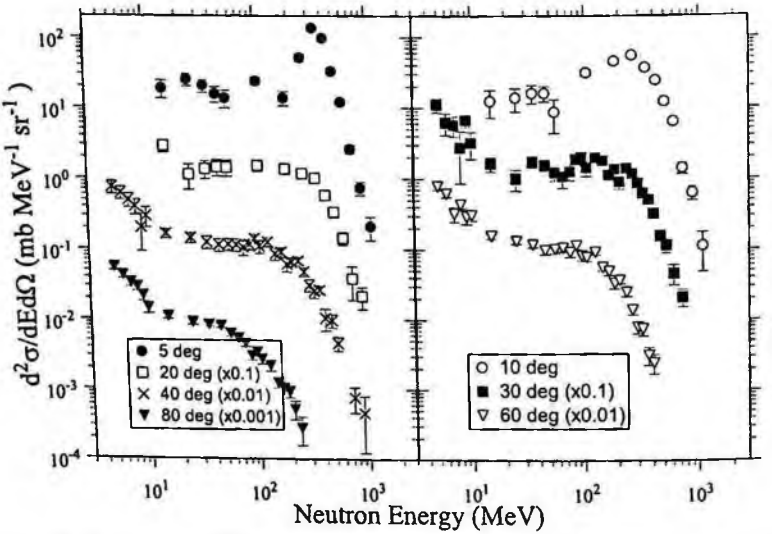

Figure 3.17: Double differential neutron production cross sections from 400 MeV/nucleon Ne + Cu.

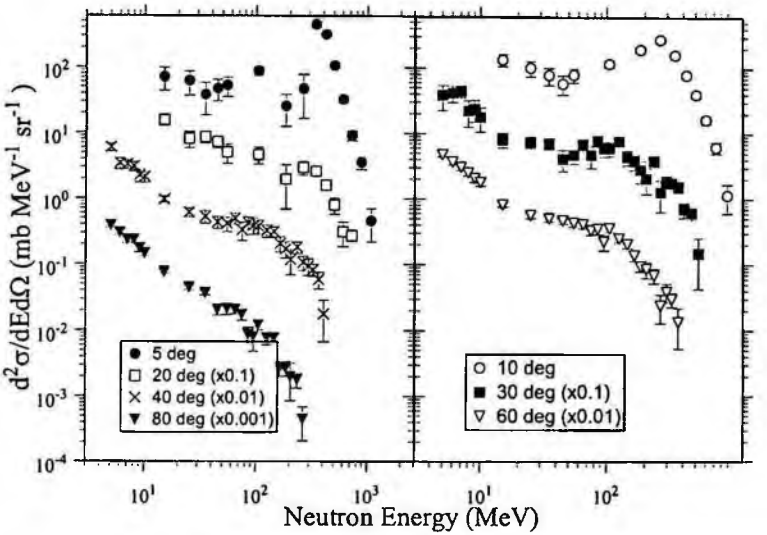

Figure 3.18: Double differential neutron production cross sections from 400 MeV/nucleon Ne + Pb.

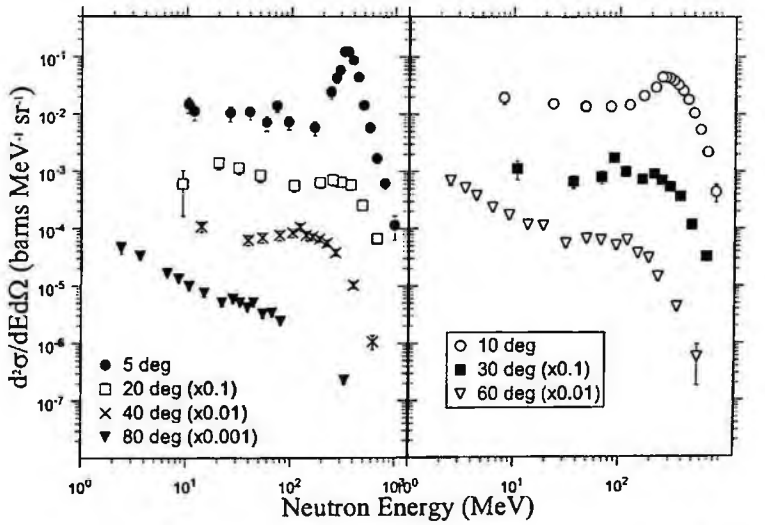

Figure 3.19: Double-differential neutron-production cross sections from 400 MeV/nucleon Ne interacting in an ISS wall segment (data not published).

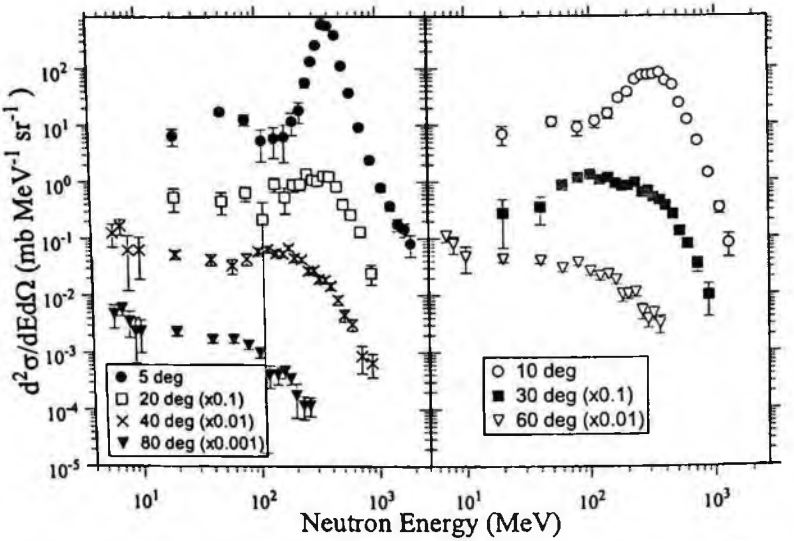

Figure 3.20: Double differential neutron production cross sections from 400 MeV/nucleon Ar + C.

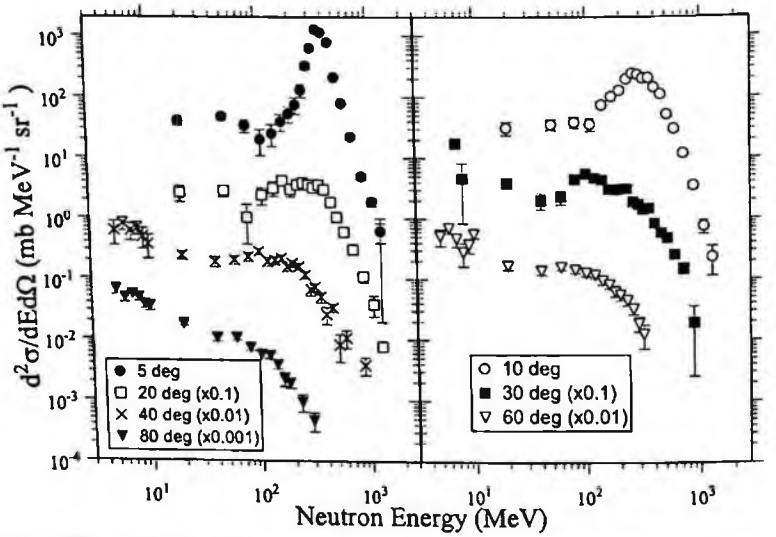

Figure 3.21: Double differential neutron production cross sections from 400 MeV/nucleon Ar + Cu.

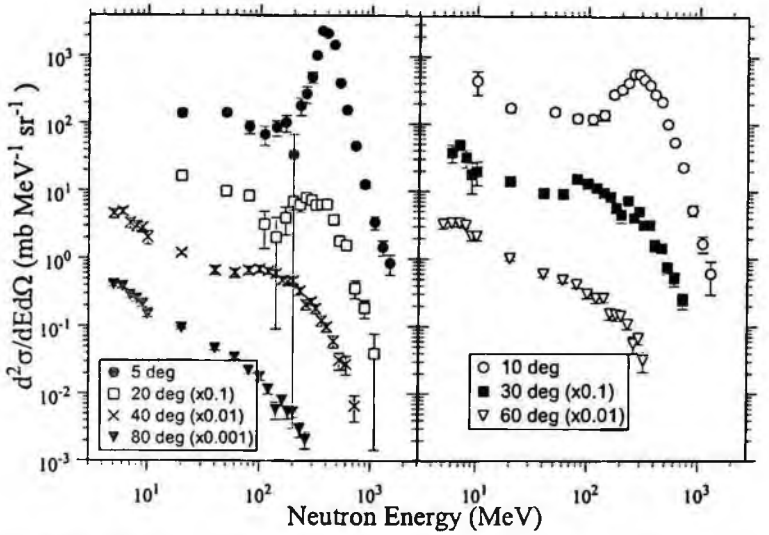

Figure 3.22: Double differential neutron production cross sections from 400 MeV/nucleon Ar + Pb.

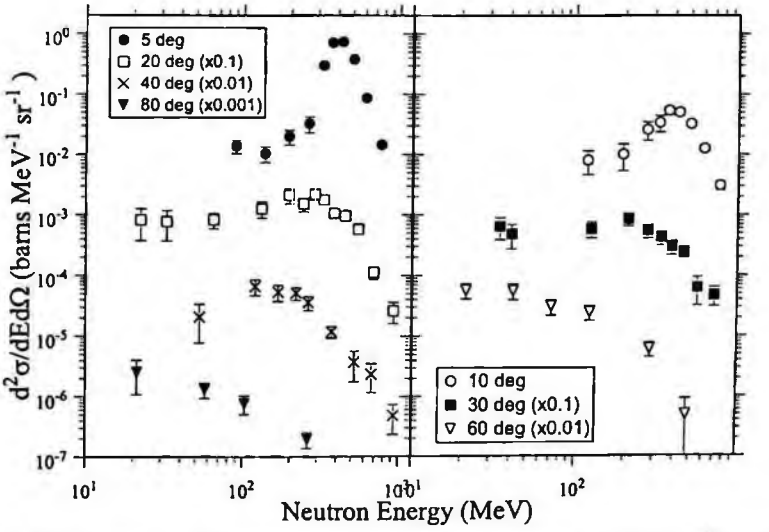

Figure 3.23: Double differential neutron production cross sections from 400 MeV/nucleon Kr + Li (data not published).

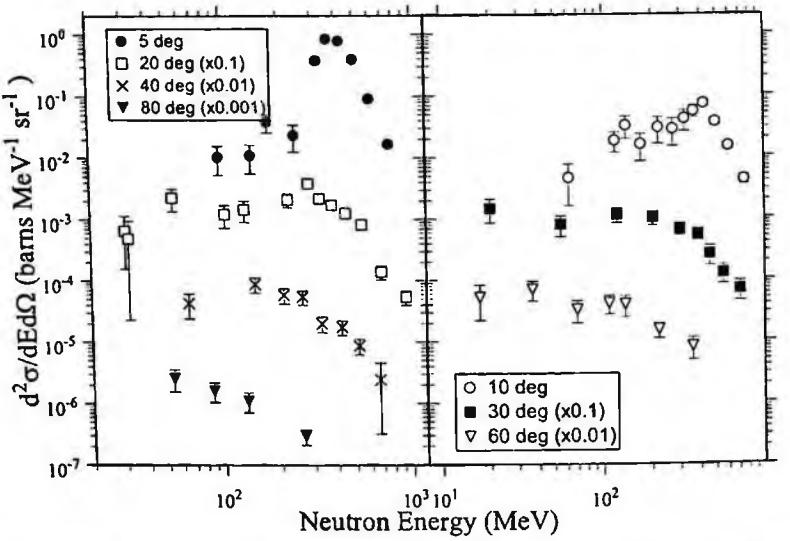

Figure 3.24: Double differential neutron production cross sections from 400 MeV/nucleon Kr + C (data not published).

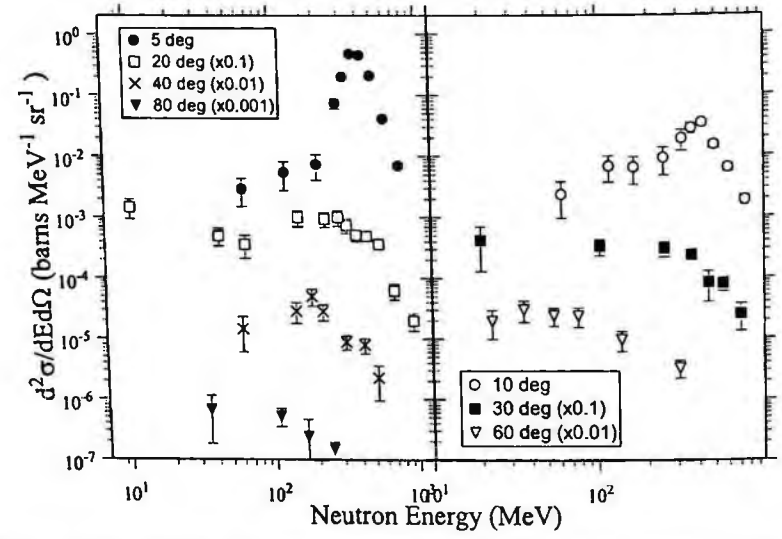

Figure 3.25: Double differential neutron production cross sections from 400 MeV/nucleon Kr + polyethylene (data not published).

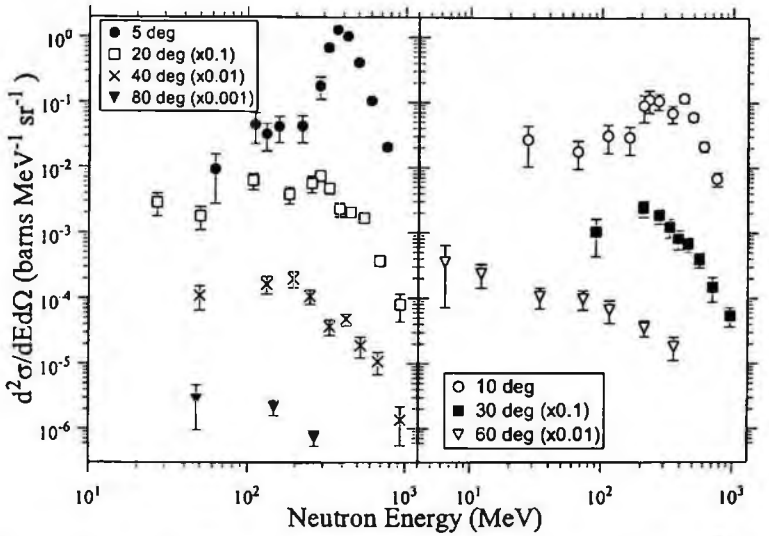

Figure 3.26: Double differential neutron production cross sections from 400 MeV/nucleon Kr + Al (data not published).

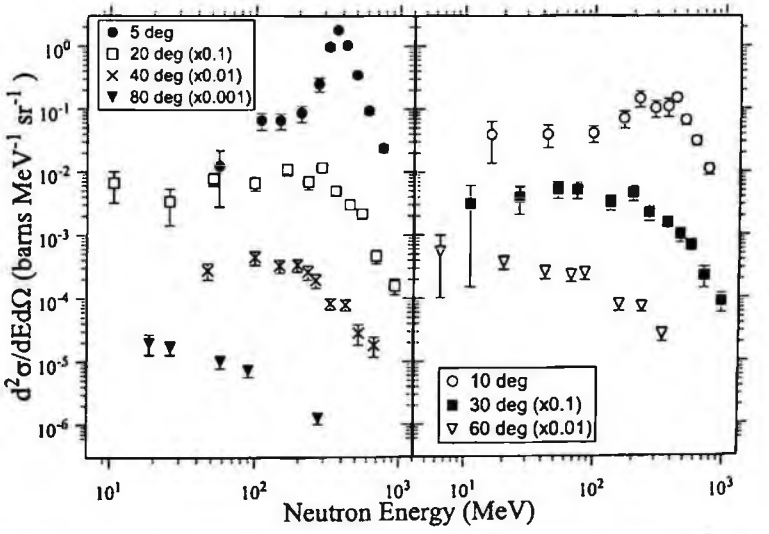

Figure 3.27: Double differential neutron production cross sections from 400 MeV/nucleon Kr + Cu (data not published).

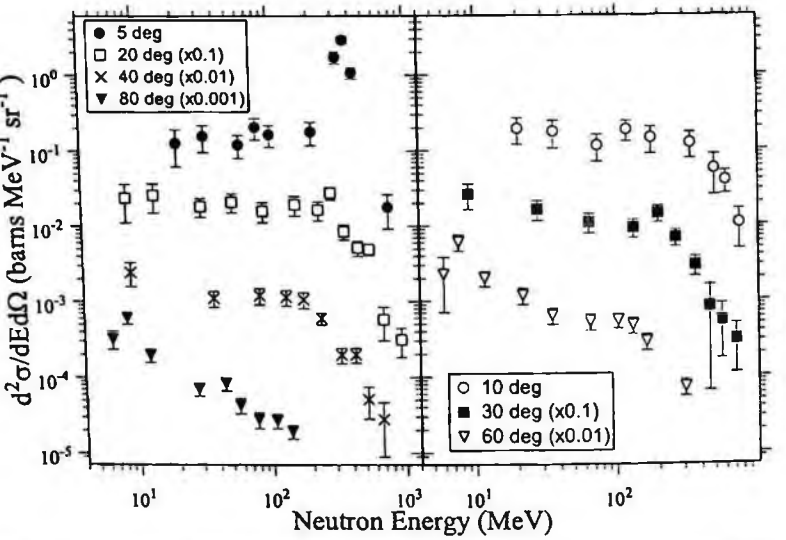

Figure 3.28: Double differential neutron production cross sections from 400 MeV/nucleon Kr + Pb (data not published).

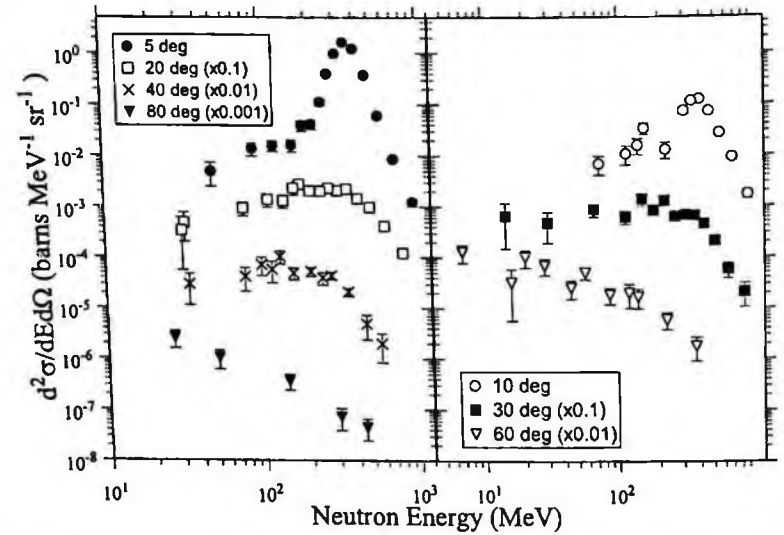

Figure 3.29: Double differential neutron production cross sections from 400 MeV/nucleon Xe + Li (data not published).

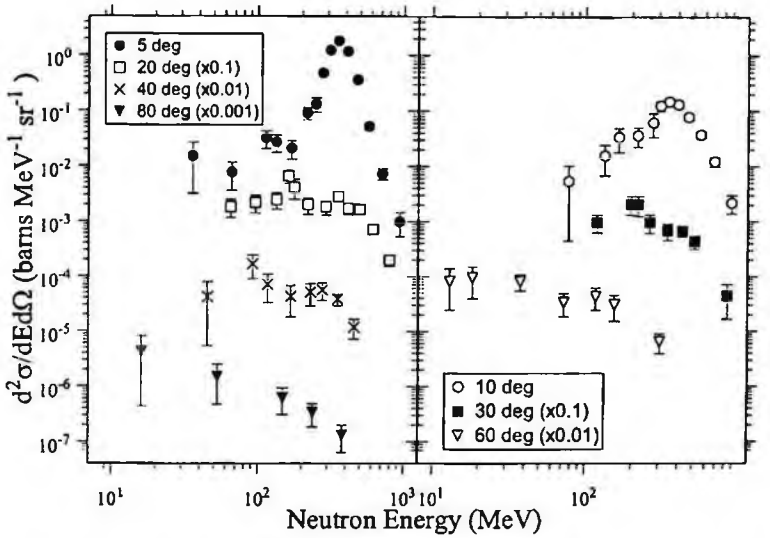

Figure 3.30: Double differential neutron production cross sections from 400 MeV/nucleon Xe + C (data not published).

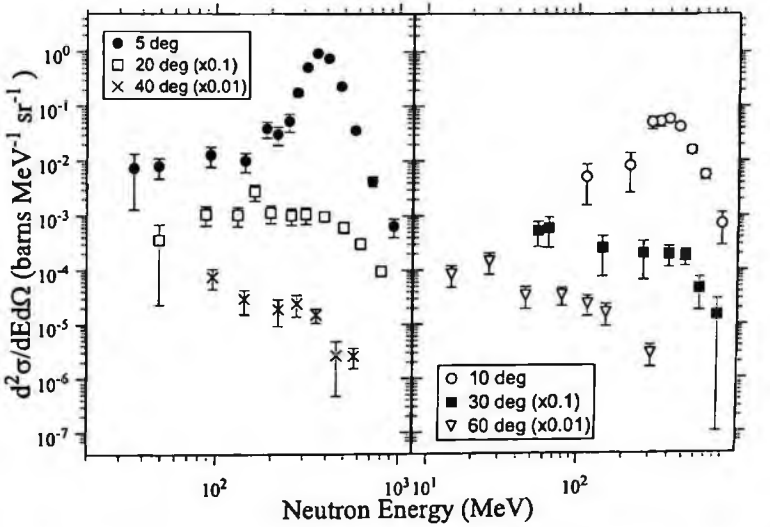

Figure 3.31: Double differential neutron production cross sections from 400 MeV/nucleon Xe + polyethylene (data not published).

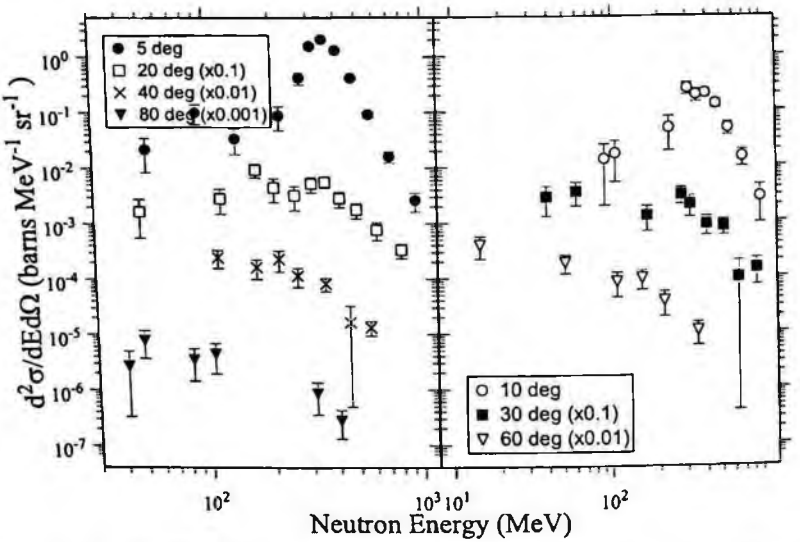

Figure 3.32: Double differential neutron production cross sections from 400 MeV/nucleon Xe + Al (data not published).

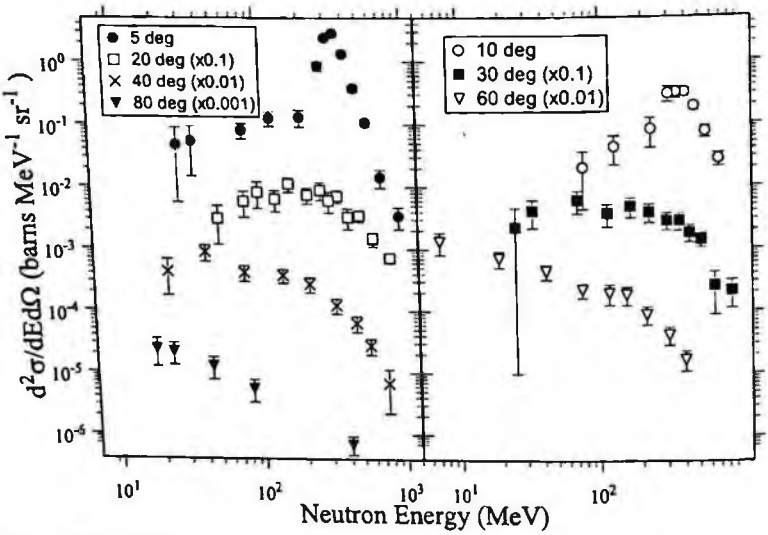

Figure 3.33: Double differential neutron production cross sections from 400 MeV/nucleon Xe + Cu (data not published).

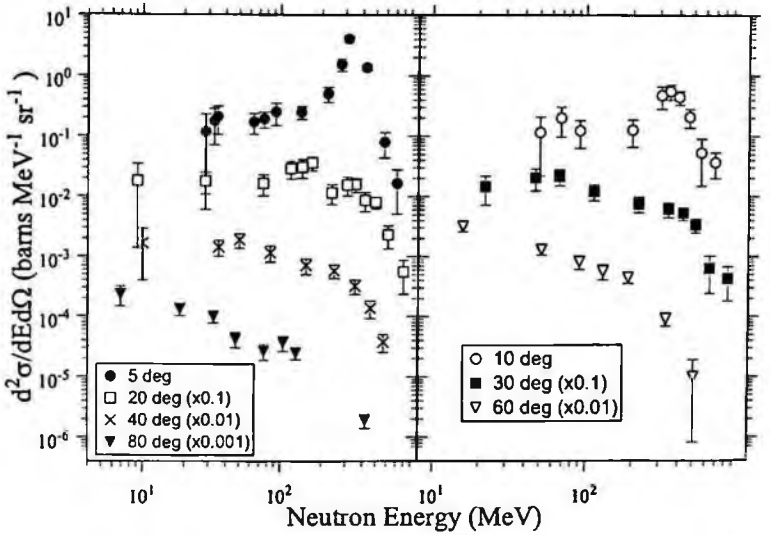

Figure 3.34: Double differential neutron production cross sections from 400 MeV/nucleon Xe + Pb (data not published).

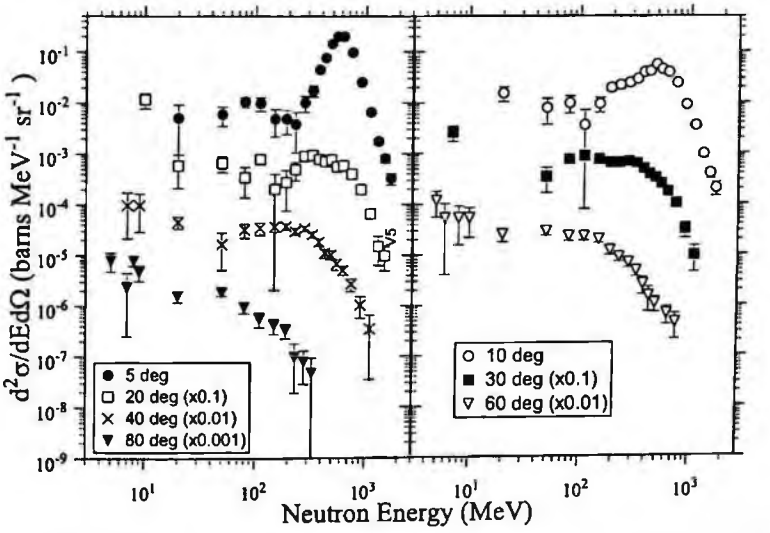

Figure 3.35: Double differential neutron production cross sections from 560 MeV/nucleon Ar + C.

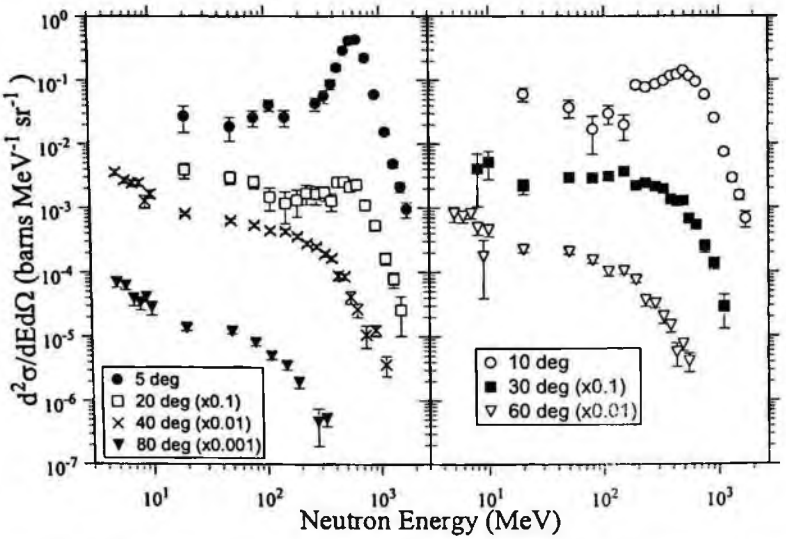

Figure 3.36: Double differential neutron production cross sections from 560 MeV/nucleon Ar + Cu.

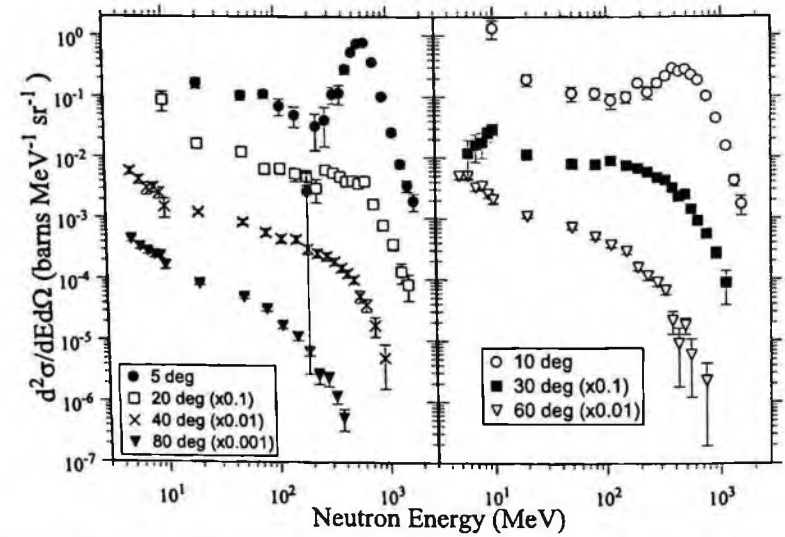

Figure 3.37: Double differential neutron production cross sections from 560 MeV/nucleon Ar + Pb.

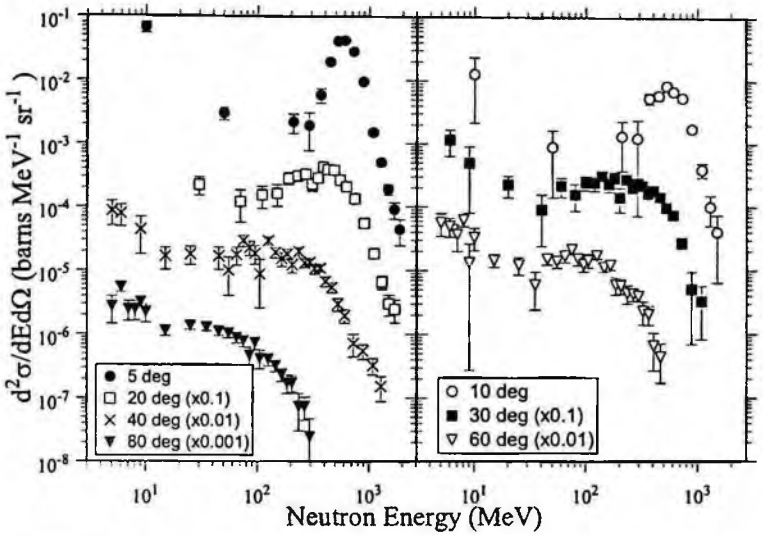

Figure 3.38: Double differential neutron production cross sections from 600 MeV/nucleon Ne + C.

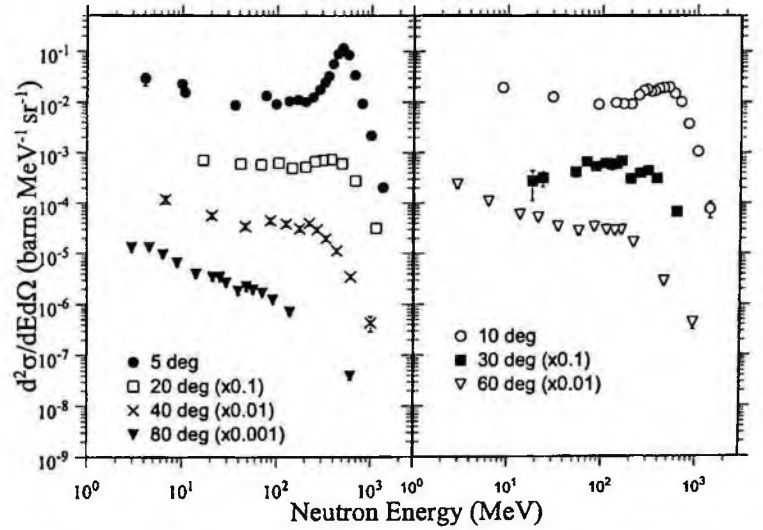

Figure 3.39: Double differential neutron production cross sections from 600 MeV/nucleon Ne + Martian regolith simulant (data not published).

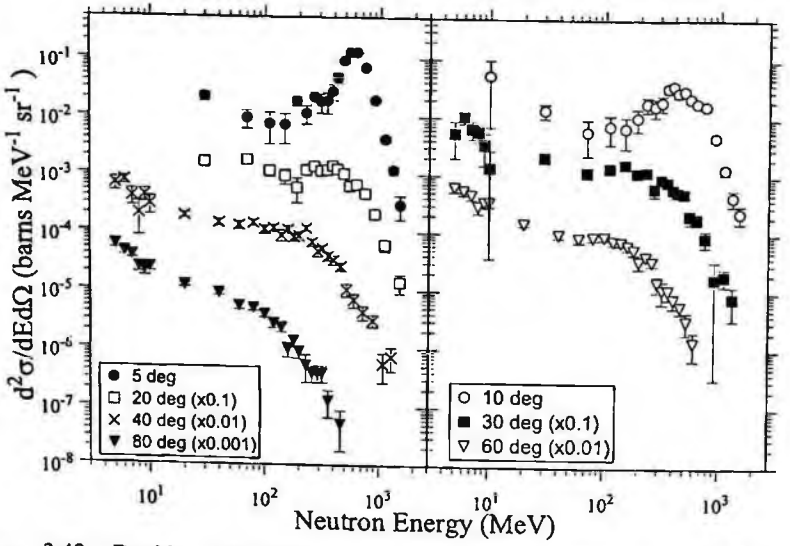

Figure 3.40: Double differential neutron production cross sections from 600 MeV/nucleon Ne + Cu.

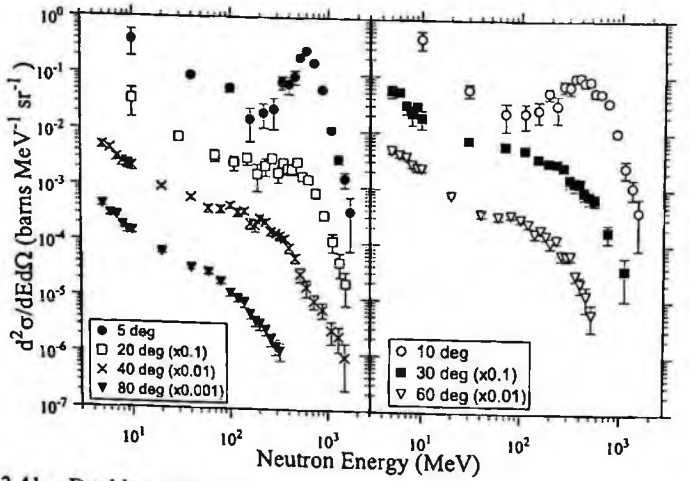

Figure 3.41: Double differential neutron production cross sections from 600 MeV/nucleon Ne + Pb.

3.5 Double Differential Neutron Production Cross Sections from RIKEN Experiments

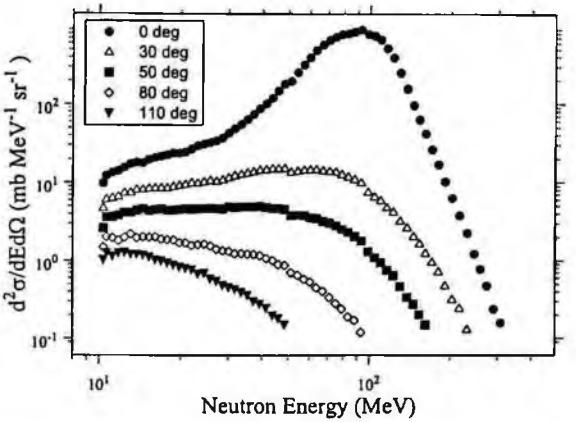

Figure 3.42: Double differential neutron production cross sections from 95 MeV/nucleon Ar + C (note that units are in mb).

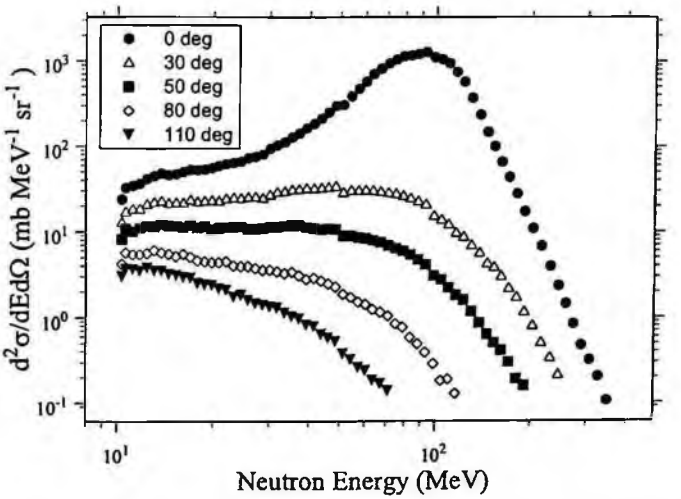

Figure 3.43: Double differential neutron production cross sections from 95 MeV/nucleon Ar + Al (note that units are in mb).

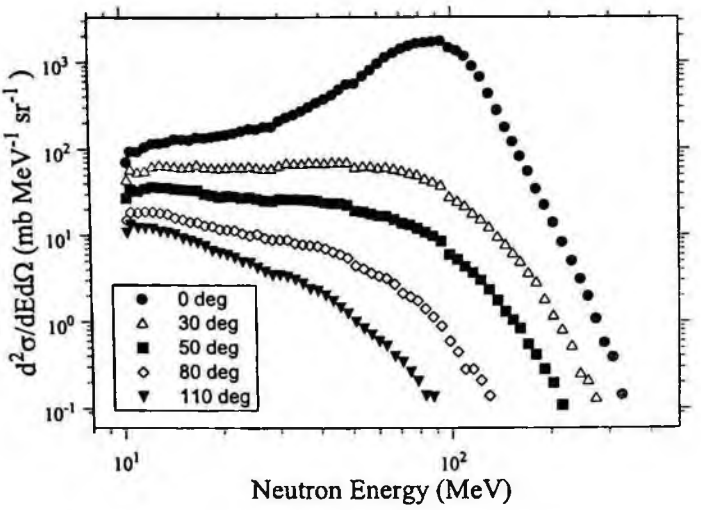

Figure 3.44: Double differential neutron production cross sections from 95 MeV/nucleon Ar + Cu (note that units are in mb).

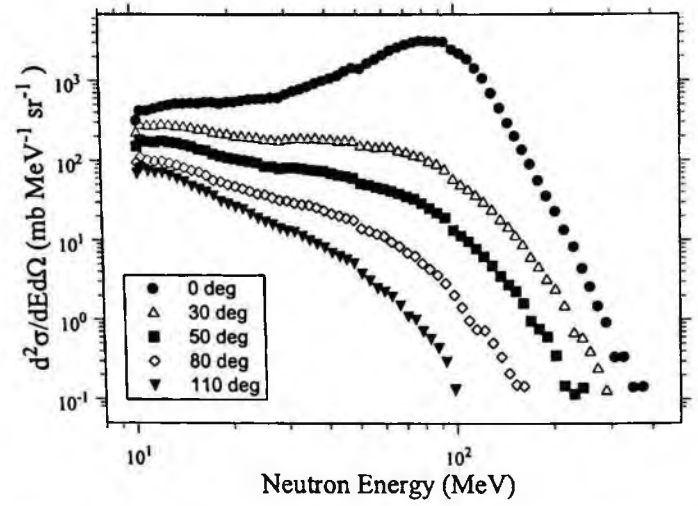

Figure 3.45: Double differential neutron production cross sections from 95 MeV/nucleon Ar + Pb (note that units are in mb).

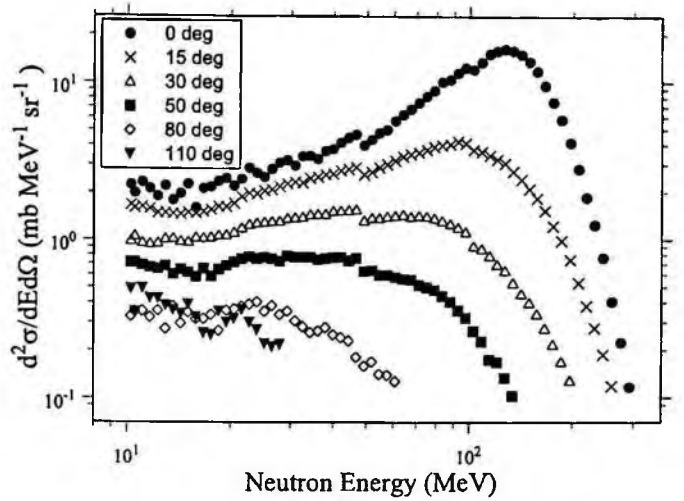

Figure 3.46: Double differential neutron production cross sections from 135 MeV/nucleon He + C (note that units are in mb).

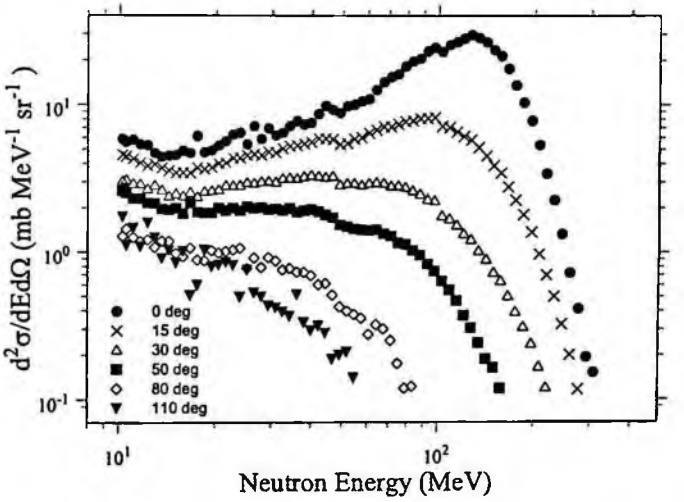

Figure 3.47: Double differential neutron production cross sections from 135 MeV/nucleon He + Al (note that units are in mb).

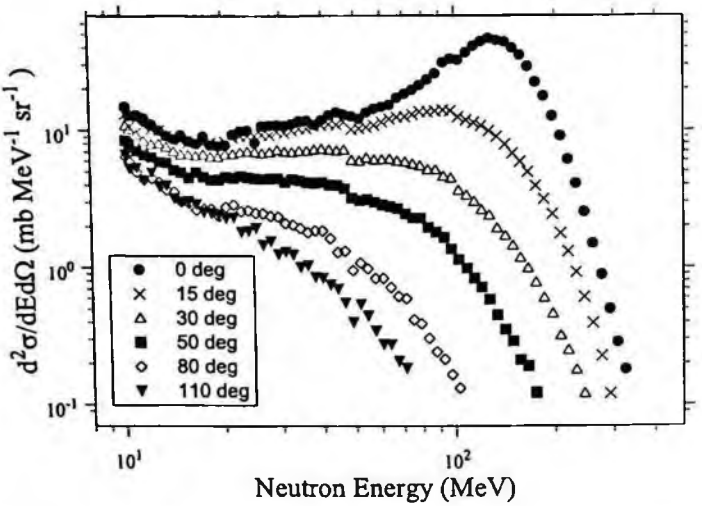

Figure 3.48: Double differential neutron production cross sections from 135 MeV/nucleon He + Cu (note that units are in mb).

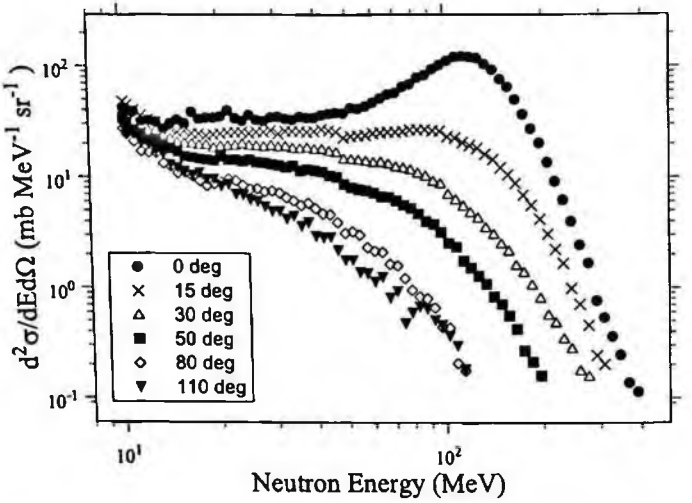

Figure 3.49: Double differential neutron production cross sections from 135 MeV/nucleon He + Pb (note that units are in mb).

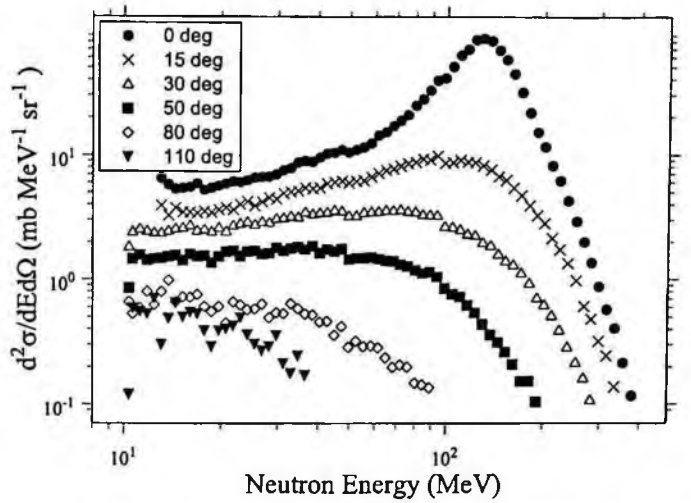

Figure 3.50: Double differential neutron production cross sections from 135 MeV/nucleon C + C (note that units are in mb).

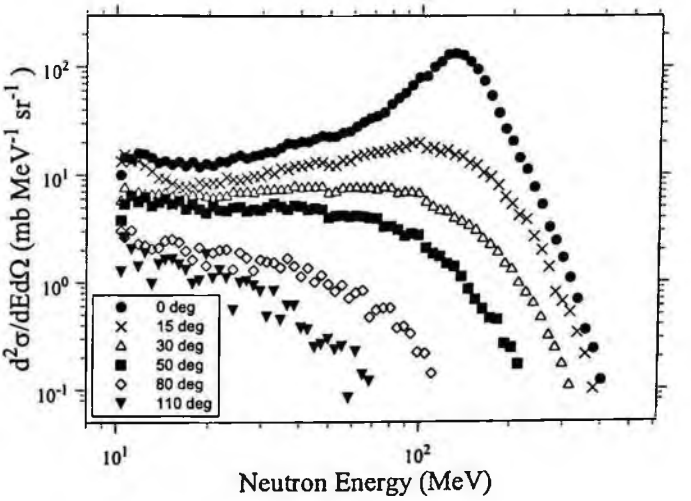

Figure 3.51: Double differential neutron production cross sections from 135 MeV/nucleon C + Al (note that units are in mb).

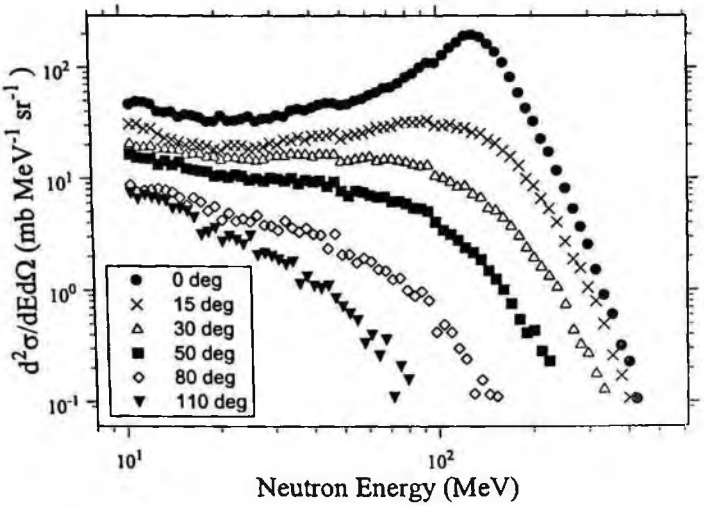

Figure 3.52: Double differential neutron production cross sections from 135 MeV/nucleon C + Cu (note that units are in mb).

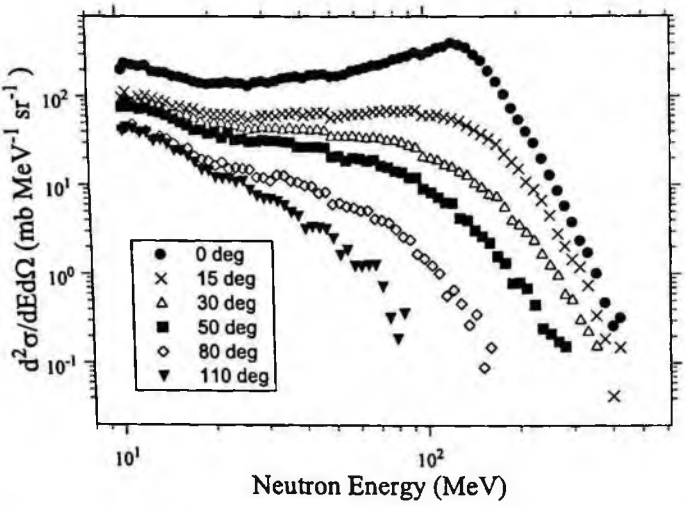

Figure 3.53: Double differential neutron production cross sections from 135 MeV/nucleon C + Pb (note that units are in mb).

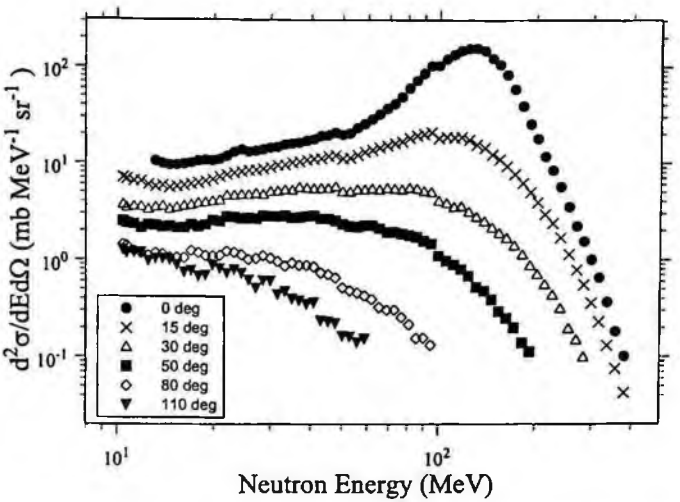

Figure 3.54: Double differential neutron production cross sections from 135 MeV/nucleon Ne + C (note that units are in mb).

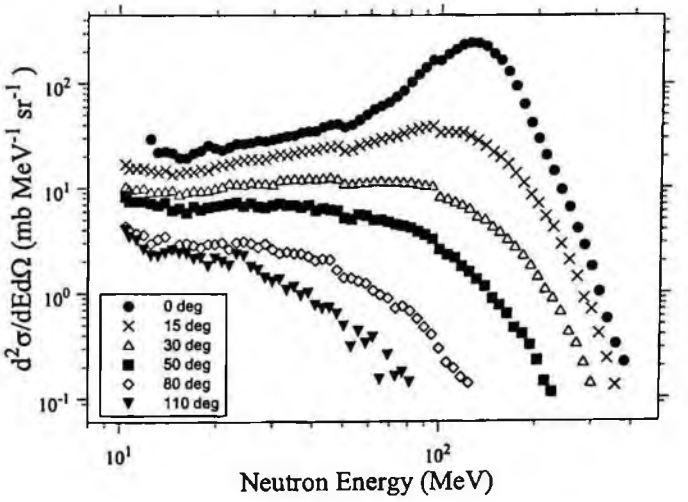

Figure 3.55: Double differential neutron production cross sections from 135 MeV/nucleon Ne + Al (note that units are in mb).

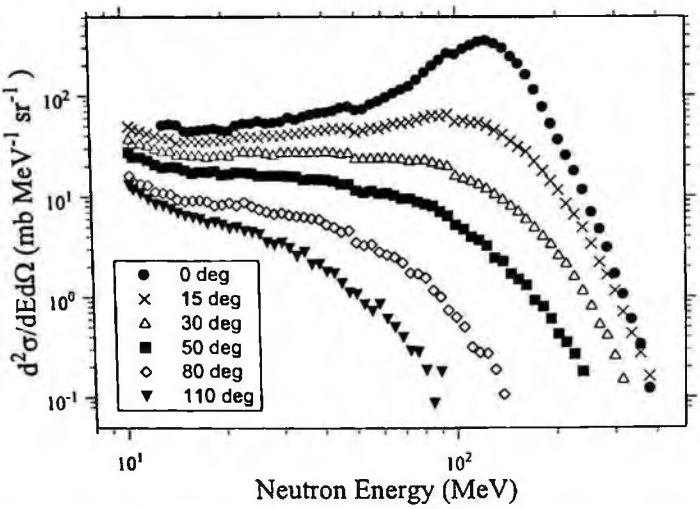

Figure 3.56: Double differential neutron production cross sections from 135 MeV/nucleon Ne + Cu (note that units are in mb).

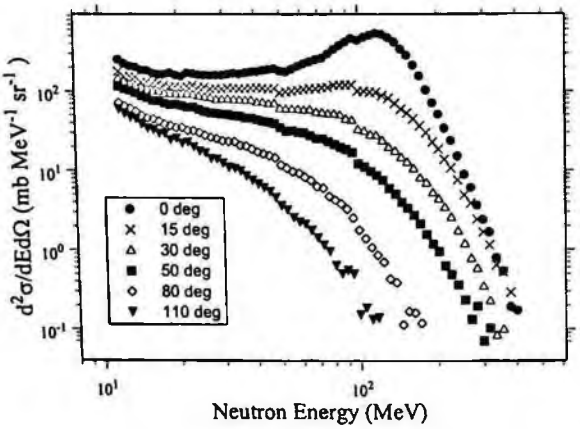

Figure 3.57: Double differential neutron production cross sections from 135 MeV/nucleon Ne + Pb (note that units are in mb).

3.6 Double Differential Neutron Production Cross Sections from Bevalac Experiments

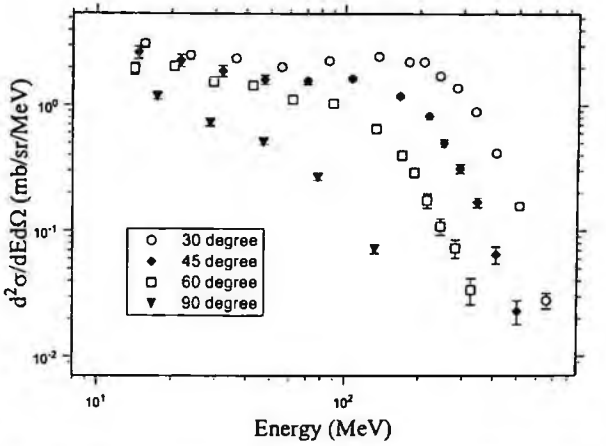

Figure 3.58: Double differential neutron production cross sections from 337 MeV/nucleon Ne + C.

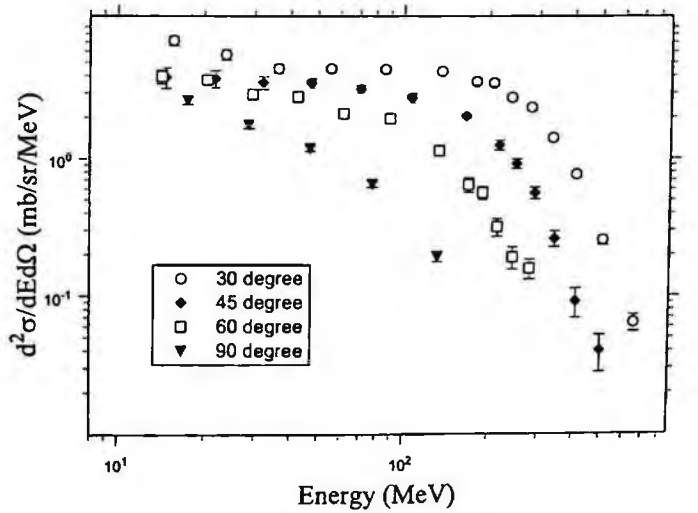

Figure 3.59: Double differential neutron production cross sections from 337 MeV/nucleon Ne + Al.

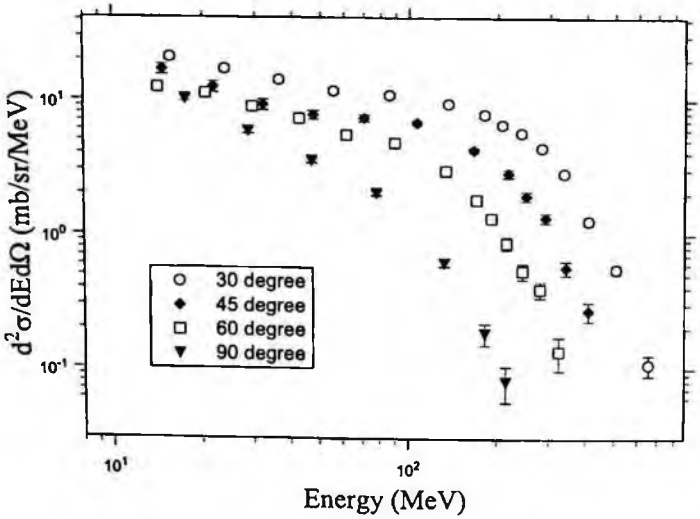

Figure 3.60: Double differential neutron production cross sections from 337 MeV/nucleon Ne + Cu.

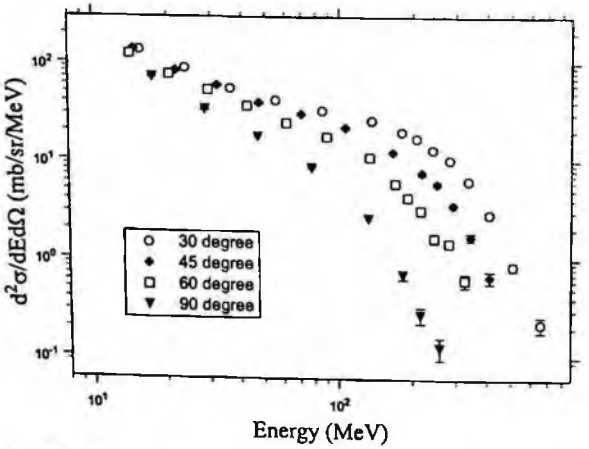

Figure 3.61: Double differential neutron production cross sections from 337 MeV/nucleon Ne + U.

3.7 Angular Distributions

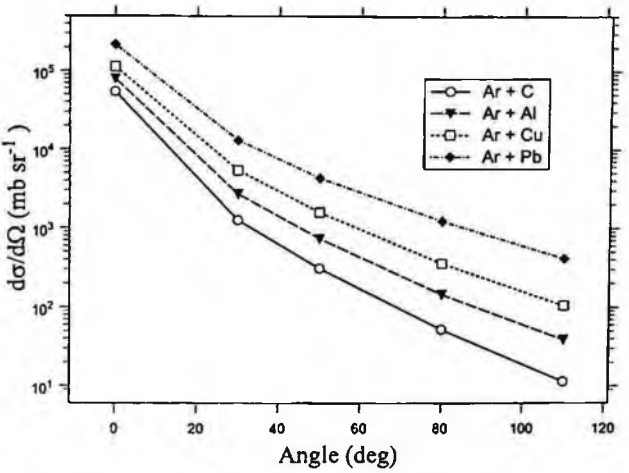

Figure 3.62: Angular distributions from 95 MeV/nucleon Ar interactions in the indicated targets. The lines are drawn as a guide to the eye.

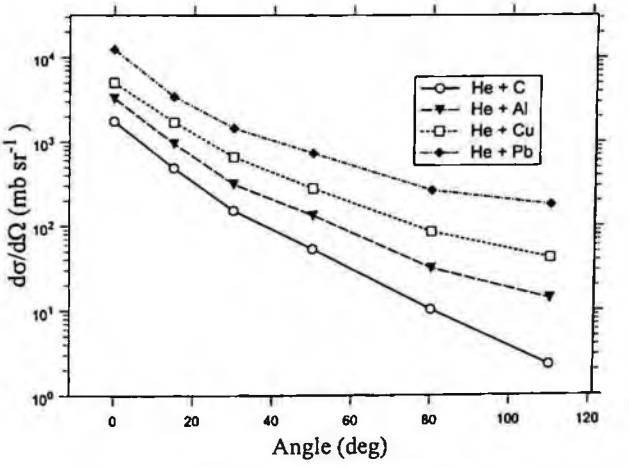

Figure 3.63: Angular distributions from 135 MeV/nucleon He interactions in the indicated targets. The lines are drawn as a guide to the eye.

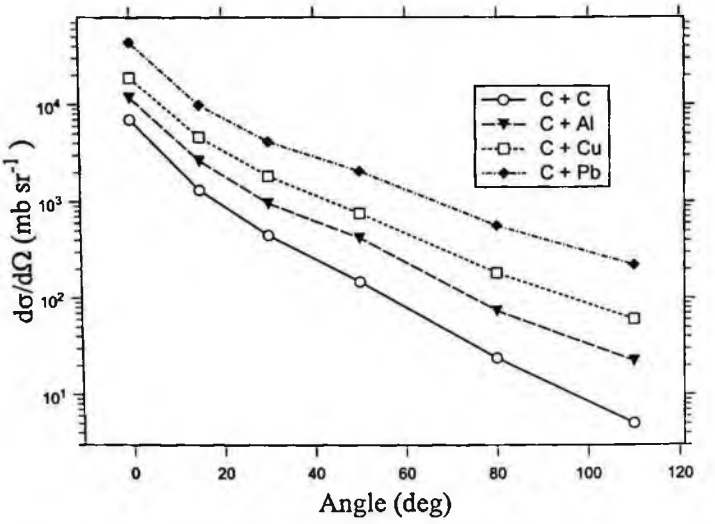

Figure 3.64: Angular distributions from 135 MeV/nucleon C interactions in the indicated targets. The lines are drawn as a guide to the eye.

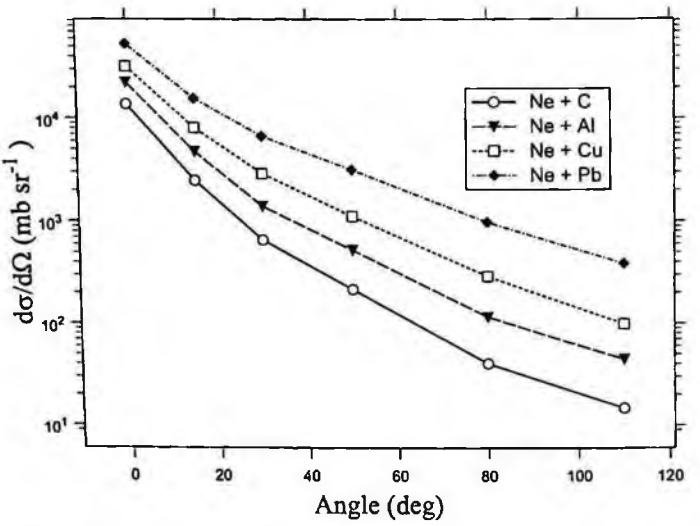

Figure 3.65: Angular distributions from 135 MeV/nucleon Ne interactions in the indicated targets. The lines are drawn as a guide to the eye.

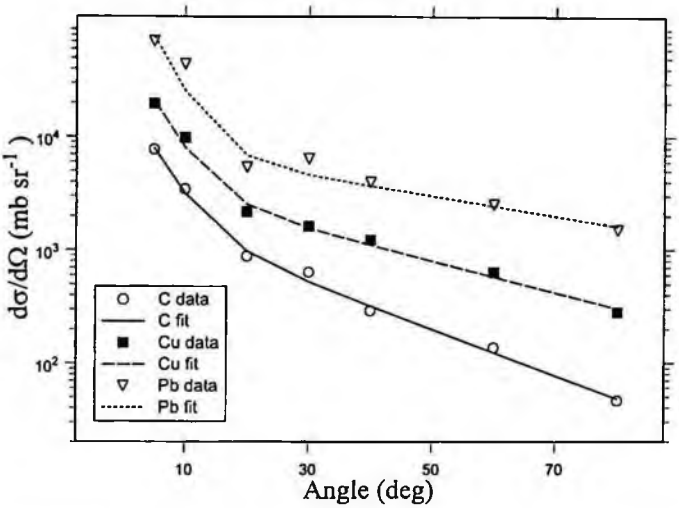

Figure 3.66: Angular distributions from 290 MeV/nucleon C interactions in the indicated targets. The lines are a fit to the data using Eqn. 3.2.

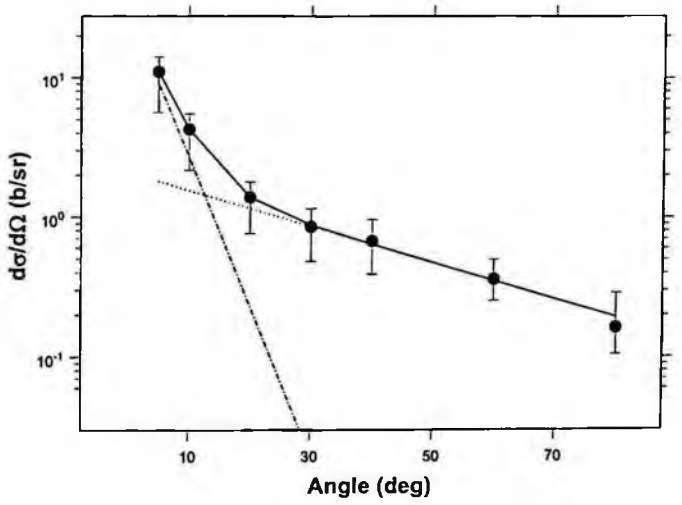

Figure 3.67: Angular distributions from 290 MeV/nucleon C interactions in simulated Martian regolith. The solid line is a fit to the data using Eqn. 3.2. The dotted and dashed lines show the two components of the fit.

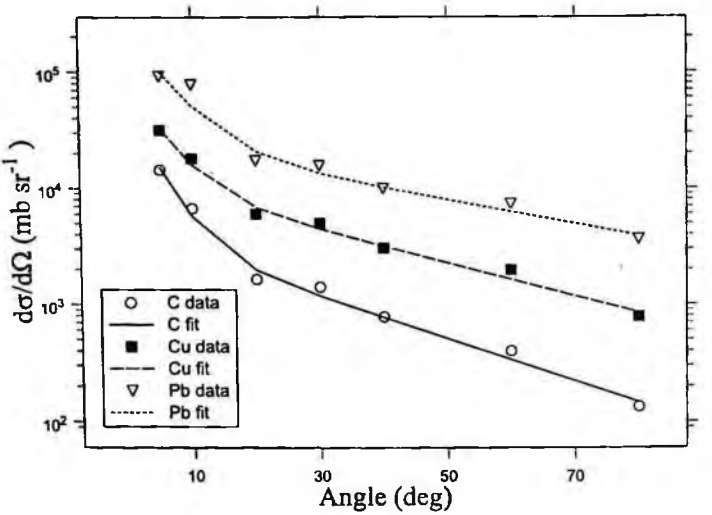

Figure 3.68: Angular distributions from 400 MeV/nucleon Ne interactions in the indicated targets. The lines are a fit to the data using Eqn. 3.2.

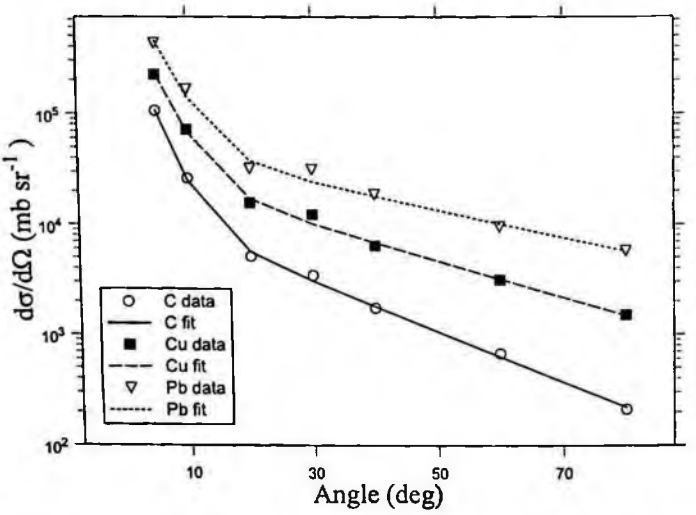

Figure 3.69: Angular distributions from 400 MeV/nucleon Ar interactions in the indicated targets. The lines are a fit to the data using Eqn. 3.2.

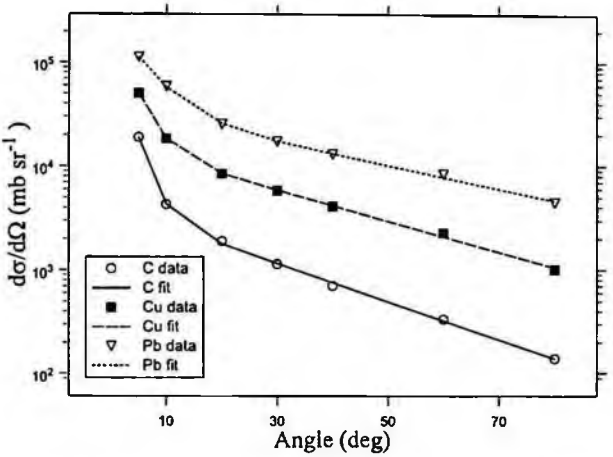

Figure 3.70: Angular distributions from 600 MeV/nucleon Ne interactions in the indicated targets. The lines are a fit to the data using Eqn. 3.2.

3.8 Total Cross Sections

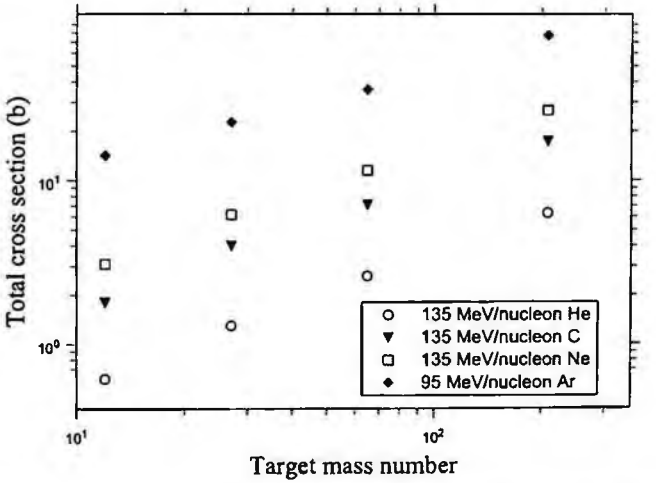

Figure 3.71: Total cross sections for neutron energies above 20 MeV as a function of target mass number. The data is taken from the RIKEN experiments.

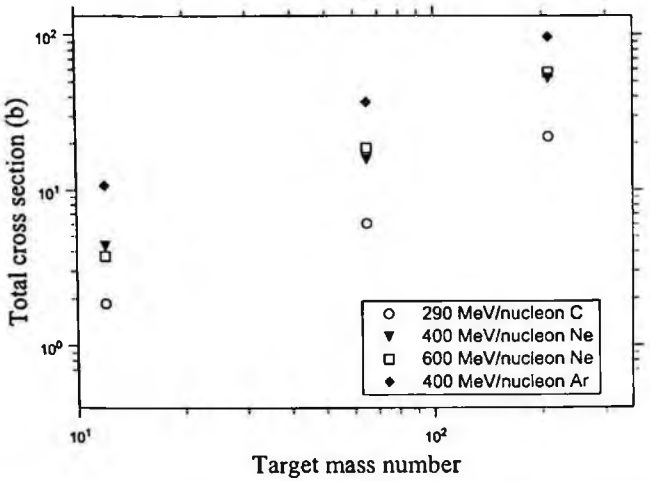

Figure 3.72: Total cross sections for neutron energies above 10 MeV as a function of target mass number. The data is taken from the HIMAC experiments.

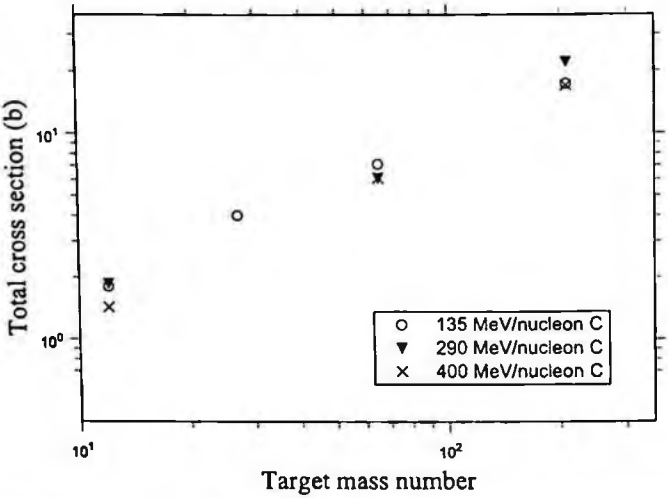

Figure 3.73: Total cross sections as a function of target mass number for the indicated C systems. The 135 MeV/nucleon total cross sections are for neutron energies above 20 MeV. The other systems are for neutron energies above 10 MeV.

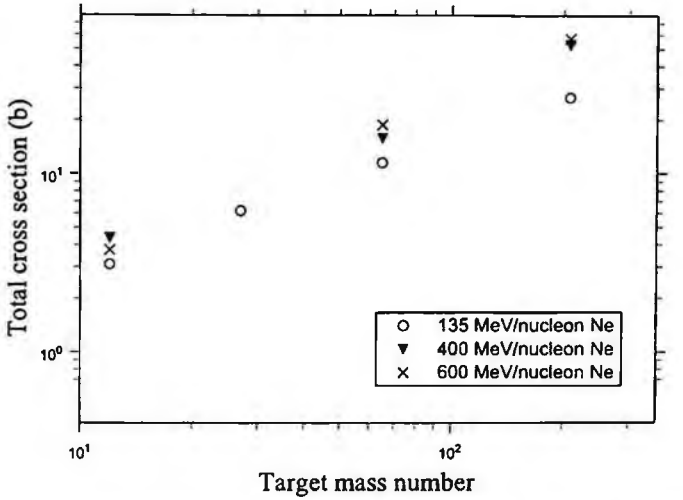

Figure 3.74: Total cross sections as a function of target mass number for the indicated Ne systems. The 135 MeV/nucleon total cross sections are for neutron energies above 20 MeV. The other systems are for neutron energies above 10 MeV.

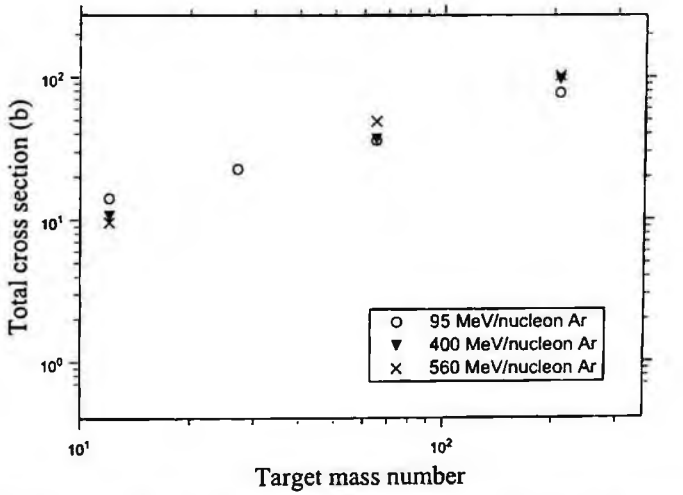

Figure 3.75: Total cross sections as a function of target mass number for the indicated Ar systems. The 95 MeV/nucleon total cross sections are for neutron energies above 20 MeV. The other systems are for neutron energies above 10 MeV.

Chapter 4

Measurements of HZE Neutrons Behind Shielding

The cost of constructing new accelerator facilities is greatly affected by the amount of shielding material deemed necessary to provide adequate protection to workers from radiological hazards. Neutrons are highly penetrable, and as such are a primary concern for workers outside the experimental halls and for nearby inhabitants. The transmission of neutrons through shielding is the leading criteria in the design of shielding, and as such, the proper modeling of neutron transport is critical in developing a cost-effective shielding plan.

Typically, the shielding design for high-energy accelerators is done using analytical calculations using the Moyer model. However, the dose-attenuation length, the most important parameter in that model, is affected by large uncertainties, especially for high-energy neutrons. More accurate shielding calculations can be accomplished by Monte Carlo codes such as HETC [4.1], LAHET [4.2], and FLUKA [4.3]. However, the accuracy of each of those codes has not been well-evaluated due to the lack of relevant experimental data. One specific need is benchmark data sets of high-energy neutrons (> few tens of MeV), especially for neutrons created by heavy-ion interactions.

Recently, measurements have been made of neutrons behind shielding materials at heavy-ion accelerator facilities. Table 4.1 gives an overview of those experiments, showing the beams and targets used to produce the neutrons, the shielding material and thickness used, and the type of detection system used, along with other information. The experiments done with the 400 MeV/nucleon C beams were performed at HIMAC (the Heavy Ion Medical Accelerator in Chiba, Japan), and the

155 MeV/nucleon experiments were done at the NSCL (National Superconducting Cyclotron Laboratory at Michigan State University, USA).

Table 4.1: General experimental information in regards to the shielding data presented here.

Beam and Energy (AMeV)	Target used to produce neutrons	Shielding material	Range of shielding thicknesses	Detection system(s) used	Reference
C (400)	Cu	Concrete	0-250 cm	Self-TOF, NE-213, Activation foils	[4.4]
C (400)	Cu	Iron	0-100 cm	Self-TOF, NE-213	[4.5]
C (400)	Cu	Concrete Iron	0-400 cm 0-100 cm	TEPC	[4.6]
He, C, and O (155)	Hevimet	Concrete Iron	0-440 cm	Bonner Spheres	[4.7]

4.1 Experimental Details

4.1.1 Concrete shielding using self-TOF, NE-213, and activation foils

Schematic diagrams of the various experimental arrangements used by Sasaki *et al.* [4.4], [4.5] are shown in Fig. 4.1a-c. A photograph of the experimental area is shown in Fig 4.1d. In all experimental arrangements, neutrons were produced by stopping 400 MeV/nucleon ^{12}C ions in a 5-cm thick Cu (10x10 cm square) target. Beam height was 125 cm from the floor of the experimental hall. An ionization chamber was placed directly upstream from the target, and was used to monitor the number of beam particles incident upon the target. In addition to the ionization chamber, and 5-mm thick NE-102 counter (labeled "NE102A" in Fig. 4.1a and 4.1b) was placed near the upstream face of the shielding to act as a relative monitor, except for the activation foil runs.

For the experimental runs that used the self-TOF counter (Fig. 4.1a), the upstream face of the concrete shields was 123 cm from the upstream

face of the Cu target. For the NE-213 runs (Fig. 4.1b), the upstream face of the shielding was 126 cm from the upstream face of the target. The upstream face of the shielding used for the activation-foil runs (Fig. 1c) was 200 cm from the upstream face of the target. The concrete shields were 50-cm thick slabs, 100x100 cm square, and they were placed centered and normal to the beam axis. In order to raise the shields to the proper height, they were placed on top of a steel platform.

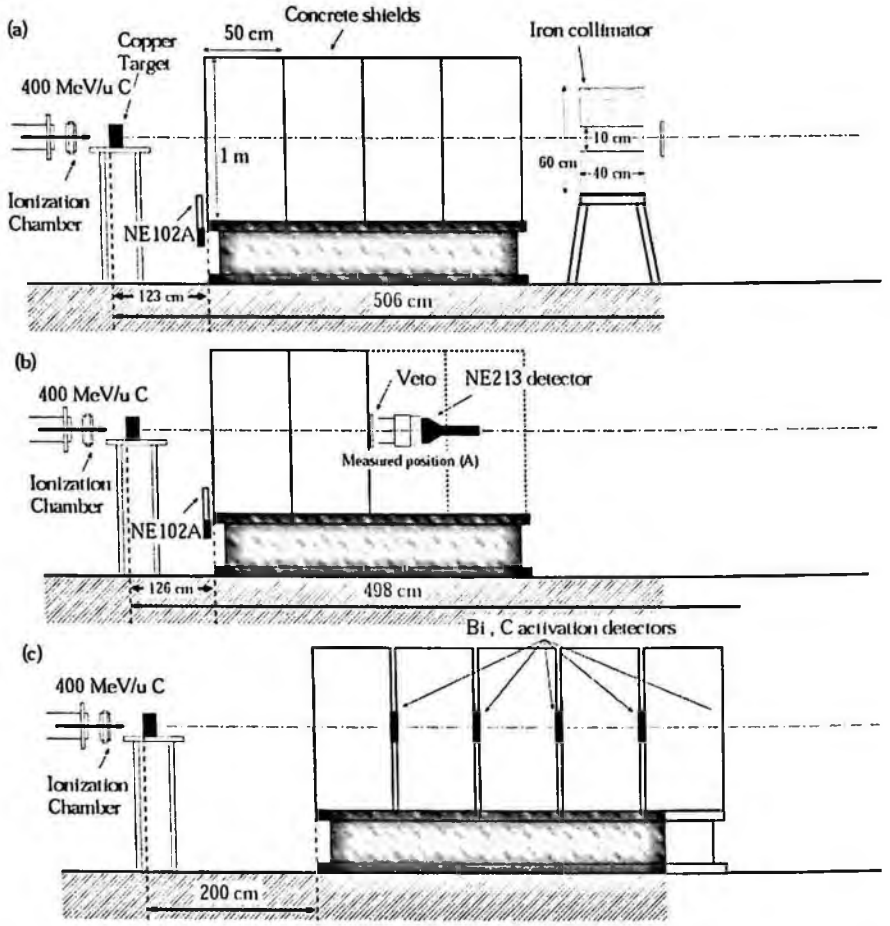

Figure 4.1(a-c): Experimental arrangement at HIMAC for (a) the self-TOF runs, (b) the NE213 runs, and (c) the activation foil runs (courtesy of Ref. 4.4).

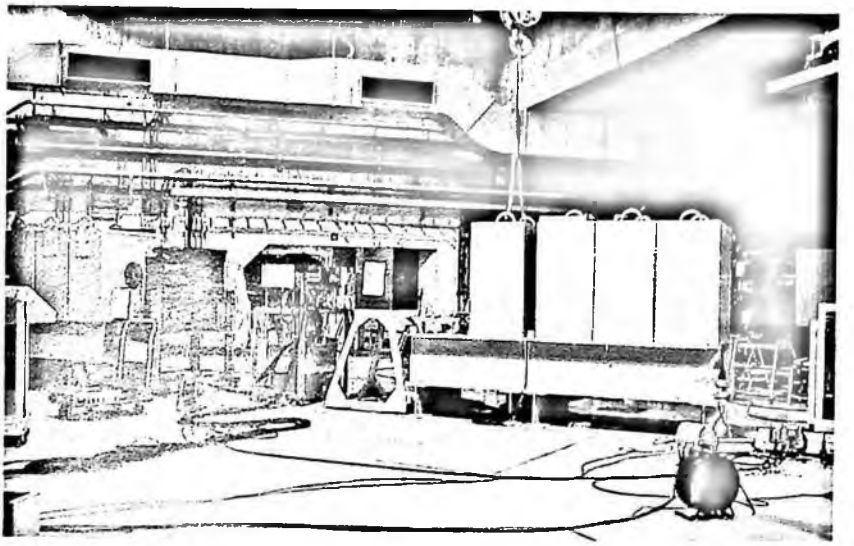

Figure 4.1(d): Photograph of the experimental setup shown schematically in Figs. 4.1(a-c).

A diagram of the self-TOF detector may be found in Fig. 4.2a. A photograph of the detector may be found in Fig 4.2b. A complete description of the self-TOF detector may be found in Refs. [4.8], [4.9], and [4.10]. Briefly, the detector consists of a 5-mm thick NE-102 scintillator in the front, which is used to veto any charged particle events incident upon the detector. Behind the veto detector is a stack of 20, 6-mm thick, NE-102 radiators with photomultiplier tubes. The radiators convert neutrons to protons. Directly behind the radiators is a 5-mm thick NE-102 scintillator that is used as the start detector for any recoil protons that make it out of the radiators. Placed at a variable distance behind the start detector is an array of 2-cm thick NE-102 "stop" detectors. The energy of the recoil proton is deduced from the time of flight, and the neutron spectrum is then calculated from the recoil proton spectrum, using measured response functions. Because low-energy recoils range out in the radiator stack, the self-TOF detector is best used for neutrons above 100 MeV. A comparison of the neutron detection efficiency for the self-TOF detector and the NE-213 detector is shown in Fig. 4.3. The self-TOF efficiency is shown with the solid line

(efficiencies are read off the left-hand scale), and the NE-213 efficiency is shown with the dashed line (efficiencies are read off the right-hand scale).

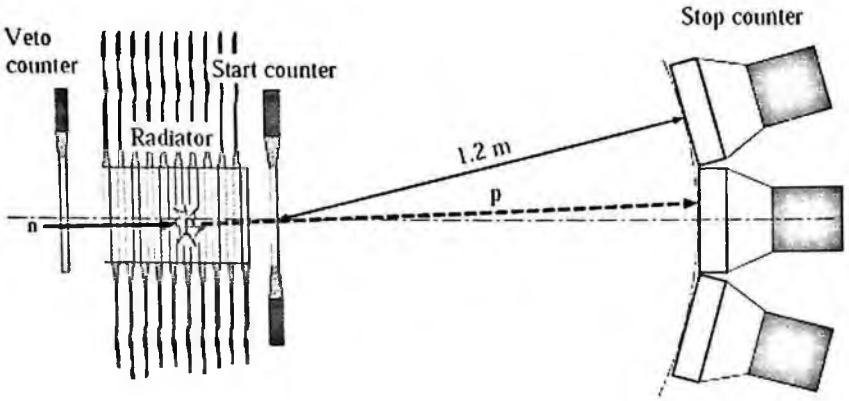

Figure 4.2(a): A schematic drawing of the self-TOF detector (courtesy of Ref. 4.4).

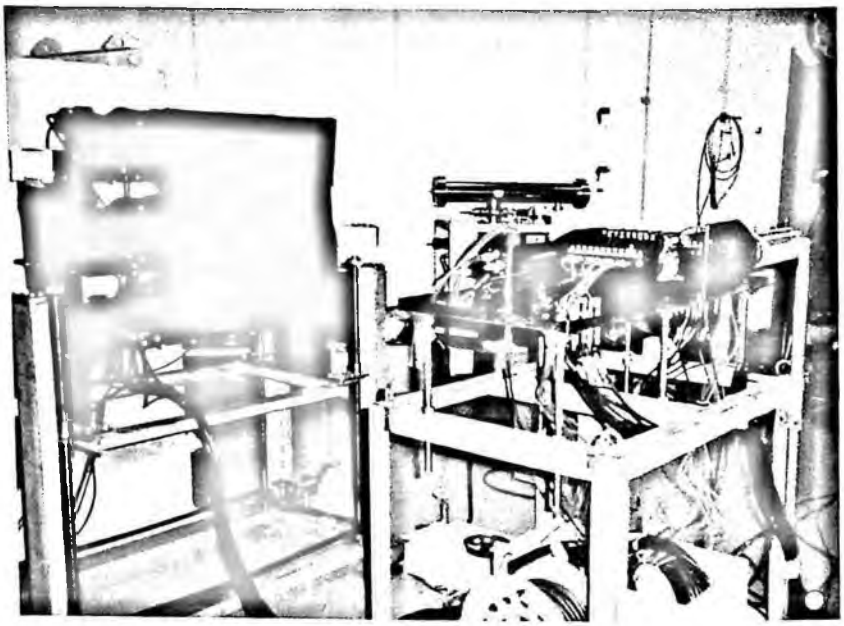

Figure 4.2(b): Photograph of the self-TOF detector used at HIMAC.

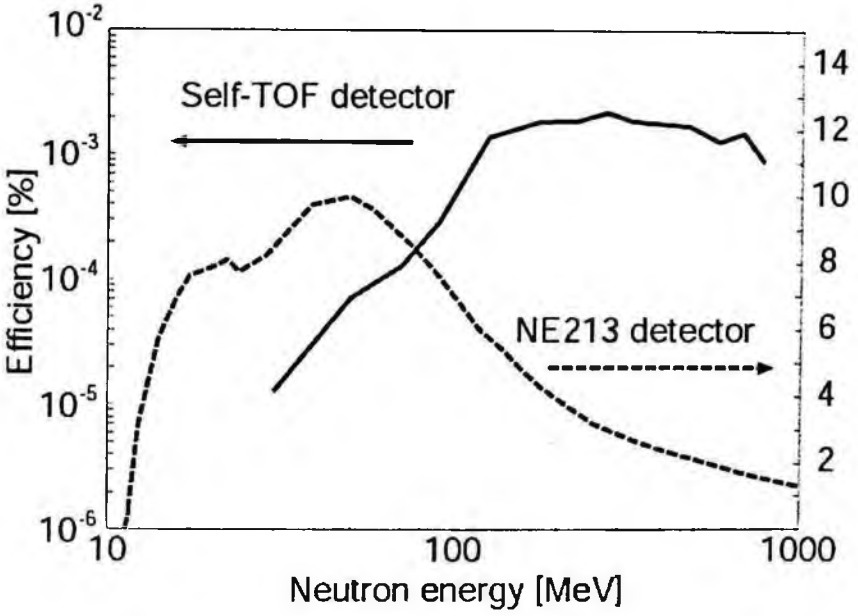

Figure 4.3: The neutron-detection efficiencies for the self-TOF detector (solid line, left-hand scale) and NE-213 detector (dashed line, right-hand scale) (courtesy of Ref. 4.4).

For the HIMAC runs, the self-TOF detector was placed 506 cm downstream from the upstream face of the target, centered on the beam axis. A 40-cm thick iron collimator (60x60 cm with a 10x10 cm hole) was centered on the beam axis and placed in front of the self-TOF detector to decrease the number of accidental signals in the stop counters from charged fragments.

For the NE-213 runs (Fig. 4.1b), the detector was placed at two locations; (1) directly behind the downstream edge of the shielding (called "position A"), and (2) 498 cm from the upstream edge of the target (called "position B"). Separate runs were performed for each location. The detector was centered along the beam axis. As with the self-TOF detector, a NE-102 detector was placed directly in front of the NE-213 detector to veto any charged-particle events. Neutron spectra were generated from the NE-213 data using the appropriate response matrix that had been previously measured [4.11].

^{209}Bi and ^{12}C activation foils were placed on the downstream edge of 5 consecutively placed concrete slabs (Fig. 4.1c). They were centered on the beam axis. The Bi foils were 1.1-cm thick, and the C foils were 1-cm thick. The foils were irradiated for a total of 10 hours.

Additional information may be found in Ref. [4.4].

4.1.2 Iron shielding using self-TOF and NE-213 detectors

The conditions for this experiment were identical to the conditions described in the section above, except no activation foils were used, and iron shielding was used instead of concrete shielding. Each iron shield was 10-cm thick and 100x100 cm square. The shields were centered along the beam axis. In order to raise the shields to the proper height, they were placed on top of a steel platform. Measurements were made behind 0, 20, 40, 60, 80, and 100 cm of iron. The density of the iron shielding is 7.8 g/cm^3. Additional details may be found in Ref. [4.5].

4.1.3 Concrete and iron shielding using a TEPC

A Tissue-Equivalent Proportional Counter (TEPC) was used to measure lineal energy (y) spectra and doses behind concrete and iron shielding. The TEPC had a 12.55-cm inner diameter and was surrounded by a 2.29-mm thick tissue-equivalent sphere of A-150 plastic. The TEPC was filled with a propane-based tissue-equivalent gas (PTE) at a pressure of 10 Torr. The tissue-equivalent diameter at that pressure is 3 μm. The mean chord length (2d/3) is 2 μm. The TEPC was placed directly behind the last slab of shielding, centered on the beam axis. A veto detector (NE-102, 5-mm thick, 15x15 cm square) was placed in front of the TEPC to detect any charged particle events incident upon the TEPC.

The experimental setup was similar to the Sasaki *et al.* experiments described above in sections 4.1.1 and 4.1.2. 400 MeV/nucleon ^{12}C stopped in a 5-cm thick Cu target. The upstream edge of the shielding was placed 154.5 cm downstream from the front edge of the target. The concrete shields (ρ=2.25 g/cm^3) and iron shields (ρ=7.8 g/cm^3) were

stacked on top of a steel platform and centered along the beam axis. Concrete shield thicknesses of 50, 100, 200, 300 and 400 cm were used. Iron shield thicknesses of 10, 20, 40, 60, 80 and 100 cm were used.

The number of beam particles that were incident upon the target for high-intensity runs (with shielding) were counted by an ion chamber that was placed upstream of the target. For low intensity runs (no shielding), a 0.5-mm thick NE-102 scintillator was placed upstream of the target and was used to count the number of beam particles.

Neutron and gamma-ray events are difficult to discriminate in the TEPC. As such, the y-distributions, D(y) (dose as a function of y), total absorbed dose D, dose equivalent H, the frequency mean of lineal energy, the dose mean of lineal energy, and the mean quality factor include both neutrons and gamma-rays. The TEPC pulse height was calibrated to lineal energy using a built-in ^{244}Cm alpha source.

4.1.4 Bonner sphere measurements behind concrete and iron

Beams of 155 MeV/nucleon He, C and O were accelerated to the Analysis Hall target station of the K1200 Cyclotron at Michigan State University. The beams stopped in a 5.093-cm thick Hevimet target. Hevimet is made of 90% tungsten, 7.5% nickel, and 2.5% copper, and it has a density that varies between 16.9 and 17.2 g/cm^3. Neutron fields were measured both before and after shielding using a Bonner Sphere spectrometer. The system had spheres of 2, 3, 5, 8, 10, and 12 inch diameters. The detector was a 4mm x 4mm cylindrical LiI(Eu) scintillator. In addition to runs with the spheres in place, runs with no spheres were made to measure very low-energy neutrons. Figure 4.4 shows a detailed drawing of the experimental arrangement and positions where measurements were taken. Table 4.2 gives the parameters of the locations where measurements were made.

In addition to the concrete shielding, a local iron shield was periodically placed directly over the target, allowing for measurements to be made both with and without the iron shield in place. The iron shield was 25.4-cm thick, and shielded neutrons in the lateral direction and the upward direction. Figure 4.5 shows a drawing of that experimental arrangement. Measurements were also made on top of the accelerator

shielding (not presented here). Additional details may be found in Ref. 4.7.

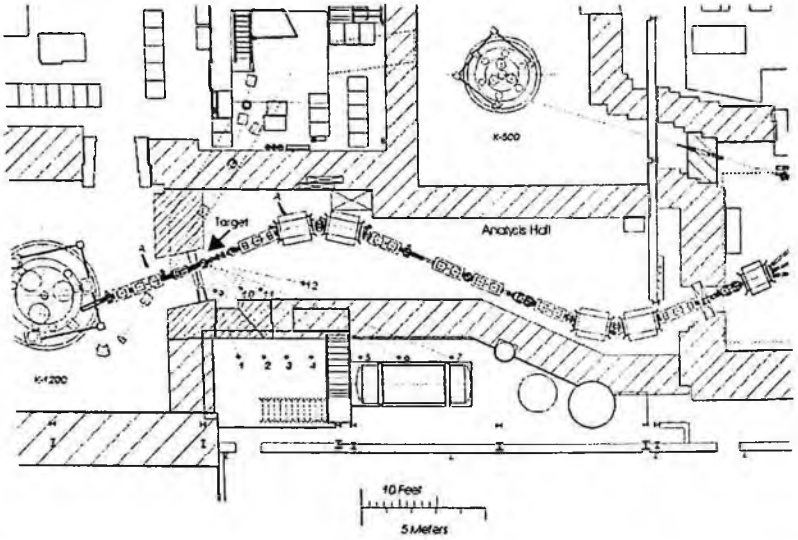

Figure 4.4: View of the Analysis Hall at the National Superconducting Cyclotron Laboratory, Michigan State University. Measurements were taken in front of and behind shielding at the numbered locations. The target location is indicated in the figure (courtesy of Ref. 4.7).

Table 4.2: Parameters of locations where Bonner Sphere measurements were made.

Before/After shielding?	Position in Fig 4.4	Angle θ (deg)	Distance from target (cm)	Concrete shield thickness (g/cm^2)
Before	12	34	402	0
Before	11	49	248	0
Before	10	59	176	0
Before	9	94	121	0
After	7	44	1055	1057
After	6	49	862	863
After	5	54	726	716
After	4	65	568	560
After	3	73	499	471
After	2	82	446	341
After	1	94	403	308

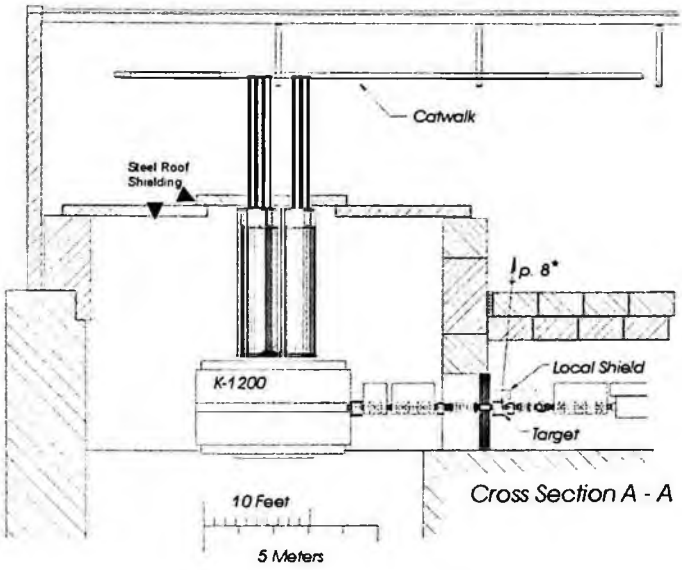

Figure 4.5: Cross sectional view of the K1200 and target location. The local shield was a 25.4-cm thick iron shield placed periodically on top of the target location (courtesy of Ref. 4.7).

4.2 Results

4.2.1 400 MeV/nucleon ^{12}C + Cu neutrons behind concrete

Figure 4.6 shows the neutron flux (# per steradian per MeV per ion) behind 0, 50, 100, 150 and 200 cm of concrete shielding, using the self-TOF detector. Because low energy recoils range out in the radiator, the low-energy threshold is 100 MeV. No spectra are reported above 600 MeV due to a lack of statistically-significant events. The spectra have a broad peak around 200 to 300 MeV, and little softening of the spectra can be seen with increasing shield thickness. This may be due to the iron collimator selecting the most direct, forward component of the neutron spectrum. The dashed lines show LAHET calculations of the spectra.

The calculations overestimate the spectra with increasing shield thickness, especially above 300 MeV.

Figures 4.7 and 4.8 show the neutron flux behind concrete shielding using the NE-213 detector at position A (directly behind the shielding) and position B (farther downstream from the shielding), respectively. The dashed lines show MCNPX calculations. The energy range of the data is 20 to 800 MeV. The broad peaks seen in Fig. 4.6 are not seen in Figs. 4.7 and 4.8 because the FORIST unfolding process spreads some of the peak counts to neighboring channels.

Figure 4.9 shows the neutron flux measured with the activation foils (Bi and C foils). The dashed lines show the results from MCNPX calculations. The spectra are, in general, greater than the calculations by a factor of three. The authors attribute part of the discrepancy due to the fact that secondary interactions from charged particle fragments are most likely adding to the yields measured by the foils.

Table 4.3 shows the neutron fluence attenuation lengths in concrete that were extracted from the data. The measured neutron fluences were integrated over the indicated energy ranges, and the attenuation lengths were calculated by fitting the fluences over the indicated ranges in shielding.

Table 4.3: Neutron flux attenuation lengths in concrete for each detector and calculation. The calculation of the self-TOF data is LAHET. All other calculations are MCNPX.

Detector	Energy range (MeV)	Shielding range (cm)	λ (g/cm^2) data	λ (g/cm^2) calculation
Self-TOF	100-600	0-200	86.9	101.2
NE-213 (A)	20-800	50-150	124.4	129.4
NE-213 (B)	20-800	50-150	99.0	108.3
Bi and C	20-800	100-250	93.0	118.5

Also shown are the attenuation lengths that were extracted from the LAHET (self-TOF) and MCNPX (all other measurements) calculations of the data. MCNPX does a good job of reproducing the NE-213 results. The disagreement with the activation foil results may be due to secondary charged particle interactions that lead to a higher counting rate in the foils.

4.2.2 400 MeV/nucleon ^{12}C + Cu neutrons behind iron

Figure 4.10 shows the neutron flux (# per steradian per MeV per ion) behind 0, 50, 100, 150 and 200 cm of iron shielding, using the self-TOF detector. As with the concrete measurement (see above), the low-energy threshold is 100 MeV. No spectra are reported above 600 MeV due to a lack of statistically-significant events. Up to 80 cm of iron, the spectra have a broad peak around 200 to 300 MeV. The softening of the spectra can be seen at 100-cm shield thickness. The dashed lines show MCNPX calculations of the spectra. The calculations, in general, give a harder spectrum than do the measurements.

Figures 4.11 and 4.12 show the neutron flux behind iron shielding using the NE-213 detector at position A (directly behind the shielding) and position B (farther downstream from the shielding), respectively. The dashed lines show MCNPX calculations. The energy range of the data is 20 to 800 MeV. Below 100 MeV, the calculations overestimate the data as the shielding thickness increases. Between 100 and 400 MeV, the agreement between data and calculation is good. The agreement between calculation and experiment is quite good over the entire energy range (20-800 MeV) at 20 cm and 40 cm of iron shielding.

Figure 4.13 shows the neutron flux measured with the activation foils (Bi and C foils). This data was not published in Ref. [4.5]. The dashed lines show the results from MCNPX calculations. The spectra are, in general, greater than the calculations by a factor of three. The authors attribute part of the discrepancy due to the fact that secondary interactions from charged particle fragments are most likely adding to the yields measured by the foils.

Table 4.4 shows the neutron fluence attenuation lengths in iron that were extracted from the data. The measured neutron fluences were integrated over the indicated energy ranges, and the attenuation lengths were calculated by fitting the fluences over the indicated ranges in shielding. Also shown are the attenuation lengths that were extracted from the MCNPX calculations of the data. MCNPX does a good job of reproducing the self-TOF and NE-213 results. The agreement between the NE-213 (B) measurement and calculation becomes better when the results from 20 cm of shielding are excluded.

Table 4.4: Neutron flux attenuation lengths in iron for each detector and MCNPX calculation.

Detector	Energy range (MeV)	Shielding range (cm)	λ (g/cm^2) data	λ (g/cm^2) calculation
Self-TOF	100-600	20-100	123.0	119.7
NE-213 (A)	20-800	20-100	160.5	165.6
NE-213 (B)	20-800	20-100	121.5	140.4
NE-213 (B)	20-800	40-100	137.0	143.7

Table 4.5: Comparison of neutron fluences between experimental results and calculated ones.

Detector	Energy range (MeV)	Shielding thickness (cm)	fluence – data (n/sr/ion)	fluence – calc (n/sr/ion)
Self-TOF	100-600	0	4.338E+0	8.786E+0
		20	2.329E+0	2.287E+0
		40	6.028E-1	5.798E-1
		60	1.606E-1	1.555E-1
		80	4.513E-2	4.302E-2
		100	1.504E-2	1.242E-2
NE-213 (A)	20-800	20	6.544E+0	5.101E+0
		40	2.083E+0	2.121E+0
		60	7.384E-1	8.295E-1
		80	3.589E-1	3.153E-1
		100	1.223E-1	1.193E-1
NE-213 (B)	20-800	20	3.222E+0	3.314E+0
		40	4.933E-1	1.004E+0
		60	1.746E-1	3.283E-1
		80	4.473E-2	1.087E-1
		100	1.744E-2	3.896E-2

Table 4.5 shows the comparison between measured neutron fluences at various thicknesses of iron shielding and MCNPX calculations. The self-TOF data was integrated over 100 to 600 MeV, and the NE-213 measurements were integrated over 20 to 80 0MeV. For the self-TOF and NE-213 (A) measurements, the agreement is quite good after the first 20 cm of shielding. There is a large (factor of 2) overestimation of the NE-213 (B) results after 20 cm of shielding.

4.2.3 400 MeV/nucleon ^{12}C + Cu neutrons behind iron and concrete, TEPC measurements

Nunomiya *et al.* [4.6] measured lineal energy over the range of 0.5 to 2000 keV/μm. High-energy proton recoils from high-energy neutrons in the hundreds of MeV are responsible for the events in the range of 0.5 to 3 keV/μm. This component of the lineal energy spectrum is prominent behind 10 cm of iron shield (and no shield), but rapidly decreases as iron shielding thickness increases. This component slightly decreases with increasing concrete shielding.

Proton recoils from neutrons of several tens of MeV, and gamma-ray events comprise the lineal-energy range between 3 and 10 keV/μm. This component is evident without shield and behind concrete shielding, and it rapidly decreases behind iron shielding. Low-energy protons from neutrons of several hundreds of keV comprise the component of lineal energy between 10 and 140 keV/μm. This component increases as shielding thickness increases; this is taken as confirmation that neutrons of several tens of MeV (and higher) are slowed down to hundreds of keV in iron shielding. Above 140 keV/μm, heavy-ion events of alphas and recoil nuclei of C, N, and O dominate the spectrum. The alpha particles come from neutron interactions in the A-150 plastic. This relative ratio of this component decreases slightly with increasing shield thickness.

Table 4.6 shows the values of mean frequency-average lineal energy $\bar{y}_f$, mean dose-averaged lineal energy $\bar{y}_d$, dose, dose-equivalent, and mean quality factor behind the various thicknesses of iron and concrete shields. These data are plotted in Figs. 4.14 through 4.18.

Table 4.7 contains the dose attenuation length (λ_D) and dose-equivalent attenuation length (λ_H) obtained from the data (integrating over the entire range of lineal energy, 0.5 - 2000 keV/μm). Also shown are calculated values of the dose-equivalent attenuation lengths using MARS [4.12] calculations. Good agreement is seen between the data and MARS calculations.

Table 4.6: Values for several parameters behind concrete and iron shields, as measured with a TEPC.

Shield thickness		y_f (keV/μm)	y_d (keV/μm)	D (Gy m^2 coulomb^{-1})	H (Sv m^2 coulomb^{-1})	Q
No shield	0	3.5	16.1	400000	1500000	3.7
Concrete	50	4.3	33.3	39000	240000	6.3
100		4.8	47.6	9800	72000	7.4
200		5.2	47.0	2000	17000	8.5
300		5.6	40.2	930	9100	9.7
400		5.4	39.0	910	9000	9.9
Iron	10	1.2	42.0	92000	530000	5.7
20		2.4	58.0	42000	390000	9.2
Iron	40	4.6	62.2	18000	200000	11.2
60		5.2	57.7	8300	96000	11.5
80		5.2	50.8	4200	49000	11.6
100		5.2	53.1	1700	20000	11.5

Table 4.7: Attenuation lengths of dose and dose-equivalent over a lineal energy range of 0.5 to 2000 keV/μm.

Shield	λ_D (g/cm^2)	λ_H (g/cm^2)	λ_H MARS (g/cm^2)
Concrete	111 ± 7	126 ± 9	115 ± 1
Iron	188 ± 8	211 ± 10	209 ± 2

4.2.4 155 MeV/nucleon He, C, and O + Hevimet neutrons behind iron and concrete

The spectra measured at 94° (both before and after shielding) were determined from the data from all the spheres. For the other measurements made inside the experimental hall (before shielding, at 34°, 49°, and 59°), the spectral characteristics were determined from only the 5-inch and 12-inch spheres. Spectra were unfolded using the unfolding code PREF [4.13]. An a priori spectrum was used in the unfolding process. That spectrum was generated from the phenomenological analysis of thick-target neutron yields by Nakamura

[4.14]. Table 4.8 shows the neutron yields inside the experimental hall (before shielding) for all three beams. The neutron spectrum outside the shielding at 94° (point 1) from 155 MeV/nucleon ^{12}C + Hevimet is shown in Fig. 4.19.

Table 4.8: Thick target neutron yields for 155 MeV/nucleon ^{4}He, ^{12}C, and ^{16}O ions stopping in a 5.093-cm Hevimet target. The last row shows the total yield (number of neutrons per incident ion).

Angle θ (deg)	^{4}He neutron yield (n/sr/ion)	^{12}C neutron yield (n/sr/ion)	^{16}O neutron yield (n/sr/ion)
34	0.596	0.169	0.202
49	0.524	0.199	0.204
59	0.509	0.162	0.185
94	0.425	0.122	0.121
Total yield	4.90 n/ion	1.56 n/ion	1.74 n/ion

In addition to generating unfolded spectra, the spectra at 94° (before and after shielding) were also deduced using the six-spheres method [4.15]. Table 4.9 shows the fluence (neutrons per cm^2 per ion), average energy (MeV), and dose equivalent per ion (Sv/ion) for the spectra at 94°, both before and after shielding, for all three beams. The results from both methods (unfolding and six-spheres) are shown.

Table 4.9: Characteristics of the spectrum at 94° using both spectral-generation techniques. "Unf" refers to the unfolding method, and "6sph" refers to the six-spheres method.

Before/After shielding?	Ion	Method	Φ (n/cm^2/ion)	<E> (MeV)	H (Sv/ion)
After	^{4}He	Unf	$(1.28 \pm 0.10)\times10^{-9}$	3.17±0.80	$(1.69\pm0.20)\times10^{-19}$
After	^{4}He	6sph	$(1.19 \pm 0.09)\times10^{-9}$	1.95±0.23	$(1.77\pm0.21)\times10^{-19}$
Before	^{4}He	Unf	$(8.34 \pm 0.72)\times10^{-5}$	4.98±1.08	$(1.59\pm0.26)\times10^{-14}$
Before	^{4}He	6sph	$(9.48 \pm 0.75)\times10^{-5}$	2.43±0.28	$(1.75\pm0.21)\times10^{-14}$
After	^{12}C	Unf	$(6.51 \pm 0.66)\times10^{-10}$	3.11±0.78	$(1.24\pm0.15)\times10^{-19}$
After	^{12}C	6sph	$(6.50 \pm 0.55)\times10^{-10}$	2.67±0.35	$(1.30\pm0.17)\times10^{-19}$
Before	^{12}C	Unf	$(2.55 \pm 0.27)\times10^{-5}$	4.60±1.77	$(5.12\pm0.77)\times10^{-15}$
Before	^{12}C	6sph	$(2.36 \pm 0.20)\times10^{-5}$	2.74±0.36	$(4.84\pm0.64)\times10^{-15}$
Before	^{16}O	Unf	$(3.95 \pm 0.43)\times10^{-5}$	3.03±1.46	$(7.13\pm1.08)\times10^{-15}$
Before	^{16}O	6sph	$(3.59 \pm 0.43)\times10^{-5}$	2.28±0.26	$(6.22\pm0.68)\times10^{-15}$

Table 4.10 shows the integral characteristics of the neutron fields generated by ^{12}C beams stopping in Hevimet, outside the concrete shielding of the experimental hall's walls. Refer to Table 4.2 for distances from the target and shielding thickness at each angle. The fluence and dose equivalent are normalized to one incident ^{12}C ion.

Table 4.10: Integral characteristic of the neutron fields outside shielding for ^{12}C ions.

Angle θ (deg)	<E> (MeV)	Φ (neutrons/cm^2/ion)	H (Sv/ion)
44	0.30	1.10×10^{-10}	8.23×10^{-21}
49	0.30	1.51×10^{-10}	1.13×10^{-20}
54	0.35	2.41×10^{-10}	1.93×10^{-20}
65	1.00	3.76×10^{-10}	6.39×10^{-20}
73	3.11	5.39×10^{-10}	1.03×10^{-19}
82	3.11	5.64×10^{-10}	1.08×10^{-19}
94	3.11	6.51×10^{-10}	1.24×10^{-19}

To test the effect of a local, 25.4-cm thick iron shield placed directly on top of the target, measurements were made on top of the accelerator shielding, at about 3 m from the target. Table 4.11 shows the integral characteristics of the neutron field measured at that point, both with and with out the additional iron shielding.

Table 4.11: Integral characteristic of the neutron fields on top of the accelerator shielding, directly above the target station, for ^{12}C ions.

Iron shield?	<E> (MeV)	Φ (neutrons/cm^2/ion)	H (Sv/ion)
No	0.300	3.19×10^{-10}	2.39×10^{-20}
Yes	0.160	3.27×10^{-10}	1.70×10^{-20}

Using the He data at 94°, the authors extracted the dose-equivalent attenuation length in concrete for the intermediate and high-energy range of neutron energies. They obtained a value of $\lambda = 38$ g/cm^2, with $<E_n> \sim$ 70 MeV. This value is in agreement with a previously determined values of $\lambda = 36$ g/cm^2, with $<E_n> = 41.5$ MeV, and of $\lambda = 46$ g/cm^2, with $<E_n> = 64.3$ MeV.

4.3 Spectra from HIMAC Experiments of Sasaki *et al.*

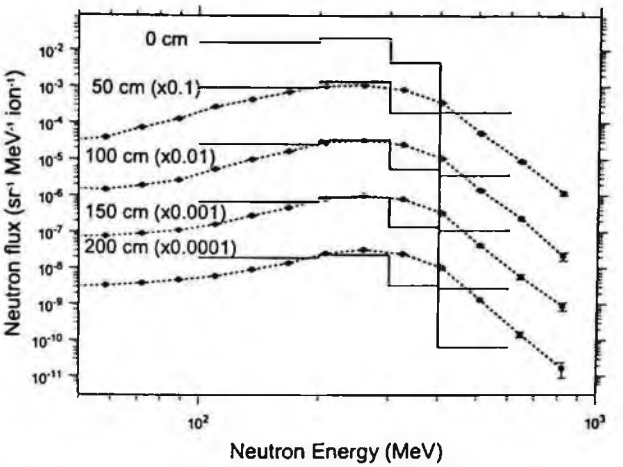

Figure 4.6: Self-TOF neutron spectra (solid histograms) measured behind the indicated thicknesses of concrete. The dashed lines and solid symbols show the results of LAHET calculations.

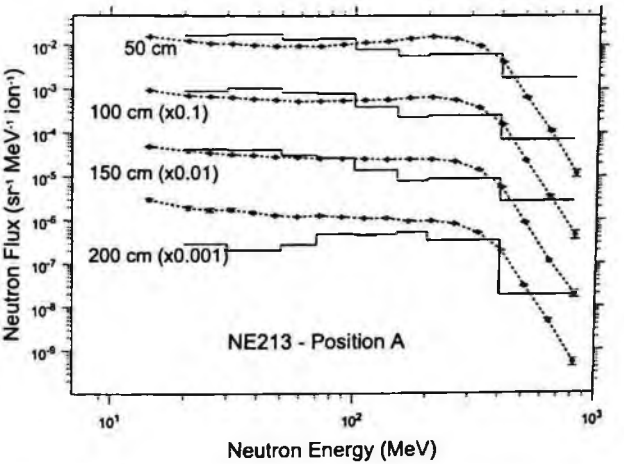

Figure 4.7: NE-213 neutron spectra (solid histograms) measured behind the indicated thicknesses of concrete at position A (see text). The dashed lines and solid symbols show the results of MCNPX calculations.

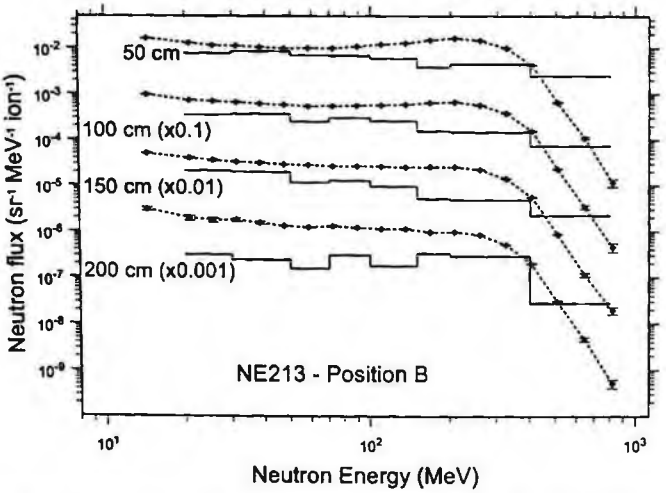

Figure 4.8: NE-213 neutron spectra (solid histograms) measured behind the indicated thicknesses of concrete at position B (see text). The dashed lines and solid symbols show the results of MCNPX calculations.

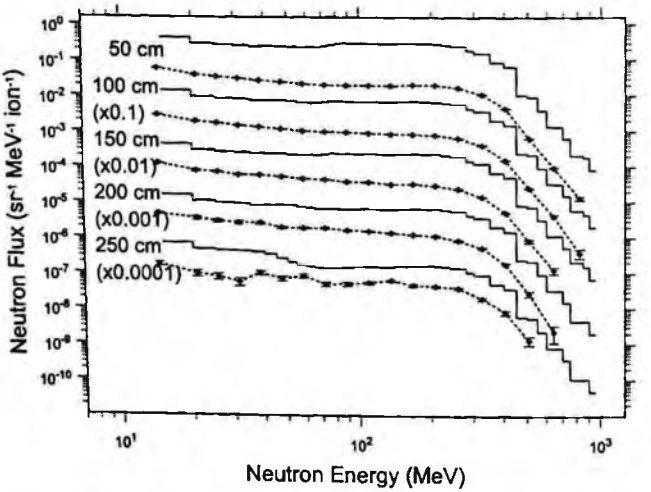

Figure 4.9: Activation foil neutron spectra (solid histograms) measured at the indicated thicknesses of concrete. The dashed lines and solid symbols show the results of MCNPX calculations.

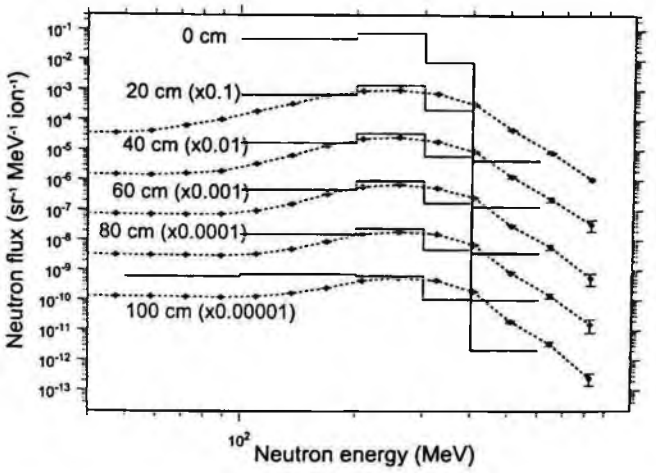

Figure 4.10: Self-TOF neutron spectra (solid histograms) measured behind the indicated thicknesses of iron. The dashed lines and solid symbols show the results of MCNPX calculations.

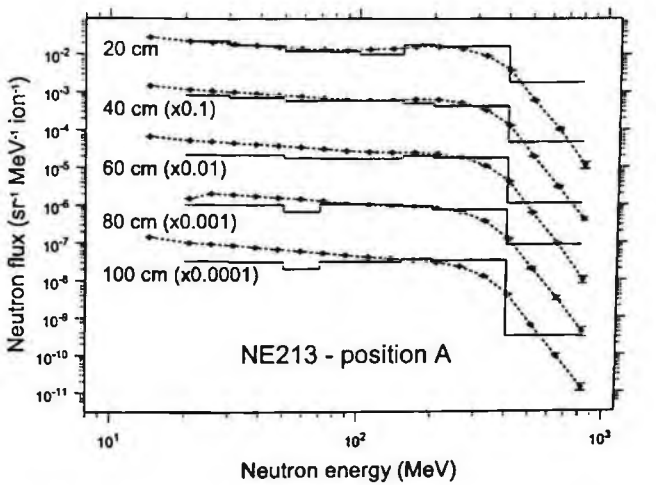

Figure 4.11: NE-213 neutron spectra (solid histograms) measured behind the indicated thicknesses of iron at position A (see text). The dashed lines and solid symbols show the results of MCNPX calculations.

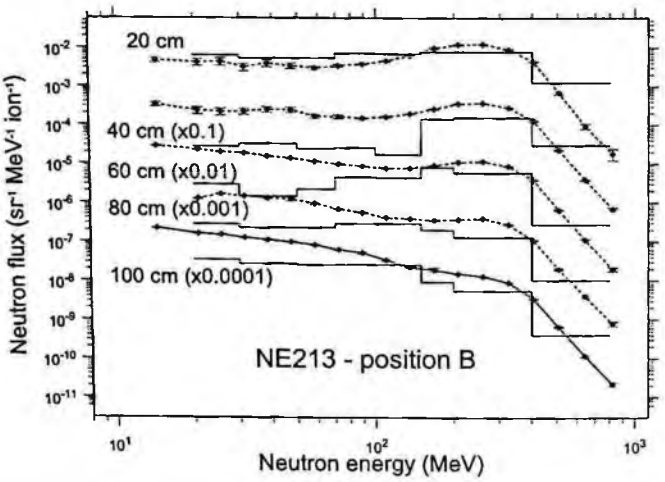

Figure 4.12: NE-213 neutron spectra (solid histograms) measured behind the indicated thicknesses of iron at position B (see text). The dashed lines and solid symbols show the results of MCNPX calculations.

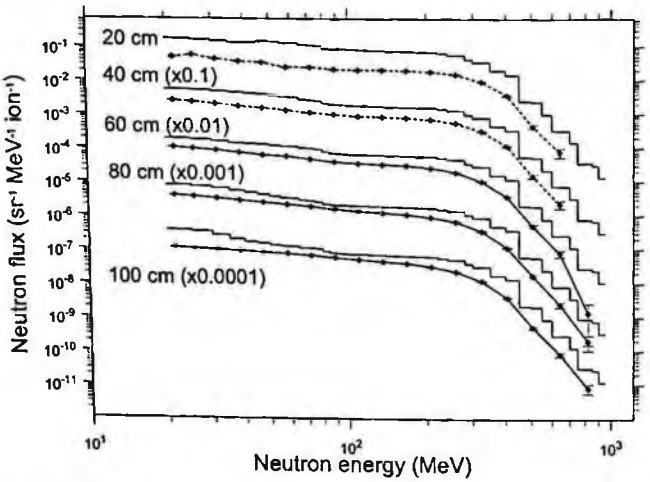

Figure 4.13: Activation foil neutron spectra (solid histograms) measured at the indicated thicknesses of concrete. The dashed lines and solid symbols show the results of MCNPX calculations. (Data and calculations not published)

4.4 Spectra from HIMAC Experiments of Nunomiya *et al.*

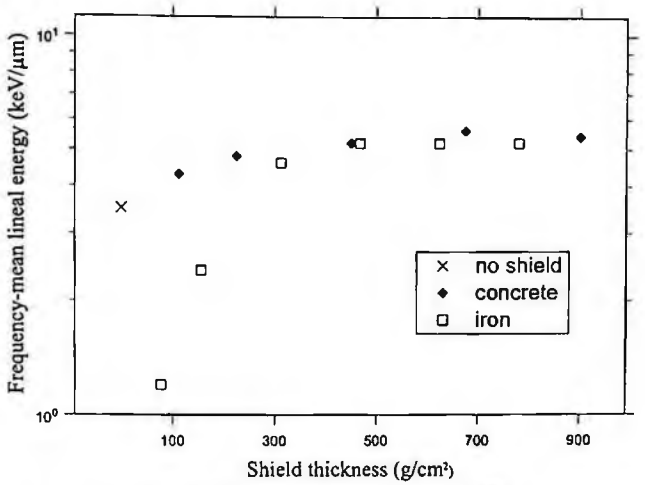

Figure 4.14: Measured frequency-mean lineal energies, $\bar{y}_{f,}$ behind concrete and iron shields of various thicknesses (in g/cm^2).

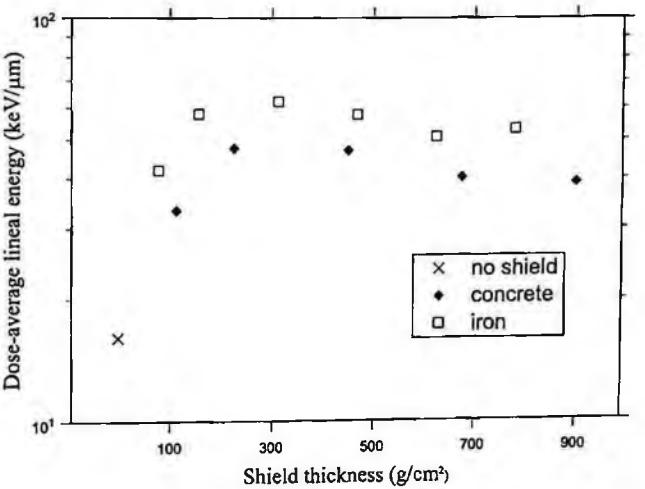

Figure 4.15: Measured dose-average lineal energies, $\bar{y}_{D)}$ behind concrete and iron shields of various thicknesses (in g/cm^2).

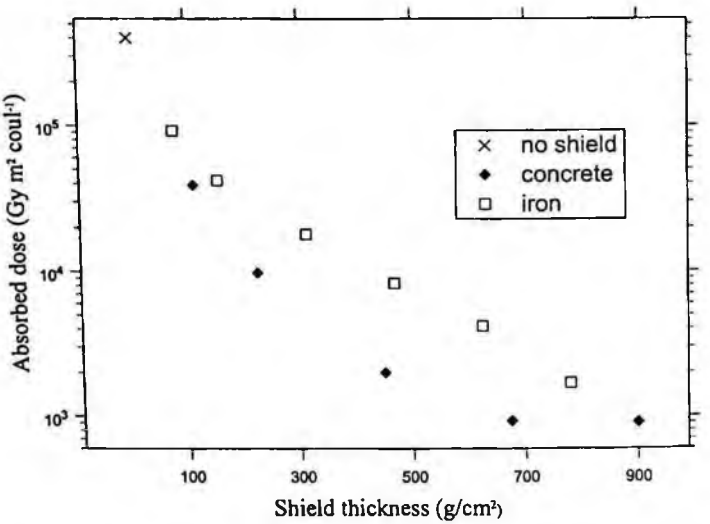

Figure 4.16: Absorbed dose behind concrete and iron shields of various thicknesses (in g/cm^2).

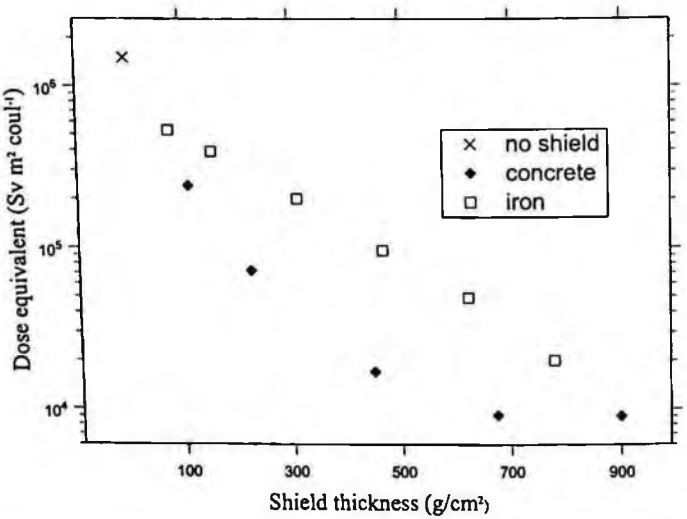

Figure 4.17: Dose-equivalent behind concrete and iron shields of various thicknesses (in g/cm^2).

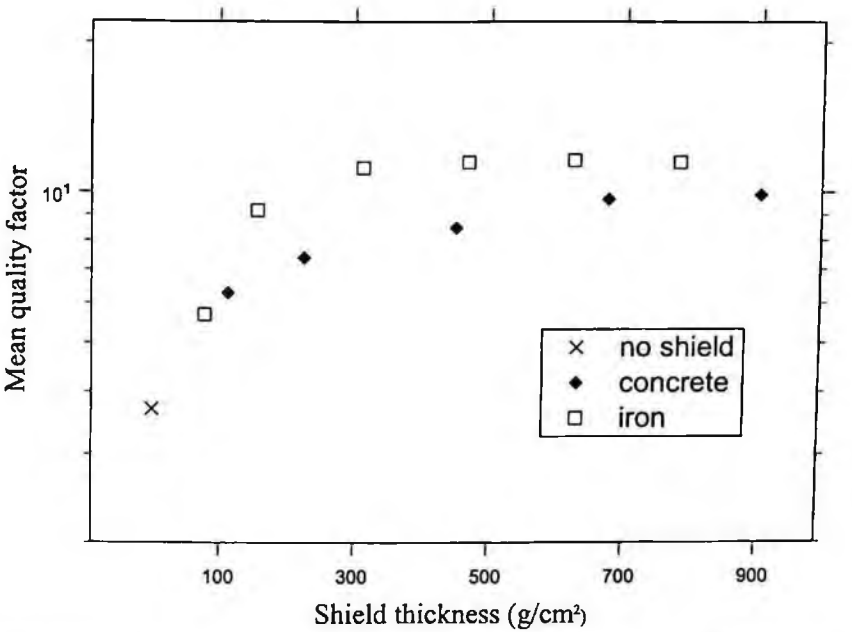

Figure 4.18: The measured mean-quality factor behind concrete and iron shields of various thicknesses (in g/cm^2).

4.5 Spectrum from NSCL Experiments

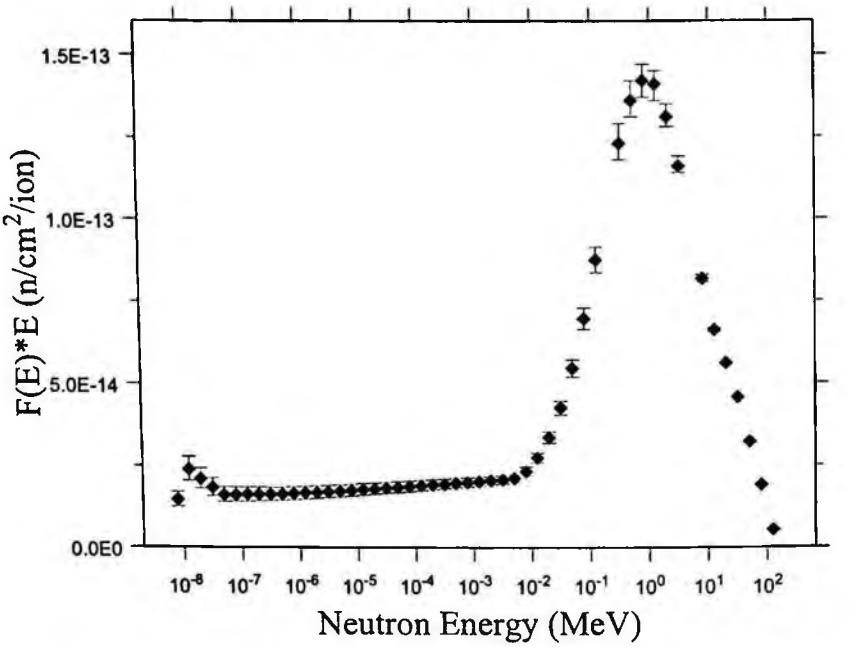

Figure 4.19: Neutron energy spectrum F(E)xE behind concrete shielding at 94° (point 1). Neutrons were produced by 155 MeV/nucleon ^{12}C stopping in a Hevimet target.

Chapter 5

Production Cross Sections of Spallation Products Created in Heavy-Ion Reactions

An important component in the design of heavy-ion accelerator facilities is an accurate estimation of the radioactivities induced by spallation products in accelerator components and in shielding materials. To this end, the production cross sections for various spallation products have been measured from heavy-ion reactions by several groups. Table 5.1 shows the various beams, targets and facilities used in the experiments, along with the relevant references. HIMAC is the Heavy Ion Medical Accelerator in Chiba, PPA is the Princeton Particle Accelerator (now defunct), RIKEN is the Institute of Physical and Chemical Research in Japan, TWA-ITEP is the U10 synchrotron Terawatt Accumulator of the Moscow Institute for Theoretical and Experimental Physics, and the Bevalac is the heavy-ion accelerator (decommissioned in 1993) at Lawrence Berkeley National Laboratory.

Table 5.1: Listing of the beams, energies (MeV/nucleon), targets and facilities used to measure spallation product cross sections. The appropriate reference(s) for each entry is also listed.

Beam	Energy	Target	Facility	Reference
^{14}N	278 AMeV	^{nat}Cu	PPA	[5.1]
^{12}C	2083 AMeV	^{nat}Cu	Bevalac	[5.2]
^{40}Ar	2000 AMeV	^{nat}Cu	Bevalac	[5.3]
^{12}C	2100 AMeV	^{nat}Ag	Bevalac	[5.4]
^{20}Ne	211 AMeV	^{nat}Cu	Bevalac	[5.5]
^{20}Ne	377 AMeV	^{nat}Cu	Bevalac	[5.5]
^{12}C	135 AMeV	^{nat}Cu	RIKEN	[5.6]
^{4}He	100 AMeV	C, Al, Cr, Fe, Ni, Cu, Pb	HIMAC	[5.7]*

Table 5.1 (continued)

Beam	Energy	Target	Facility	Reference
^{12}C	100 AMeV	C, Al, Cr, Fe, Ni, Cu, Pb	HIMAC	[5.7]*
^{20}Ne	100 AMeV	C, Al, Cr, Fe, Ni, Cu, Pb	HIMAC	[5.7]*
^{4}He	230 AMeV	C, Al, Cr, Fe, Ni, Cu, Pb	HIMAC	[5.7]*
^{12}C	230 AMeV	Al, Cr, Fe, Ni, Cu, Pb	HIMAC	[5.7]*
^{20}Ne	230 AMeV	C, Al, Cr, Fe, Ni, Cu, Pb	HIMAC	[5.7]*
^{40}Ar	230 AMeV	C, Al, Cr, Fe, Ni, Cu, Pb	HIMAC	[5.7]*
^{12}C	400 AMeV	C, Al, Cr, Fe, Ni, Cu, Pb	HIMAC	[5.8]*
^{20}Ne	400 AMeV	C, Al, Cr, Fe, Ni, Cu, Pb	HIMAC	[5.8]*
^{40}Ar	400 AMeV	C, Al, Cr, Fe, Ni, Cu, Pb	HIMAC	[5.8]*
^{28}Si	800 AMeV	C, Al, Cr, Fe, Ni, Cu, Pb	HIMAC	[5.8]*
^{12}C	200 AMeV	^{63}Cu, ^{65}Cu, Al, Co	TWA-ITEP	[5.13]

* - see also [5.9] - [5.12]

5.1 Experimental Details

5.1.1 278 MeV/nucleon ^{14}N + Cu (Cumming et al., Princeton Particle Accelerator)

Measurements done with 278 MeV/nucleon ^{14}N ions at the Princeton Particle Acccelerator [5.1] used three copper targets. Each target was comprised of three discs of Cu (1.6-cm diam, 345 mg/cm^2 thick) held together by a wrapping of 10.5-mg/cm^2 Cu. The three targets were separated by about 30 cm along the beam line, and the total irradiation time was 290 minutes. Beam intensity was about 3×10^5 ^{14}N ions/sec, although just a part of the beam was intercepted by the targets. The upstream target was dissolved and subjected to radiochemical analysis, with emphasis on products with an atomic number greater than Cu. Two of the discs from the middle target underwent a γ-ray assay starting 40 minutes after irradiation, using a Ge(Li) detector. All three discs from the downstream target underwent a separate γ-ray assay starting 99 minutes after irradiation, using a Ge(Li) detector that had a similar response-vs-energy curve to the detector used for the middle target. Additional experimental details may be found in Ref. [5.1].

5.1.2 ^{12}C + Cu, ^{40}Ar + Cu (Cumming et al., Bevalac (LBNL))

5.1.2.1 2083 MeV/nucleon ^{12}C + Cu

The target used for the 2083 MeV/nucleon ^{12}C irradiation was comprised of several Al and polystyrene foils in front of 6 Cu foils. The foils were 5x5 cm square. The forward and backward Cu foils were 12.6-mg/cm^2 thick, and the middle foils were 234-, 233.9-, 232.5-, and 233.4-mg/cm^2 thick. The total thickness of all the foils was 1158.2 mg/cm^2. The irradiation lasted 27 minutes, giving 10^{11} ^{12}C ions through the stack. The production of ^{24}Na in the second and third Al foils (approximately 20.8 mg/cm^2 each) was used as a relative beam monitor. Beam spot size was less than 0.5 cm in diameter. After irradiation, the activated foils were flown to Brookhaven for analysis. As was done for the Princeton Particle Accelerator experiment, the foils underwent both radiochemical analysis (front foil only) and γ-ray assay (all foils). The γ-ray assay was done using a Ge(Li) detector with higher efficiencies than the detectors used for the Princeton irradiations. Irradiations were also conducted using a 28-GeV proton beam for comparison with the 2083 MeV/nucleon ^{12}C results. Two different target thicknesses were used for the proton irradiations. One target had the same thickness as the target used for the ^{12}C irradiation, and the second target was much thinner (154.4 g/cm^2). The two different target thicknesses were used to estimate the effect of secondary reactions on the measured cross sections, and to extract the production cross sections to a target thickness of 0 g/cm^2. Additional experimental details may be found in Ref. [5.2].

5.1.2.2 2083 MeV/nucleon ^{40}Ar + Cu

The target used for the 2000 MeV/nucleon ^{40}Ar irradiation contained Al, mylar, and Cu foils. In the order as seen by the beam, the first three foils were Al (4.8-, 42.7-, and 4.7-mg/cm^2 thick, respectively), the next two foils were mylar (17.5- and 17.7-mg/cm^2 thick, respectively), the next four foils were Cu (9.3-, 233.9-, 234.4-, and 9.3-mg/cm^2 thick, respectively), and the last two foils were mylar (both 17.6-mg/cm^2 thick).

The mylar foils were designed to catch any spallation products that escaped the Cu foils. Beam intensity was about $6x10^7$ particles per second, and the irradiation time was 497 minutes. The total beam fluence ($2.9x10^{10}$ ^{40}Ar ions) was determined from ^{24}Na activation in the Al foils. After irradiation, 2.7-cm diameter discs (centered on the beam spot) were cut from the foils. The foils were then flown to Brookhaven National Laboratory. Fourteen hours after the end of the irradiation, γ-ray assays were begun. The analysis was identical to the methods described above for the 2083 MeV/nucleon ^{12}C and 278 MeV/nucleon ^{14}N irradiations done by this group. After γ-ray assay, the front Cu foil was dissolved for radiochemical analysis. The γ-ray assay was performed using Ge(Li) detectors. Additional experimental details may be found in Ref. [5.3].

5.1.3 2100 MeV/nucleon ^{12}C + Ag (Porile et al., Bevalac (LBNL))

The silver targets used for the 2100 MeV/nucleon ^{12}C irradiations were either 250 μm- or 75 μm-thick, highly-pure foils surrounded by 25 μm-thick guard foils. Upstream from the targets was a 75 μm aluminum foil surrounded by 25 μm aluminum guard foils. Beam intensity was checked with both the Al foils (via ^{24}Na activation) and ion chambers downstream from the target. Typical beam intensities varied between $5x10^8$ and $1x10^{10}$ ions per minute. Seven separate irradiations were performed with durations between 1 and 8 hours. Beam spot size was 1-2 cm in diameter, and was centered on the 5x5 cm-square foils. Targets were assayed with a Ge(Li) γ-ray spectrometer. Assays started as soon as 8 to 13 minutes after irradiation, and continued up to 1.5 years after irradiation. Additional experimental and analysis details may be found in Ref. [5.4].

5.1.4 211 and 377 MeV/nucleon Ne + Cu (Hicks et al., Bevalac (LBNL))

The beam intensities for the ^{20}Ne irradiations performed at the Bevalac were measured using an ion chamber. The current on target for the 377 MeV/nucleon irradiation was $7.56x10^7$ ^{20}Ne ions per second, and the

current was 8.57×10^7 ions per second for the 211 MeV/nucleon irradiation. The Cu target thicknesses were 2.046 g/cm^2 (377 MeV/nucleon) and 3.255 g/cm^2 (211 MeV/nucleon), and were 10x10 cm square. Beam spot size was about 1 cm in diameter, and was centered on the Cu targets. Ten days after irradiation, the targets were transferred to another facility and were γ-assayed with 45-cm3 Ge(Li) detectors. The detector efficiencies were calibrated to ± 3%. The targets were counted in a low geometry where summing effects of coincident gamma rays could be neglected. The absorption of low-energy γ-rays in the thick targets was taken into account by measuring the detector efficiency with Cu absorbers of the appropriate thicknesses. The targets were counted daily for the first several weeks, and then counted weekly thereafter over a period of 15 weeks. Additional details may be found in Ref. [5.5].

5.1.5 135 MeV/nucleon ^{12}C + Cu (Kim et al., RIKEN)

The target stacks used for the RIKEN experiments consisted of a 23.7-mg/cm^2 thick Cu foil surrounded by forward and backward catcher foils made of 10.5 mg/cm^2-thick mylar foils. Forward and backward guard foils made of the same thickness of mylar comprised the outer layers. The stacks were mounted in a vacuum system. Two stacks were irradiated for 10 minutes and 2 hours, respectively, at a beam intensity of about 3.7×10^{10} beam particles per second. The ^{12}C beam energy at the center of the Cu foil was 134.5 MeV/nucleon. Gamma ray spectra were measured using a Ge detector. The Ge detector was intercalibrated using a mixed radionuclide γ-ray source. Short half-life products were measured using the 10-minute target, and the longer half-life products were measured using the 2-hour target. Additional details may be found in Ref. [5.6].

5.1.6 Yashima et al., HIMAC

The HIMAC series of experiments [5.7]-[5.12] used a target stack comprised of two to seven 5-mm thick Cu plates. Each plate had an areal dimension of 10 cm by 10 cm. For each beam, the number of plates was determined such that the total thickness of the Cu target was

slightly thicker than the range of the beam. In between each plate, samples of C (0.2-mm thick, 5x5 cm square), Al (0.1-mm thick, 9x10 cm^2), and Cu (0.1-mm thick, 9x10 cm^2) were placed in order to measure the spatial distributions of spallation products, and to determine the energy dependence on the cross section. Foils of the same thickness were placed at the front of the stack to measure the reaction cross sections and mass-yield distributions. A schematic diagram of the experimental setup may be seen in Figure 5.1.

Two runs per target were measured; one shorter irradiation time to measure short-lived isotopes, and one longer irradiation time to measure the long-lived isotopes. Table 5.2 shows the parameters of each experiment in the series. Beam currents were integrated using an ion chamber placed upstream of the target stack. Gamma ray spectra were measured using four high-purity germanium detectors.

Table 5.2: Experimental parameters from the HIMAC series of irradiations.

Projectile type and energy [MeV/nucleon]	Beam Intensity [particles/sec]	Irradiation time (short/long) [min]	Thickness (short/long) [g/cm^2]	Range [g/cm^2]
Ar[230]	2.78E+08	60/444	10.68	6.07
Ne[230]	5.03E+08	61/364	9.89/14.62	9.79
C[230]	1.84E+09	36/359	14.51/19.24	16.29
He[230]	9.15E+09	21/304	55.60	48.86
p[230]	2.28E+10	10/312	55.60	48.86
Ne[100]	7.40E+08	31/366	5.06	2.37
C[100]	1.95E+09	60/405	6.22	3.93
He[100]	1.05E+10	48/360	14.79	11.76
p[100]	2.04E+10	46/301	14.79	11.75
Ar[400]	2.37E+08	61/489	24.080	14.90
Ne[400]	7.62E+08	60/463	33.539	24.09
C[400]	1.77E+09	58/457	55.599	40.13
Si[800]	2.60E+08	61/435	64.529	48.92

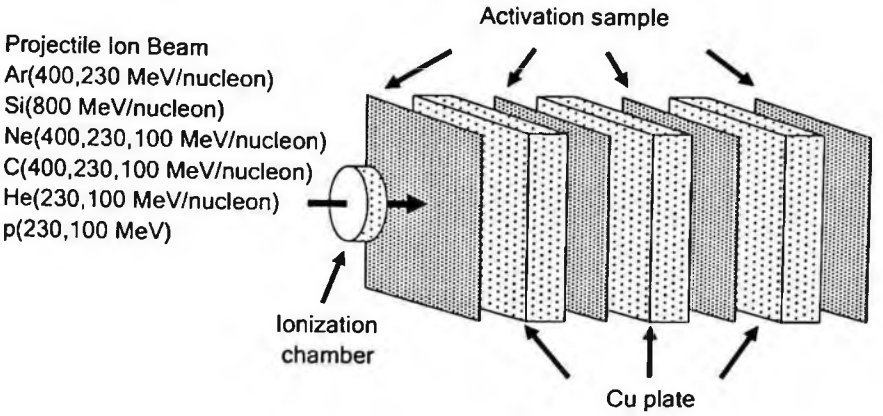

Figure 5.1: Schematic diagram of the HIMAC setup (courtesy of Ref. 5.7).

5.1.7 200 MeV/nucleon $^{12}C + {}^{nat}Cu$, ^{27}Al, ^{59}Co, Titarenko et al., TWA-ITEP

The heavy-ion experiments conducted at the TWA-ITEP facility in Moscow [5.13] utilized a target stack comprised of six foils. The first two foils, as seen by the beam, were ^{nat}Cu foils. The next two foils were ^{59}Co, and the last two foils were ^{27}Al. Only the second (downstream) foils in each pair were analyzed for spallation product production. The second foils had thicknesses of 0.25 mm (Cu), 0.40 mm (Co) and 0.10 mm (Al). Gamma spectral measurements of the first Al foil did not find any occurrences of spallation products with mass numbers above 27 that may have escaped the second Co foil. This was taken as an indication that the effect from forward (and backward) recoil escape was negligible.

Once the number of various spallation products were determined using gamma spectroscopy, the production cross sections were deduced using beam monitor data. The beam monitor used for the heavy-ion experiments was a BERGOZ FCT-082-20:1 current transformer. The output of the FCT was recorded by a TDS-220 digital oscilloscope, and the number of incident beam particles was determined by counting the number of events recorded in the oscilloscope. Additional details may be found in Ref. 5.11.

5.2 Results

5.2.1 278 MeV/nucleon $^{14}N + Cu$

Reference [5.1] reported the relative cross sections for nuclide production from 278 MeV/nucleon ^{14}N, using measured 3.9-GeV proton-induced cross sections as the reference. The authors in Ref. [5.1] report that counting rates used to produce the relative production rates were corrected for detector efficiency, γ-ray summing, radiation abundance, and temporal variation of the beam. The peak efficiency and total efficiency vs γ-ray energy calibration curves were measured for both Ge(Li) detectors, using a variety of standardized sources. The calibration curve for the detector used at BNL was measured using copper absorbers to simulate the 1 g/cm^2 counting sample. The calibration curve for the detector used at Princeton was measured with bare sources. Corrections for self-absorption were made.

The authors converted the proton-induced production rates to absolute cross sections based on assays of ^{24}Na in the central Al foil of the upstream stack used in the proton experiments. The reported standard deviations include statistical errors, a 2% uncertainty in chemical yield determination, a 4% systematic uncertainty in the reproducibility of the β counts and 2% uncertainty in the reproducibility of the γ counts. The authors note that the value reported for ^{65}Ga comes from a single determination and appears to be highly anomalous.

5.2.2 2083 MeV/nucleon $^{12}C + Cu$

The analysis of the 2083 MeV/nucleon ^{12}C-induced spallation-products experiment [5.2] proceeded in the same manner as the ^{14}N analysis above [5.1]. The ratios of the thick-target to thin-target production cross sections from the proton irradiations were determined for a wide range of product masses. For product masses between A=7 and A=43, the ratio of thick-to-thin cross sections was constant, with a value of about 0.91. The authors interpret this result to mean there was no contribution from secondary reactions, but instead there was a 9% contribution in ^{24}Na production from secondaries in the Al-foil beam monitors. Above A=43,

the ratio steadily increases to about 1.24 for A=61. The authors fit the ratio values between A=7 and A = 61 with a single curve. For masses above A=61, the authors used the experimentally determined values. To extract cross sessions to zero target thickness, the authors used a linear extrapolation using the ratios determined with the above method.

For the ^{12}C irradiations, the authors estimated the effects from secondary interactions in the measured cross sections. Because no thin target was used in those irradiations, the part of Cu foils outside the irradiation zone were assayed (γ assay only) to determine the production of isotopes from secondary interactions. It was found that the out-of-beam fractions exhibited a similar dependence on mass as was found in the thick-thin ratios from the proton irradiations. For low-mass products, the flux of secondary particles from ^{12}C interactions was found to be 1.2 times greater than the proton interactions (on a per-interactions basis). For A=57 products, the factor was found to be 2.8. From this analysis, the authors concluded that the contribution from secondary effects in the thick targets was small for low mass targets and are approximately independent of beam particle. For products with mass near the target, the secondary effects are larger, but no larger than 2.8 times the effect seen in proton irradiations.

5.2.3 2000 MeV/nucleon ^{40}Ar + Cu

The analysis of the 2000 MeV/nucleon ^{40}Ar irradiations by Cumming *et al.* [5.3] proceeded in the same manner as their previous two analyses [5.1], [5.2]. The total fluence of ^{40}Ar ions on the Cu target was determined to be 2.9×10^{10}. The authors report a 15% systematic uncertainty in the monitor cross section that is not included with the uncertainties reported with each cross section. Uncertainties that are taken into account with the reported overall uncertainty are statistical, spectral resolution, and spread in the values determined from multiple measurements.

The authors also correct the measured cross sections for secondary effects such as production of nuclides from secondary fragment interactions. Only one target thickness was used, so the correction for secondary interactions involved the use of data from previous

experiments run by this group [5.1], [5.2]. The first step in the method was to divide the production cross sections from all the systems studied by the $^{54}Mn^{g}$ production cross sections from the same systems. This "normalization" effectively eliminates the increase in production cross due to the increase in total reaction cross section as one goes from proton-induced production to heavy-ion-induced production. The secondary effects in the production of $^{54}Mn^{g}$ are nearly identical to those present in the production of ^{24}Na in Al (which was used in beam monitoring for these experiments). The production of $^{62}Zn/^{54}Mn^{g}$ was used as an internal monitor of secondary reactions for each system because most of the ^{62}Zn production is believed to come from secondary reactions. Analysis of their 28-GeV proton production of ^{62}Zn at several Cu foil thicknesses indicates that 90% of that yield in thick targets is due to secondary reactions.

For each isotope in question, a correlation plot of the its production cross (divided by the appropriate $^{54}Mn^{g}$ production cross section) versus the $^{62}Zn/^{54}Mn^{g}$ production ratio was generated. In those plots, a straight-line least-squares fit to the 28-GeV proton points (three points in total, representing the 154-, 1158-, and 2269-mg/cm^2 Cu foil thicknesses used in those irradiations) was calculated. A strong, positive slope resulting from that fit indicated a strong contribution from secondary reactions, whereas a negative slope indicated those isotopes were less sensitive to contributions from secondary reactions. After the lines from the least-squares fit were drawn in each correlation plot, the next step was to check if the ratios from the heavy-ion systems (2000 MeV/nucleon Ar, 2083 MeV/nucleon C, and 283 MeV/nucleon N) lay close to those lines. If they did, it was assumed that the primary to secondary yield ratios were similar to the ones measured in the proton system. The relevant isotope production cross section could then be corrected for secondary reactions using the measured corrections from the 28 GeV proton + Cu (1158 mg/cm^2) system. The final correction factor was the product of the factor used in the 28-GeV proton system times the ratio of the ^{62}Zn yield from ^{40}Ar to the ^{62}Zn yield from the 28-GeV proton (1158 mg/cm^2 Cu foil) system. For example, the ^{61}Cu yield in the 1158 mg/cm^2 foil was 28.7% higher than the thin foil measurement from proton irradiation. The yield of ^{62}Zn produced from secondary reactions in the ^{40}Ar system

(609-mg/cm^2 Cu foil) was 1.8 times higher than the same production in the 28-GeV proton (1158- mg/cm^2 Cu foil) system. The total correction was then 28.7% x 1.8, or 51.7%. Thus, the ^{61}Cu yield from the ^{40}Ar system is divided by 1.517 to obtain the thin-target yield. Additional details regarding the correction for secondary reactions may be found in Ref. [5.3].

5.2.4 2100 MeV/nucleon ^{12}C + Ag

The resulting γ-ray spectra were analyzed with the code SAMPO and the decay curves were fitted with the code CLSQ. The disintegration rates for low-energy γ-rays were corrected for attenuation in the thick target runs. A total of 380 distinct γ-rays were observed. Of those, nuclide assignments were made on 280 γ-rays, resulting in cross sections for 99 nuclides.

The Ge(Li) detectors were calibrated against NBS (now known as NIST) mixed radionuclide γ-ray emission-rate standards. Because the spatial distribution of nuclides resulting from the ^{12}C irradiation was larger than the NBS standard, geometrical correction factors (on the order of 2% - 4%) were applied. The counting rate was low enough that the assays were conducted in a high geometry, which necessitated a correction for the reduction in photopeak efficiency due to summing effects. That correction varied between 10% and 30%.

Two target thicknesses were used in the ^{12}C + Ag irradiations in order to measure the effect of secondary processes on the measured cross sections. Analysis of that data [5.4] indicates that for A < 90, the ratio of the two cross sections was 1.05, which corresponds to an enhancement of 2.5% per 100 mg/cm^2 of silver. For A > 90, the authors observed a rising, linear dependence on A. For A = 106, the ratio is 1.45.

5.2.5 211 and 377 MeV/nucleon ^{20}Ne + Cu

The γ-ray spectra were analyzed with the code SAMPO. The individual γ-ray decay curves were corrected back to the end of the irradiations. The reported uncertainties in the production cross sections ranged from 12 to 20 percent. The cross sections were corrected for secondary

production processes in the manner of Cumming *et al.* (see sections 5.2.3 and 5.2.2). The authors report that the corrections amounted to a 5% reduction in the yield of ^{54}Mn and increased with A to 20% for ^{60}Co and 35% for ^{65}Zn. They estimated an uncertainty of 20% in this correction, which led to additional uncertainties in the reported cross sections of a few percent. ^{7}Be yields were corrected by 30%, and ^{24}Na yields were corrected by 15% to reach their zero-thickness yields.

5.2.6 135 MeV/nucleon ^{12}C + Cu

The γ-ray spectra obtained with the Ge(Li) detectors were analyzed using the code BOB. Nuclide assignments were made on the basis of γ-ray energy and half-life. An additional check on nuclide assignment was made using the relative intensities of all of the detected γ-rays emitted by a presumed nuclide.

The cross sections were determined from the weighted averages of determinations from both the long and short exposures, and, when applicable, of determinations from several γ-rays emitted by the same nuclide. The reported uncertainties include the statistical uncertainties, systematic uncertainty in the detection-efficiency calibration, and systematic uncertainty in the analysis software used to analyze the γ-ray spectra. In addition to the production cross sections, Kim *et al.* also reported average forward ranges and forward-to-backward ratios.

5.2.7 HIMAC series of experiments at 100, 230, 400 and 800 MeV/nucleon

Yashima *et al.* [5.7] - [5.12] reported that the statistical uncertainties varied between 1 and 40 percent. The systematic uncertainties which were considered were errors in beam intensity, peak efficiency, and the coincidence-summing effect (which was found to be small). The cross sections were measured from the foils placed on the surface of the Cu target. Residual activities were measured from the foils inserted in between the Cu plates. Activities and cross sections include corrections for the peak efficiency of the HPGe detector, the coincidence-summing effect, and beam-current fluctuation during the irradiation. The reaction

rate per unit beam current (R), corrected for current fluctuations, was determined from:

$$R = \frac{\lambda C}{\varepsilon\gamma e^{-\lambda t_c}\left(1-e^{-\lambda t_m}\right)\sum_{i=1}^{n}\left(Q_i e^{-\lambda(n-i)\Delta t}\right)} \tag{5.1}$$

where λ is the decay constant, C is the total counts in the gamma-ray peak area, ε is the peak efficiency, γ is the gamma-ray branching ratio, t_c is the cooling time, t_m is the counting time, Q is the beam current during irradiation time interval Δt, and t_i is the irradiation time ($=n\Delta t$).

For foils placed in between the Cu plates, the fraction of nuclides produced by secondary reactions was considered to be small. Degradation of the beam energy in the target was taken into account, as was the attenuation of beam particles through the target due to multiple nuclear scattering.

For nuclides whose fraction produced by secondary interactions is negligibly small, excitation functions could be generated by measuring production cross sections in the foils placed in between Cu plates. In addition to the heavy-ion data, Yashima *et al.* also measured proton-induced cross sections. That data may be found in Ref. [5.7].

5.2.8 TWA-ITEP experiments with 200 MeV/nucleon ^{12}C

Spallation product cross sections were determined by counting the number of products within the downstream foils, and then normalized to the number of incident beam particles as determined by a beam monitor. No corrections were made for forward or backward recoil loss after it was found that no forward recoils from the second Co foil made it into the first Al foil that directly proceeded the Co foil.

5.2.9 ^{12}C + Cu excitation functions

Using the data of Yashima *et al.*, Kim *et al.*, Titarenko *et al.*, and Cumming *et al.*, it is possible to plot the ^{12}C + Cu reaction cross sections

for various nuclides as a function of beam energy. Figures 5.2 through 5.12 show the excitation functions for isotopes of various elements.

Only isotopes that were measured at all five energies are shown. The points at 100 MeV/nucleon, 230 MeV/nucleon and 400 MeV/nucleon come from Yashima *et al.* [5.7], [5.8], the points at 135 MeV/nucleon come from Kim *et al.* [5.6], the points at 200 MeV/nucleon come from Titarenko *et al.* [5.13], and the points at 2083 MeV/nucleon come from Cumming *et al.* [5.2]. In general, as the beam energy increases, the cross section decreases. This trend is especially evident for elements near the mass of the target (Cu).

5.2.9.1 ^{20}Ne + Cu excitation functions

It is also possible to use the data above to generate excitation functions for ^{20}Ne interactions ranging from 100 MeV/nucleon to 400 MeV/nucleon, using the data of Hicks *et al.* and Yashima *et al.* However, the cross sections of Hicks *et al.* [5.5] are, in general, higher than the cross sections of Yashima *et al.* [5.7] - [5.12], even though the energies are similar.

Figures 5.13 through 5.15 show the comparisons between the two data sets for ^{22}Na, ^{46}Sc and ^{60}Co nuclides. The reported cross sections of Hicks *et al.* were corrected for contributions from secondary interactions, whereas the reported cross sections from Yashima *et al.* were not. Presumably, any correction for secondary interactions will decrease the measured cross section. Unfortunately, this most likely means if one was to remove the correction for secondaries in the Hicks data or correct for secondaries in the Yashima data, that would make the discrepancy larger.

5.2.10 Mass-yield distributions

The data can be summed over the same mass numbers to produce mass-yield distributions. Figures 5.16 through 5.19 show the mass-yield distributions (in mb) for the 100-, 230-, 400-, and 800-MeV/nucleon systems interacting in a Cu target, respectively. In general, as the mass of the beam increases, the yield also increases. This trend is especially

evident as the mass of the beam increases from He to C in the 100- and 230-MeV/nucleon systems. Figure 5.20 shows the mass-yield distributions from 100-, 230-, and 400-MeV/nucleon C interacting in Cu. As can be expected from the trends noted in the excitation functions shown in Figs. 5.2-5.12, the mass yields are somewhat independent of energy, although there appears to be a slight decrease in yield with increasing energy for the higher mass yields.

5.2.11 Comparisions between measured cross sections and calculations

Figures 5.21 – 5.31 show the comparison between the data of Yashima with PHITS calculations, QMD+GEM calculations, and QMD+SDM calculations. The QMD models are compared with the 100 MeV/nucleon He + Cu, C + Cu, and Ne + Cu systems and the 230 MeV/nucleon He + Cu, C + Cu, and Ne + Cu systems (Figs. 5.21 – 5.26). PHITS calculations of the 230 MeV/nucleon Ar + Cu, 400 MeV/nucleon C + Cu, Ne + Cu and Ar + Cu, and 800 MeV/nucleon Si + Cu systems are shown in Figs. 5.27 – 5.31. In general, the models tend to underestimate the cross sections, especially for the heavy-mass products. For light-mass products, PHITS calculations tend to overestimate the cross sections.

5.2.12 Spatial distribution of residual activities induced by spallation products

Figures 5.32 – 5.33 show the spatial distributions of residual activities per incoming projectile ion, with the target depth normalized to the range of the ion. Units are in Bq g/cm^2. Comparisons of the data with PHITS calculations are shown. The data are shown with the filled symbols, and the PHITS calculations are shown with the open symbols. In general, the calculations follow the shapes of the distributions very well, and in most cases the agreement in magnitude is also very good. In the worst cases, the data and calculations differ by factors of 2-3 in magnitude.

5.3 Spallation Products Excitation Functions

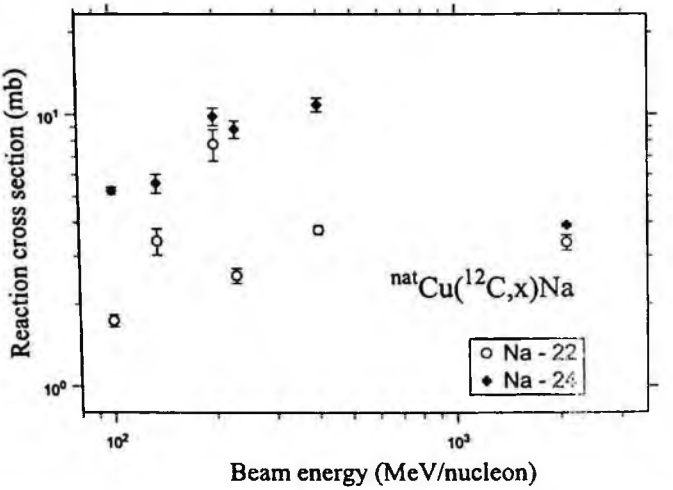

Figure 5.2: Excitation functions for Na isotopes produced by ^{12}C interactions in Cu.

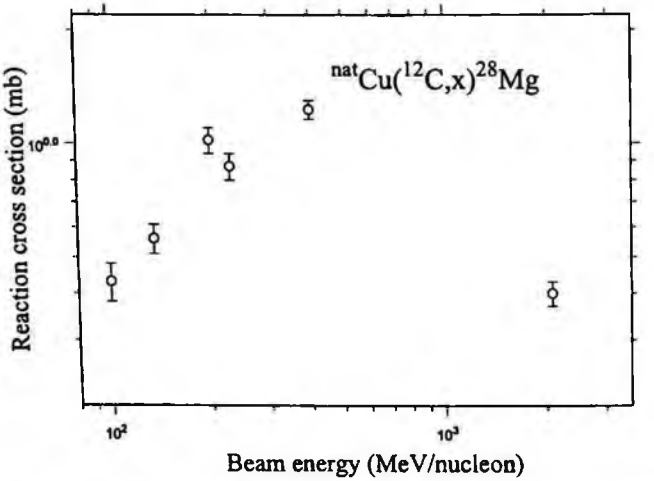

Figure 5.3: Excitation function for ^{28}Mg produced by ^{12}C interactions in Cu.

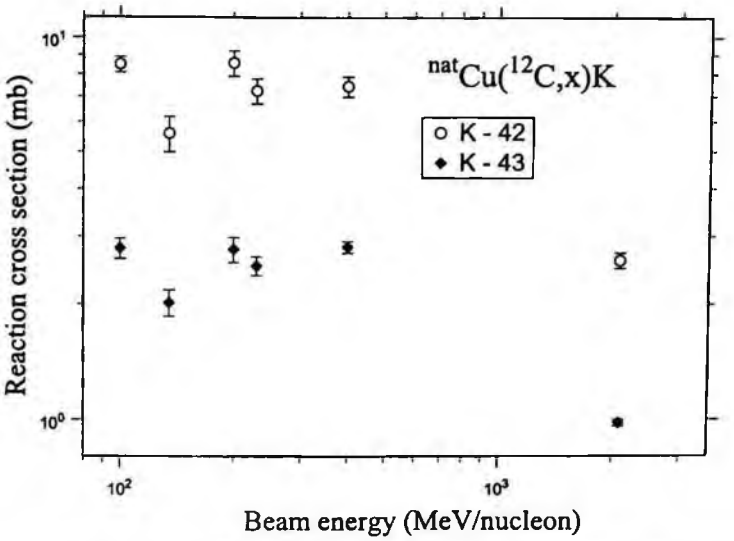

Figure 5.4: Excitation functions for K isotopes produced by ^{12}C interactions in Cu.

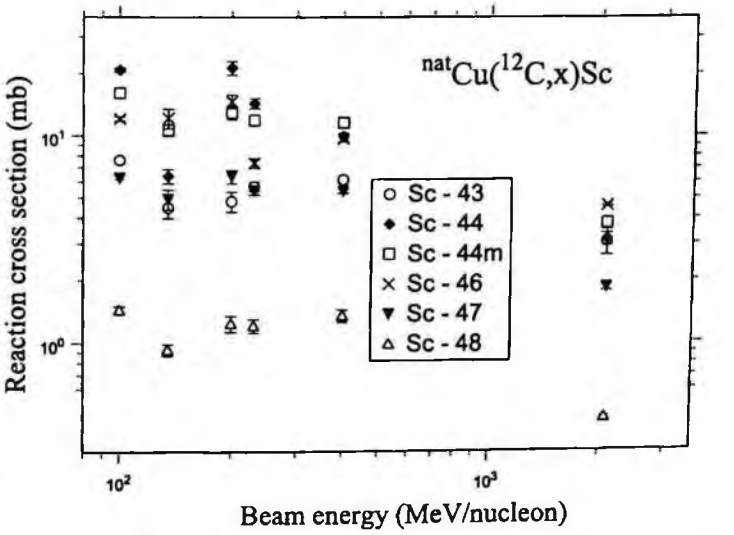

Figure 5.5: Excitation functions for Sc isotopes produced by ^{12}C interactions in Cu.

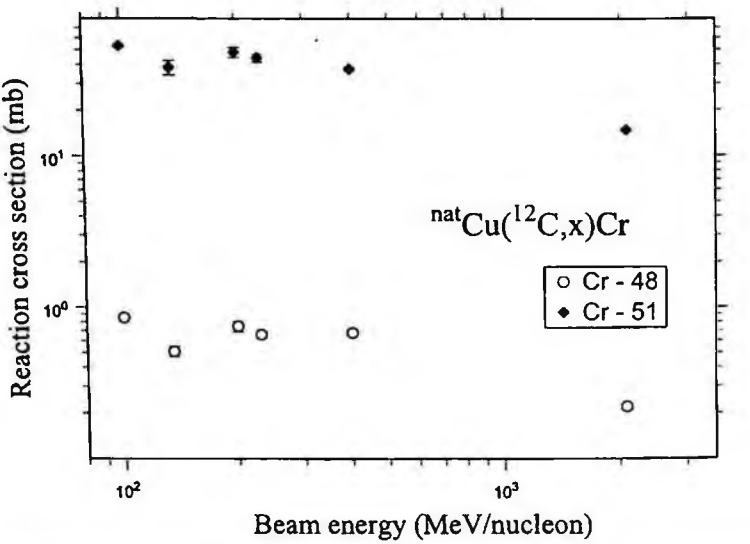

Figure 5.6: Excitation functions for Cr isotopes produced by ^{12}C interactions in Cu.

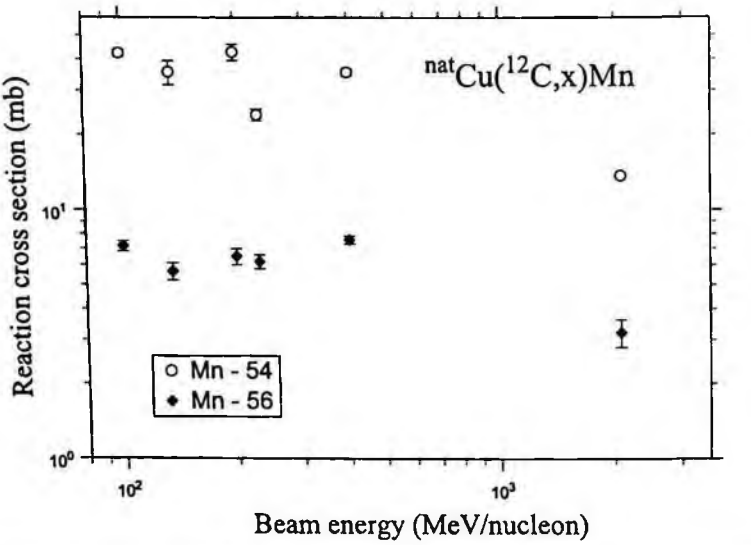

Figure 5.7: Excitation functions for Mn isotopes produced by ^{12}C interactions in Cu.

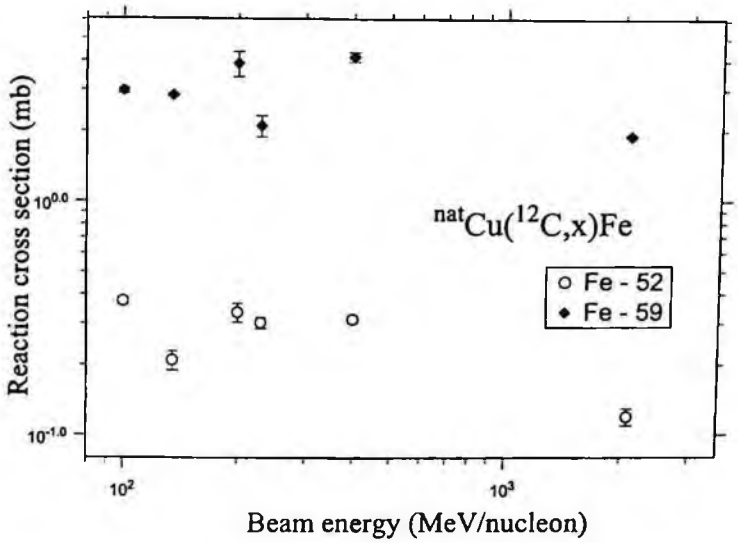

Figure 5.8: Excitation functions for Fe isotopes produced by ^{12}C interactions in Cu.

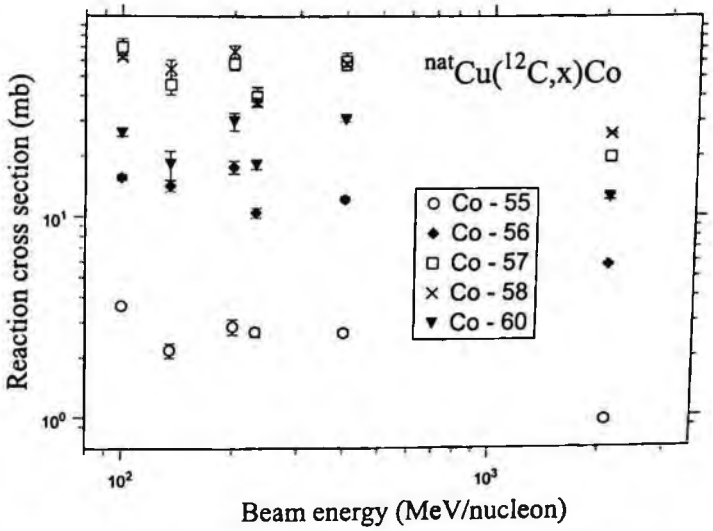

Figure 5.9: Excitation functions for Co isotopes produced by ^{12}C interactions in Cu.

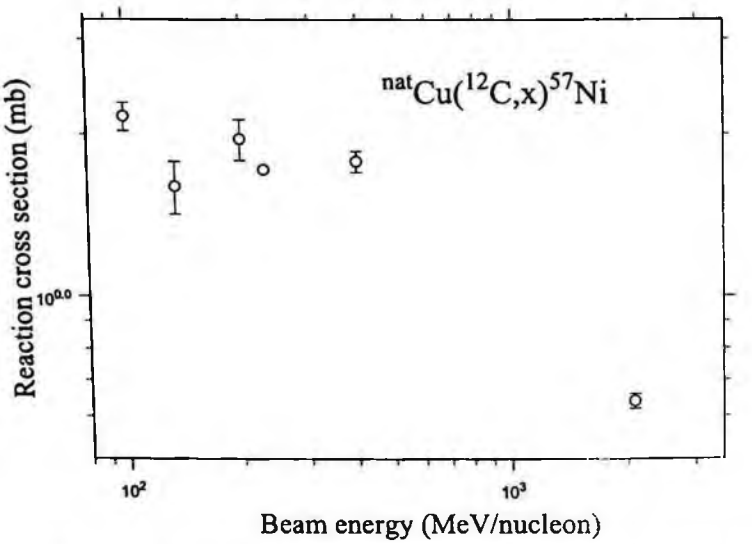

Figure 5.10: Excitation function for ^{57}Ni produced by ^{12}C interactions in Cu.

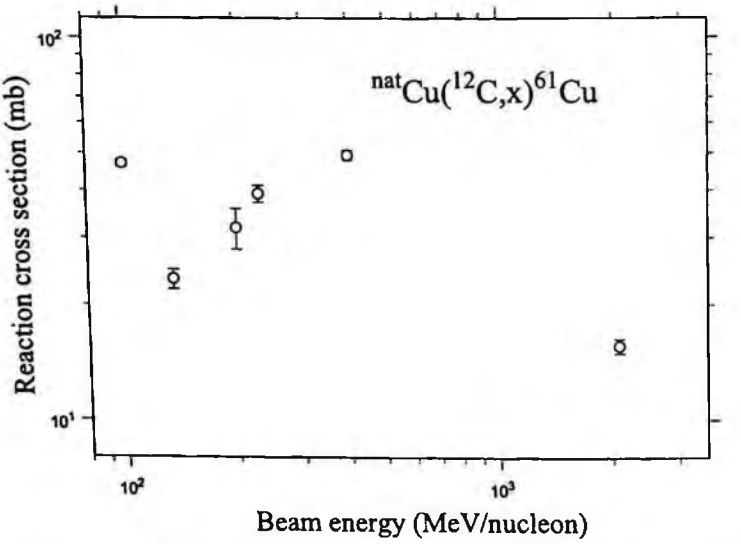

Figure 5.11: Excitation function for ^{61}Cu produced by ^{12}C interactions in Cu.

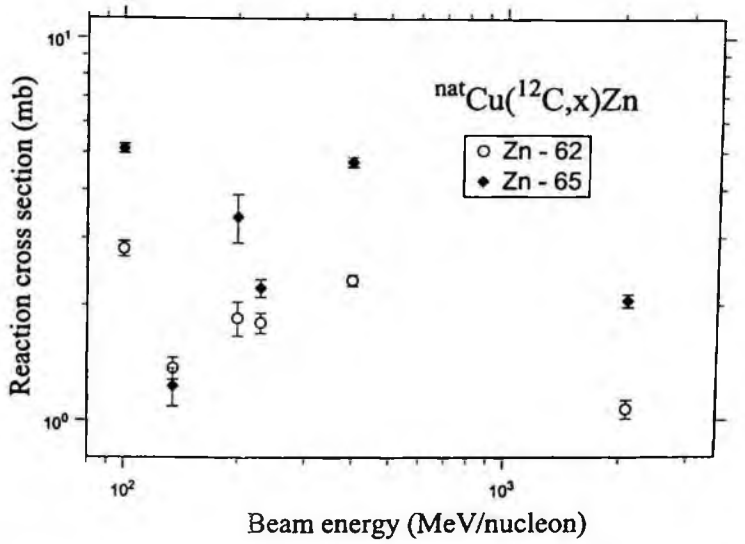

Figure 5.12: Excitation functions for Zn isotopes produced by ^{12}C interactions in Cu.

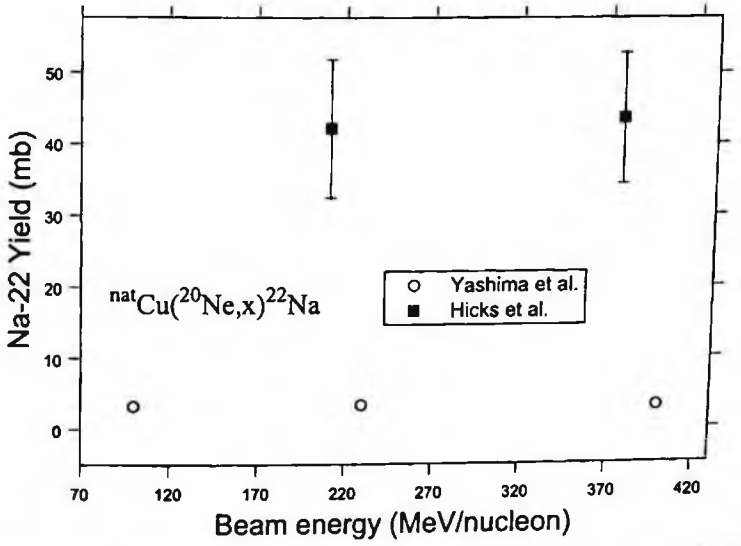

Figure 5.13: Excitation functions for ^{22}Na isotopes produced by ^{20}Ne interactions in Cu.

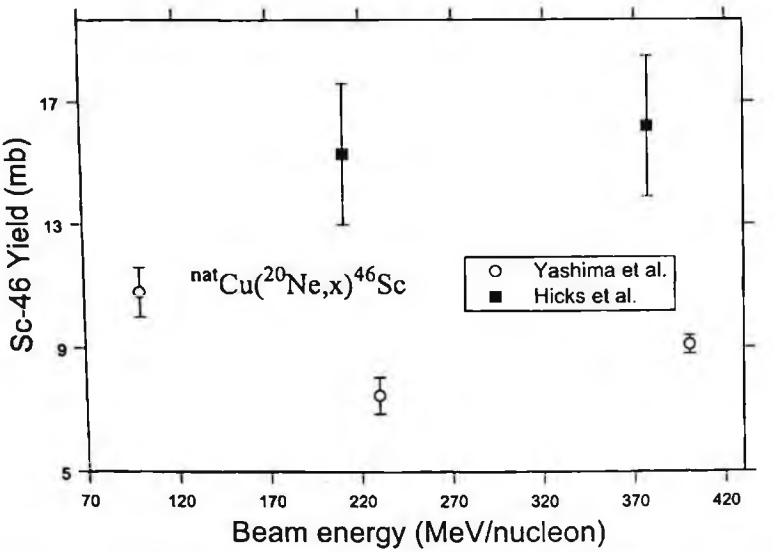

Figure 5.14: Excitation functions for ^{46}Sc isotopes produced by ^{20}Ne interactions in Cu.

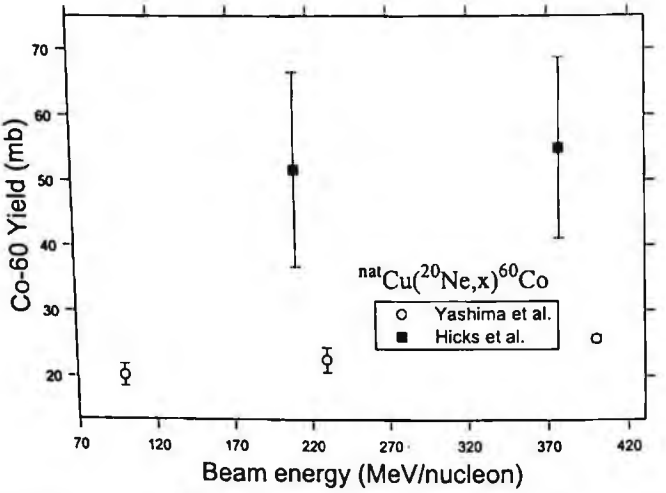

Figure 5.15: Excitation functions for ^{60}Co isotopes produced by ^{20}Ne interactions in Cu.

5.4 Spallation Products Mass Distributions

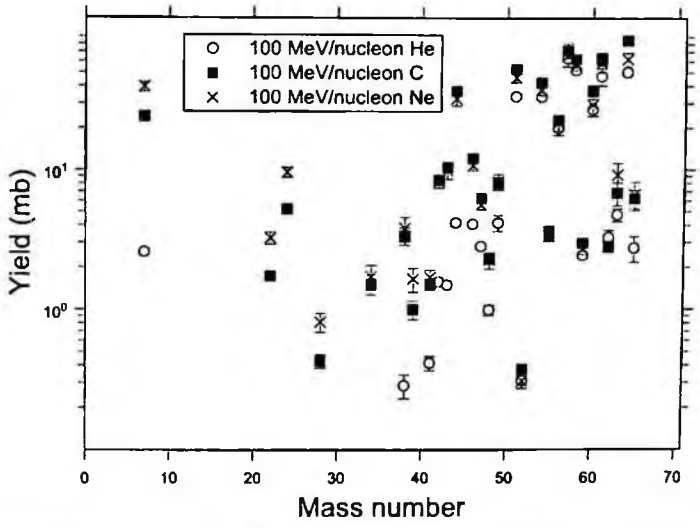

Figure 5.16: Mass yields from the indicated 100 MeV/nucleon systems in Cu.

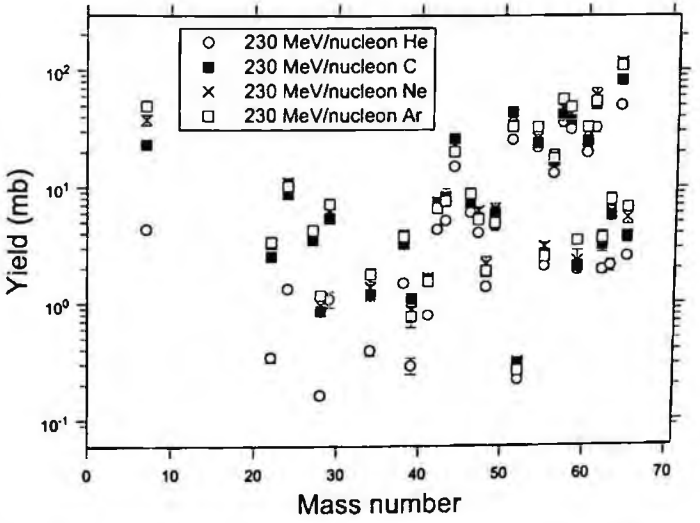

Figure 5.17: Mass yields from the indicated 230 MeV/nucleon systems in Cu.

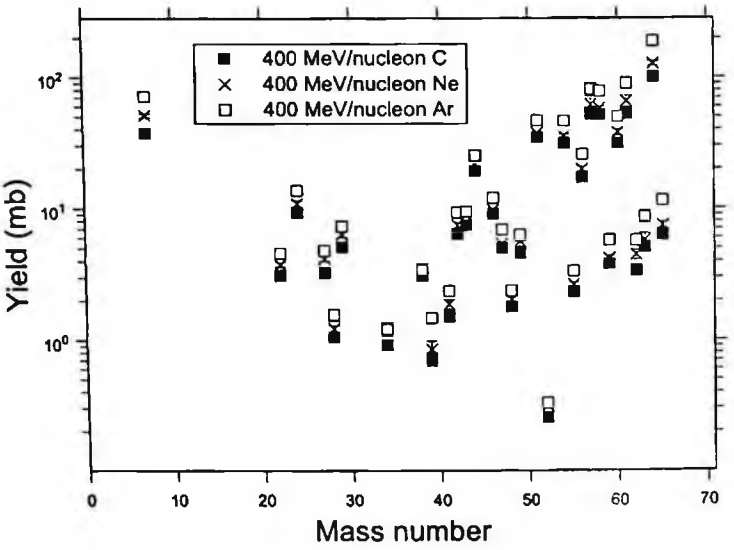

Figure 5.18: Mass yields from the indicated 400 MeV/nucleon systems in Cu.

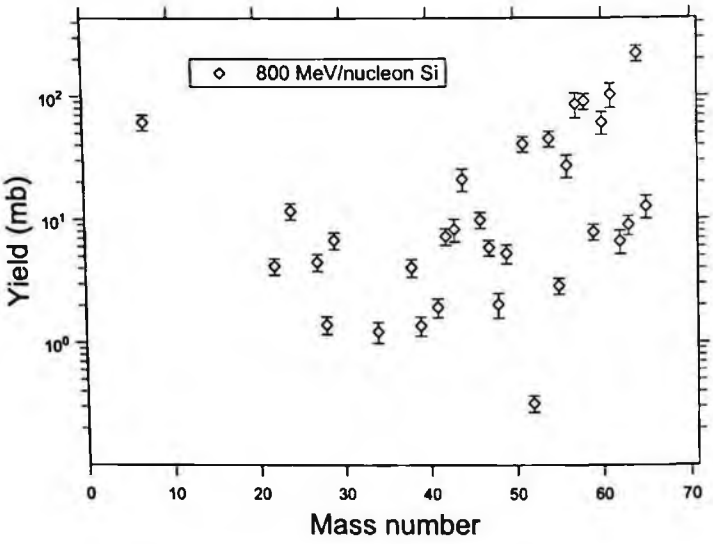

Figure 5.19: Mass yields from 800 MeV/nucleon Si + Cu.

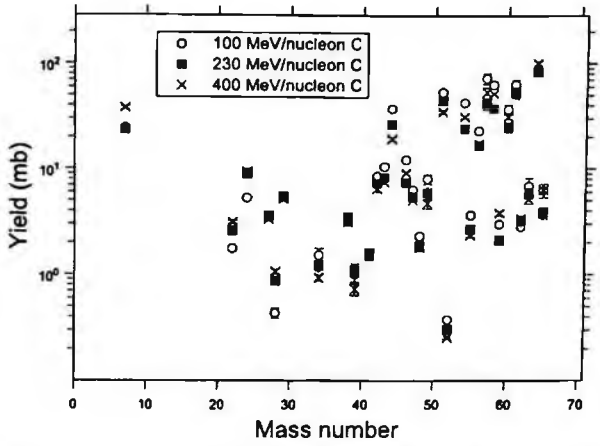

Figure 5.20: The mass-yield distributions (in mb) from the indicated C beams interacting in a Cu target.

5.5 Comparisons between Spallation Products Cross Sections and Calculations

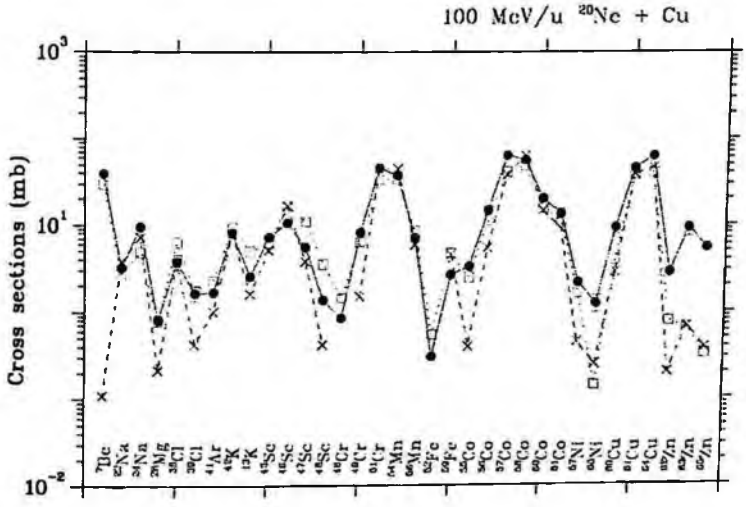

Figure 5.21: Comparisons between 100 MeV/nucleon Ne + Cu spallation products cross sections (filled circles) and QMD+GEM (open squares) calculations and QMD+SDM (crosses) calculations.

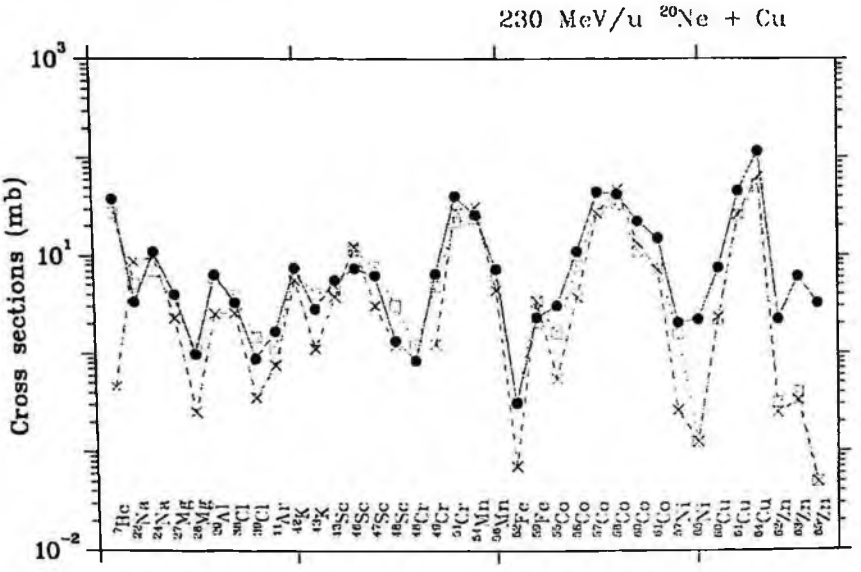

Figure 5.22: Comparisons between 230 MeV/nucleon Ne + Cu spallation products cross sections (filled circles) and QMD+GEM (open squares) calculations and QMD+SDM (crosses) calculations.

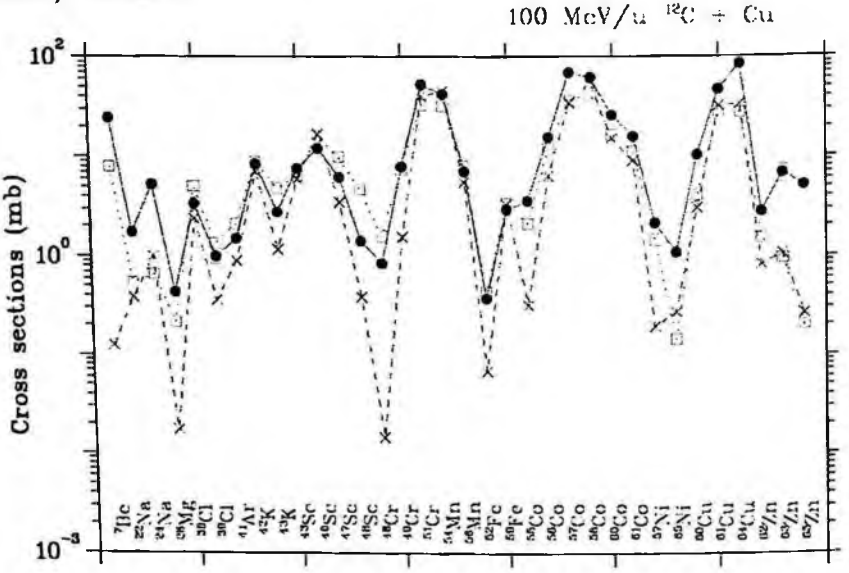

Figure 5.23: Comparisons between 100 MeV/nucleon C + Cu spallation products cross sections (filled circles) and QMD+GEM (open squares) calculations and QMD+SDM (crosses) calculations.

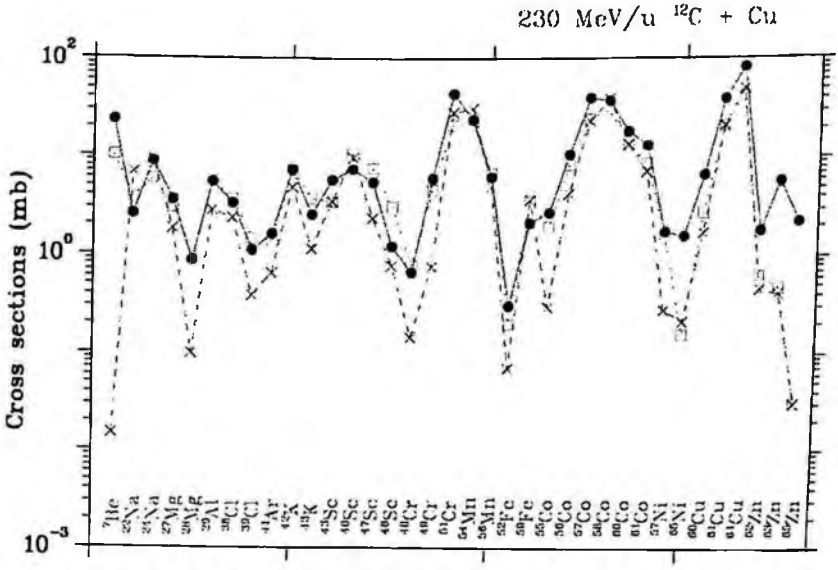

Figure 5.24: Comparisons between 230 MeV/nucleon C + Cu spallation products cross sections (filled circles) and QMD+GEM (open squares) calculations and QMD+SDM (crosses) calculations.

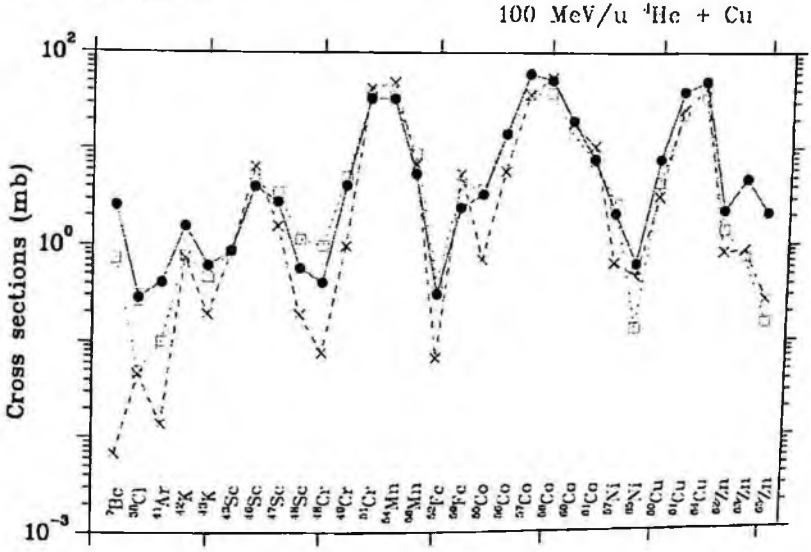

Figure 5.25: Comparisons between 100 MeV/nucleon He + Cu spallation products cross sections (filled circles) and QMD+GEM (open squares) calculations and QMD+SDM (crosses) calculations.

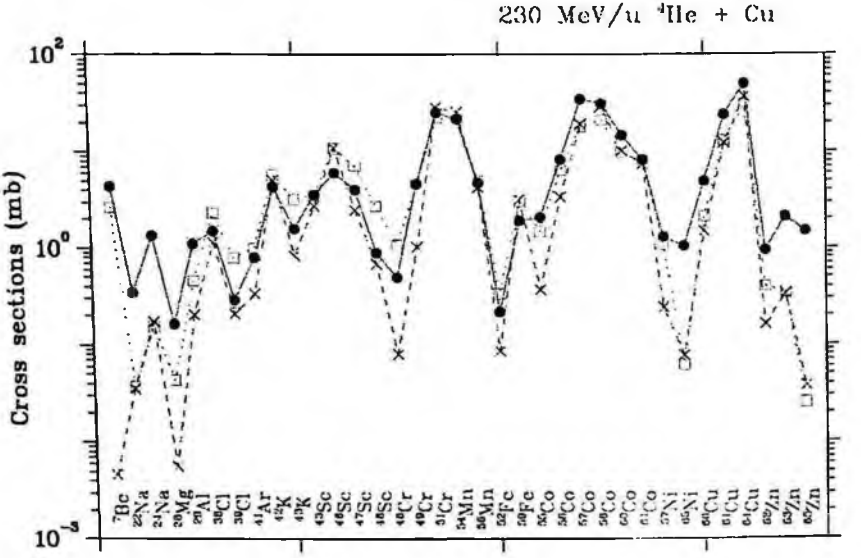

Figure 5.26: Comparisons between 230 MeV/nucleon He + Cu spallation products cross sections (filled circles) and QMD+GEM (open squares) calculations and QMD+SDM (crosses) calculations.

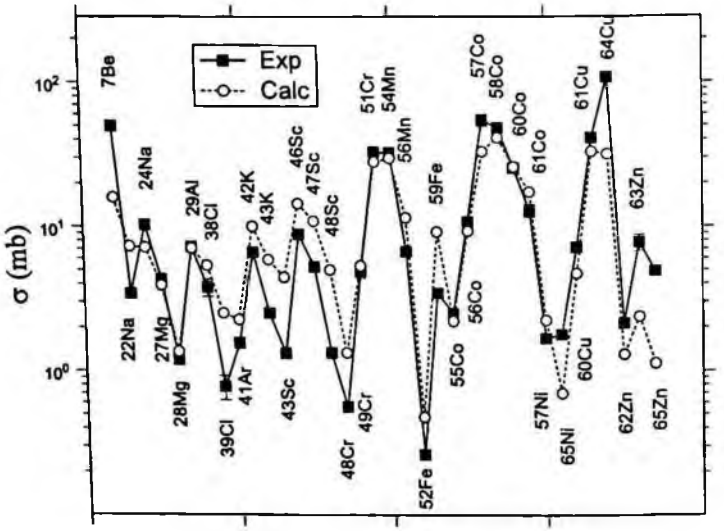

Figure 5.27: Comparisons between 230 MeV/nucleon Ar + Cu spallation products cross sections (filled squares) and PHITS (open circles) calculations.

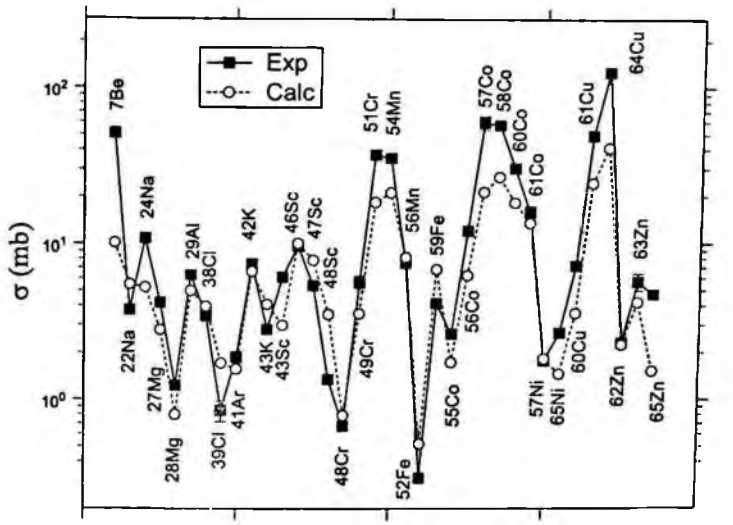

Figure 5.28: Comparisons between 400 MeV/nucleon C + Cu spallation products cross sections (filled squares) and PHITS (open circles) calculations.

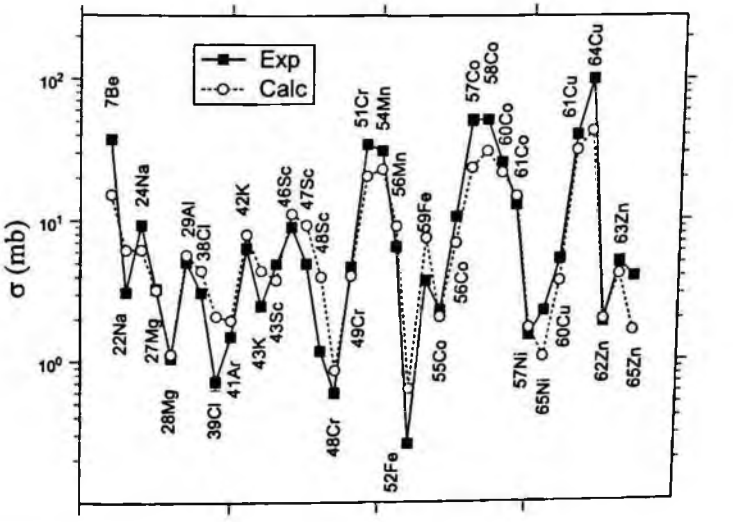

Figure 5.29: Comparisons between 400 MeV/nucleon Ne + Cu spallation products cross sections (filled squares) and PHITS (open circles) calculations.

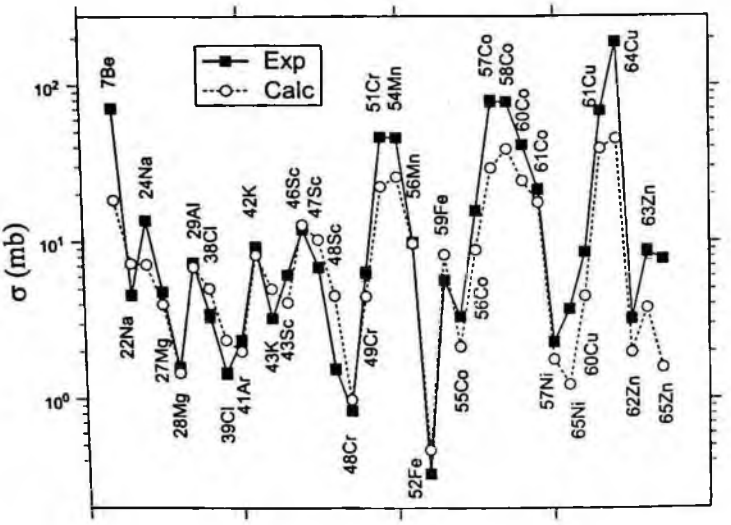

Figure 5.30: Comparisons between 400 MeV/nucleon Ar + Cu spallation products cross sections (filled squares) and PHITS (open circles) calculations.

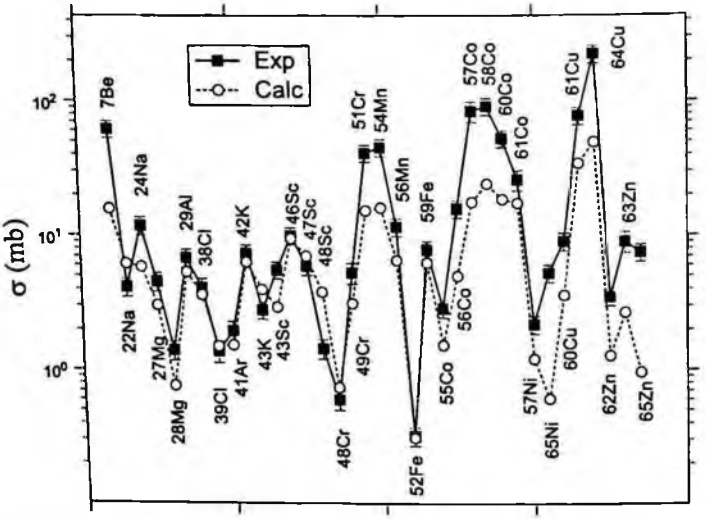

Figure 5.31: Comparisons between 800 MeV/nucleon Si + Cu spallation products cross sections (filled squares) and PHITS (open circles) calculations.

5.6 Spatial Distributions of Residual Activities Induced in the Target by Spallation Products

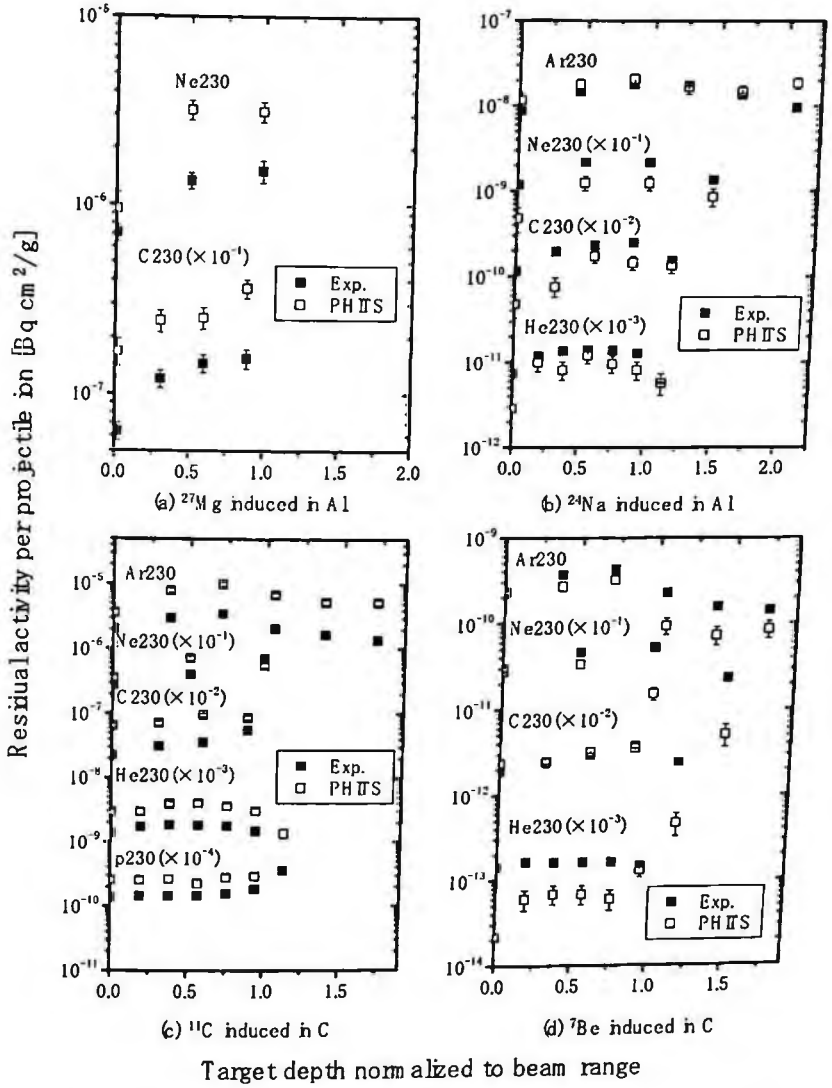

Figure 5.32: The spatial distribution of residual activities in a Cu target, for the indicated beams (energies are MeV/nucleon) and the indicated spallation products [5.7]. The data (filled squares) are compared with PHITS calculations (open squares).

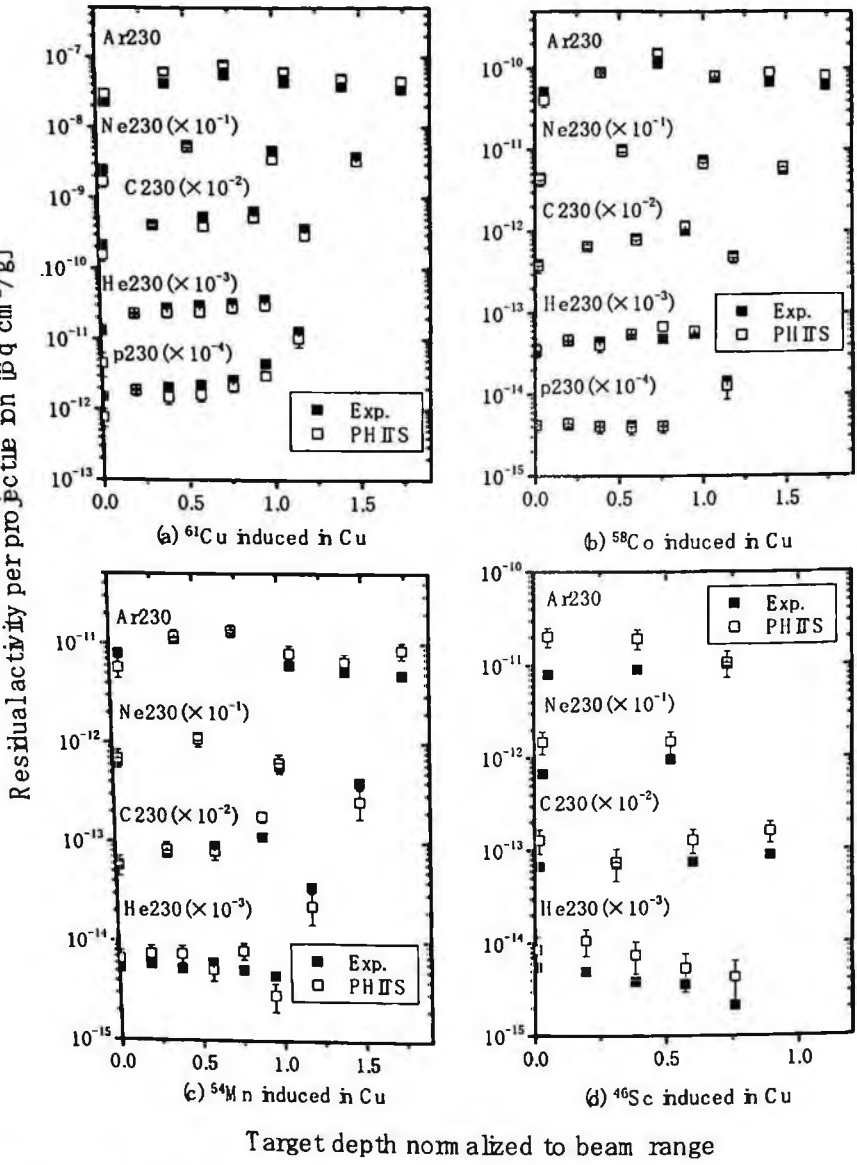

Figure 5.33: The spatial distribution of residual activities in a Cu target, for the indicated beams (energies are MeV/nucleon) and the indicated spallation products [5.7]. The data (filled squares) are compared with PHITS calculations (open squares).

Chapter 6

Moving-Source Parameterizations of Secondary Neutron Production

The moving-source parameterization has been used successfully in reproducing inclusive charged-particle and neutron spectra from heavy-ion interactions [6.1] – [6.9]. The model assumes there are three, thermal moving sources: One projectile-like source moving at a velocity near the incoming beam velocity; a second, target-like source moving very slowly in the laboratory frame, and a third "overlap" source moving ½ to 1/3 of the velocity of the beam. Each source is assumed to thermally emit nucleons with an isotropic distribution in its own rest frame. The spectrum of nucleons in the source's rest frame has the Maxwellian form:

$$\sqrt{E}e^{-E/T}, \tag{6.1}$$

where E is the energy of the nucleon, and T is the temperature of the source. In the laboratory, the complete distribution with respect to energy and angle is given by [6.1]:

$$\frac{d^2\sigma}{dEd\Omega} = \sum_{i=1}^{3} \frac{N_i (E/\pi)^{1/2}}{2\pi T_i^{3/2}} \times \exp\left\{-\left[\frac{E - 2(\varepsilon_i E)^{1.2}\cos\theta + \varepsilon_i}{T_i}\right]\right\}, \tag{6.2}$$

where T is the temperature parameter, N is the normalization parameter, and ε is the source-velocity parameter (actually $v^2/2$). Alternative forms of Eqn. 6.2 exist, although they still assume thermal emission of nucleons. For heavy-ion interactions, many analyses [6.3], [6.9] have modified the projectile-like source to model the knock-on nature of high-energy, forward-focussed nucleon emission.

The utility of the moving-source parameterization is that it provides a simple and fast method to estimate neutron yields. However, no matter what form of the moving-source parameterization is used, it is important to note that the fitted parameters do not constitute a unique solution. As such, caution is warranted if one wishes to extrapolate from a set of fitted parameters to calculate a spectrum from a system that has not been fitted. However, some analyses [6.3], [6.5], [6.9] have studied the systematic trends of the parameters extracted from their fits, and those trends can be used with some confidence to apply the moving-source model to predict unmeasured spectra.

Moving source parameterizations of the thick-target neutron yields (Chapter 2) and secondary-neutron production cross sections (Chapter 2) presented in this handbook are detailed here. The work of Kato *et al.* [6.9] is used for the thick-target yields. The form used by Iwata *et al.* [6.10] is used to describe the secondary-neutron cross sections.

6.1 Moving-Source Parameterization of Thick-Target Neutron Yields

Kato *et al.* [6.9] fit the thick-target neutron yield data of Kurosawa *et al.* (see Chapter 2) with the following moving source parameterization:

$$\frac{d^2Y}{dEd\Omega} = \left\{ \frac{N_0}{\sqrt{2\pi\sigma_c(\theta)^2}} \exp\left(-\frac{(E_n - E_c(\theta))^2}{2\sigma_c(\theta)^2} \right) \right\} + \left\{ \sum_{i=1}^{2} N_i \frac{\sqrt{E_n}}{2(\pi T_i)^{3/2}} \exp\left(-\frac{E_s}{T_i} \right) \right\}, \tag{6.3}$$

where Y is the neutron fluence (neutron MeV^{-1} sr^{-1} ion^{-1}), E_n is the neutron energy in the laboratory reference frame, N is the source normalization parameter (n MeV^{-1} sr^{-1} ion^{-1}), T is the source nuclear-temperature parameter (MeV), θ is the emission angle in the laboratory (degrees), $E_c(\theta)$ is the peak energy fitting parameter (MeV), $\sigma_c(\theta)$ is the width (variance) fitting parameter (MeV), and E_s is the neutron energy is the source's rest frame, given by:

$$E_s = E_n + \varepsilon_i - 2\sqrt{\varepsilon_i E_n}\cos\theta. \tag{6.4}$$

Table 6.1 gives the fitted parameters from all of the systems measured by Kurosawa *et al.*, except for the 800 MeV/nucleon Si data set.

By studying the systematic trends in the fitting parameters, analytical forms of each parameter can be deduced. This provides a simpler, systematic version of Table 6.1, and allows for a reliable means to extend the moving source calculation beyond the systems that were measured. Sections 6.1.1 – 6.1.3 give the analytical forms for each source [6.9]. Figures 6.1 through 6.8 show the fits to selected systems using the values from Table 6.1.

Table 6.1: Fitting parameters from Eqn. 6.3.

Projectile (energy) MeV/nucleon	Target	Equil. N_1	T_1	ε_1	Pre-equil N_2	T_2	ε_2
He (100)	C	0.0529	2.50	0.000259	0.0435	3.05	2.73
	Al	0.134	1.92	0.000580	0.0776	4.25	3.38
	Cu	0.369	1.91	0.000456	0.142	3.54	0.317
	Pb	1.086	1.64	0.000456	0.195	6.28	2.35
He (180)	C	0.263	3.23	0.989	0.148	13.97	1.08
	Al	0.402	3.07	0.231	0.221	14.82	0.406
	Cu	0.545	2.60	0.536	0.296	16.29	2.36
	Pb	1.412	2.41	0.127	0.458	13.75	2.35
C (100)	C	0.0330	1.42	0.0282	0.0619	7.42	0.404
	Al	0.0861	1.73	0.00147	0.0725	7.70	0.176
	Cu	0.162	2.07	0.0738	0.0719	4.85	0.073
	Pb	0.541	1.99	0.00350	0.101	5.18	0.277
C (180)	C	0.224	2.11	0.00661	0.357	10.41	1.96
	Al	0.322	2.22	0.00635	0.452	11.91	6.25

Table 6.1 (continued)

Projectile (energy) MeV/nucleon	Target	Equil. N_1	T_1	ε_1	Pre-equil N_2	T_2	ε_2
C (180)	Cu	0.370	3.36	0.0706	0.385	12.55	6.29
	Pb	0.997	3.33	0.0876	0.626	11.81	5.83
C (400)	C	0.852	1.97	0.0277	1.242	16.20	1.57
	Al	1.487	2.07	0.0175	1.438	14.86	3.01
	Cu	1.799	2.18	0.0121	1.326	14.72	3.64
	Pb	4.909	2.17	0.0287	2.453	11.94	3.79
Ne (100)	C	0.00676	1.16	0.00236	0.0459	5.26	1.85
	Al	0.0256	3.49	0.000353	0.049	3.66	1.57
	Cu	0.045	3.69	0.133	0.104	3.02	0.145
	Pb	0.086	2.00	0.000429	0.320	3.56	0.244
Ne (180)	C	0.123	2.91	0.0635	0.148	13.48	1.28
	Al	0.155	2.58	0.0406	0.202	10.82	0.716
	Cu	0.415	2.54	0.0507	0.287	13.74	1.39
	Pb	1.141	2.50	0.176	0.511	10.71	2.57
Ne (400)	C	0.451	2.36	0.0235	0.874	18.80	1.84
	Al	0.738	3.05	0.135	0.738	14.57	1.35
	Cu	2.217	2.25	0.0273	1.666	16.73	1.94
	Pb	4.496	1.75	0.0485	2.592	11.08	5.21
Ar (400)	C	0.673	3.26	1.764	1.087	21.20	2.65
	Al	0.947	3.09	1.523	1.551	22.51	10.54
	Cu	1.411	3.76	2.899	1.689	21.41	14.29
	Pb	3.173	3.80	2.774	2.883	18.45	14.35
Fe (400)	C	0.424	3.11	0.154	1.104	34.82	2.87
	Al	0.582	3.11	1.135	1.133	36.19	1.89
	Cu	1.12	6.40	0.633	1.244	37.12	1.76
	Pb	2.357	5.79	0.338	1.856	36.91	1.13
Xe (400)	C	0.432	3.74	0.389	1.477	27.68	5.06
	Al	0.633	3.80	0.439	1.503	27.85	9.01
	Cu	1.28	3.50	0.381	2.365	24.27	14.54
	Pb	3.58	3.15	1.141	3.419	18.32	8.64

Projectile (energy) MeV/nucleon	Target	θ (deg)	N_0	E_C (MeV)	σ_C (MeV)
He (100)	C	0	0.605	40.6	59.9
		7.5	0.436	34.9	63.4
		15	0.340	4.3	62.0
		30	0.129	6.8	51.7

Table 6.1 (continued)

Projectile (energy) MeV/nucleon	Target	θ (deg)	N_0	E_C (MeV)	σ_C (MeV)
He (100)	C	60	0.0236	8.9	25.1
		90	0.00862	5.8	17.4
He (100)	Al	0	0.611	39.2	75.0
		7.5	0.395	50.3	61.8
		15	0.305	5.6	80.5
		30	0.100	7.6	56.5
		60	0.0197	7.6	27.6
		90	0.00983	3.3	19.5
He (100)	Cu	0	0.608	8.5	84.0
		7.5	0.375	27.5	69.9
		15	0.260	4.4	76.4
		30	0.124	4.7	52.9
		60	0.0281	2.7	26.8
		90	0.0167	1.7	20.5
He (100)	Pb	0	0.335	22.6	81.5
		7.5	0.189	46.9	63.2
		15	0.143	4.8	81.5
		30	0.0592	17.2	50.6
		60	0.0151	7.0	29.5
		90	0.0113	3.9	22.8
He (180)	C	0	1.80	127.9	72.3
		7.5	1.08	108.9	81.0
		15	0.567	94.3	91.2
		30	0.320	34.5	83.0
		60	0.0813	19.0	58.3
		90	0.0235	8.8	37.3
He (180)	Al	0	1.38	125.1	73.4
		7.5	0.898	105.9	79.4
		15	0.613	53.6	121.5
		30	0.329	10.3	90.7
		60	0.0761	15.6	63.0
		90	0.0174	9.5	37.8
He (180)	Cu	0	0.978	124.6	71.1
		7.5	0.672	108.2	73.3
		15	0.364	78.6	83.2
		30	0.248	15.9	86.5
		60	0.0364	30.1	64.1
		90	0.00884	4.9	46.9
He (180)	Pb	0	0.681	116.0	77.9

Table 6.1 (continued)

Projectile (energy) MeV/nucleon	Target	θ (deg)	N_0	E_C (MeV)	σ_C (MeV)
He (180)	Pb	7.5	0.556	84.2	89.6
		15	0.307	64.9	80.3
		30	0.268	2.7	88.4
		60	0.0307	47.3	49.1
		90	0.00958	9.4	53.4
C (100)	C	0	1.04	42.2	51.2
		7.5	0.621	41.5	49.8
		15	0.534	8.3	60.2
		30	0.139	10.1	54.3
		60	0.0234	9.4	40.2
		90	0.00315	4.0	29.1
C (100)	Al	0	0.751	38.8	53.6
		7.5	0.522	28.0	60.2
		15	0.459	4.2	65.7
		30	0.127	4.3	50.3
		60	0.0232	3.7	37.7
		90	0.00354	1.8	33.7
C (100)	Cu	0	0.773	22.6	59.5
		7.5	0.512	12.2	61.8
		15	0.476	5.5	66.1
		30	0.0894	11.8	48.3
		60	0.0275	5.7	32.2
		90	0.00651	4.8	21.7
C (100)	Pb	0	0.714	8.2	59.5
		7.5	0.442	5.5	61.4
		15	0.381	4.2	60.0
		30	0.105	4.2	44.8
		60	0.0241	9.9	43.3
		90	0.00806	5.7	22.3
C (180)	C	0	3.74	135.9	92.6
		7.5	1.50	95.8	84.1
		15	0.664	84.1	80.5
		30	0.808	10.3	93.8
		60	0.0936	11.7	62.2
		90	0.0168	4.8	53.7
C (180)	Al	0	2.77	136.9	89.8
		7.5	1.02	110.6	69.9
		15	0.442	100.4	77.2
		30	0.556	10.3	90.6
		60	0.0656	11.4	65.9

Table 6.1 (continued)

Projectile (energy) MeV/nucleon	Target	θ (deg)	N_0	E_C (MeV)	σ_C (MeV)
C (180)	Al	90	0.0145	4.8	60.9
C (180)	Cu	0	1.97	169.9	101.8
		7.5	1.00	113.6	78.2
		15	0.440	92.4	88.5
		30	0.288	5.2	124.0
		60	0.0339	26.8	71.0
		90	0.0186	9.5	48.0
C (180)	Pb	0	1.31	155.0	112.1
		7.5	0.669	118.6	76.5
		15	0.285	84.8	91.1
		30	0.160	37.9	111.3
		60	0.0253	56.4	56.8
		90	0.0241	7.9	55.1
C (400)	C	0	23.8	289.0	118.6
		7.5	6.97	313.7	181.6
		15	2.70	245.9	193.0
		30	1.61	80.1	246.6
		60	0.204	20.3	108.6
		90	0.0312	2.8	89.2
C (400)	Al	0	15.6	309.6	145.2
		7.5	5.02	299.8	194.0
		15	1.97	240.1	168.3
		30	1.04	125.7	213.1
		60	0.184	15.6	101.0
		90	0.0487	13.5	72.4
C (400)	Cu	0	11.4	287.5	142.2
		7.5	4.17	271.3	205.2
		15	1.95	173.8	224.2
		30	1.09	63.2	231.3
		60	0.122	26.1	132.8
		90	0.0596	13.5	75.8
C (400)	Pb	0	7.44	280.7	149.0
		7.5	3.39	237.2	221.4
		15	1.53	177.0	198.3
		30	0.801	63.8	217.4
		60	0.0806	77.5	70.3
		90	0.0774	13.5	78.0
Ne (100)	C	0	0.861	88.1	73.2
		7.5	0.538	68.3	45.4

Table 6.1 (continued)

Projectile (energy) MeV/nucleon	Target	θ (deg)	N_0	E_C (MeV)	σ_C (MeV)
Ne (100)	C	15	0.239	42.9	53.1
		30	0.115	5.5	59.4
		60	0.0185	2.7	37.4
		90	0.00764	1.7	27.8
Ne (100)	Al	0	0.632	84.3	70.0
		7.5	0.388	63.4	45.5
		15	0.214	344	55.0
		30	0.0980	15.4	55.2
		60	0.0207	2.7	38.1
		90	0.00900	1.7	24.1
Ne (100)	Cu	0	0.339	45.9	37.6
		7.5	0.315	50.4	51.0
		15	0.163	35.9	48.4
		30	0.108	4.2	53.8
		60	0.0219	2.7	34.4
		90	0.00965	3.2	25.3
Ne (100)	Pb	0	0.289	52.7	43.1
		7.5	0.238	50.7	50.4
		15	0.165	21.3	57.4
		30	0.0938	4.4	54.9
		60	0.0222	2.7	37.8
		90	0.0117	2.0	27.3
Ne (180)	C	0	3.89	134.4	75.0
		7.5	1.48	104.6	82.4
		15	0.907	51.3	96.5
		30	0.570	10.3	94.4
		60	0.0756	11.4	59.0
		90	0.0159	6.2	46.2
Ne (180)	Al	0	4.04	147.6	66.4
		7.5	1.27	107.6	73.7
		15	0.898	24.4	109.7
		30	0.359	21.7	94.0
		60	0.0712	12.2	64.9
		90	0.0211	6.5	56.2
Ne (180)	Cu	0	2.11	121.8	113.1
		7.5	0.910	91.1	85.8
		15	0.546	52.4	99.7
		30	0.269	23.7	91.6
		60	0.0513	16.1	64.9
		90	0.0107	13.1	67.8

Table 6.1 (continued)

Projectile (energy) MeV/nucleon	Target	θ (deg)	N_0	E_C (MeV)	σ_C (MeV)
Ne (180)	Pb	0	1.39	124.5	89.4
		7.5	0.632	100.9	71.6
		15	0.319	85.6	75.9
		30	0.178	28.5	93.5
		60	0.0399	32.4	63.4
		90	0.0210	5.4	62.4
Ne (400)	C	0	57.2	362.6	148.9
		7.5	7.33	258.1	220.0
		15	2.70	64.1	228.1
		30	1.89	64.1	236.0
		60	0.459	17.3	112.2
		90	0.0704	13.5	103.7
Ne (400)	Al	0	9.30	281.0	140.6
		7.5	2.70	149.2	215.5
		15	1.64	43.1	241.5
		30	1.04	37.7	209.8
		60	0.369	14.1	112.4
		90	0.0855	13.5	57.5
Ne (400)	Cu	0	18.8	321.3	156.6
		7.5	5.36	216.8	213.7
		15	2.27	54.4	229.0
		30	1.42	74.9	241.7
		60	0.254	20.5	117.9
		90	0.0737	13.5	108.6
Ne (400)	Pb	0	5.61	267.8	139.4
		7.5	1.68	209.0	169.0
		15	0.824	168.8	179.8
		30	0.446	73.5	214.0
		60	0.169	36.5	151.9
		90	0.0623	13.5	76.5
Ar (400)	C	0	93.5	328.8	130.3
		7.5	33.3	288.1	154.0
		15	17.2	206.2	250.8
		30	3.04	94.2	207.7
		60	1.33	27.0	125.5
		90	0.0580	13.5	85.4
Ar (400)	Al	0	61.9	323.5	129.8
		7.5	17.2	290.4	158.0
		15	13.3	200.3	222.2
		30	1.92	170.6	158.7

Table 6.1 (continued)

Projectile (energy) MeV/nucleon	Target	θ (deg)	N_0	E_C (MeV)	σ_C (MeV)
Ar (400)	Al	60	1.24	28.8	128.5
		90	0.0561	13.5	82.7
Ar (400)	Cu	0	42.8	338.4	147.5
		7.5	16.0	279.9	152.9
		15	11.0	160.9	241.7
		30	1.58	160.4	189.2
		60	1.27	30.1	139.6
		90	0.0616	13.5	81.6
Ar (400)	Pb	0	25.7	325.5	133.5
		7.5	10.3	282.4	150.3
		15	8.33	138.1	257.2
		30	1.05	189.6	181.3
		60	1.29	36.8	154.4
		90	0.0849	13.5	90.5
Fe (400)	C	0	82.0	293.4	110.7
		7.5	23.1	265.3	161.8
		15	5.41	195.4	175.9
		30	1.82	110.4	197.3
		60	0.480	7.4	130.1
		90	0.0126	6.8	28.6
Fe (400)	Al	0	58.2	307.1	135.8
		7.5	17.5	243.4	183.7
		15	4.73	188.6	178.2
		30	1.67	105.5	215.0
		60	0.423	2.7	129.9
		90	0.0101	4.3	23.5
Fe (400)	Cu	0	34.7	305.0	124.7
		7.5	12.3	251.7	165.7
		15	4.40	155.9	221.1
		30	2.14	44.9	200.7
		60	0.341	31.9	137.9
		90	0.0561	15.2	82.7
Fe (400)	Pb	0	21.8	305.6	138.2
		7.5	8.25	224.6	180.7
		15	4.12	93.5	230.6
		30	1.98	55.3	210.6
		60	0.349	29.9	143.8
		90	0.0449	13.5	64.9
Xe (400)	C	0	460	240.5	138.4

Table 6.1 (continued)

Projectile (energy) MeV/nucleon	Target	θ (deg)	N_0	E_C (MeV)	σ_C (MeV)
Xe (400)	C	7.5	108	277.0	114.7
		15	29.1	291.5	288.9
		30	2.82	142.8	222.9
		60	0.774	2.7	196.8
		90	0.0103	2.7	111.7
Xe (400)	Al	0	171	299.0	118.7
		7.5	39.3	272.7	124.5
		15	17.6	283.0	248.2
		30	2.33	162.1	219.8
		60	0.715	2.7	220.1
		90	0.0157	2.8	170.9
Xe (400)	Cu	0	123	315.2	112.4
		7.5	26.4	283.3	128.7
		15	14.7	289.4	294.9
		30	1.78	208.7	210.2
		60	0.576	79.1	234.7
		90	0.0640	13.5	94.3
Xe (400)	Pb	0	86.5	347.0	133.7
		7.5	17.3	287.5	127.8
		15	8.78	285.1	206.4
		30	1.62	217.5	210.2
		60	0.634	75.1	217.7
		90	0.0635	65.4	93.6

6.2 Moving-Source Parameterization of Neutron Production Cross Sections

Iwata *et al.* used a three-source model to fit neutron production cross sections [6.10], and that model is used here. The three sources are: (1) The breakup of the projectile, (2) a thermal source describing the breakup of the decay of the overlap region, and (3) a thermal source describing the decay of the target remnant. The projectile-like source is described by:

$$\frac{d^2\sigma}{p_c^2 dp_c d\Omega_c} = N \exp\left(-\frac{p_c^2}{2\sigma^2}\right), \tag{6.5}$$

where p_c is the momentum of the neutron in the rest frame of the source and σ is a width parameter that is related to the internal momentum of nucleons within the source[6.11]. The double-differential spectra reported here are related to the cross section in Eqn. 6.5 by

$$\frac{d^2\sigma}{dEd\Omega} = pE_c \frac{d^2\sigma}{p_c^2 dp_c d\Omega_c}, \tag{6.6}$$

where E_c is the neutron's kinetic energy in the source's frame, and p is the neutron's momentum in the lab frame. E_c is related to the kinetic energy in the lab frame by

$$E_c = \gamma(E - \beta p \cos\theta), \tag{6.7}$$

where β is the source velocity (v/c), γ is the Lorentz factor, and θ is the lab angle.

The other three sources assume an isotropic decay in their rest frame and are assumed to have the following Maxwellian form (in the rest frame) as:

$$\frac{d^2\sigma}{p_c^2 dp_c d\Omega_c} = \frac{N}{(2\pi T)^{3/2}} \exp\left(-\frac{p_c^2}{2mT}\right). \tag{6.8}$$

In contrast to the fits to the thick-target yields, only 9 parameters are used to fit all the spectra from a specific system. The difference between the model used here and the model used in section 6.1 is the knock-out source used in section 6.1 has fit parameters at each angle, whereas here the projectile-like source has one set of parameters for the spectra at all

angles. Table 6.2 contains the fit parameters from Eqns. 6.5 and 6.8 for the indicated systems.

Table 6.2: Fit parameters from Eqns. 6.5 and 6.8. The first half contains the parameters from the Maxwellian sources (Eqn. 6.8) describing the decay of the target remnant and the decay of the overlap region. The second half of the table contains the parameters from the projectile-like source (Eqn. 6.5). The target labeled "mb" is a Martian regolith composite, and "ISS" is a section of a wall from the International Space Station (see chapter 3 for details).

Projectile (energy) AMeV	Target	Target N_1 (b)	Target T_1 (MeV)	Target β_1	Overlap N_2 (b)	Overlap T_2 (MeV)	Overlap β_2
C (290)	C	0.25	3.61	0.0597	1.54	46.5	0.362
	mb	0.94	7.79	0.0417	2.77	50.1	0.355
	Cu	3.41	3.74	0.156	5.35	47.3	0.292
	Pb	28.47	3.54	0.0025	19.82	42.4	0.225
C (400)	C	0.39	5.02	0.0314	1.41	57.0	0.333
	Cu	4.87	3.64	0.0210	6.04	53.8	0.268
	Pb	36.75	3.60	0.0105	18.25	48.0	0.196
Ne (400)	C	0.65	7.56	0.0426	3.80	63.0	0.427
	ISS	3.26	4.78	0.0094	10.17	78.0	0.339
	Cu	6.08	3.86	0.0222	15.69	62.1	0.328
	Pb	47.45	4.12	0.0106	50.02	55.3	0.269
Ne (600)	C	0.57	9.98	0.0010	3.25	87.9	0.436
	Mb	4.00	49.5	0.162	4.64	74.0	0.625
	Cu	6.54	6.98	0.0313	16.90	82.1	0.378
	Pb	46.83	5.57	0.0237	51.62	74.4	0.303
Ar (400)	C	0.85	4.49	0.0696	7.23	67.3	0.416
	Cu	8.93	6.29	0.0140	29.95	69.0	0.378
	Pb	55.57	7.01	0.0094	78.97	64.8	0.341
Ar (560)	C	1.68	1.49	0.0198	6.36	86.3	0.463
	Cu	9.28	5.56	0.0633	40.70	79.5	0.432
	Pb	57.00	6.87	0.0092	82.62	80.3	0.359

Projectile (energy) AMeV	Target	Projectile N_0 (b)	Projectile σ (MeV/c)	Projectile β_0
C (290)	C	8.38E-08	75.3	0.615
	mb	1.7e-07	63.3	0.598
	Cu	1.88E-07	81.4	0.596
	Pb	7.67E-07	81.3	0.594
C (400)	C	2.07E-08	84.1	0.690
	Cu	4.70E-08	86.1	0.684
	Pb	5.88E-08	112	0.668

Table 6.2 (continued)

Projectile (energy)		Projectile		
AMeV	Target	N_0 (b)	σ (MeV/c)	β_0
Ne (400)	C	1.02E-07	85.0	0.701
	ISS	1.71e-07	85.7	0.673
	Cu	1.49E-07	98.9	0.689
	Pb	4.44E-07	111	0.676
Ne (600)	C	5.35E-08	109	0.796
	mb	1.80e-07	83.4	0.758
	Cu	1.44E-07	114	0.790
	Pb	2.36E-07	131	0.781
Ar (400)	C	1.11E-06	73.7	0.706
	Cu	2.18E-06	76.2	0.702
	Pb	3.82E-06	78.9	0.701
Ar (560)	C	2.23E-07	117	0.784
	Cu	4.30E-07	123	0.785
	Pb	6.59E-07	136	0.775

In the case of the 290 MeV/nucleon C + Marsbar, 400 MeV/nucleon Ne + ISS wall, and 600 MeV/nucleon Ne + Marsbar spectra, it was found that much better fits were obtained when a third Maxwellian source was added. Table 6.3 contains the fit parameters to those systems assuming three Maxwellian sources and a projectile-like source.

Figures 6.9 – 6.11 show the fits to those three systems using the 4-source fit. Figures 6.12 through 6.15 show fits to selected systems using the standard 3-source fit.

Comparing the 3-source fits with the 4-source fits, it appears that the 3-source fits sometimes have difficulties fitting the intermediate to high-energy regions. The problem may be due to the fact that neutrons with those energies (energies from approximately 1/3 of the incoming beam energy per nucleon up 2-3 times the beam energy per nucleon) come from sources with a wide range of initial excitation energy. Representing that wide range of sources with just one Maxwellian (assuming the other Maxwellian source is a target-like source) may not be enough.

Table 6.3: Moving-source model fit parameters for the given systems assuming three Maxwellian sources (Eqn. 6.8) and a projectile source (Eqn 6.5).

		290 C + marsbar	400 Ne + ISS wall	600 Ne + marsbar
Source 1	N (b)	$(2.06 \pm 0.07) \times 10^{-7}$	$(1.78 \pm 0.09) \times 10^{-7}$	$(2.01 \pm 0.08) \times 10^{-7}$
	σ (MeV/c)	52 ± 1	83 ± 2	76 ± 2
	β	0.599 ± 0.001	0.673 ± 0.002	0.759 ± 0.001
Source 2	N (b)	0.55 ± 0.04	8.3 ± 0.4	2.3 ± 0.1
	T (MeV)	15.6 ± 1.0	78 ± 2	45 ± 3
	β	0.584 ± 0.004	0.39 ± 0.01	0.713 ± 0.005
Source 3	N (b)	2.61 ± 0.05	2.9 ± 0.3	6.3 ± 0.2
	T (MeV)	49.3 ± 0.7	24 ± 5	95 ± 2
	β	0.309 ± 0.005	0.04 ± 0.02	0.36 ± 0.01
Source 4	N (b)	0.86 ± 0.04	3.0 ± 0.2	1.61 ± 0.09
	T (MeV)	6.7 ± 0.4	2.4 ± 0.3	5.9 ± 0.5
	β	0.040 ± 0.006	0.014 ± 0.005	0.043 ± 0.005

6.3 Moving-Source Fits to Thick-Target Yields

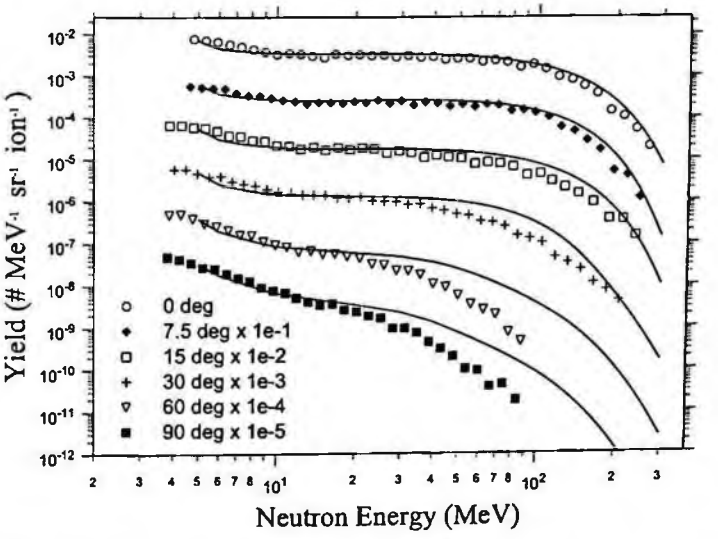

Figure 6.1: Moving source fits (solid lines) to data from 100 MeV/nucleon He stopping in Cu. Note the spectra are offset by the indicated factors of ten.

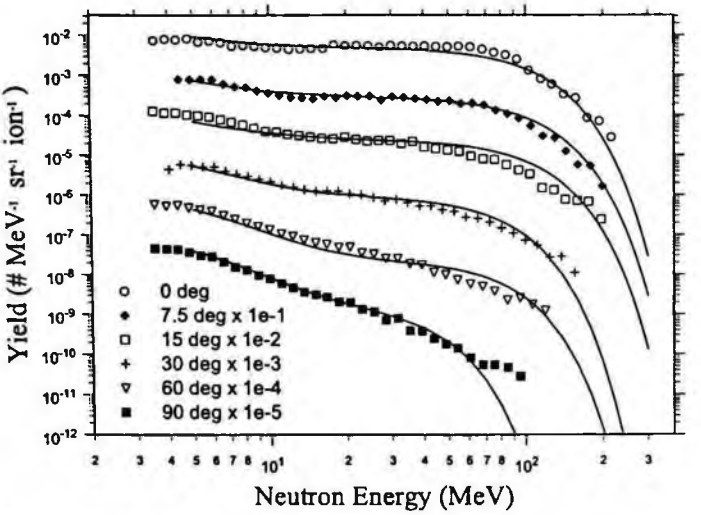

Figure 6.2: Moving source fits (solid lines) to data from 100 MeV/nucleon C stopping in Pb. Note the spectra are offset by the indicated factors of ten.

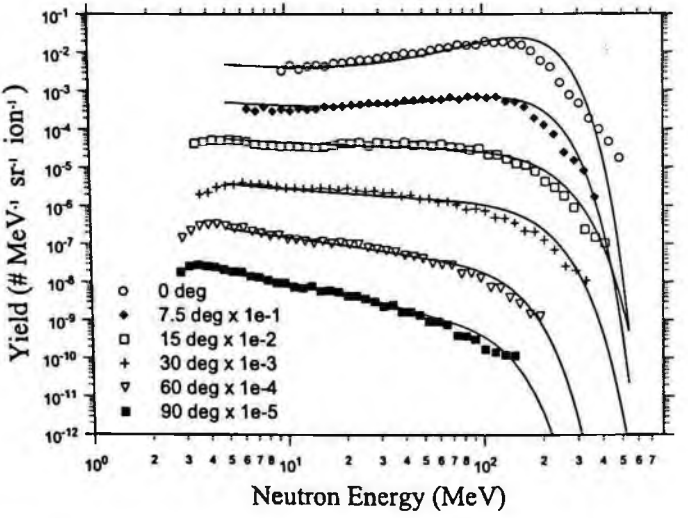

Figure 6.3: Moving source fits (solid lines) to data from 180 MeV/nucleon Ne stopping in Al. Note the spectra are offset by the indicated factors of ten.

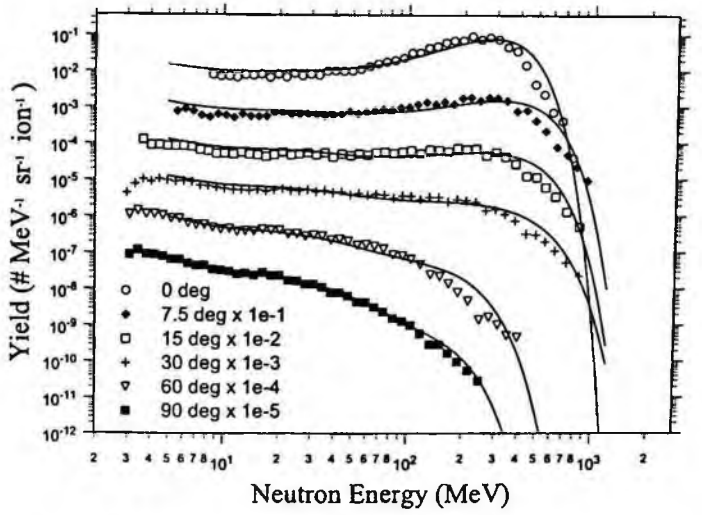

Figure 6.4: Moving source fits (solid lines) to data from 400 MeV/nucleon C stopping in C. Note the spectra are offset by the indicated factors of ten.

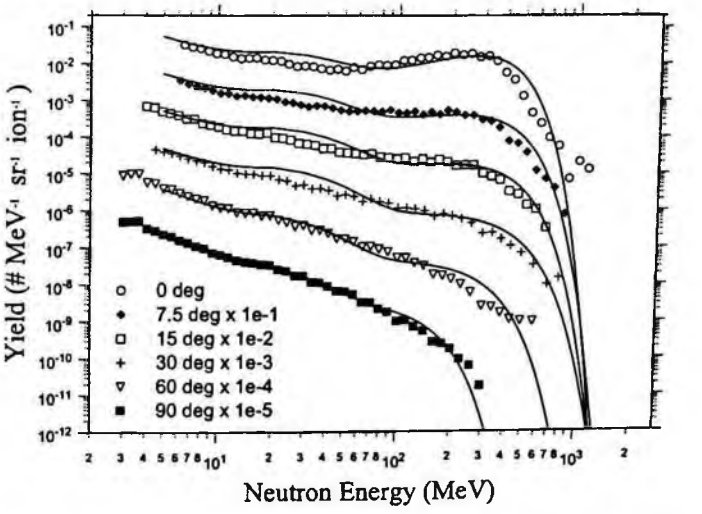

Figure 6.5: Moving source fits (solid lines) to data from 400 MeV/nucleon Ne stopping in Cu. Note the spectra are offset by the indicated factors of ten.

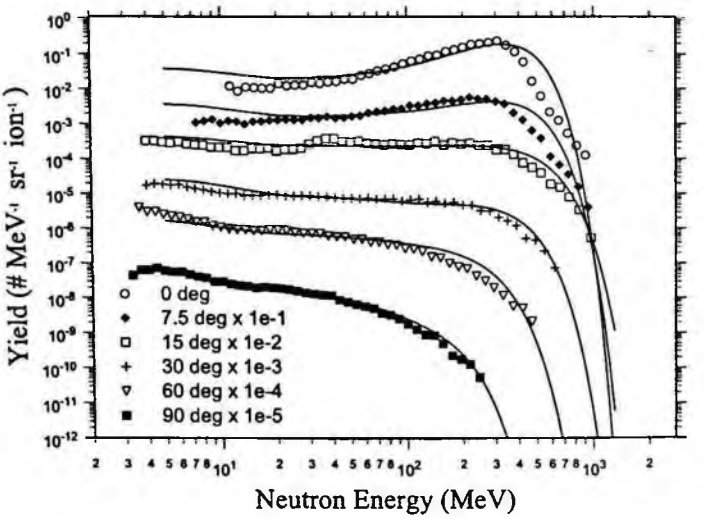

Figure 6.6: Moving source fits (solid lines) to data from 400 MeV/nucleon Ar stopping in Al. Note the spectra are offset by the indicated factors of ten.

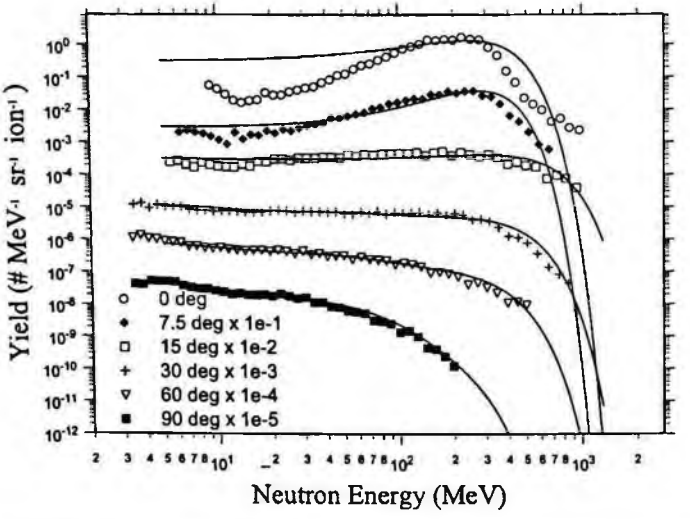

Figure 6.7: Moving source fits (solid lines) to data from 400 MeV/nucleon Xe stopping in C. Note the spectra are offset by the indicated factors of ten.

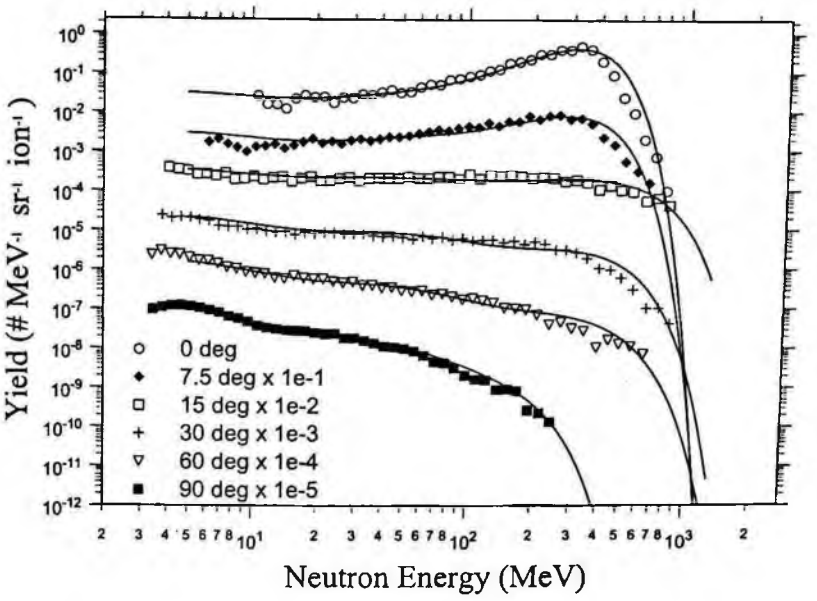

Figure 6.8: Moving source fits (solid lines) to data from 400 MeV/nucleon Xe stopping in Cu. Note the spectra are offset by the indicated factors of ten.

6.4 Moving-Source Fits to Neutron Production Cross Sections

The following plots show moving-source fits to selected neutron production cross section data. The data are fitted using Eqns. 6.5 and 6.8. Table 6.2 lists the fitted parameters for the three-source fits (two Maxwellian sources plus a projectile source), and Table 6.3 list the fitted parameters for the four-source fits (three Maxwellian sources plus a projectile source).

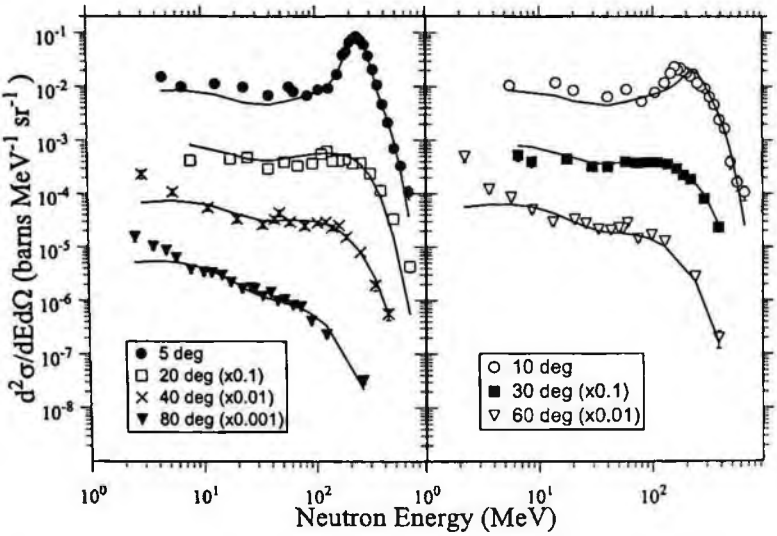

Figure 6.9: Four-source fits (solid lines) to 290 MeV/nucleon C + Marsbar cross-section data. Note the spectra are offset by the indicated factors of ten.

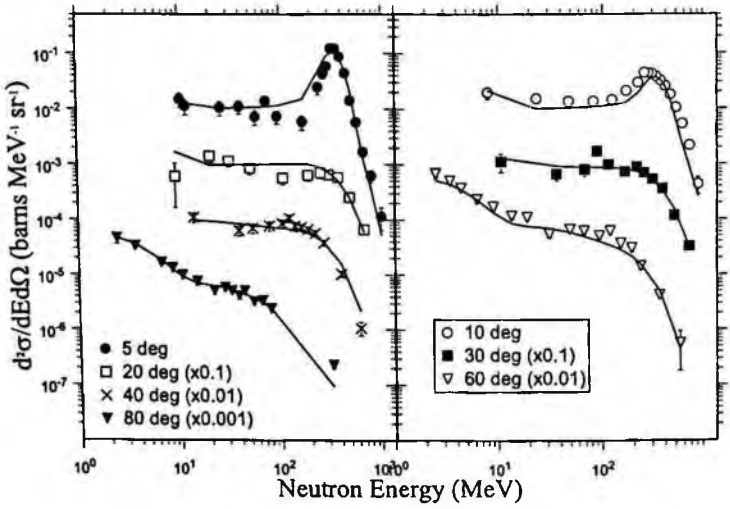

Figure 6.10: Four-source fits (solid lines) to 400 MeV/nucleon Ne + ISS wall cross-section data. Note the spectra are offset by the indicated factors of ten.

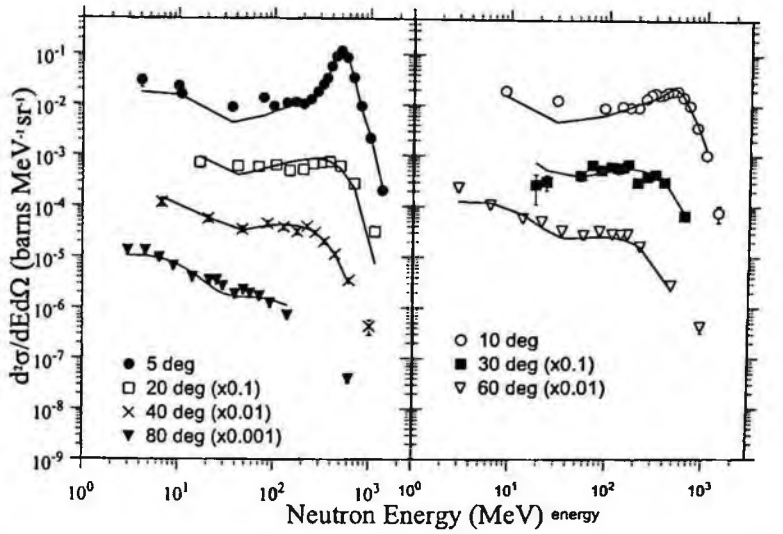

Figure 6.11: Four-source fits (solid lines) to 600 MeV/nucleon Ne + Marsbar cross-section data. Note the spectra are offset by the indicated factors of ten.

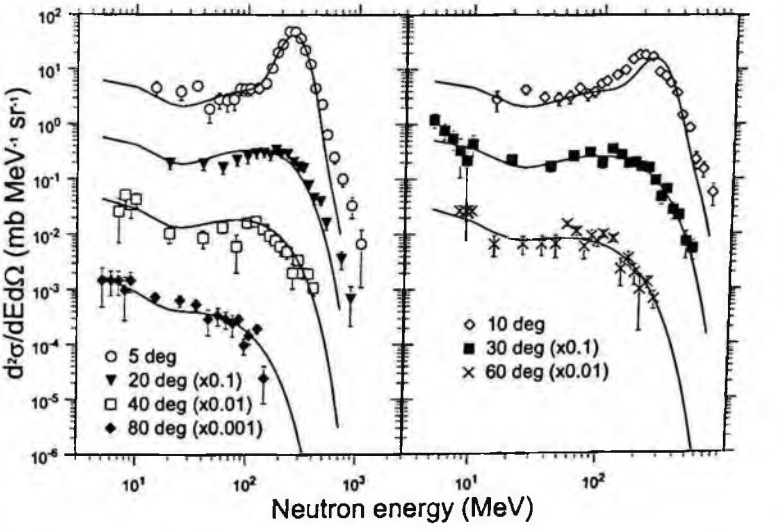

Figure 6.12: Three-source fits (solid lines) to 290 MeV/nucleon C + C cross-section data. Note the spectra are offset by the indicated factors of ten.

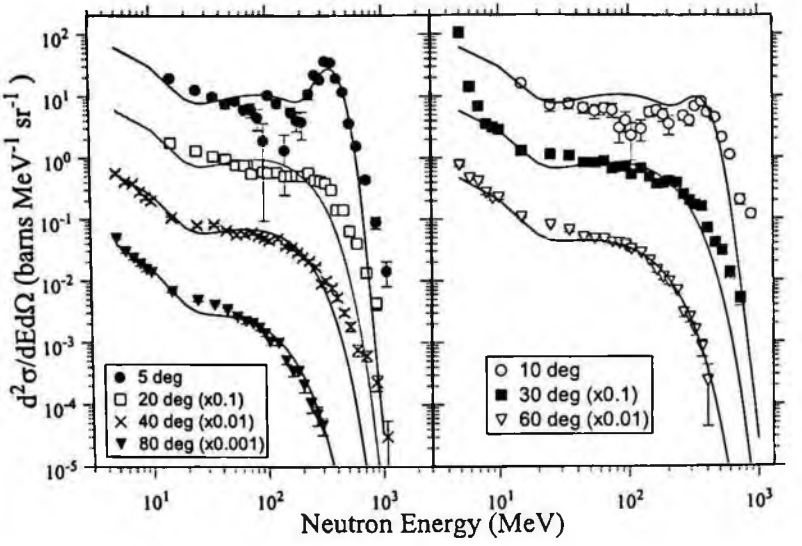

Figure 6.13: Three-source fits (solid lines) to 400 MeV/nucleon C + Cu cross-section data. Note the spectra are offset by the indicated factors of ten.

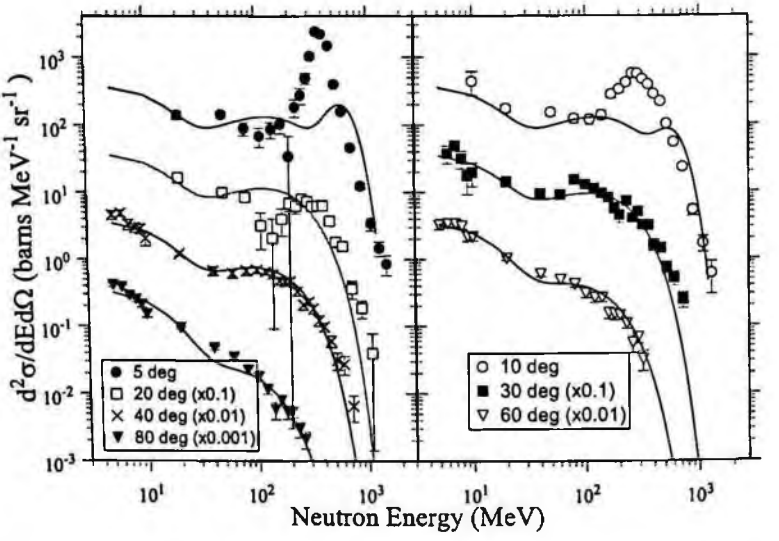

Figure 6.14: Three-source fits (solid lines) to 400 MeV/nucleon Ar + Pb cross-section data. Note the spectra are offset by the indicated factors of ten.

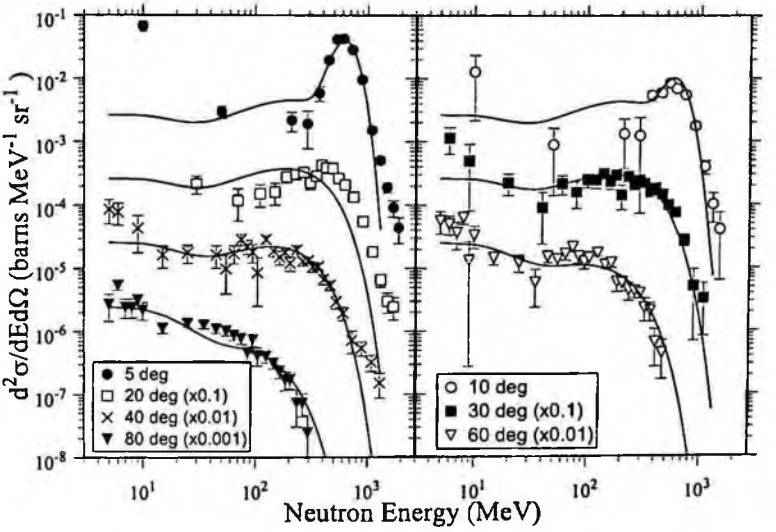

Figure 6.15: Three-source fits (solid lines) to 600 MeV/nucleon Ne + C cross-section data. Note the spectra are offset by the indicated factors of ten.

Chapter 7

Conclusion

The data described in this handbook comes from the efforts of high-energy, heavy-ion physicists over the last 25 years. The experiments described in this text come from facilities all over the world, including Japan, the U.S. and Europe. Many of the experiments were originally performed in the interest of advancing the general knowledge of the field of heavy-ion physics. However, today these data are also of particular interest to several applied fields that have also grown over the last 25 years, such as accelerator-based cancer radiotherapy, radioactive beam facilities, and shielding in space related activities. It was the goal of the editors to provide researchers in those applied fields with a single-source reference of data that was directly applicable to their research programs, as well as provide many details in regards to the experimental setup and data analysis for all of the experiments contained herein. It is our hope that you will the data and details in this handbook useful.

Professor Takashi Nakamura, Ph.D.
Lawrence Heilbronn, Ph.D.

February, 2005.

Appendix A

Application of Data to Benchmark Transport Model Calculations

During the time of the writing of this handbook (2002-2004), many particle transport models, such as SHIELD-HIT, FLUKA, HETC-HEDS, GEANT4, MARS15, and PHITS, were incorporating heavy-ion interactions into their codes. The purpose of this appendix is to illustrate the utility of the data contained within the handbook in regards to serving as benchmarks for transport code development. Information in regards to experimental details and details of the data analysis must be considered when attempting to reproducing the data with calculations, and many of the critical details have been provided with this handbook. If any detail is missing, the user will need to consult the references provided at the end of each chapter.

The heavy-ion transport code used for illustrative purposes in this section is PHITS (Particle and Heavy Ion Transport code System) [A.1]. It is based on the NMTC/JAM code [A.2]. NMTC/JAM is a nucleon and meson transport code that uses the high-energy nucleon-nucleus reaction code JAM [A.3] for the intranuclear cascade calculation and GEM [A.4] for the evaporation and fission processes. To extend the capabilities of NMTC/JAM to include heavy-ion transport, PHITS uses Shen's formula [A.5] to calculate the heavy-ion total-reaction cross section, the SPAR code [A.6] to calculate the stopping powers and ranges, and JQMD [A.7] to simulate heavy-ion nuclear interactions. JQMD is based on the QMD model in which nuclei are described as a self-binding system of nucleons that are interacting with each other within the framework of molecular dynamics. Both the CG geometry system (typically used in HETC,

LAHET and NMTC calculations) and the GG geometry system (used in MCNP calculations) are available for use in PHITS.

The experimental data used for comparison with PHITS calculations are the neutron double-differential cross sections taken by Iwata *et al* [A.8] (see chapter 2). Figure A.1 shows the experimental setup used for those measurements.

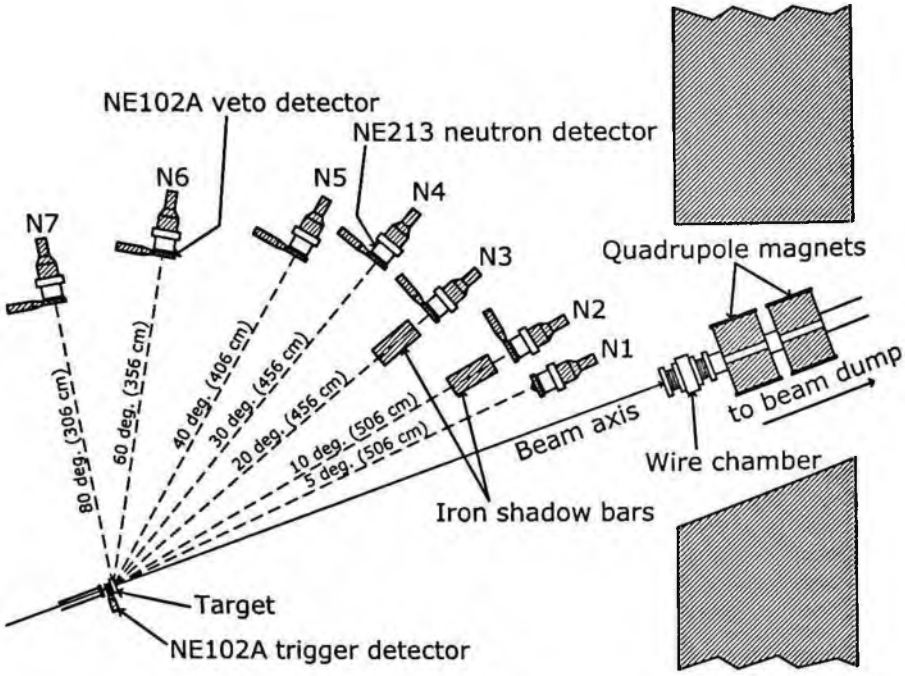

Figure A.1: Schematic drawing of the experimental setup of the neutron double differential cross section measurement (courtesy of Ref. A.8).

Neutrons were measured by NE213 liquid scintillators illustrated by white cylinders in Fig. A.1. Seven NE213 detectors, N1-N7, were arranged at laboratory angles 5, 10, 20, 30, 40, 60, and 80 degrees with respect to the beam direction. A 5 mm thick NE102A plastic scintillator (VETO), which covers whole surface of the NE213 scintillator, was placed in front of each NE213 for the purpose of detecting and discriminating charged particles events. A 0.5 mm thick NE102A

plastic scintillator (trigger detector) was located behind the beam exit for a beam monitoring and for an event trigger of data acquisition system. Various thick targets were placed behind the trigger detector. These targets had depths of several mm to a few cm thick, depending on the projectile species and energy used in the measurement.

The transport calculation is executed using a geometry that is identical with the experimental setup. For example, one can arrange the beam exit, the trigger detector, the target, the VETO detectors, and the NE213 detectors in three dimensions with the same sizes and distances, and one can simulate reactions and the transport of primary beams and secondary particles in that geometry. The published experimental cross sections had the scattered, background neutrons subtracted from the data, so it is not required to include the floor, roof and walls in the calculation. The next step is to calculate how many neutrons of various energies come into the detection regions. The calculation results can be then converted into double-differential cross sections in units of barns (b) by

$$\frac{d^2\sigma}{dEd\Omega} = \frac{a}{nt}\cdot\frac{1}{\Delta E\cdot\Delta\Omega}\cdot\phi(E,\theta)\cdot S = \frac{a}{nt}\cdot\frac{1}{\Delta E}\cdot\frac{r^2}{S}\cdot S\cdot\phi(E,\theta) = \frac{a}{nt}\cdot\frac{r^2}{\Delta E}\cdot\phi(E,\theta) \qquad \text{(A.1)}$$

where r is a distance from the target to the detector face (cm), S is the area of detector face (cm^2), a is the conversion factor from cm^2 to barn $1x10^{24}$ (cm^{-2}·b), n is a particle density (number of atoms per unit volume) of the target (cm^{-3}), t is the target thickness (cm), ΔE is an width of each energy bin of the flux (MeV), and $\Phi(E, \theta)$ is the calculated neutron flux per projectile (cm^{-2}).

The method mentioned above simulates the primary particle transport, reactions, secondary particle production and their transport, and so on, with the same geometrical arrangements. Obtained results are easy to process, as it requires no special normalization factor after the calculation. For example, one can compare the results obtained in detectors N1 and N7 directly without any additional factoring. However, it is hard to obtain good statistics with this method because of the small detection area utilized for particle counting. The next method can be used, instead.

A large ring-type detector on a spherical surface can be used, which has an equivalent angle with the experimental one. An example of a set of the ring detector is shown in Fig. A.2.

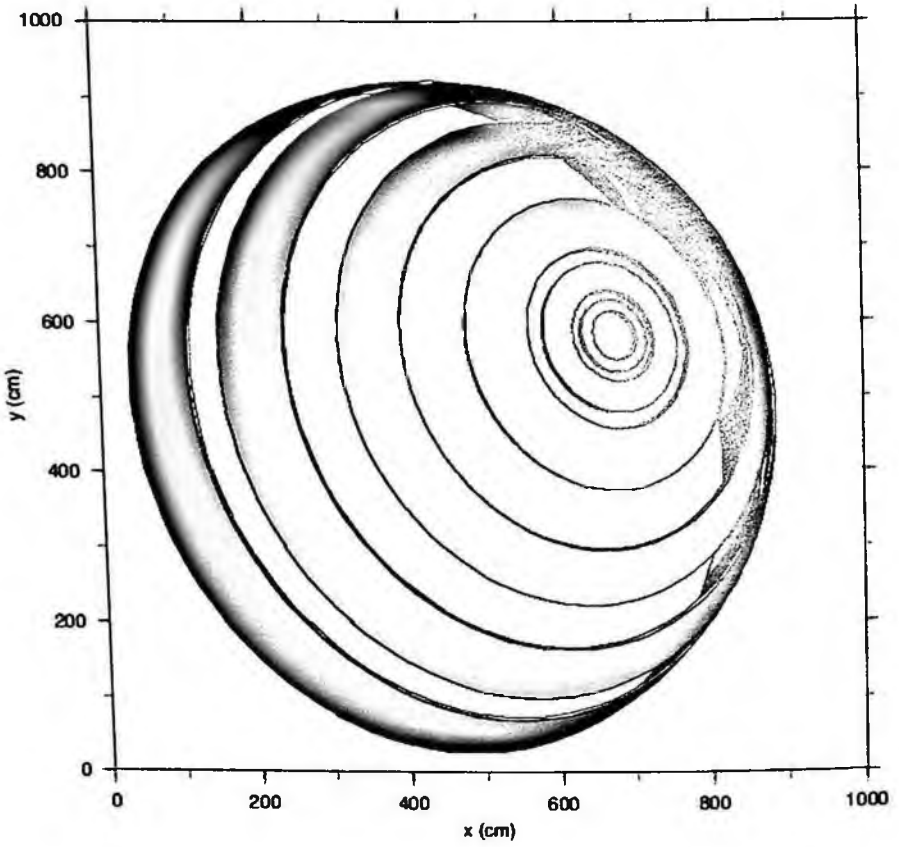

Figure A.2: A set of ring detectors.

The rings have a certain width that is formed by the detection angle $\theta \pm \Delta\theta$, with both angles $\theta_1=\theta+\Delta\theta$ and $\theta_2=\theta-\Delta\theta$ making a solid angle $\Delta\Omega$ that is given by

$$\Delta\Omega = 2\pi \cdot \left(\cos\theta_2 - \cos\theta_1\right). \tag{A.2}$$

Figure A.3 illustrates the definition of θ and Δθ. The Δθ should not be given an extremely large value compared with the experimental one, especially at forward angles in which there is a strong angular dependence for particle emission. Particularly for heavier fragments, such as alpha particles, the same Δθ should be set with the experimental value near 0 degrees, even though Δθ becomes quite small. The surface-crossing tally is used on the ring detector in the calculation. The distance from the target to the ring detector can be applied to any values as it is not related to Δθ geometrically, but in the calculation the distance was set as same as experimental ones as shown in Table A.1 for each detector in order to consider reactions of charged particles with air, especially for primary beams.

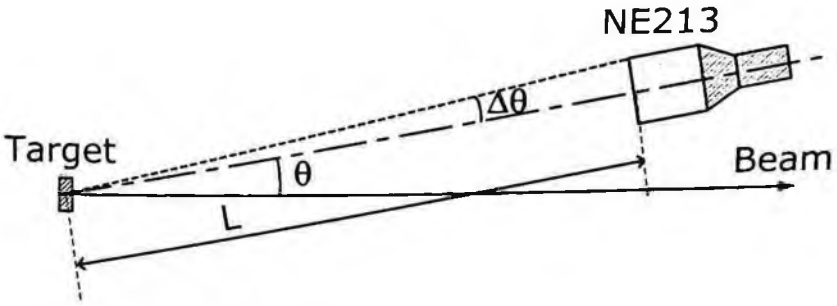

Figure A.3: Schematic view of Δθ in the experiment.

The results can be converted to neutron double-differential cross-sections with Eqn. A.1, or with

$$\frac{d^2\sigma}{dEd\Omega} = \frac{a}{nt}\cdot\frac{1}{\Delta E\cdot\Delta\Omega}\cdot y(E,\theta) = \frac{a}{nt}\cdot\frac{1}{\Delta E}\cdot\frac{1}{2\pi\left(\cos\theta_2-\cos\theta_1\right)}\cdot y(E,\theta) \quad \text{(A.3)}$$

where $y(E, \theta)$ is a number of neutrons passing through each ring detector. Equations A.1 and A.3 are in principle same formulas, but Eqn. A.3 might provide a simple handling in treating calculation results, as we don't need to consider the area of surface of the ring detectors for Eqn. A.3.

The target is set to the same size in three dimensions as the experimental one so as to treat interactions of all primaries and secondaries in the target, including the beam-loss and energy-loss of the projectiles.

Table A.1 shows the $\Delta\theta_{exp}$, which is made by "target-center to NE213-center" and "target-center to NE213-edge" (see Fig. A.3) in the experiment, and the $\Delta\theta_{calc}$ defined for the calculation.

Table A.1: Experimental parameters used for the calculation.

Detectors	Angle	L (cm)	$\Delta\theta_{exp}$(deg)	$\Delta\theta_{calc}$(deg)
N1	5	506	0.72	1.0
N2	10	506	0.72	2.5
N3	20	456	0.80	5.0
N4	30	456	0.80	5.0
N5	40	406	0.90	5.0
N6	60	356	1.0	6.0
N7	80	306	1.2	7.5

Calculation geometry, i.e. the target and regions for neutron counting, can be represented by both GG [A.9] and CG geometry system in PHITS. Here GG was applied. In the GG system, the unit of configurations called "surface", which contains different shapes such as flat planes (P, PX, PY, PZ), rectangular parallelepiped (BOX, RPP), spheres (SO, S, SX, SY, SZ, SPH), cylinders (C/X, C/Y, C/Z, CX, CY, CZ, RCC), cylindrical cones (K/X, K/Y, K/Z, KX, KY, KZ), ellipses (SQ), and so on, are given. These combinations build up an actual geometry; for example, a tube can be created by a combination of two cylinder surfaces, which have different diameters. The region, which is defined by the combination of some surfaces, is called "cell" in the GG system, and each cell can contain any materials like aluminum, lead, H_2O, and so on, which are defined in the [material] section in the input.

In this calculation, a rectangular parallelepiped (RPP) surface was used to represent the target. Two different radius spheres (SPH) and two different circular cones (KZ) were combined to make each neutron counting cell. For example, the neutron counting cell for 5 degrees (region 11), which corresponds to the first NE213 called N1, can be made by the combination of {outside of the surface-32 (sphere) AND inside of the surface-31 (sphere)} AND {outside of the surface-11 (cone) AND inside of the surface-12 (cone)}. The "surface" and the "cell" are defined by [surface] and [cell] sections, respectively, in the input. Figure A.4 shows a schematic view of the calculation geometry. In the figure, the arranged surfaces are indicated with numbering, and the cell numbers are also identified within white circles. In the calculation, the surface-crossing tally is used for neutron counting. Neutrons, which pass through the face made by the cell 10 and 11, are scored as $y(E, 5°)$ in Eqn. A.3. This is defined in the [t-cross] section for each detection angle in the input.

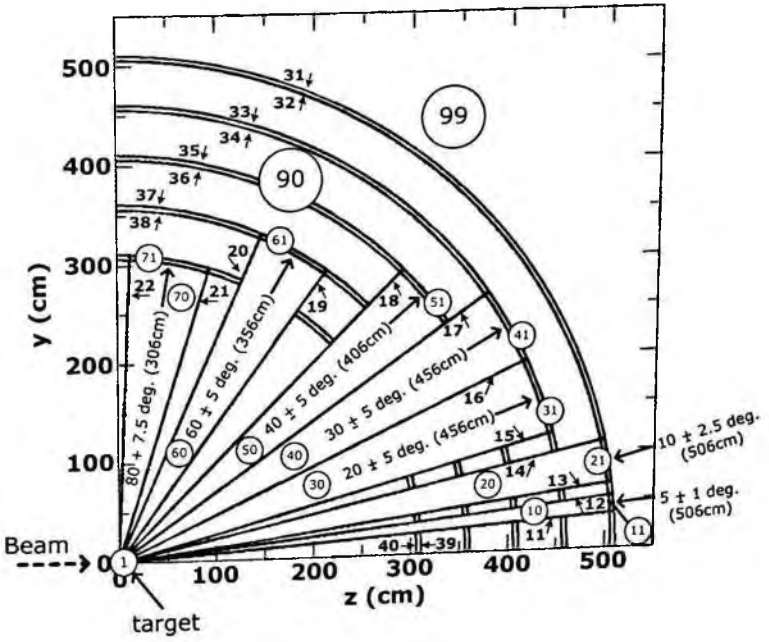

Figure A.4: Calculation geometry.

Table A.2 shows the input for this calculation in the PHITS code. Main control, number of histories, energy cutoff, library settings, and other general parameters are defined in the [parameters] section. In the [source] section, one can define a variety of source types. If the properties of beams in an experiment are known, one can define a source that has beam distributions given with a Gaussian function. The number of materials, composition, particle densities (or mass densities), and cross-section data are defined in the [material] section. The surface and cell are defined in the [surface] and [cell] section respectively. The [mat name color] is just for setting colors of materials for graphical plots.

One can set user-variables like "set: c1[value]". In the input, a solid angle for each detection face, and a factor for converting the results to the cross sections (b) that correspond the first and the third terms in Eqn. A.3, are defined and combined as a factor for each detector. In addition, a factor 1000 to convert from (b) to (mb) is set. The final factor will be called in the [t-cross] section.

The [t-cross] is the surface-crossing tally. Seven surface-crossing tallies are used for seven detection faces. In order to use Eqn. A.3, the area of the detecting face is set to 1. The number of neutrons in an energy bin is divided by the bin width in the code when using the option "output=2". The solid angle and the factor for the cross section converting, which are already prepared by the user variables, are multiplied to the results by using the option "factor = ". Then, the double-differential cross sections, with units of (mb MeV^{-1}, sr^{-1}) for each detection face, will be outputted. Figure A.5 shows the calculated results compared with the experimental data.

The [t-track] is not an essential definition in the calculation, but it is used here to obtain spatial distributions of secondary particles.

The [t-gshow] and [t-3dshow] are for two- and three- dimensional geometry plots respectively.

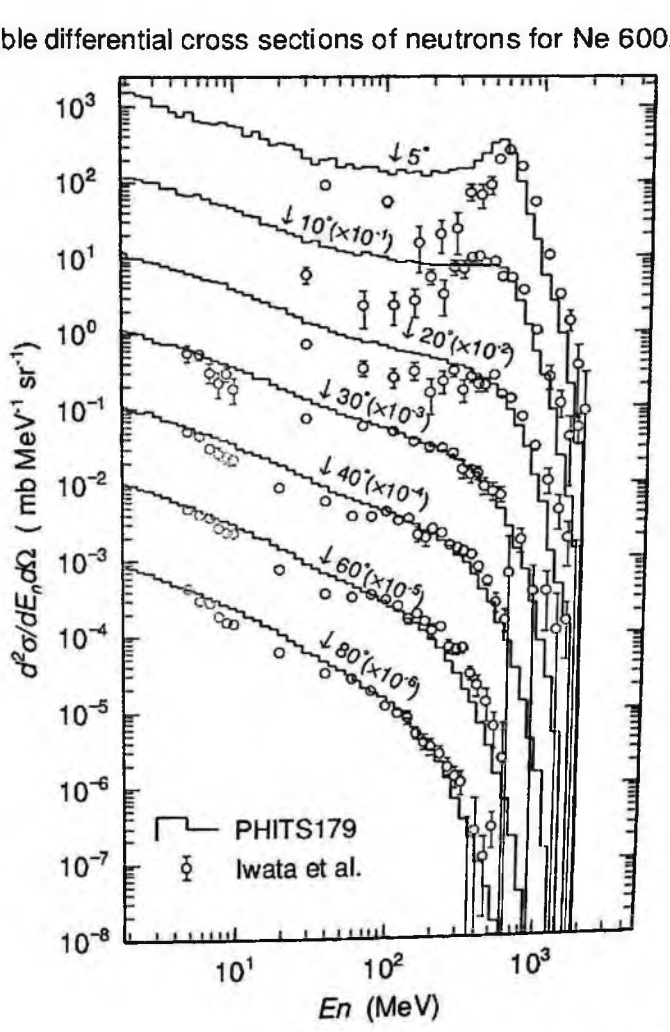

Figure A.5: Comparison of neutron double differential cross section for 600 MeV/u Ne on Pb target between the data taken by Iwata *et al.* [A.8] and the result calculated in this appendix by PHITS.

Table A.2: Input data for PHITS for double differential cross calculation.

```
[ Title ]
Neutron double differential cross section calculation.
600 MeV/nucleon Ne ion on 0.4 cm (4.54 g/cm2) thick Pb target.

[ Parameters ]
  icntl = 0       $ Main control parameter.
                  $ 0:normal, 7: 2D-geometry plot, 11: 3D-geometry plot.
                  $ It requires [t-gshow] section for icntl=7, and
                  $          [t-3dshow] section for icntl=11
                                $
 maxcas = 1000    $ Number of calculation in each batch
 maxbch = 5000    $ Number of batch
 emin(1) = 1.e-2  $ Energy cutoff for proton (MeV)      (D=1.0)
 emin(2) = 1.e-2  $              neutron (MeV)      (D=1.0)
emin(12) = 1.0    $              electron (MeV)     (D=1.d9)
emin(13) = 1.0    $              positron (MeV)     (D=1.d9)
emin(14) = 1.0    $               photon (MeV)      (D=1.d9)
emin(15) = 1.0    $              deuteron (MeV/u)   (D=1.d9)
emin(16) = 1.0    $               triton (MeV/u)    (D=1.d9)
emin(17) = 1.0    $                 3He (MeV/u)     (D=1.d9)
emin(18) = 1.0    $                Alpha (MeV/u)    (D=1.d9)
emin(19) = 1.0    $            Heavy Ion (MeV/u)    (D=1.d9)
 dmax(1) = 150.   $ Maximum E (MeV) of cross section use for p (D=emin(1))
 dmax(2) = 150.   $ Maximum E (MeV) of cross section use for n (D=emin(2))
  itall = 1.      $ Output results after each batch
 file(7) = xsdir  $ Cross section data file name
 file(6) = phits.out $ General output file name
  itstep = 1      $ 1: Tally output after each batch
   icrhi = 1      $ Total reac. XS for HI; 0: Shen, 1: Tripathi
  nspred = 1      $ Coulomb diffusion on

[ Source ]
s-type = 1        $ Source type. 1: cylinder source
  proj = 20Ne     $ Projectile
    e0 = 600.     $ Energy (MeV/u)
    r0 =  0.5     $ Radius of the cylinder (cm)
    z0 = -5.0     $ Position z of one cylinder surface (cm)
    z1 = -5.0     $ Position z of anohter cylinder surface (cm)
   dir =  1.0     $ Direction of the beam (cos(theta_z))

[ Material ]
mat[1]            $ Lead target, density = 11.342 (g/cm3)
207Pb.24c  3.2965E-2
```

```
mat[2]          $ Air, density = 0.00125 (g/cm3)
14N.24c  4.680E-05
16O.24c  7.943E-06

mat[3]          $ This is a dummy material for detector regions
14N.24c  4.680E-05
16O.24c  7.943E-06

[ Surface ]
1  rpp  -5.0 5.0   -5.0 5.0    -0.2 0.2   $ target

31  sph  0.0 0.0 0.0   506.0+5.0       $ spheres
32  sph  0.0 0.0 0.0   506.0
33  sph  0.0 0.0 0.0   456.0+5.0
34  sph  0.0 0.0 0.0   456.0
35  sph  0.0 0.0 0.0   406.0+5.0
36  sph  0.0 0.0 0.0   406.0
37  sph  0.0 0.0 0.0   356.0+5.0
38  sph  0.0 0.0 0.0   356.0
39  sph  0.0 0.0 0.0   306.0+5.0
40  sph  0.0 0.0 0.0   306.0
                        $ cones
11  kz  0.0  {( 506*sin( 4.0/180.*pi) )**2./( 506*cos( 4.0/180.*pi) )**2.} +1
12  kz  0.0  {( 506*sin( 6.0/180.*pi) )**2./( 506*cos( 6.0/180.*pi) )**2.} +1
13  kz  0.0  {( 506*sin( 7.5/180.*pi) )**2./( 506*cos( 7.5/180.*pi) )**2.} +1
14  kz  0.0  {( 506*sin(12.5/180.*pi) )**2./( 506*cos(12.5/180.*pi) )**2.} +1
15  kz  0.0  {( 456*sin( 15./180.*pi) )**2./( 456*cos( 15./180.*pi) )**2.} +1
16  kz  0.0  {( 456*sin( 25./180.*pi) )**2./( 456*cos( 25./180.*pi) )**2.} +1
17  kz  0.0  {( 456*sin( 35./180.*pi) )**2./( 456*cos( 35./180.*pi) )**2.} +1
18  kz  0.0  {( 406*sin( 45./180.*pi) )**2./( 406*cos( 45./180.*pi) )**2.} +1
19  kz  0.0  {( 356*sin( 54./180.*pi) )**2./( 356*cos( 54./180.*pi) )**2.} +1
20  kz  0.0  {( 356*sin( 66./180.*pi) )**2./( 356*cos( 66./180.*pi) )**2.} +1
21  kz  0.0  {( 306*sin(72.5/180.*pi) )**2./( 306*cos(72.5/180.*pi) )**2.} +1
22  kz  0.0  {( 306*sin(87.5/180.*pi) )**2./( 306*cos(87.5/180.*pi) )**2.} +1


[ Cell ]
1   1  -11.342  -1          $ Target

10  2  -0.00125  11 -12  -32 #1  $ Air_region in front of each detector
20  2  -0.00125  13 -14  -32 #1
30  2  -0.00125  15 -16  -34 #1
40  2  -0.00125  16 -17  -34 #1
50  2  -0.00125  17 -18  -36 #1
60  2  -0.00125  19 -20  -38 #1
70  2  -0.00125  21 -22  -40 #1

11  3  0.0   32 -31  11 -12     $ Detectors (inner void)
```

```
21  3  0.0   32 -31     13 -14
31  3  0.0   34 -33     15 -16
41  3  0.0   34 -33     16 -17
51  3  0.0   36 -35     17 -18
61  3  0.0   38 -37     19 -20
71  3  0.0   40 -39     21 -22

90  2 -0.00125  -31 #1          $ Air
                #10 #20 #30 #40 #50 #60 #70
                #11 #21 #31 #41 #51 #61 #71

99  -1          31          $ Outer void

[ Mat name color ]
mat name       color
1  C-target    brown
2  Air         {0.25 0.2 1.0}
3  Detectors   pastelmagenta

$
$ User defined values
$
set:c1[ 2*pi*( cos( 4.0/180.*pi) - cos( 6.0/180.*pi) ) ] $ solid angle for N1
set:c2[ 2*pi*( cos( 7.5/180.*pi) - cos(12.5/180.*pi) ) ] $ solid angle for N2
set:c3[ 2*pi*( cos(15.0/180.*pi) - cos(25.0/180.*pi) ) ] $ solid angle for N3
set:c4[ 2*pi*( cos(25.0/180.*pi) - cos(35.0/180.*pi) ) ] $ solid angle for N4
set:c5[ 2*pi*( cos(35.0/180.*pi) - cos(45.0/180.*pi) ) ] $ solid angle for N5
set:c6[ 2*pi*( cos(54.0/180.*pi) - cos(66.0/180.*pi) ) ] $ solid angle for N6
set:c7[ 2*pi*( cos(72.5/180.*pi) - cos(87.5/180.*pi) ) ] $ solid angle for N7

set:c8[ 6.022137d23 * 4.54 / 207.2 ]  $  factor "nt"
set:c9[ 1d24 *1000 ]                  $  factor "a" and factor "b > mb"

set:c10[c9/c1/c8]                  $ final factor for N1
set:c20[c9/c2/c8]                  $ final factor for N2
set:c30[c9/c3/c8]                  $ final factor for N3
set:c40[c9/c4/c8]                  $ final factor for N4
set:c50[c9/c5/c8]                  $ final factor for N5
set:c60[c9/c6/c8]                  $ final factor for N6
set:c70[c9/c7/c8]                  $ final factor for N7

[ T-cross ]
  part = neutron
  mesh = reg
   reg = 1
        r-in r-out area
          10   11    1.0
 e-type = 3
```

```
   ne = 100
  emin = 1e-2
  emax = 3000
  unit = 2
  axis = eng
  file = ne600pb.5.out
output = f-curr
 x-txt = {\it En}  (MeV)
 y-txt = {\it d^2  \sigma/dE_n  d\Omega}  ( mb MeV^{-1}  sr^{-1}  )
epsout = 1
factor = c10

[ T-cross ]
  part = neutron
  mesh = reg
   reg = 1
       r-in r-out area
        20   21    1.0
e-type = 3
   ne = 100
  emin = 1e-2
  emax = 3000
  unit = 2
  axis = eng
  file = ne600pb.10.out
output = f-curr
 x-txt = {\it En}  (MeV)
 y-txt = {\it d^2  \sigma/dE_n  d\Omega}  ( mb MeV^{-1}  sr^{-1}  )
epsout = 1
factor = c20

[ T-cross ]
  part = neutron
  mesh = reg
   reg = 1
       r-in r-out area
        30   31    1.0
e-type = 3
   ne = 100
  emin = 1e-2
  emax = 3000
  unit = 2
  axis = eng
  file = ne600pb.20.out
output = f-curr
 x-txt = {\it En}  (MeV)
 y-txt = {\it d^2  \sigma/dE_n  d\Omega}  ( mb MeV^{-1}  sr^{-1}  )
epsout = 1
```

```
factor = c30

[ T-cross ]
  part = neutron
  mesh = reg
   reg = 1
        r-in r-out area
         40   41    1.0
 e-type = 3
    ne = 100
  emin = 1e-2
  emax = 3000
  unit = 2
  axis = eng
  file = ne600pb.30.out
 output = f-curr
  x-txt = {\it En}  (MeV)
  y-txt = {\it d^2  \sigma/dE_n  d\Omega}  ( mb MeV^{-1}  sr^{-1}  )
 epsout = 1
 factor = c40

  [ T-cross ]
    part = neutron
    mesh = reg
     reg = 1
          r-in r-out area
           50   51    1.0
   e-type = 3
      ne = 100
    emin = 1e-2
    emax = 3000
    unit = 2
    axis = eng
    file = ne600pb.40.out
   output = f-curr
    x-txt = {\it En}  (MeV)
    y-txt = {\it d^2  \sigma/dE_n  d\Omega}  ( mb MeV^{-1}  sr^{-1}  )
   epsout = 1
   factor = c50

    [ T-cross ]
      part = neutron
      mesh = reg
       reg = 1
            r-in r-out area
             60   61    1.0
     e-type = 3
        ne = 100
```

```
  emin = 1e-2
  emax = 3000
  unit = 2
  axis = eng
  file = ne600pb.60.out
output = f-curr
 x-txt = {\it En}  (MeV)
 y-txt = {\it d^2  \sigma/dE_n  d\Omega}  ( mb MeV^{-1}  sr^{-1}  )
epsout = 1
factor = c60

[ T-cross ]
  part = neutron
  mesh = reg
   reg = 1
        r-in r-out area
         70   71    1.0
e-type = 3
    ne = 100
  emin = 1e-2
  emax = 3000
  unit = 2
  axis = eng
  file = ne600pb.80.out
output = f-curr
 x-txt = {\it En}  (MeV)
 y-txt = {\it d^2  \sigma/dE_n  d\Omega}  ( mb MeV^{-1}  sr^{-1}  )
epsout = 1
factor = c70

[ T-track ]
  part = neutron proton deuteron 3he alpha 20Ne
  mesh = xyz
x-type = 2
    nx = 100
  xmin = -5
  xmax = 5
y-type = 2
    ny = 1
  ymin = -5
  ymax = 5
z-type = 2
    nz = 100
  zmin = -5
  zmax = 1
e-type = 3
    ne = 1
  emin = 1
```

```
 emax = 4e4
 unit = 1
 axis = xz
 file = track_xz.out
gshow = 1
epsout = 1

[ T-gshow ]
  mesh = xyz
x-type = 2
    nx = 1
  xmin = -1.
  xmax = 1.
y-type = 2
    ny = 100
  ymin =  -1
  ymax = 1
z-type = 2
    nz = 100
  zmin = -1
  zmax = 1
  axis = yz
  file = gshow.out
 resol = 1
 width = 1.5
epsout = 1
 angel = noms nofr port


 [ T-3Dshow ]
      x0 = 0
      y0 = 0
      z0 = 150
 material = -1
            2
   output = 3
    l-the = -30
    l-phi = 60
    l-dst = 1500
    e-the = -35
    e-phi = 30
    w-wdt = 1000
    w-hgt = 1000
    w-dst = 800
   heaven = y
   mirror = 0
     line = 2
```

```
 r-out = 4000
shadow = 2
 x-txt = x (cm)
 y-txt = y (cm)
 z-txt = z (cm)
 angel = nofr noms
epsout = 1
  file = 3dshow.out
 resol = 10
```

Bibliography

Chapter 1

[1.1] NASDA homepage: http://www.nasda.go.jp/press/1999/03/radiat 990303a 02 j.html

[1.2] Adams Jr., et. al.: Cosmic Ray Effects on Microelectronics. Part I - The Near-Earth Particle Environment. NRL Memo. Rep. 4506- Pt. I. U.S. Navy, Aug(1981). (Available from DTIC as AD A103 897.) Cosmic Ray Effects on Microelectronics. Part IV

[1.3] NIRS homepage :http://www.nirs.go.jp/tiryou/himac/himac2.htm (in Japanese)

[1.4] Kato T. and Nakamura T.: Estimation of Neutron Yields from Thick Targets by High Energy ^{4}He Ions for the Design of Shielding for a Heavy Ion Medical Accelerator, Nucl. Instrum. Methods, A 311, 548 (1992).

[1.5] P. Cloth, D. Filges, R. D. Neef, G. Sterzenbach, Ch. Reul, T. W. Armstrong, B. L. Colborn, B. Anders, H. Brueckmann, HERMES – A Monte Carlo Program System for Beam-Materials Interaction Studies, Juel-2203, KFA Juelich, (May, 1988).

[1.6] Cecil R.A., Anderson B.D., Baldwin A.R., Madey R., Galonsky A., Miller P., Young L., and Waterman F.M.: Neutron Angular and Energy Distributions from 710-MeV Alphas Stopping in Water, Carbon, Steel and Lead, and 640-MeV Alphas Stopping in Lead, Phys. Rev. C 21, 2471 (1980).

Chapter 2

[2.1] – N. Nakao, T. Nakamura, M. Baba, Y. Uwamino, N. Nakanishi, H. Nakashima, and S. Tanaka, Nucl. Instrum. Meth. Phys. Res. A **362**, 454 (1995).

[2.2] – N. Nakao, T. Kurosawa, T. Nakamura, and Y. Uwamino, Nucl. Instrum. Meth. Phys. Res. A **463**, 275 (2001).

[2.3] – R.A. Cecil, B.D. Anderson, and R. Madey, Nucl. Instrum. Meth. **161**, 439 (1979).

[2.4] – T. Kurosawa, T. Nakamura, N. Nakao, T. Shibata, Y. Uwamino, and A. Fukumura, Nucl. Instrum. Meth. **A 430**, 400 (1999).

[2.5] – T. Kurosawa, N. Nakao, T. Nakamura, Y. Uwamino, T. Shibata, A. Fukumura, and K. Murakami, Journ. of Nucl. Sci. Tech. **36**, 41 (1999).

[2.6] – T. Kurosawa, N. Nakao, T. Nakamura, Y. Uwamino, T. Shibata, N. Nakanishi, A. Fukumura, and K. Murakami, Nucl. Sci. Eng **132**, 30 (1999).

[2.7] – T. Kurosawa, N. Nakao, T. Nakamura, H. Iwase, H. Sato, Y. Uwamino, A. Fukumura, Phys. Rev. C **62**, 044615 (2000).

[2.8] – L. Heilbronn, R.S. Cary, M. Cronqvist, F. Deák, K. Frankel, A. Galonsky, K. Holabird, Á. Horvath, Á. Kiss, J. Kruse, R.M. Ronningen, H. Schelin, Z. Seres, C. E. Stronach, J. Wang, P. Zecher, and C. Zeitlin, Nucl. Sci. Eng. **132**, 1 (1999).

[2.9] – L. Heilbronn, R. Madey, M. Elaasar, M. Htun, K. Frankel, W.G. Gong, B.D. Anderson, A.R. Baldwin, J. Jiang, D. Keane, M.A. McMahan, W.H. Rathbun, A. Scott, Y. Shao, J.W. Watson, G.D. Westfall, S. Yennello, and W.-M. Zhang, Phys. Rev. C **58**, 3451 (1998).

[2.10] – R.A. Cecil, B.D. Anderson, A.R. Baldwin, R. Madey, A. Galonsky, P. Miller, L. Young, and F.M. Waterman, Phys. Rev. C **21**, 2471 (1980).

[2.11] – R. Madey, B. D. Anderson, R. A. Cecil, P. C. Tandy, and W. Schimmerling, Phys. Rev. C **28**, 706 (1983).

Chapter 3

[3.1] – Y. Iwata, T. Murakami, H. Sato, H. Iwase, T. Nakamura, T. Kurosawa, L. Heilbronn, R.M. Ronningen, K. Ieki, Y. Tozawa, and K. Niita, Phys. Rev C **64**, 054609 (2001).

[3.2] – N. Nakao, T. Nakamura, M. Baba, Y. Uwamino, N. Nakanishi, H. Nakashima, and S. Tanaka, Nucl. Instrum. Meth. Phys. Res. A **362**, 454 (1995).

[3.3] - N. Nakao, T. Kurosawa, T. Nakamura, and Y. Uwamino, Nucl. Instrum. Meth. Phys. Res. A **463**, 275 (2001).

[3.4] – R.A. Cecil, B.D. Anderson, and R. Madey, Nucl. Instrum. Meth. **161**, 439 (1979).

[3.5] – L. Heilbronn, Y. Iwata, H. Iwase, T. Murakami, H. Sato, T. Nakamura, T. Kurosawa, R.M. Ronningen, K. Ieki, Y. Tozawa, I. Gudowska, and N. Sobolevsky, in review, 2004

[3.6] – H. Sato, T. Kurosawa, H. Iwase, T. Nakamura, Y. Uwamino, and N. Nakao, Phys. Rev. C **64**, 034607 (2001).

[3.7] – W. Schimmerling, J. W. Kast, D. Ortendahl, R. Madey, R. A. Cecil, B. D. Anderson, and A. R. Baldwin, Phys. Rev. Lett. **43** 1985 (1979).

[3.8] – R. A. Cecil, B. D. Anderson, A. R. Baldwin, R. Madey, W. Schimmerling, J. W. Kast, and D. Ortendahl, Phys. Rev. C **24**, 2013 (1981).

Chapter 4

[4.1] – T. W. Armstrong, K. C. Chandler, Nucl. Sci. Eng. **49**, 110 (1972).

[4.2] – R. E. Prael, H. Lichtenstein, "User guide to LCS: The LAHET code system," MS B226, LANL (1989).

[4.3] – A. Fasso, A. Ferrari, J. Ranft, P. R. Sala, Proceedings of the IV International Conference on Calorimetry in High Energy Physics, La Biodola, Italy (1993).

[4.4] – M. Sasaki, E. Kim, T. Nunomiya, T. Nakamura, N. Nakao, T. Shibata, Y. Uwamino, S. Ito, and A. Fukumura, Nucl. Sci. Eng. **141**, 140 (2003).

[4.5] – M. Sasaki, N. Nakao, T. Nunomiya, T. Nakamura, A. Fukumura, and M. Takada, Nucl. Instrum. Meth. B **196**, 113 (2003).

[4.6] – T. Nunomiya, S. Yonai, M. Takada, A. Fukumura, and T. Nakamura, Rad. Prot. Dosim., **106**, 207 (2003).

[4.7] – G. I. Britvich, A. A. Chumakov, R. M. Ronningen, R. A. Blue, and L. H. Heilbronn, Rev. Sci. Instrum. **70**, 2314 (1999).

[4.8] – M. Sasaki, M. Nakao, T. Shibata, N. Nakao, and T. Nakamura, Nucl. Instrum. and Meth. A **446**, 545 (2000).

[4.9] – M. Sasaki, N. Nakao, T. Nunomiya, T. Nakamura, T. Shibata, and A. Fukumura, J. Nucl. Sci. Technol. (Suppl. 1) 794 (March 2000).

[4.10] – M. Sasaki, N. Nakao, T. Nunomiya, T. Nakamura, T. Shibata, and A. Fukumura, J. Nucl. Sci. Technol. **38** 8 (2001).

[4.11] – M. Sasaki, N. Nakao, T. Nakamura, T. Shibata, and A. Fukumura, Nucl. Instrum. and Meth. A, **480**, 440 (2002).

[4.12] – N. V. Mokhov , "The Mars Code System User's Guide", Fermilab-FN-628 (1995), N. V. Mokhov and O. E. Krivosheev, "MARS Code Status" Fermilab-Conf-00/181 (2000), http://www-ap.fnal.gov/MARS

[4.13] – E. A. Belogorlov and V. P. Zhigunov, Nucl. Instrum. Meth A **235**, 146 (1985).

[4.14] – T. Nakamura, Nucl. Instrum. Meth. A **240**, 207 (1985).

[4.15] – J. D. Nachtigall and F. Rohlaff, Nucl. Instrum. Meth **50**, 137 (1967).

Chapter 5

[5.1] – J. B. Cumming, P. E. Haustein, R. W. Stoenner, L. Mausner and R. A. Naumann, "Spallation of Cu by 3.9-GeV ^{14}N ions and 3.9-GeV protons", Phys. Rev. C 10, 739 (1974).

[5.2] – J. B. Cumming, R. W. Stoenner and P. E. Haustein, "Spallation of copper by 25-GeV ^{12}C ions and 28-GeV protons", Phys. Rev. C 14, 1554 (1976).

[5.3] – J. B. Cumming, P. E. Haustein, T. J. Ruth, and G. J. Virtes, "Spallation of copper by 80-GeV ^{40}Ar ions", Phys. Rev. C 17, 1632 (1978).

[5.4] – N. T. Porile, G. D. Cole, and C. R. Rudy, "Nuclear reactions of silver with 25.2 GeV ^{12}C ions and 300 GeV protons", Phys. Rev. C 19, 2288 (1979).

[5.5] – K. H. Hicks, T. E. Ward, H. Bowman, J. G. Ingersoll, J. O. Rasmussen, J. P. Sullivan, M. Koike, and J. Peter, "Interaction of 4.22-GeV and 7.54-GeV ^{20}Ne and Cu", Phys. Rev. C 26, 2016 (1982).

[5.6] – Y. K. Kim, J. C. Kim, C-B Moon, S. Y. Cho, Y. H Chung, Y. Ohkubo, "Heavy-ion reactions of Cu with 135 MeV/nucleon ^{12}C", Nucl. Phys. A578, 621 (1994).

[5.7] – H. Yashima, Y. Uwamino, H. Iwase, H. Sugita, T. Nakamura, S. Ito, and A. Fukumura, "Measurement and calculation of radioactivities of spallation products by high-energy heavy ions", Radio Chimica Acta 91, 689 (2003).

[5.8] – H. Yashima, "Study on the nuclide-production cross-sections and the spatial distribution of radioactivities in materials for spallation reactions of high-energy heavy-ions", Ph.D. Thesis, Tohoku University, Sendai, Japan, (March 2004).

[5.9] – H. Yashima, H. Sugita, T. Nakamura, S. Ito, and A. Fukumura, Phys. Rev. C 66, 044607 (2002).

[5.10] – H. Yashima, H. Sugita, T. Nakamura, T. Shiomi, Y. Uwamino, S. Ito, and A. Fukumura, J. Nucl. Sci. Technol. Supplement 2, 1179 (2002).

[5.11] – H. Yashima, Y. Uwamino, H. Sugita, S. Ito, T. Nakamura, and A. Fukumura, "Induced Radioactivity in Cu targets produced by high-energy heavy ions and the corresponding estimated photon dose rates", Radiat. Prot. Dosim. 112, 195-208 (2004).

[5.12] – H. Yashima, Y. Uwamino, H. Iwase, H. Sugita, T. Nakamura, S. Ito, and A. Fukumura, "Cross sections for the production of residual nuclides by high-energy heavy-ions", Nucl. Instrum. Meth. B, 226, No. 3, 243-263 (2004).

[5.13] – Yu. E. Titarenko, V. F. Batyaev, V. M. Zhivun, A.B. Koldobsky, Yu.V. Trebukhovsky, E.I. Karpikhin, R.D. Mulambetov, S.V. Mulambetova, Yu.V. Nekrasov, A.Yu. Titarenko, K.A. Lipatov, B.Yu. Sharkov, A.A. Golubev, A.D Fertman, V.I Turtikov, A.V. Kantsyrev, I.V Roudskoy, G.N. Smirnov, V. S. Barashenkov, K. Gudima, M. Baznat, S.G. Mashnik, and R.E. Prael, published in the conference proceedings of the AccApp'03 conference held in San Diego, CA, USA June 2003.

Chapter 6

[6.1] – T. C. Awes, G. Poggi, S. Sanni, C. K. Gelbke, T. Legrain, and G. D. Westfall, Phys. Lett., **103B**, 417 (1981).

[6.2] – B. A. Remington, G. Caskey, A. Galonsky, C. K. Gelbke, L. Heilbronn, J. Heltsley, M. B. Tsang, F. Deak, A. Kiss, Z. Seres, J. Kasagi, and J. Kolata, Phys. Rev. C **34**, 1685 (1986).

[6.3] – F. Deak, A. Kiss, Z. Seres, C. Caskey, A. Galonsky, C. K. Gelbke, B. Remington, M. B. Tsang, and J. J. Kolata, Nucl. Phys. **A464**, 133, (1987).

[6.4] – C. Bloch, W. Benenson, A. I. Galonsky, E. Kashy, J. Heltsley, L. Heilbronn, M. Lowe, R. J. Radtke, B. Remington, J. Kasagi, D. J. Morrissey, Phys. Rev. C **37**, 2469 (1988).

[6.5] – A. Kiss, F. Deak, Z. Seres, G. Caskey, A. Galonsky, B. Remington, Phys. Rev. C **38**, 170 (1988).

[6.6] – D. Sackett, A. Galonsky, C. K. Gelbke, H. Hama, L. Heilbronn, D. Krofcheck, W. Lynch, H. R. Schelin, M. B. Tsang, X. Yang, F. Deak, A. Horvath, A. Kiss, Z. Seres, J. Kasagi and T. Murakami, Phys. Rev. C **44**, 384 (1991).

[6.7] – K. Ishibashi, K. Higo, S. Sakaguchi, Y. Matsumoto, Y. Wakuta, H. Takada, T. Nishida, Y. Nakahara, and Y. Kaneko, J. Nucl. Sci. Technol. **29**, 499 (1992).

[6.8] – H. R. Schelin, A. Galonsky, C. K. Gelbke, H. Hama, L. Heilbronn, D. Krofcheck, W. Lynch, D. Sackett, , M. B. Tsang, X. Yang, F. Deak, A. Horvath, A. Kiss, Z. Seres, J. Kasagi and T. Murakami, Nucl. Sci. Eng. **113**, 184 (1993).

[6.9] – T. Kato, T. Kurosawa, and T. Nakamura, Nucl. Instrum. Meth. **A480**, 571 (2002).

[6.10] – Y. Iwata, T. Murakami, H. Sato, H. Iwase, T. Nakamura, T. Kurosawa, L. Heilbronn, R.M. Ronningen, K. Ieki, Y. Tozawa, and K. Niita, Phys. Rev C **64**, 054609 (2001).

[6.11] – R. Serber, "The Production of High Energy Neutrons by Stripping", Phys. Rev. **72**, 1008 (1947).

Appendix

[A.1] – H. Iwase, K. Niita and T. Nakamura, "Development of General-Purpose Particle and Heavy Ion Transport Monte Carlo Code", Journ. Nucl. Sci. Tech., **39**, 1142-1151 (2002).

[A.2] – K. Niita, H. Takada, S. Meigo, Y. Ikeda, *Nucl. Instrum. Methods* **B184**, 406 (2001).

[A.3] – Y. Nara, N. Otuka, A. Ohnishi, K. Niita, S. Chiba, *Phys. Rev.* **C61**, 024901 (1999).

[A.4] – S. Furihata, *Nucl. Instrum. Methods*, **B171**, 251 (2000).

[A.5] – S. Wen-quinf, W. Bing, F. Jun, Z. Wen-logn, Z. Yong-tai, F. En-pu, *Nucl. Phys.*, **A491**, 130 (1989).

[A.6] – T. W. Armstrong, K. C. Chandler, ORNL-4869, Oak Ridge National Laboratory (1973).

[A.7] – K. Niita, S. Chiba, T. Maruyama, H. Takada, T. Fukahori, Y. Nakahara, A. Iwamoto, *Phys. Rev.* **C52**, 2620 (1995).

[A.8] – Y. Iwata, T. Murakami, L. Heilbronn, H. Sato, H. Iwase, T. Nakamura, T. Kurosawa, R. M. Ronningen, K. Ieki, Y. Tozawa, and K. Niita, *Phys. Rev.* **C64**, 054609 (2001)

[A.9] – Judith F. Briesmeister, Editor, MCNP4C manual (LA–13709–M), Los Alamos National Laboratory, USA (2000)

Index

Handbook on Secondary Particle Production and Transport by High-Energy Heavy Ions

(with CD-Rom)

This handbook is a timely resource for the rapidly growing field of heavy-ion transport-model theory and its applications to the fields of accelerator development, heavy-ion radiotherapy, and shielding of accelerators and in space.

Data from over 20 years of experiments in the production of secondary neutrons and spallation products are contained in the handbook, and are available on the accompanying CD. Transport modelers and experimentalists will find the detailed descriptions of the experiments and subsequent analyses to be a valuable aid in utilizing the data for their particular applications.

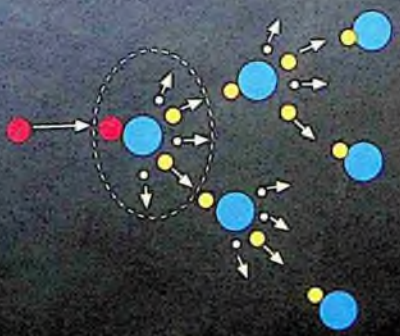

World Scientific
www.worldscientific.com
5973 hc

ISBN 981-256-558-2
9 789812 565587